

Understanding the Ultrafast Dynamics of Molecular Rotor based Probes in Amyloid Fibrils

By

Aruna Kumar M

CHEM01201204001

Bhabha Atomic Research Center

Mumbai

*A thesis submitted to the
Board of Studies in Chemical Sciences*

*In partial fulfillment of requirements
for the Degree of*

DOCTOR OF PHILOSOPHY

of

HOMI BHABHA NATIONAL INSTITUTE



August, 2017

STATEMENT BY AUTHOR

This dissertation has been submitted in partial fulfillment of requirements for an advanced degree at Homi Bhabha National Institute (HBNI) and is deposited in the Library to be made available to borrowers under rules of the HBNI.

Brief quotations from this dissertation are allowable without special permission, provided that accurate acknowledgement of source is made. Requests for permission for extended quotation from or reproduction of this manuscript in whole or in part may be granted by the Competent Authority of HBNI when in his or her judgment the proposed use of the material is in the interests of scholarship. In all other instances, however, permission must be obtained from the author.

(Aruna Kumar M)

DECLARATION

I, hereby declare that the investigation presented in the thesis has been carried out by me. The work is original and has not been submitted earlier as a whole or in part for a degree / diploma at this or any other Institution / University.

(Aruna Kumar M)

List of Publications arising from the thesis

Journal

1. Effect of fibrillation on the excited state dynamics of Tryptophan in serum protein- A Time resolved fluorescence study. **A. K. Mora**, S. Murudkar, P. K. Singh, S. Nath. *J. Photochem. Photobiol. A: Chem.* **2015**, 299, 73-79.
2. Benzothiazole based neutral ratiometric fluorescence sensor for amyloid fibril. **A. K. Mora**, S. Murudkar, A. Alamelu, P. K. Singh, S. Chattopadhyay, S. Nath. *Chem. Euro. J.*, **2016**, 22, 16505-16512.
3. PicoGreen: A superior amyloid probe than Thioflavin-T. **A. K. Mora**, P. K. Singh, B. S. Patro, S. Nath. *Chem. Comm.* **2016**, 52, 12163-12166.
4. Photophysical studies of benzothiazole based neutral amyloid probe. **A. K. Mora**, S. Murudkar, A. Alamelu, P. K. Singh, S. Chattopadhyay, S. Nath. (manuscript under preparation).
5. SYPRO Orange as a sensitive zwitterionic probe for amyloid fibril. **A. K. Mora** et al. (manuscript under preparation).
6. Ultrafast excited state dynamics of cyanine based a novel amyloid probe: PicoGreen. **A. K. Mora** et al. (manuscript under preparation).

Conferences

1. Controlled transfer of Intercalated drug from DNA to a mixed micellar phase, **A. K. Mora**, S. Murudkar, P. K. Singh, S. Nath; National symposium on Radiation & Photochemistry (NSRP) - 2013 at North-East Hill University, Shillong
2. Hydration dynamics in protein and fibril probed by intrinsic tryptophan fluorescence **A. K. Mora**, S. D. Murudkar, P. K. Singh, S. Nath. Trombay Symposium on Radiation & Photochemistry (TSRP-2014) at BARC, Mumbai.
3. 2DIR study of small molecular probe, azide ion, in AOT reverse micelles **A. K. Mora**, P. K. Singh S. Nath TSRP-2016 at BARC, Mumbai
4. Ultrafast dynamics in imidazolium based ionic liquids: A 2DIR study. **A. K. Mora**, P. K. Singh S. Nath UFS-2016 at BARC, Mumbai

Others

7. Probing the DNA–ionic liquid interaction using an ultrafast molecular rotor. P. K. Singh, J. Sujana, **A. K. Mora**, S. Nath *J. Photochem. Photobiol. A: Chem.* **2012**, *246*, 16-22.
8. Ultrafast excited state dynamics of an environmental pollutant, 1-Nitropyrene: Effect of H-bonding. **A. K. Mora**, S. Murudkar, P. K. Singh, N. S. K. Gowthaman, T. Mukherjee, S. Nath. *J. Photochem. Photobiol. A: Chem.* **2013**, *271*, 24– 30.
9. Photophysics of Soret-excited free base tetraphenylporphyrin and its zinc analog in solution. M. Ghosh, **A. K. Mora**, S. Nath, A. K. Chandra, A. Hajra, S. Sinha, *Spectrochim. Acta Part A: Mol. Biomol. Spectroscopy*, **2013**, *116*, 466-472
10. Ultrafast molecular rotor based DNA sensor: An insight into the mode of interaction. S. Murudkar, **A. K. Mora**, S. Jakka, P. K. Singh, S. Nath. *J. Photochem. Photobiol. A: Chem.* **2014**, *295*, 17-25
11. Dynamics under Confinement: Torsional Dynamics of Auramine O in a Nanocavity. P.K. Singh, **A. K. Mora**, S. Murudkar, S. Nath. *RSC Adv.*, **2014**, *4*, 34992-35002.
12. Ultrafast molecular rotor based ternary complex in a nanocavity: A potential “turn on” fluorescence sensor for hydrocarbon chain. S. Murudkar, **A. K. Mora**, P.K. Singh, T. Bandyopadhyay, S. Nath. *Phys. Chem. Chem. Phys.*, **2015**, *17*, 5691-5703.
13. Ultrafast Torsional Dynamics of Thioflavin-T in an Anionic Cyclodextrin Cavity. P.K. Singh, S. Murudkar, **A. K. Mora**, S. Nath. *J. Photochem. Photobiol. A: Chem.* **2015**, *298*, 40-48.
14. Photoinduced electron transfer from Zinc tetraphenylporphyrin to 2 nitrofluorene in polar solvent acetonitrile. M. Ghosh, **A. K. Mora**, S. Nath, P. H. Kumar, P. R. Bangal, S. Sinha *J. Photochem, Photobiol. A: Chem.*, **2015**, *306*, 55-65.
15. Ultrafast fluorescence spectroscopy reveals a dominant weakly-emissive population of fibril bound thioflavin-T. P. K. Singh, **A.K. Mora**, S. Nath. *Chem. Comm.*, **2015**, *51*, 14042-14045.
16. Ultrafast Torsional Relaxation of Thioflavin-T in Tris(pentafluoroethyl) trifluorophosphate (FAP) Anion-Based Ionic Liquids. P. K. Singh, **A. K. Mora**, S. Nath. *J. Phys. chem. B.* **2015**, *119*, 14252-14260.
17. Fluorescence quenching of 9-cyanoanthracene by metallo-octaethylporphyrins in cyanobenzene. M. Ghosh, B. Roy, K. Majhi, **A. K. Mora**, S. Nath, S. Sinha. *J. Porphyrins Phthalocyanines*, **2015**, *19*, 1063-1071.

18. Free volume dependence of an ionic molecular rotor in Fluoroalkylphosphate (FAP) based ionic liquids. P. K. Singh, **A. K. Mora**, S. Nath. *Chem. Phys. Lett.* **2016**, *644*, 296-301.
19. Controlled sequestration of DNA intercalated drug by polymer-surfactant supramolecular assemblies. **A. K. Mora**, P. K. Singh, S. Nath. *J. Phys. Chem. B.* **2016**, *120*, 4143-4151.
20. Interaction of a Julolidine-based Neutral Ultrafast Molecular Rotor with Natural DNA: Spectroscopic and Molecular Docking Studies. R. Kalel, **A. K. Mora**, R. Ghosh, D. Dhavale, D. K. Palit, S. Nath. *J. Phys. Chem. B*, **2016**, *120*, 9843–9853.
21. Ultrafast Dynamics of Hydrogen Bond Breaking and Making in the Excited State of Fluoren-9-one: Time-Resolved Visible Pump–IR Probe Spectroscopic Study. R. Ghosh, **A. K. Mora**, S. Nath, D. K. Palit. *J. Phys. Chem. B*, **2017**, *121*, 1068–1080.
22. Synergistic enhancement in the drug sequestration power and reduction in cytotoxicity of surfactant. R. Kalel, **A. K. Mora**, R. Ghosh, D. Dhavale, D. K. Palit, S. Nath. *Phys. Chem. Chem. Phys.* 2017, **19**, 25446-25455.

(Aruna Kumar M)

Dedicated to

My Family

ACKNOWLEDGEMENTS

I would like to take this opportunity to acknowledge everyone who supported me during throughout this thesis. I would like to express my deepest gratitude to my Ph.D guide, **Dr. Sukhendu Nath**, for his aspiring guidance, constant encouragement, motivation and good wishes. His enthusiasm, wide knowledge, critical thinking of scientific problem greatly helped me during this work. I'm also grateful to him for critically reviewing this thesis with patience.

It gives me immense pleasure to thank my senior colleague, **Dr. Prabhat K. Singh**, for his technical help, fruitful scientific discussions and moral support given to time from time to time throughout the course of my work.

My special thanks to my friend, lab mate, **Sushant Murudkar**, for his cooperative attitude, diversified help and several funs, which I will cherish in my life. I wish to express sincere thanks to all MPS members for creating such friendly, cooperative and competitive environment in the lab. I'm highly grateful to my doctoral committee members **Dr. S. Chattopadhyay** (Chairman), **Dr. H. Pal** (Member), **Dr. D. K. Palit** (Member) and **Dr. B. S. Patro** (Member) for their critical review and suggestions during the progress review and pre-synopsis seminar.

I also extend many thanks to my gang **Mhejabeen di, Chandralekha, Shalini, Snehal, Krishna, Sushant, Jerina, Juby, Neha, Sunil, Veer, Shailesh, Ahmed, GM, Dilip, Vivek, Yusuf, Suresh, Sugosh, Bhavana, Hari** for their support during the period of my doctoral work. I would like to appreciate my roommates, **Ganesh, Ramamohan, and Sunil** for being there for me all the time. It gives me an immense pleasure in thanking my dear friends **Siva, Anand, Chanty, Prasanth, Radha, Kishore, Pratap** who always encouraged and supported me in all aspects.

Most importantly, I owe a special gratitude to my parents and grandparents for their love and encouragement. Finally, I would like to thank my wife, **Meenu**, who has been my closest company on this journey. Words will fail me to express my appreciation for her whose love and care has taken the load off my shoulder. I take this opportunity to express my deepest gratitude to her.

CONTENTS

	Page No
Synopsis	i-x
List of Figures	xi-xx
List of tables	xxi-xxii
Chapter1 Introduction	1-36
1.1 General introduction about amyloid fibrils	1
1.2 Techniques for the characterization of amyloid fibrils	7
1.2.1 Imaging techniques	8
1.2.2 Fluorescence imaging of amyloid fibrils	9
1.3 Classification of amyloid probes based on excited state processes	12
1.3.1 Intramolecular charge transfer (ICT)	12
1.3.2 Fluorescence resonance energy transfer (FRET)	19
1.3.3 Aggregation induced quenching (AIQ) and enhancement (AIE)	22
1.3.4 Ultrafast molecular rotors (UMR)	24
1.4 Classification based on molecular structure	27
1.4.1 Congo Red based molecules	27
1.4.2 Thioflavin T based molecules	28
1.4.3 Curcumin based molecules	30
1.4.4 Luminescent conjugated polymers	31
1.4.5 Cyanine based molecules	32

1.4.6 BODIPY based molecules	33
1.4.6 Other probes	33
Chapter 2 Instruments and Methods	37-64
2.1 Introduction	37
2.2 Ground state absorption measurements	37
2.3 Steady state fluorescence measurements	39
2.4 Fluorescence lifetime measurements	40
2.4.1 Basic principles of TCSPC technique	41
2.4.2 Important components of TCSPC spectrometer	42
2.4.3 Analysis of the fluorescence decay curves	46
2.5 Fluorescence anisotropy measurements	49
2.6 Fluorescence upconversion measurements	52
2.6.1 Basic principle of fluorescence upconversion	52
2.6.1.1 Sum-frequency generation	52
2.6.1.2 Time resolution	55
2.6.1.3 Instrument response function	58
2.7 Fluorescence microscopy	59
2.7.1 Principle	60
2.7.2 Epi fluorescence microscope	61
2.7.3 Confocal microscope	62
2.8 Quantum chemical calculations	63
2.9 Molecular docking studies	63

Chapter 3 PicoGreen as amyloid fibril sensor and deciphering its ultrafast dynamics 65-112

3.1 Introduction	65
3.2 Materials and methods	68
3.3 Results and discussion	72
3.3.1 Steady state emission measurements	72
3.3.2 Time resolved fluorescence measurements	74
3.3.3 Time resolved anisotropy studies	76
3.3.4 Effect of ionic strength	78
3.3.5 Comparison with standard amyloid staining dye Thioflavin T	79
3.3.6 Competitive binding and energy transfer studies	82
3.3.7 Quantum chemical calculations and molecular docking studies	85
3.3.8 Photophysical studies of PG	88
3.3.8.1 Steady state fluorescence measurements	88
3.3.8.2 Time resolved fluorescence studies	91
3.3.8.3 Effect of viscosity on ultrafast dynamics of PG	99
3.3.8.4 Effect of polarity on ultrafast dynamics of PG	104
3.3.8.5 Dynamics of PG in insulin fibril	107
3.5 Conclusions	110

Chapter 4 Synthesis, Photophysics and interaction with amyloid fibrils of neutral benzothiazole derivative 113-148

4.1	Introduction	113
4.2	Materials and methods	116
4.3	Synthesis and characterization of 2Me-DABT	119
4.3.1	Synthesis of 4-(dimethylamino)-2 methyl benzaldehyde	119
4.3.2	Synthesis of 2Me-DABT	120
4.4	Results and discussion	120
4.4.1	Photophysical studies of 2Me-DABT	120
4.4.1.1	Ground state absorption studies	120
4.4.1.2	Steady state fluorescence measurements	122
4.4.1.3	Time resolved fluorescence studies	128
4.4.1.4	Isotope effect	131
4.4.2	Interaction with insulin fibrils	133
4.4.2.1	Steady state fluorescence measurements	133
4.4.2.2	Time resolved measurements	137
4.4.2.3	Fluorescence microscopic studies	139
4.4.2.4	Energy transfer studies	139
4.4.2.5	Quantum chemical calculations and molecular docking studies	143
4.5	Conclusions	146
Chapter 5 Zwitterionic SYPRO Orange as sensitive amyloid probe		149-185
5.1	Introduction	149
5.2	Materials and methods	152
5.3	Results and discussion	153

5.3.1	Ground state absorption studies	153
5.3.2	Steady state fluorescence measurements	155
5.3.3	Time resolved fluorescence measurements	157
5.3.4	Comparison of SYPRO Orange with Thioflavin T	159
5.3.4.1	Steady state fluorescence spectra	159
5.3.4.2	Fluorescence microscopic studies	161
5.3.4.3	Limit of detection	162
5.3.5	Mechanistic investigation of binding modes of SYPRO Orange with fibrils	164
5.3.5.1	Effect of ionic strength	164
5.3.5.2	Effect of solvent polarity	165
5.3.5.3	Effect of solvent viscosity	170
5.3.5.4	Effect of hydrogen bonding	175
5.3.5.5	Effect of aggregation	177
5.3.5.6	Mechanism of binding of SYPRO Orange to insulin fibrils	181
5.3.6	Quantum chemical calculations and Molecular docking studies	182
5.4	Conclusions	184
Chapter 6	Solvation dynamics in amyloid fibrils	186-204
6.1	Introduction	186
6.2	Materials and methods	189
6.3	Results and Discussion	190
6.3.1	HSA fibril formation	190

6.3.2 Steady state fluorescence measurements	192
6.3.3 Time resolved fluorescence measurements	193
6.3.4 Time resolved anisotropy studies	201
6.4 Conclusions	202
Chapter 7 Summary and Outlook	205-208
References	209-223

Synopsis

Aggregation of proteins, especially caused by the physical and chemical instability is one of the major problems that are related to many scientific fields ranging from biochemistry, biophysics to pharmaceutical and medical sciences.¹⁻³ Amyloid fibrils, a filamentous form of aggregated protein, are responsible for several neurological diseases such as Alzheimer's, Parkinson's, Type 2 diabetes, etc. As of now, more than twenty diseases have been implicated to be associated with the formation of amyloid fibrils in different tissues and organs.⁴⁻⁸ The amyloid fibrils are characterized by the presence of common β -sheet structure which is irrespective of constituent polypeptides indicates the aggregation into amyloid fibrils is a generic nature of proteins.

The early diagnosis and therapy of amyloidosis is crucially depend on techniques that can lead to sensitive detection of these fibrils or plaques both *in-vitro* and *in-vivo*⁹ and thus it is of great significance to develop such methods and techniques. Neuro imaging using magnetic resonance imaging (MRI), positron emission tomography (PET) and single photon emission computed tomography (SPECT), are currently used for the detection of amyloid related diseases.⁹ However, various factors such as low sensitivity of MRI probes, high cost, narrow isotope availability and radioactivity of PET probes limits their usage. Therefore, relatively inexpensive and simple technologies for amyloid imaging have recently attracted the attention of researchers. One of such promising alternative to the existing technologies is the optical imaging using amyloid specific fluorescence probes.

Thioflavin-T (ThT), a benzothiazole based molecule, is considered as gold standard amyloid stain and has been used for the amyloid detection since its discovery

in 1958. However, recently it has been shown that ThT itself promotes protein fibrillation by stabilizing the ordered β -sheet like conformations.¹⁰ Additionally, emission of ThT in amyloid fibrils depends on the external conditions, like pH and ionic strength, etc¹¹. Recently, our group has shown that only 10% of the amyloid bound ThT are responsible for its fluorescence enhancement.¹² It has been shown that molecular rotors based molecules show significant changes in their photophysical properties upon binding with amyloid fibril. However, such probes are less sensitive than ThT¹³. In this regard, recently we have shown that one of the cyanine based molecular rotor has high affinity towards the amyloid fibril with large emission enhancement and the result will be discussed in chapter 3 of the thesis.

The positive charge on the ThT makes it difficult to penetrate the Blood Brain Barrier (BBB) and hence, cannot be used for *in-vivo* detection of amyloid fibrils. A neutral analogue of ThT can increase the penetration through the BBB. Several neutral analogue of ThT has been reported to bind the amyloid fibril but without any modulation in their optical properties and hence cannot be used for the optical imaging.⁹ In this regard, we have successfully designed a neutral ThT analogue which shows significant modulation in its photophysical properties upon binding to amyloid fibrils. In chapter 4, synthesis, photophysics and binding interaction of this neutral ThT analogue with amyloid fibrils will be discussed.

To avoid the interference from the cellular auto fluorescence in cellular amyloid imaging, probes with longer emission wavelength is desired. It has been reported that apart from neutral molecules, zwitterionic probes have been also shown to be promising in neuro imaging as they have capability of the BBB penetration.¹⁴

The interaction between amyloid fibrils and a zwitterionic fluorescence probe with long wavelength emission has been investigated, and will be presented in chapter 5.

Apart from the detection, the dynamics in amyloid fibrils also plays important role in understanding the structure and the nature of amyloid fibrils. Thus, it is very important to understand the dynamical nature of the amyloid fibrils. Studies on amyloid fibrils are mostly focused on the effect of protein's sequence, conformation, and external conditions such as pH, ionic strength^{1,15-17} etc, but the most important constituent of biological system,¹⁸ water, has been treated as spectator. In fact, it has been shown that water assists the protein to aggregate. Actually, initial water- protein electrostatic interactions play a vital role in protein aggregation.¹⁹ This shows importance of the understanding of the dynamics of water in fibril and their modulation due to fibrillation. Dynamics of water molecules in amyloid fibrils have been investigated and compared with native protein and results will be discussed in chapter 6.

Chapter 1: Introduction

This chapter deals with the general introduction about the structure and importance of amyloid fibrils especially on the perspective of its general structural properties. Details about the variety of interactions that can be offered by the amyloid fibrils will be presented. Techniques currently used for the detection, diagnosis and evaluation of therapeutic drugs for the amyloidosis will be discussed. The advantages of fluorescence based probes over the other probes and the current status of the fluorescent based amyloid imaging probes will be described. Further, the need for the new, sensitive, efficient amyloid fluorescent markers and the present approaches for

the designing aspects will be highlighted. Later part of this chapter deals with the general introduction about the photophysical processes with the emphasis on the possible excited state dynamics will be presented. The chapter ends with the scope of the work and future perspectives in the field presented in this dissertation.

Chapter 2: Experimental techniques

Brief description on the experimental techniques used in the work, presented in this dissertation, will be presented. Basic working principles of spectroscopic techniques such as spectrophotometry, spectrofluorimetry and fluorescence imaging techniques like epifluorescence and confocal fluorescence microscopy will be described. Working principles of time-resolved emission techniques, like, time-correlated single photon counting (TCSPC) and femtosecond fluorescence upconversion, will be discussed in greater detail as they are extensively used in the work presented in this thesis. Finally, quantum chemical calculations and blind molecular docking used in this work will be presented briefly.

Chapter 3: PicoGreen (PG) as amyloid fibril sensor and deciphering its ultrafast dynamics

First half of this chapter describes about the screening of PicoGreen as new sensitive amyloid probe and its comparison with Thioflavin T. It is seen that PG, a cyanine based molecular rotor, interact strongly with protein fibrils with ~1000 fold increase in its emission yield. Further, under similar condition, only 400 times emission enhancement has been observed for gold standard amyloid probe, ThT. Detailed binding analysis reveals that only one mode of binding exists between PG

and fibril with large binding affinity. PG can also probe fibrillation kinetics similar to ThT. Fluorescence microscopy studies revealed that under similar conditions, PG give brighter images compared to ThT. Time-resolved emission studies shows that the excited state lifetime of PG increases from 1.5 ps in water to 3.45 ns in amyloid fibril indicating extensive modulation in the excited state dynamics of PG upon binding with amyloid fibrils. Unlike ThT, interaction between cationic PG and amyloid fibrils is unaffected by the ionic strength of the medium suggesting that the hydrophobic forces are primarily responsible for the PG-fibril interaction. The competitive binding studies shows that ThT and PG has distinct binding sites in amyloid fibril and they are separated by ~ 52 Å. Blind molecular docking studies have been performed to understand the binding of PG in fibril. Docking studies further supports distinct binding sites for ThT and PG in amyloid fibrils.

In the second part of this chapter, detailed photophysical properties of PG has been investigated to understand the fundamental mechanism that is responsible for its amyloid sensing activity. Steady-state emission studies show that viscosity of the solvents largely modulates the emission yield of PG indicating the presence of a non-radiative torsional motion of large amplitude in its excited state. Detailed femtosecond resolved transient emission studies in solvents with different polarity and viscosity indicates the presence of faster excited state decay which is independent of the solvent viscosity. Such, faster decay is followed by a relative slower decay that is largely controlled by the solvent viscosity. Detail analysis of the excited state dynamics revealed that the ultrafast intramolecular charge transfer (ICT) process takes place within ~ 200 fs which precedes the bond twisting leading to the formation of twisted ICT (TICT) state. In case of insulin fibril, the torsional dynamics of PG has been

slowed down and extends over nanosecond region. Such extensive retardation in the non-radiative torsional motion is claimed to be primarily responsible for the observed large increase in its emission yield upon binding with amyloid fibrils.

Chapter 4: Synthesis, Photophysics and interaction with amyloid fibrils of neutral benzothiazole derivative.

First part of this chapter presents the details of synthesis, photophysical properties of a neutral analog of ThT, 2-[2'-Me,4'-(dimethylamino)phenyl] benzothiazole (2'-Me-DABT). 2'-Me-DABT has been synthesized by the formylation of N,N,3-trimethylaniline by Vilsmeier-Haack reaction followed by the condensation reaction with 2-amino thiophenol. Unlike, ThT, emission characteristics of 2'-Me-DABT is found to be very sensitive to solvent polarity and independent on the solvent viscosity indicating absence of torsional motion in the excited state of 2'-Me-DABT. Fluorescence spectra of 2'-Me-DABT in solvents of varying polarity suggested that it is very good solvatochromic dye. From detailed photophysical studies, it has been understood that in aprotic solvents, the Stokes' shift follows a linear relationship with solvent polarity function, Δf and has excited state dipole moment of 10.8D. However, in protic solvents, variation in the Stokes' shift with Δf shows a break at Δf values of 0.30. The excited state dipole moment is estimated to be 12.1 and 19.1 D for protic solvents with Δf values <0.30 and >0.30 respectively. Such high dipole moment of the excited state indicates the ICT nature of the excited state. Formation of ICT is also supported by the fact that both electron donating anilino moiety and electron accepting benzothiazole moiety are present in 2'-Me-DABT. The fluorescence quantum yield decreases slowly in low polar protic solvents and falls down drastically in high polar

protic solvents. From detail analysis of radiative and non-radiative rate constants, it is inferred that H-bond assisted additional non-radiative process is responsible for such drastic decrease in the quantum yield in protic solvents. Role of H-bonding is confirmed by the isotopic effect on the photophysical properties of 2'-Me-DABT.

In the second half of this chapter, the interaction of 2'-Me-DABT with the insulin fibrils will be presented. The emission intensity of 2'-Me-DABT in water increases by ~65 times and a blue shift of ~55 nm in emission maxima is observed upon interaction with insulin fibrils. Such spectral shift makes 2'-Me DABT a very good ratiometric sensor for amyloid fibrils. The advantages of such properties in view of amyloid imaging agent will be projected. Two modes of binding is observed for 2'-Me-DABT in fibrils with binding constant very similar to that for ThT. Dye replacement experiments revealed that ThT and 2'-Me-DABT do not share same binding location. Large overlap of emission of 2'-Me-DABT and absorption spectra of ThT in insulin fibril leads to energy transfer from photoexcited 2'-Me-DABT to ThT in amyloid fibrils. The mean separation between 2'-Me-DABT and ThT in amyloid fibrils has been estimated to be 42 Å by using Forster theory of energy transfer. The nature of binding and structure of 2'-Me-DABT and ThT in amyloid fibrils has also been investigated through blind molecular docking studies.

Chapter 5: Zwitterionic SYPRO Orange as sensitive amyloid probe

This chapter contains the results of the interaction of a zwitterionic stilbazolim based probe, SYPRO Orange (SO) with amyloid fibrils. SO shows remarkable fluorescence enhancement of ~1200 fold along with large blue shift of ~40 nm in its emission upon binding with amyloid fibrils. Detailed spectral analysis shows that

there are two modes of binding interactions between SO and fibril. Fluorescence microscopic studies revealed that SO gives brighter images of the fibril than ThT under similar conditions. Fluorescence studies also show that the limit of detection (LOD) for SO is 35 times lower than ThT which makes it an efficient amyloid probe. The mechanism for such large fluorescence enhancement of SO upon binding with amyloid fibrils has been understood from the basic photophysics of SO in molecular solvents of different properties, like polarity, viscosity, H-bonding ability etc. From the polarity dependent studies it has been revealed that SO acts as solvatochromic dye. Additionally, it is seen that the quantum yield of SO drastically reduces with increase in the solvent polarity. Increase in solvent viscosity also causes increase in its emission yield along with a blue shift in the emission spectrum. H-bonding with solvent molecules leads to red shift in absorption spectra. The photophysics in methanol-water mixtures indicate the formation of aggregates in aqueous solution. From all these detailed experiments, we have concluded that at low concentration of fibril (1 μ M), SO aggregates break and bind to the hydrophobic site in fibrils. At high concentration of fibril, SO binds to a restricted location where sulphonate group of dye interacts with the fibril through hydrogen bonding that leads to the red shift in the absorption spectrum and blue shift in the emission spectrum. Such propositions are also supported by the blind molecular docking studies.

Chapter 6: Solvation dynamics in HSA fibril

In this chapter, by employing time-resolved fluorescence spectroscopy, solvent relaxation dynamics in Human Serum Albumin (HSA) fibril using intrinsic tryptophan (W214) as fluorescent probe have been studied and compared with the dynamics in

native protein. It is seen from steady state fluorescence measurements that the intensity of W214 fluorescence decreases along with ~8 nm blue shift in the emission maxima due to fibrillation of HSA protein indicating W214 becomes closer to the quencher charged amino acid residues in the fibrillar phase than in the native protein. The shorter lifetime of W214 in amyloid fibril as compared to native protein also supports such proposition. From detailed wavelength dependent dynamics, time-resolved emission spectra (TRES) has been constructed for both protein and fibril. It is well established that the dynamic Stokes' shift is a measure of solvent relaxation process. It is observed that the extent of change in peak frequency is large and faster for fibril compared to native protein indicating faster solvent relaxation in structurally more ordered fibril than in native protein. Thus, the present results indicate that the fibrillation of the protein leads to the exposure of the tryptophan moiety either to the bulk water or to the some water channels inside the fibril where water is more labile than that in the interior of the native protein. Further, our fluorescence depolarization studies also indicate that the W214 residue is located in a relatively more flexible region of the ordered amyloid fibril than that in the native protein.

References :

1. Harper, J. D.; Lansbury, P. T., *Models of amyloid seeding in Alzheimer's disease and scrapie: mechanistic truths and physiological consequences of the time-dependent solubility of amyloid proteins. Annu. Rev. Biochem.* 1997, 66, 385.
2. Koo, E. H.; Jr., P. T. L.; Kelly, J. W., *Amyloid diseases: Abnormal protein aggregation in neurodegeneration. Proc. Natl. Acad. Sci. USA* 1999, 96, 9989.
3. Murphy, R. M., *Peptide aggregation in neurodegenerative disease. Annu. Rev. Biochem.* 2002, 4, 155.
4. Chiti, F.; Dobson, C. M., *Protein misfolding, functional amyloid, and human disease. Annu. Rev. Biochem.* 2006, 75, 333.
5. Fandrich, M., *Cell. Mol. Life Sci.* 2007, 64, 2066.
6. Shahi, P.; Sharma, R.; Sanger, S.; Kumar, I.; Jolly, R. S., *Formation of amyloid fibrils via longitudinal growth of oligomers Biochemistry* 2007, 46, 7365.

7. Vander Linden, E.; Venema, P., *Self-assembly and aggregation of proteins*. *Curr. Opin. Colloid Interface Sci.* 2007, 12, 158.
8. Wang, W., *Protein aggregation and its inhibition in biopharmaceutics* *Int. J. Biopharmaceutics* 2005, 289, 1.
9. Klunk, W. E.; Wang, Y.; Huang, G. F.; Debnath, M. L.; Holt, D. P.; Mathis, C. A., *Uncharged thioflavin-T derivatives bind to amyloid-beta protein with high affinity and readily enter the brain*. *Life Sci.* 2001, 69, 1471.
10. D'Amico, M.; Di Carlo, M. G.; Groenning, M.; Militello, V.; Vetri, V.; Leone, M., *Thioflavin T promotes Ab (1-40) amyloid fibrils formation*. *J. Phys. Chem. Lett.* 2012, 3, 1596.
11. LeVine, H., III, *Stopped-Flow Kinetics Reveal Multiple Phases of Thioflavin T Binding to Alzheimer b(1-40) Amyloid Fibrils*. *Arch. Biochem. Biophys.* 1997, 342, 306.
12. Singh, P. K.; Mora, A. K.; Nath, S., *Ultrafast fluorescence spectroscopy reveals a dominant weakly-emissive population of fibril bound thioflavin-T*. *Chem. Commun.* 2015, 51, 14042.
13. Amdursky, N.; Huppert, D., *Auramine O as a Fluorescence Marker for the Detection of Amyloid Fibrils*. *J. Phys. Chem. B* 2012, 116, 13389.
14. Tsuji, A., *Small Molecular Drug Transfer across the Blood-Brain Barrier via Carrier-Mediated Transport Systems*. *The Journal of the American Society for Experimental NeuroTherapeutics* 2005, (2), 54.
15. Jahn, T. R.; Radford, S. E., *The Yin and Yang of protein folding*. *FEBS J.* 2005, 272, 5962.
16. Popova, L. a.; Kodali, R.; Wetzel, R.; Lednev, I. K., *Structural variations in the cross-beta core of amyloid beta fibrils revealed by deep UV resonance Raman spectroscopy*. 2010, 132, 6324.
17. Yoon, G.; Lee, M.; Kim, J. I.; Na, S.; Eom, K., *Role of Sequence and Structural Polymorphism on the Mechanical Properties of Amyloid Fibrils*. *Plos One* 2014, 9, 1-13.
18. Ball, P., *Water as an active biological constituent in cell biology*. *Chem. Rev.* 2008, 108, 74.
19. Chong, S.-H.; Ham, S., *Interaction with the Surrounding Water Plays a Key Role in Determining the Aggregation Propensity of Proteins*. *Angew. Chem. Int. Ed.* 2014, 126, 4042.

List of figures

Figure No.	Title	Page No.
1.1	The characteristic cross- β spacing from X-ray diffraction from amyloid fibrils. (Adopted from ref [25] with the permission from Elsevier.)	4
1.2	The typical kinetic profile for the amyloid fibril formation.	6
1.3	Pictorial representation of most-common fluorescence measurements used to extract kinetic and structural information on amyloid fibrils.	11
1.4	Schematic presentation of the dynamic Stokes' shift caused by solvent relaxation process following photoexcitation of the fluorescent probe. Adopted from reference [155]	15
1.5	Structures of selected extrinsic fluorescence probes employed in amyloid fibrils detection.	19
2.1	Schematic diagram of a Time-Correlated Single Photon Counting (TCSPC) Spectrometer.	42
2.2	Functioning of a TAC unit used in a TCSPC instrument. Start indicates the initiation of the charging process. Stop signal can arrive at TAC unit at any time within the TAC range following the arrival of the start pulse.	44
2.3	Creation of ground-state and excited state anisotropies from an isotropic distribution of molecules due to photoselective absorption of photons.	49
2.4	Schematic diagram for the measurement of fluorescence anisotropy.	51

2.5	Schematic representation of sum frequency generation in a non-linear crystal.	53
2.6	Schematic representation of fluorescence decay measurement using fluorescence up-conversion technique.	56
2.7	The Schematic diagram of the femtosecond fluorescence up-conversion instrument.	57
2.8	A typical instrument response function of the present fluorescence up-conversion instrument measured for 440 nm excitation light. The full-width at half maximum of the instrument response function is ~175 fs.	59
2.9	The schematic diagram of a typical epi-fluorescence microscope.	61
2.10	Schematic diagram of typical confocal fluorescence microscope.	62
3.1	(A) The fluorescence spectra of PG in water in the presence of different concentrations of insulin fibril. Arrow indicates the increase in insulin fibril concentration, 0-30 μM . Concentration of PG is 130nM. The excitation wavelength is 480 nm. Inset: The fluorescence Spectra of PG in water (B) Variation in the emission intensity of PG at 540 nm with the fibril concentration. Circles represent the experimental data points and the solid line represents the fitted line according to Eq. 3.6.	73
3.2	(A) Time-resolved fluorescence decays of PG (130 nM) in insulin fibril of different concentrations (0-30 μM). Excitation wavelength 445 nm and the emission were monitored at 540 nm. The dotted line represents lamp profile. (B) The variation in the average lifetime of PG with the concentration of insulin fibrils.	75
3.3	Time resolved fluorescence anisotropy of PG with varying concentration of insulin fibril (1) water (2) 0.30 (3) 1.18 (4) 5.21	77

- and (5) 25.62 μM .
- 3.4** (A) Fluorescence spectrum of PG in insulin fibril without salt (solid curve) and with 500 mM NaCl (dashed curve). (B) Fluorescence decays of PG fibril with (solid) and without salt (dashed). Dotted curve represents IRF. 79
- 3.5** (A) The emission spectra of ThT and PG (0.1 μM) in the presence of 30 μM of insulin fibril. Dotted curves represent the emission spectra in water for both dyes. (B) Fibrillation kinetics of Insulin fibril with both ThT (black circles) and PG (red triangles). Solid lines represent their fits with equation 3.1. 81
- 3.6** Microscopic images of insulin fibrils strained with (A) PG and (B) ThT. Concentration of dye and fibrils are same in both measurements. 81
- 3.7** Emission spectra of PG (0.1 μM) in 30 μM fibril in the presence of different concentrations (0-3 μM) of ThT. 82
- 3.8** Normalized absorption (dashed) and emission (solid) spectra of ThT (green) and PG (red) in Insulin fibrils. 83
- 3.9** (A) Emission spectra of ThT (0.1 μM) in fibrils in presence of different concentrations of PG (0-1 μM). Dashed line represents the emission spectra of 1 μM PG on excitation with 440 nm light. **Inset:** Intensity normalized emission spectra of ThT-fibril solution with different PG concentrations. (B) Emission decays traces for ThT in fibrillar solution in the absence and presence of PG. Excitation wavelength is 440 nm. 84
- 3.10** Ground state optimized structures of (A) PG and (B) ThT 86
- 3.11** (A) The most stable configuration of PG in fibril obtained from molecular docking studies. (B) Closer look at the interactions between PG and amino acids of fibril at the binding pocket. For clarity, PG is shown by ball- stick model and amino acids are 87

	shown by sticks.	
3.12	Binding pose of ThT in the fibril incorporated with PG.	88
3.13	(A) The fluorescence spectra of PG in ACN-EG solvent mixtures with different compositions. (B) The variation of emission quantum yield of PG with viscosity of the solvent medium.	90
3.14	Variation of $\log(\phi)$ with $\log((\eta))$. The solid line is the fitting of the experimental data by Forster-Hoffmann equation.	91
3.15	Fluorescence transients decay traces for PG in ACN-EG solvent mixtures: (1) 0, (2) 50, (3) 70, (4) 80 and (5) 100 % EG. The dashed line represents instrument response function (IRF).	93
3.16	Fluorescence transient decays in ACN for different concentrations of PG: 4 μM (black), 7.8 μM (red) and 13.3 μM (green).	94
3.17	Fluorescence decay traces of PG in ACN at different emission wavelengths: (1) 500 nm, (2) 540 nm and (3) 620 nm. The dashed line represents the IRF.	95
3.18	(A) Time-resolved emission spectra (TRES) of PG in ACN. Circles denote the experimental points and solid lines are their respective log-normal fits Inset: Variation of integrated area under the emission spectra with time. (B) Peak intensity normalized (TRES) of PG in ACN at 0.1 ps (black), 0.2 ps (red), 0.5 ps (green), 1 ps (yellow), 2 ps (blue), 3 ps (magenta) and 4 ps (olive green).	97
3.19	The change in the emission peak position (\circ) and FWHM (∇) with time for PG in ACN. Solid lines represent their bi-exponential fits.	98
3.20	Time-resolved area normalized emission spectra (TRANES) for PG in ACN: (A) 0.1-1.3 ps (B) 2-4 ps.	99

3.21	The variation of integrated area under the emission curve with time for PG in ACN (O), 1:1 ACN: EG mixture (∇), and EG (□).	101
3.22	The variation of (A) mean frequency and (B) FWHM with time for PG in different solvents: ACN (O), 1:1 EG: ACN (∇), and EG (□).	102
3.23	TRANES of PG in 1:1 ACN: EG mixture at (A) 0.2-1.5 ps and (B) 8-24 ps.	104
3.24	The fluorescence transient decays of PG in ACN and EA. The dotted curve is the IRF.	105
3.25	Variation in (A) integrated area and (B) mean frequency of PG in EA (O) and ACN (∇).	106
3.26	TRANES of PG in EA at different times. Inset: magnified figure of TRANES of PG in EA.	107
3.27	(A) Wavelength dependent decay traces of PG in 30 μM insulin fibril. (B) TRES of PG in 30 μM fibril. Circles represent experimental data points and solid curves represent their lognormal fits Inset: variation in the integrated area of PG in fibril.	108
3.28	(A) Variation of mean frequency (O) and spectral width (Δ) with time. (B) TRANES of PG in fibril at different times.	109
4.1	Ground state absorption spectra of 2Me-DABT in 3MP (solid) and water (dashed).	122
4.2	Normalized emission spectra of 2Me-DABT in solvents with different polarity.	123
4.3	Variation of Stokes' shift of 2Me-DABT with Δf in aprotic (O) and protic (∇) solvents. Solid lines represent the fitting of the experimental data with Lippert-Mataga equation (eq. 4.4).	125

4.4	Variation in Stokes' shift of 2Me-DABT with α value in protic solvents.	127
4.5	Variation in the emission yield of 2Me-DABT with Δf in aprotic (○) and protic (▽) solvents.	127
4.6	Transient fluorescence decays of 2Me-DABT in (A) aprotic and (B) protic solvents.	129
4.7	The variation of the fluorescence lifetime of 2Me-DABT with Δf for aprotic (○) and protic (▽) solvents.	129
4.8	Variation of (A) k_r and (B) k_{nr} with Δf in aprotic (○) and protic (▽) solvents.	130
4.9	Normalized emission spectra of 2Me-DABT in H ₂ O (solid) and D ₂ O (dashed).	132
4.10	(A) Transient fluorescence decays of 2Me-DABT in H ₂ O (black) and D ₂ O (red). The dotted curve represents IRF. (B) The variation in fluorescence lifetime of 2Me-DABT in MeOH-D ₂ O (○) and MeOH-H ₂ O (▽) solvent mixtures.	132
4.11	(A) The emission spectra ($\lambda_{ex}=340$ nm) of 2Me-DABT in the presence of different concentrations of insulin fibrils (0-30 μ M). (B) Peak intensity normalized emission spectra of 2Me-DABT in amyloid fibrils.	135
4.12	Double reciprocal Benesi-Hildebrand plot for the variation in emission intensity of 2Me-DABT with the concentration of insulin amyloid fibrils. Straight lines are fitted data following eq. 4.8.	137
4.13	(A) The fluorescence transient decays for 2Me-DABT in the presence of different concentrations of insulin fibrils (1) 0, (2) 0.30, (3) 1.17, (4) 4.44 and (5) 15.56 μ M. The black curve represents the IRF of the TCSPC instrument. (B) Variation in	138

	the average lifetime of 2Me-DABT with insulin fibril concentration.	
4.14	Fluorescence microscopic images of 2Me-DABT with (A) native insulin and (B) fibrils.	139
4.15	(A) The emission spectra ($\lambda_{\text{ex}}=340$ nm) of 2Me-DABT in fibrillar solution in the presence of different concentrations of ThT (0-3 μ M). The dashed curve shows the emission spectrum ($\lambda_{\text{ex}}=340$ nm) of 3 μ M ThT in the fibrillar solution. (B) Variation in the emission intensity at (O) 445 nm and (∇) 490 nm with the ThT concentration in the fibrillar solution.	140
4.16	Normalized absorption (dashed curves) and emission spectra (solid curves) of 2Me-DABT (blue) and ThT (green) in insulin fibrils.	141
4.17	Emission transient decays for fibril bound 2Me-DABT in the presence of different concentrations of ThT (0-3 μ M). The dashed curve represents the IRF.	142
4.18	Ground state optimized structure of 2Me-DABT	143
4.19	(A) Two most probable binding sites for 2Me-DABT in amyloid fibril. The mode 1 is the most energetically stable binding mode. (B) Close look of the binding pocket for the mode 1. The dashed lines indicate the different types of interaction between 2Me-DABT and fibril.	145
4.20	Binding pose of the ThT in the amyloid fibril with incorporated 2Me-DABT. The solid lines indicate the distance between 2Me-DABT and docked ThT.	146
5.1	Ground state absorption spectra of SYPRO Orange in insulin fibril: (A) at 0-1 μ M and (B) 1-30 μ M insulin fibrils.	154
5.2	(A) Fluorescence spectra of SYPRO Orange in water in the	156

- presence of different concentrations (0-30 μM) of addition of fibril. **Inset:** Photograph of SYPRO Orange in water (left) and 30 μM insulin fibril (right) under UV irradiation. **(B)** Intensity normalized emission spectra of SYPRO Orange in water in presence of fibrils (0-30 μM).
- 5.3** Modified Benesi-Hildebrand plot for the fluorescence changes due to SYPRO Orange-fibril complexation. Open circles represent experimental data points while solid lines represent fit to the experimental data according to eq. 5.1. 158
- 5.4** **(A)** Fluorescence transients of SYPRO Orange in water with addition of fibril. Blue dashed curve represents IRF **(B)** Variation in the average lifetime of SYPRO Orange with fibril concentration. 159
- 5.5** Fluorescence spectra of ThT (λ_{ex} is 440 nm) and SYPRO Orange (λ_{ex} is 500 nm) in water (dashed) and in presence of 30 μM insulin fibril (solid). 161
- 5.6** Fluorescence microscopic images of insulin fibril stained with **(A)** SYPRO Orange and **(B)** ThT. 162
- 5.7** The variation in the fluorescence intensity of SYPRO Orange (\circ) and ThT (∇) with the concentration of insulin fibril. Solid line represents their linear fits. 163
- 5.8** **(A)** Emission spectra and **(B)** emission transient decays of SYPRO Orange in fibril solution in the absence (—) and presence of 500 mM NaCl (- - -). The dotted curve in panel B represents IRF. 165
- 5.9** Normalized absorption **(A)** and emission **(B)** spectra of SYPRO Orange in solvents with different Δf values. 166
- 5.10** Variation of Stokes' shift of 2Me-DABT with Δf . \circ represents the experimental data. Solid lines represent the fitting of the 168

	experimental data with Lippert-Mataga equation (eq. 4.4).	
5.11	Variation in the fluorescence quantum yield of SYPRO Orange with Δf values of solvents.	169
5.12	(A) Transient fluorescence decays of SYPRO Orange in solvent mixtures with different polarity. (B) Variation in the average lifetime of SYPRO Orange with solvent polarity.	170
5.13	The absorption spectra of SYPRO Orange in glycerol at different temperatures (15- 70 ⁰ C)	171
5.14	(A) Fluorescence spectra and (B) intensity normalized fluorescence spectra of SYPRO Orange in glycerol at different temperatures.	172
5.15	Forster-Hoffmann plot for SYPRO Orange in glycerol. Circles represent the data points and solid line represents their linear fit by eq. 5.3.	174
5.16	(A) The fluorescence decay traces of SYPRO Orange in glycerol at different temperatures. (B) Plot for the changes in the average lifetime of SYPRO Orange with solvent viscosity.	175
5.17	(A) Absorption spectra and (B) Emission spectra of SYPRO Orange in ACN-MeOH solvent mixtures.	176
5.18	Normalized absorption spectra of SYPRO Orange in MeOH-H ₂ O mixtures with different compositions. (A) 0-50% H ₂ O. (B) 50-80% H ₂ O. (C) 80-100% H ₂ O.	178
5.19	Fluorescence spectra of SYPRO Orange in MeOH-H ₂ O mixtures with different compositions. (A) 0-50% H ₂ O. (B) 50-80% H ₂ O. (C) 80-100% H ₂ O.	178
5.20	The variation in the ratio of (A) absorbance ratio of 450 nm to 500 nm and (B) fluorescence intensity ratio of 575 nm to 610 nm for SYPRO Orange as a function of percentage of water in MeOH.	180

5.21	Fluorescence transient decays for SYPRO Orange in MeOH-H ₂ O mixtures with different compositions. (A) 50-80 % water (B) 80-100 % water.	180
5.22	The variation in the average lifetime of SYPRO Orange with the water content in MeOH-H ₂ O mixtures.	181
5.23	Minimum energy configuration of SYPRO Orange	182
5.24	(A) Two most probable binding sites for SYPRO Orange in amyloid fibrils obtained from molecular docking studies. Close look of (B) mode I (C) mode II. The dashed lines indicate that H-bonding interactions between SYPRO Orange and side chain of glutamic acid.	184
6.1	(A) Fluorescence spectra of ThT in HSA protein (dashed) and fibril (solid). Inset: Variation in the ThT fluorescence intensity during HSA fibrillation. (B) Far-UV circular dichroism spectra of (a) HSA protein and b) HSA fibril.	191
6.2	Steady state emission spectra ($\lambda_{\text{ex}}=295$ nm) of HSA native protein (solid) and fibril (dashed).	192
6.3	Fluorescence transients of tryptophan in HSA protein and fibril at their corresponding emission peak wavelength.	194
6.4	Fluorescence transients for W214 in HSA fibril at different emission wavelengths. The black curve represents the IRF.	195
6.5	(A) Time-resolved emission spectra (TRES) of HSA fibril. Circles show the data points and solid lines represents corresponding log-normal fits. (B) Peak normalized TRES of HSA fibril from 0.3 to 10 ns.	195
6.6	The variation in the area under the emission spectrum of fibril (∇) and native protein (\circ). The solid line represents their multi exponential fits.	196
6.7	Variation in the emission maxima with time for protein (\circ) and fibril (\square). The solid lines represent the bi-exponential fits	197

- 6.8 Time dependent variation of FWHM for HSA protein (Δ) and fibril (\circ). 199
- 6.9 Time-resolved anisotropy of HSA protein (\circ) and fibril (\square). 201
The solid lines represent the bi-exponential fits to the experimental data.

List of tables:

Table No	Title	Page No.
1.1	List of some protein aggregation related diseases and associated proteins	3
3.1	Fitting parameters and average lifetime of PG in amyloid fibril solutions	76
3.2	Fitting parameters for anisotropy decay of PG in fibrillar solutions	77
3.3	The emission quantum yield of PG in ACN-EG solvent mixtures.	90
3.4	Fitted parameters for transient emission decay of PG in ACN-EG solvent mixtures.	93
3.5	Fitting parameters of mean frequency decay and FWHM growth of PG in ACN-EG solvent mixtures and EA	102
3.6	Fitting parameters of intensity decay of PG in ACN and EA.	105
3.7	Fitting parameters for the temporal variation of mean frequency and FWHM of PG in fibril	109
4.1	Photophysical parameters of 2Me-DABT dye as estimated in different solvents and solvent mixtures. Subscripts indicate their corresponding percentage volume fractions.	121
4.2	Fitting parameters of 2Me-DABT in presence of different concentrations of fibril	138

5.1	Fitting parameters of fluorescence decay traces of SYPRO Orange in presence of at different concentrations of fibrils.	160
5.2	Photophysical parameters of SYPRO Orange dye as estimated in different solvents and solvent mixtures. Subscripts indicate their corresponding percentage volume fractions.	167
5.3	Photophysical parameters of SYPRO Orange dye in glycerol solution at different temperatures.	173
6.1	Fitting parameters of fluorescence decay traces of HSA protein and fibril	194
6.2	Fitting parameters for the time-resolved anisotropy decay of HSA protein and fibrils.	202

Chapter-1

Introduction

1.1 General introduction about amyloid fibrils

Peptides and proteins, under certain conditions, undergoes structural transformation from their folded native state to highly ordered filamentous fibrillar aggregates, commonly known as amyloid fibrils.¹⁻⁸ Formation of such fibrillar aggregates leads to a reduced availability of the protein and affects their normal biological activity. The appearance of these aggregates is one of the observed pathological conditions in many protein misfolding diseases.¹⁻⁸ It is believed that the region which is enriched with amyloidogenic proteins will be of more risk for amyloid based diseases, like Alzheimer's, Parkinson's, type II diabetes etc.⁹⁻¹³ Unfortunately, currently there is no effective treatment available to reverse or stop the progress of these devastating diseases, primarily due to difficulties in identification of their etiology. Due to the severe neurotoxicity of these protein aggregates, early diagnosis can increase the chances of treating such diseases at proper time.¹⁴ Particularly, early diagnosis allows the people to avail the possible treatments, enroll for the clinical trials and even to understand the progress of the disease.¹⁴

In all these amyloid related diseases, a particular protein or protein fragment converts from its native soluble form to extracellular insoluble amyloid plaques which

accumulate in different tissues and organs.^{1, 10, 15} More than 20 proteins have been identified to be related to the amyloid related diseases.¹⁶ However, these proteins are unrelated in terms of their secondary structure or sequence.¹⁶ Aggregation of some of these proteins is also responsible for the intracellular deposits and formation of amorphous aggregates. Native amyloidogenic proteins may be rich in α - helix, β -helix, β -sheet or random coiled structure or combination of all.¹⁷⁻²² They may be rigid globular proteins or intrinsically disordered proteins.^{23,24} In spite of these differences, the fibrils formed by proteins with largely different secondary structures have common structural feature, β -sheet structure.²⁵ However, depending of the relative orientation of the successive β -strand with respect to the fibrillar axis, aggregation may results in formation of fibrils with parallel or anti parallel β -sheets.²⁵⁻²⁸ Most of the fibrils show rope like structure. These fibrils can be formed in vitro from many proteins, perhaps all, independent of their relation with the pathology of the diseases.^{10, 29, 30} Further, it is believed that the formation of fibrils is a generic property of proteins i.e., many proteins have inherent tendency to form amyloid fibrils under certain denaturizing conditions.^{29, 30}

In order to get the molecular understanding of the amyloid formation, it has been proposed that the formation of misfolded protein is the prerequisite for the formation of amyloid fibrils.^{11, 31-34} The reason for such proposal is that the fibril has common cross β -sheet structure independent of the secondary structure in their native form.^{25, 27, 28} Such common structural feature indicates that it is prerequisite for the proteins to undergo unfolding to a specific conformation which is required to form the oligomers and matured fibrils.³²⁻³⁴ Such a partially unfolded proteins or peptides can offer variety of interactions, such as electrostatic, hydrogen bonding, hydrophobic

contacts and Van der Waals forces, which are required for the oligomerization and further advancement towards the formation of matured fibrils.^{32, 34, 35} Table 1.1 lists some of the diseases and the proteins associated with such diseases.

Table 1.1 List of some protein aggregation related diseases and associated proteins

Sr. No	Disease	Corresponding protein
1.	Alzheimer's	β -Amyloid, ³⁶ Tau ^{37, 38}
2.	Parkinson's	α -synuclein ³⁹⁻⁴¹
3.	Huntington's	expanded Glu repeats of Huntingtin ^{12, 16}
4.	Pick disease	Tau ¹
5.	Hemodialysis-related amyloidosis	β 2-microglobulin ⁴²
6.	Injection localized amyloidosis	Insulin ⁴³
7.	Type II diabetes	Amylin ⁴⁴
8.	Scrapie	Prion ^{22, 45}
9.	Senile amyloidosis	Transthyretin ^{46, 47}
10.	Creutzfeldt-Jakob disease	PrP ²²
11.	Spongiform encephalopathies	Prion ²²

Although proteins involved in these aggregation induced disorders lack strong similarities in their sequence,^{20, 48} amino acid composition,⁴⁸ size and structure of native soluble state,⁴⁹ the final fibrillar structures are having significant similarity in their external morphology as well as internal architecture.^{27, 50, 51} The fibrillar aggregates have unbranched rod like structures which are comprised of intertwined protofilaments (small aggregates of β -strands).^{27, 50, 51} The X-ray diffraction studies on amyloid fibrils revealed a characteristic pattern of 'cross β ' structure.^{27, 28} This pattern

indicates that these fibrils share a common structure consists of β sheets, in which the direction of hydrogen bonding runs parallel to fibril axis and stacking of β sheets runs perpendicular to the fibril axis.²⁸ The X-ray diffraction pattern of amyloid fibrils consists of two reflections at 4.8\AA and $10\text{-}11\text{\AA}$ found on perpendicular axes.⁵² The meridional reflection at 4.8\AA arises due to the hydrogen bonding patterns between the β strands in the same β sheet in parallel alignment while same reflection arises at 9.6\AA in the case of antiparallel fibrils with repeat being every other β -strand.^{52, 53} The long equatorial reflection at $10\text{-}11\text{\AA}$ appears due to inter β sheet hydrogen bonding. This is pictorially shown in figure 1.1. This pattern has also been adopted by several proteins and synthetic peptides from variety of sources.^{27, 28, 52-54}

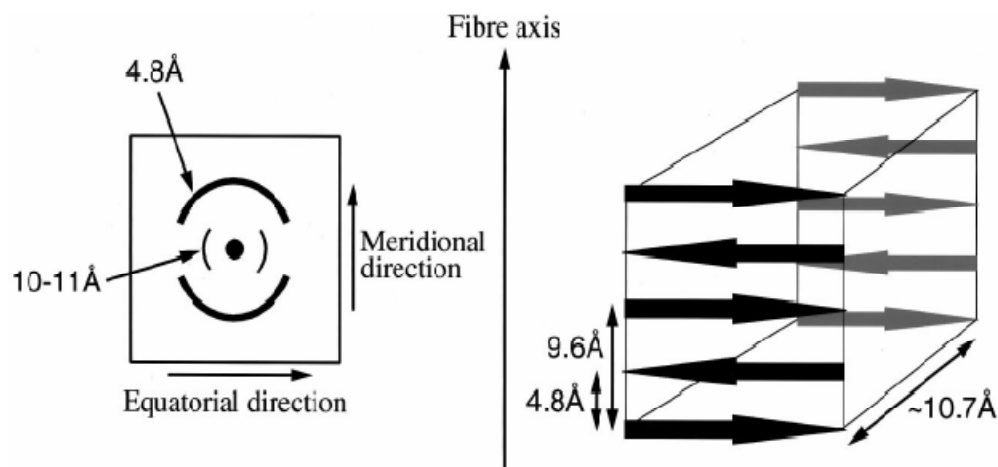


Figure 1.1 The characteristic cross- β spacing from X-ray diffraction from amyloid fibrils. (Adopted from ref [25] with the permission from Elsevier)

There are different types of mechanisms have been proposed for the formation of amyloid fibrils.⁵⁵⁻⁵⁷ Among them, most accepted mechanism is nucleation induced growth mechanism.⁵⁸ In this mechanism, the native protein has low tendency to form small oligomers i.e., attachment of monomeric proteins to small oligomers is not

thermodynamically favorable.²¹ At this stage, the formation of small aggregates is reversible in nature until they manage to form aggregates of sufficient size. Such aggregate is called as critical nucleus through which the attachment of unfolded monomeric proteins is thermodynamically favorable.⁵⁸⁻⁶¹ This will trigger the formation of fibril. During this phase, the conformational rearrangements of the native protein takes place in order to favor the formation of critical nucleus. The formation of such nucleus depends on the size of the native protein, experimental conditions such as low pH, elevated temperatures, ionic strength and presence of co-solvents in the solution.^{41, 62-64} The effect of all such parameters on the lag phase has been well studied and reported in the literature. After the formation of critical nucleus, further association of unfolded monomers is very rapid and shows exponential growth which is known as elongation phase.⁵⁸⁻⁶¹ During this phase, the formation of protofibrils which is further converted to fibrils takes place. These fibrils will convert in to mature fibrils by the equilibration of surrounding interactions such as hydrogen bonding and hydrophobic forces. Thus, this phase is called as equilibrium phase or saturation phase.⁵⁸⁻⁶¹ The acceleration of fibril formation due to the addition of preformed fibrils as seeds also supports the nucleation induced growth mechanism.⁵⁸⁻⁶¹ The fibrillation mechanism is pictorially represented in figure 1.2.

For most of the studies presented in this dissertation, bovine insulin has been used as a model protein⁶⁵. Insulin is a small disulfide-containing helical protein whose main activities include regulating glucose metabolism,⁶⁶ stimulating lipogenesis,⁶⁷ and increasing cellular transport of amino acids.^{67, 68} Fibrillar insulin aggregates have been found earlier in patients with type II diabetes^{69, 70} and during normal aging.⁷¹ During the treatment of diabetes, intravenous injection of insulin is used to control glucose

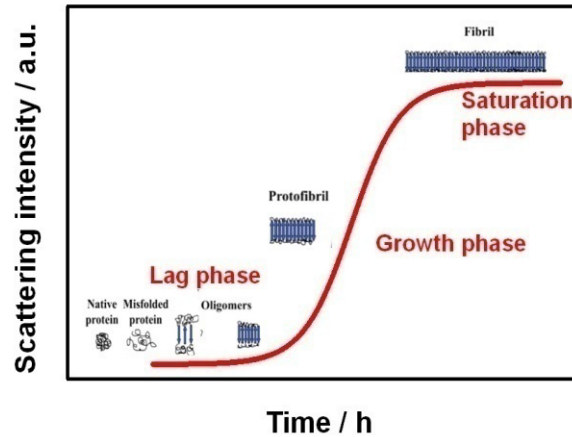


Figure 1.2 The typical kinetic profile for the amyloid fibril formation.

metabolism.⁴³ However, such treatment is suffered from the pathogenic deposition or fibrillation of insulin due to its high local concentration at the sites of frequent injections and leads to injection localized amyloidosis.⁴³ Fibrillar form of insulin becomes therapeutically ineffective, and the injection of such species is likely to trigger an unwanted/adverse immune response.⁷² In addition, the fibrillar form of insulin has been shown to be toxic to pancreatic β -cells⁷³ and rat pheochromocytoma PC12 cells.⁷⁴ *In vitro*, insulin has been shown to exhibit an increased propensity for fibrillation upon exposure to conditions that favors the formation of partially folded intermediates such as mutation,⁷⁵ addition of co-solvents,⁶⁴ acidic pH,^{76, 77} elevated temperatures,^{76, 77} and dissolution with organic solvents.^{43, 64} Results from previous investigations suggest that the key driving force for insulin fibrillation is hydrophobic interaction, which is attributed to the enhanced exposure of buried aminoacids to solvent.^{43, 76, 78} In pharmaceutical industry, protein stability is one of the limiting factors to be overcome to develop protein based drugs.⁷⁹ The fibrillation of insulin creates additional difficulties for the storage and transport of insulin based drugs.^{79, 80} To be mentioned, the choice of insulin as model amyloidogenic protein in the present

work is primarily due to its high propensity to form amyloid fibrils with the same mechanism and morphology as the other disease related proteins.^{76, 81} The reasons for choosing bovine insulin out of different variant as the model amyloidogenic protein are as follows: (1) Posses similar sequence and structure of human variants.^{82, 83} (2) Availability of large amount of biochemical and structural data.^{77, 84} (3) Retains a high fibril-forming propensity at the acidic pH.⁸⁵ (4) Easy availability and low cost.

1.2 Techniques for characterization of amyloid fibrils

Since the discovery of amyloid fibrils by Rudolph Virchow in the year of 1854,⁸⁶ large amount of information about their origin, morphology, structural features,²⁷ formation mechanism,⁶¹ pathological features and mechanism of their toxicity⁸⁷ through several biochemical and biophysical techniques are available in the literature.^{88, 89} Large number of physical techniques such as sedimentation,⁹⁰ turbidity measurements,⁹¹ light scattering techniques,⁹² size exclusion chromatography,⁹³ small angle X-ray scattering (SAXS)⁸⁹ techniques has been complemented to understand the mechanism of fibrillation and for differentiating intermediate species such as oligomers, protofibrils etc., based on the differences in their sizes, shapes and diffusion properties. Morphological features of amyloid fibrils has been examined by the experimental techniques such as atomic force microscopy (AFM)^{94, 95} and electron microscopic techniques like, scanning electronic microscopy (SEM) and transmission electron microscopy (TEM).^{27, 93} Complementary techniques such as X-ray diffraction (XRD),²⁸ circular dichroism (CD),^{96, 97} Fourier transform infrared spectroscopy (FTIR),⁹⁷ electron paramagnetic resonance (EPR),⁹⁸ solution and solid state nuclear magnetic resonance (NMR)^{99, 100} spectroscopic techniques have also been utilized for

the characterization of structural features of intermediates as well as matured fibrils produced *in-vitro*. However, usage of such techniques is limited to *in-vitro* and *ex-vivo* studies only and also suffers from limited sensitivity.¹⁰¹

1.2.1 Imaging techniques

Recently, the increased enthusiasm for the detection of the amyloid fibrils in the brain of living patients has led to the development of *in-vivo* imaging techniques. Hence, imaging techniques such as magnetic resonance imaging (MRI)¹⁰²⁻¹⁰⁴ and nuclear techniques such as positron emission tomography (PET)^{38, 105-107} and single photon emission computed tomography (SPECT)^{38, 105-107} are being employed regularly nowadays for the *in-vivo* detection and quantification of amyloid fibrils. MRI uses a strong magnetic field and radio waves to create detailed images of the affected organs and tissues within the body. It has been suggested that iron concentrated in AD plaques may enable their MRI detection using ultra high magnetic field strength (>7 Tesla).¹⁰⁸ In general, MRI contrasting agent must be added to get better images of amyloid plaques during brain imaging.¹⁰⁹ For proper MRI imaging of A β plaques, a contrast agent is usually required, such as ¹⁹F¹¹⁰ and gadolinium-labeled probes.¹¹¹ However, these contrast agents may have limited brain uptake and potential toxicity. Low sensitivity and blurred signal contrast between the A β plaques and surrounding tissues makes MRI not suitable for real-time amyloid imaging.¹¹² In PET, the positron emitting radioisotopes such as ¹¹C, ¹⁸F etc., are attached to the amyloid specific probes and injected in the body for imaging.¹⁰⁷ The positron emitted at the location of fibrils is combined with the electron in the vicinity to emit two γ -rays of equal energy of ~511 keV exactly in the opposite direction.¹⁰⁵ Detection of such

correlated event led to the identification of fibrillar deposits in the tissues. Several PET probes show very strong affinity towards Amyloid β plaques.¹⁰⁵ Among them Florbetapir-F18³⁸, Flutemetamol-F18¹¹³ and Florbetaben-F18¹¹⁴ are US FDA approved PET diagnostic agents.¹¹⁵ SPECT is also a related technique, which can be used to construct three dimensional images. This technique requires delivery of a gamma emitting radioisotope into the patient, normally through injection into the bloodstream. Normally gamma emitting isotopes such as ¹²³I, ^{99m}Tc and ¹¹C has been attached with amyloid specific markers and the emitted gamma rays have been imaged through gamma camera.^{106, 116} The collection of different images at different depths has been utilized to construct 3D image of brain. However, risk of handling radioactive probes, narrow isotope availability, short lifetimes, high cost, etc limited the clinical usage of PET, SPECT techniques for *in-vivo* amyloid imaging.^{112, 117-120} In addition, expensive instrumentation, high skilled personnel, time consuming data analysis, etc also makes the usage of PET and SPECT limited for neuroimaging.^{112, 117-120} All such limitations result in the high cost for PET scanning. For example, the cost of one PET scan is about \$1000 which is heavy burden for average families in developing countries.

1.2.2 Fluorescence imaging of amyloid fibrils

Due to such limitation of radioactive based imaging techniques, a thrust for the development of relatively inexpensive and easily available techniques for the neuroimaging has been initiated. Optical imaging is very promising alternative technique for amyloid imaging both *in-vitro* as well as *in-vivo*.¹²¹ Compared to PET, SPECT and MRI, fluorescence imaging possesses advantages such as real time

monitoring, absence of radioactivity, high special resolution and most importantly high sensitivity.^{118, 121, 122} Additionally, it is relatively less expensive than any other radio nuclide based imaging techniques. The imaging speed scan is rapid which is helpful in high throughput of the samples and for real time monitoring of the disease progression. Analysis does not need very highly skilled personnel. The method can be applied to detect fibrils *in-vitro*, *ex-vivo* and *in-vivo* as well. In recent days, researchers have developed many fluorescent amyloid specific probes to (1) monitor the aggregation in real time (2) differentiate intermediate species from both native and fibrillar states of protein (3) obtain information at single molecular level and (4) to gain fundamental knowledge on the structure and dynamics of fibrils.^{117, 123, 124} Figure 1.3 schematically depicts the information that can be extracted from the most common fluorescence readouts. The unique advantage of fluorescence based methodologies is its versatility. Fluorescence sensors are multiparametric, reporting on changes in intensity, spectral position, excited state lifetime, anisotropy as well as energy transfer and excimer formation etc. Such features cannot be offered by a radio ligand or magnetic imaging agent. The intensity, band position of fluorescence spectra reports on the nature of surrounding environment of the probe and excited state lifetime tells about the nature of the excited state processes that are responsible for the observed changes.¹²⁵ Fluorescence anisotropy helps in distinguishing different intermediates in the fibrillation processes by measuring the tumbling motions, which are primarily controlled by their sizes. FRET experiments allowed finding the inter-residue distances in oligomers as well as in fibrils by deploying site specific fluorescent reporters.⁴⁶

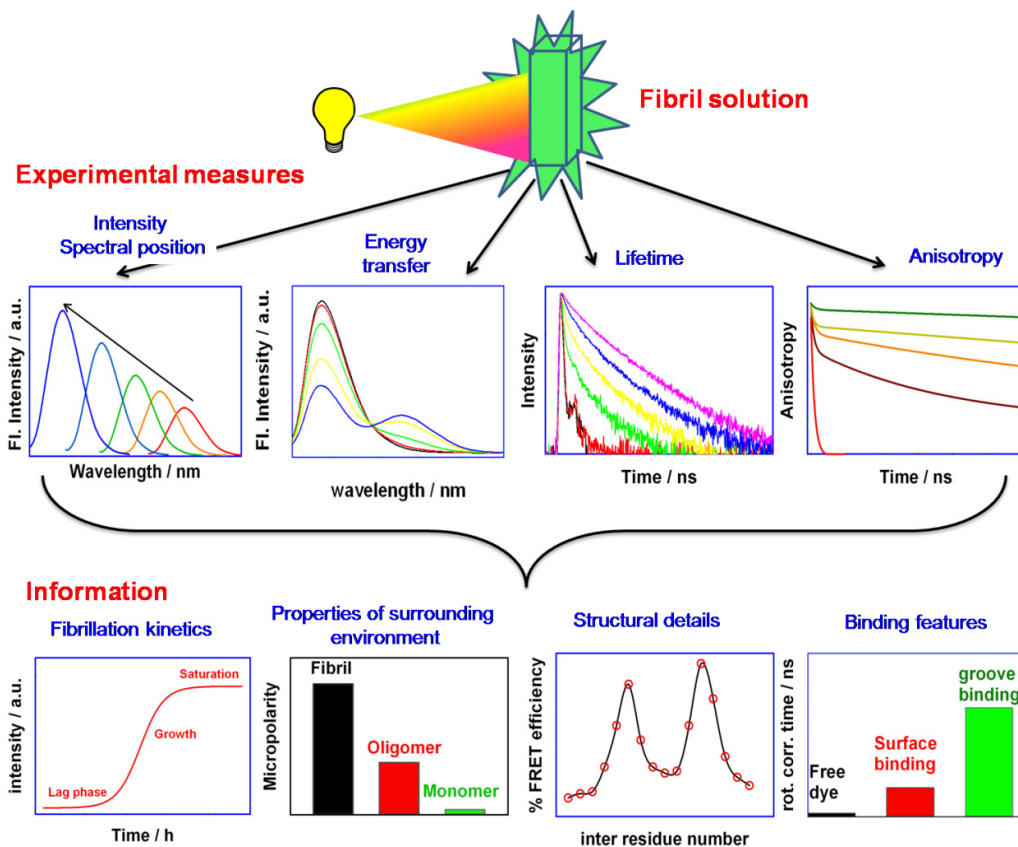


Figure 1.3 Pictorial representation of most-common fluorescence measurements used to extract kinetic and structural information on amyloid fibrils.

All these emission properties of fluorophore are mainly governed by the processes that take place in their photoexcited state. Different types of excited state processes of these fluorescent molecules and their modulation in the presence of the fibrils will govern their sensitivity.^{126, 127} The information of such excited state processes will help us in understanding the mechanism of their binding to protein aggregates. Such knowledge will also help us to design and develop new probes with required excited state processes which can lead to a better sensitivity towards the detection of amyloid fibrils. Preferably, an amyloid probe should possess very low emission quantum yield in its free form and should enhance its fluorescence intensity

to a great extent due to its association with amyloid fibrils. Thus, a sensitive amyloid probes generally have an efficient non-radiative decay channel in their photo excited state leading to extremely low emission yield in their free form.¹²⁸ However, on association with amyloid fibril, the immediate surroundings of these probes are such that it restricts such principal non-radiative decay channel leading to large increase in its emission yield.^{129, 130} Factors that are responsible for the restriction in the non-radiative decay channel, may be reduced polarity, increased viscosity, any special interactions such as electrostatic forces, hydrogen bonding, etc. Beside the changes in the emission intensity, these environmental factors also affect the position of the emission spectrum of the probe due to its interaction with protein aggregates. Such changes in the spectral position upon binding with the amyloid fibrils have opened up another path to interrogate the fibrillation processes. Probes that changes its spectral position upon binding with amyloid fibrils are generally known as ratiometric sensor.^{131, 132} As the emission maximum of the fluorophore in its free form is very different from its amyloid bound form, the intensity ratio at these two different wavelengths will be very useful in identifying fibrils and monitoring the fibrillation process.¹³¹

1.3 Classification of amyloid probes based on excited state processes

Different excited processes of the fluorescent probes that are being modulated due to their association with amyloid fibrils have been discussed below.

1.3.1 Intramolecular charge transfer

Following photoexcitation, electronic charge can transverse from electron rich moiety to electron deficient part in the same molecule results in the charge separation

in the excited state of the molecule. Such transfer of charge within a molecule results in the formation of intramolecular charge transfer (ICT) state of the molecule.^{133, 134} Because of such ICT process, the molecular dipole moment in the excited state becomes higher than ground state.¹³⁵ Such increase in the excited state dipole moment is manifested in the large red shift in the absorption as well as emission spectrum of the molecule with the increase in the solvent polarity. Due to higher dipole moment of the excited state than ground state, the increase in the solvent polarity causes more stabilization of the excited state than its ground state.¹³⁵ Hence, such preferential stabilization of the excited state results in the red shift in the absorption and the emission spectra of the molecules due to increase in the polarity of the surrounding media. Such spectral shift with the change in the solvent polarity is commonly known as solvatochromism and molecules which show solvatochromism are known as solvatochromic probes.¹³⁶⁻¹³⁸ A large number of probes deployed for the detection of amyloid fibrils possess electron rich and electron deficient moieties connected through spacer.¹³⁹ Hence, ICT process can take place in such amyloid probes. As amyloid fibrils are formed by the aggregation of misfolded proteins through hydrophobic interactions, they offer varieties of hydrophobic binding sites for the amyloid probes. Upon binding into such hydrophobic sites in amyloid fibrils, ICT based probes experience low polarity as compared to the bulk water. Such decrease in the surrounding polarity results in blue shifted emission bands of the probes upon binding with the amyloid fibrils.¹⁴⁰ The extent of changes in the spectral position of the probe in amyloid fibrils is utilized to quantify the fibrils as well as to monitor the fibrillation process.¹⁴⁰

There are several solvatochromic probes which along with the changes in the spectral position also show large changes in their emission intensity on association with amyloid fibrils.¹³¹ Such changes in the emission intensity along with the changes in the spectral position lead to the ratiometric detection of amyloid fibrils. A ratiometric sensor has much higher sensitivity than a normal intensity based probes due to lack of interference from several factors like, fluctuation in the excitation light intensity, concentration variation, etc during measurements.¹³²

Apart from the sensing activity, ICT based probes can also elucidate the solvent relaxation dynamics in complex environments such as macro molecules such as cyclodextrins,¹⁴¹ proteins,¹⁴²⁻¹⁴⁴ DNA,¹⁴⁵ reverse micelles^{146, 147} etc. Studies on solvent relaxation are extremely important to study the mechanism of fibril formation and also in understanding the nature of solvent molecules in different parts of the fibrils.^{148, 149} In fact, the intermolecular interactions of proteins are highly dependent on the nature of the water molecules in their hydration shell.¹⁵⁰ ICT based molecules have been used to study the solvation dynamics through the time-dependent fluorescence Stokes' shifts measurements.¹⁵¹⁻¹⁵⁴ On photoexcitation, the dipole moment of the probe molecule increases instantaneously. The polarisation of the surrounding solvent molecules responds to this dipole change in the solute and start reorganizing around the new dipole. Therefore, the energy relaxation process, caused by the solvent reorganization around the photoexcited probe, shifts the fluorescence spectrum to longer wavelengths with time.¹⁵⁵ The idea of solvent relaxation process has been conceptually illustrated in figure 1.4.

The reaction coordinate for the solvation process is considered to be represented by a so-called generalized solvation coordinate. In the case of a polar

solvent the reaction coordinate is a measure for the nuclear solvent polarization that can be considered to be in equilibrium with an effective dipole moment $\mu(t)$ of the

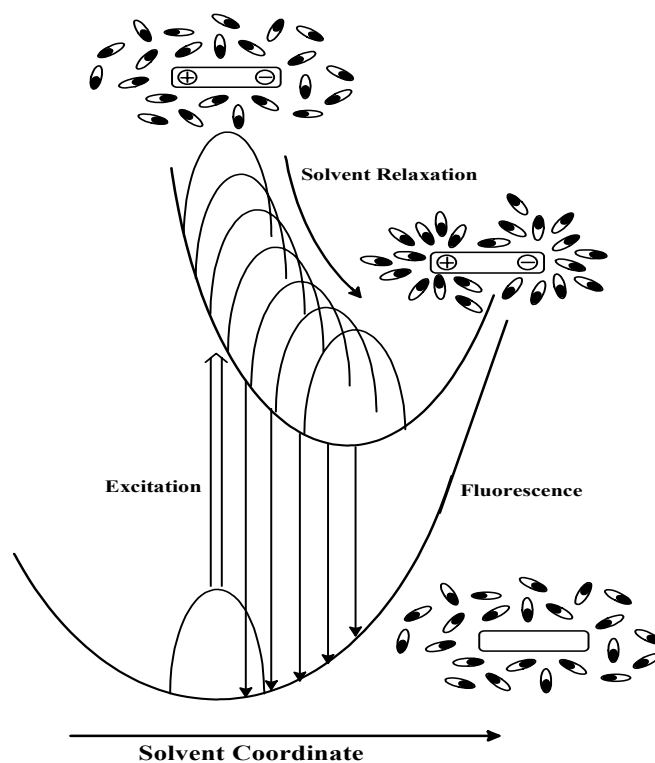


Figure 1.4 Schematic presentation of the dynamic Stokes' shift caused by solvent relaxation process following photoexcitation of the fluorescent probe. Adopted from reference [155]

solute molecule. Normalization leads to the relative coordinate $x(t)$, given as,

$$x(t) = \frac{\mu(t) - \mu_g}{\mu_e - \mu_g} \quad (1.1)$$

where μ_g and μ_e represent the ground and the excited state dipole moments of the probe.¹³⁸ The relaxation of the excited state population is usually studied by

monitoring the temporal characteristics of the spectral response function, $C(t)$, which is defined by following equation.¹³⁸

$$C(t) = \frac{\nu(t) - \nu(\infty)}{\nu(0) - \nu(\infty)} \quad (1.2)$$

where $\nu(t)$, $\nu(\infty)$ and $\nu(0)$ are the fluorescence peak frequencies at times t , ∞ and 0, respectively.

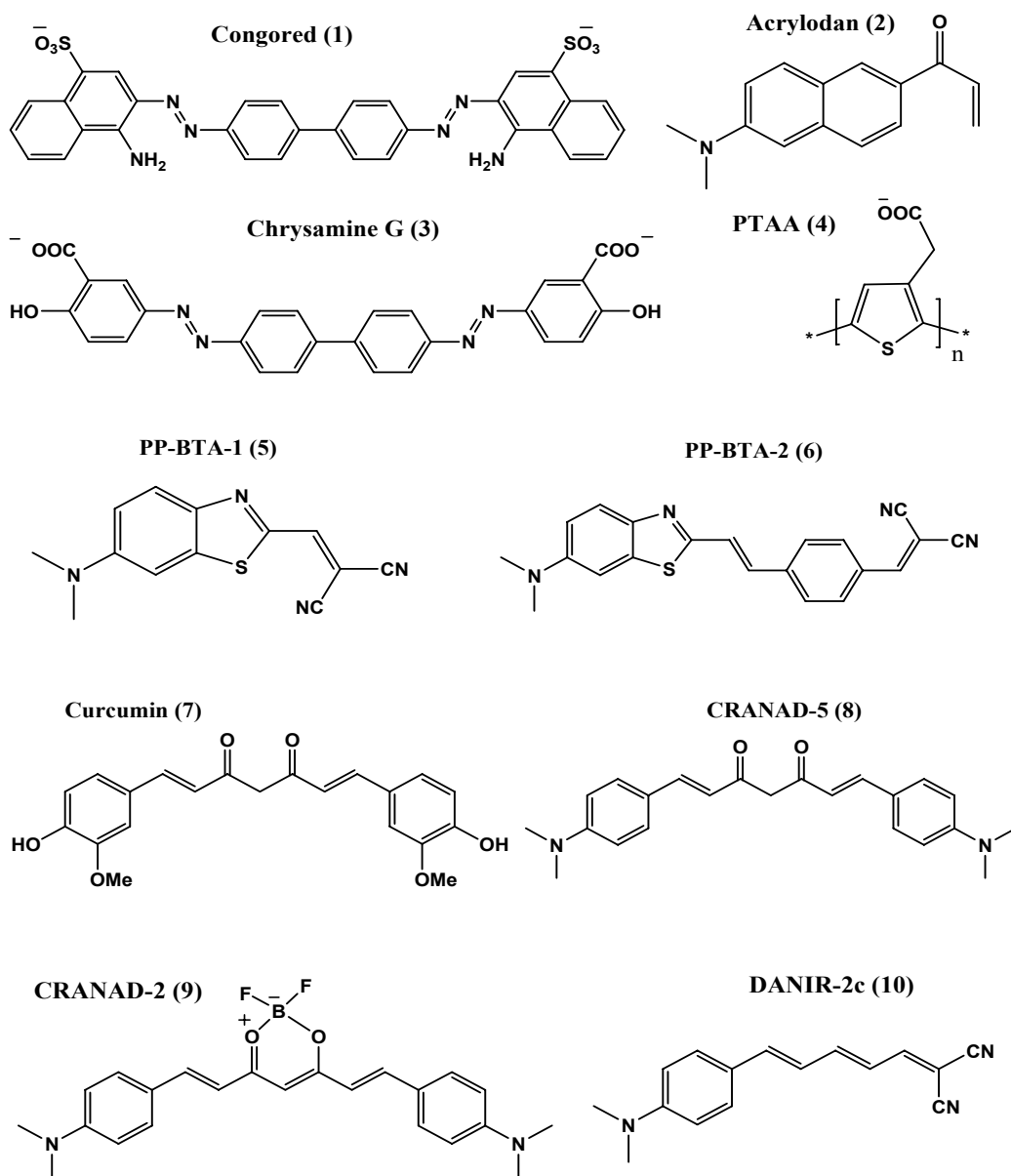
For the measurements of time-resolved emission spectra (TRES), a set of fluorescence decays are collected at different wavelengths, covering the entire emission band of the probe. These decays are fitted using a suitable functional form (usually a multi-exponential function) to obtain the fitted curves $D(\lambda, t)$. The TRES spectra, $S(\lambda, t)$, are then constructed using the fitted decays, $D(\lambda, t)$, after their normalization with respect to the steady-state fluorescence spectrum, $S_0(\lambda)$, using following relation.^{138, 156, 157}

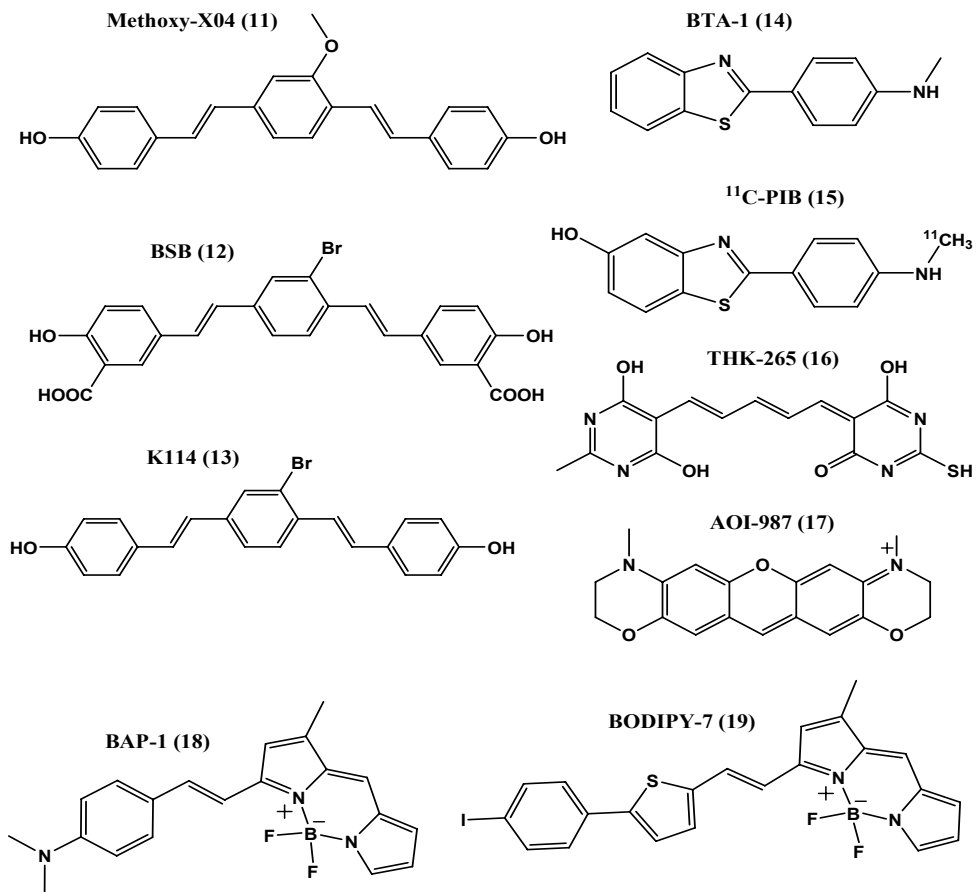
$$S(\lambda, t) = D(\lambda, t) \frac{S_0(\lambda)}{\int_0^{\infty} D(\lambda, t) dt} \quad (1.3)$$

To obtain smooth TRES, the data points obtained for the spectra $S(\lambda, t)$ using equation 1.3 are fitted following some line-shape function (usually log-normal function) for the emission band.^{138, 156, 157} The smooth TRES thus obtained are then used to estimate the emission maxima at different times and consequently to construct the dynamic Stokes' shift correlation function, $C(t)$. The function $C(t)$ thus obtained is the measure of the solvent relaxation dynamics. By using this method, recently, Mukhopadhyay and his coworkers studied the solvation dynamics in amyloid fibril of an intrinsically

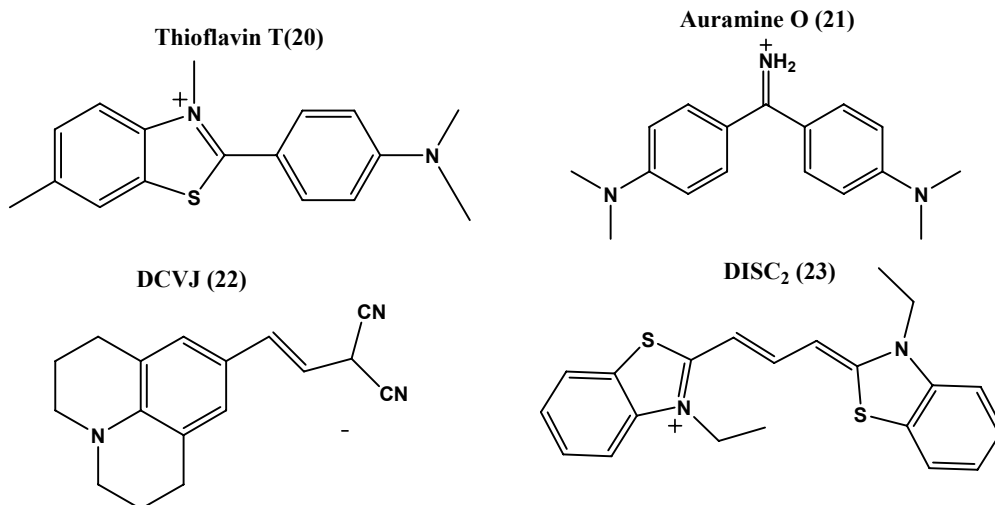
disordered protein, κ -casein by labelling an ICT based probe acrylodan (**2**, figure 1.5) at N-terminal of the protein. They revealed that the water dynamics got slowed down due to fibril formation.¹⁴⁸ This is explained on the basis of trapped water in between beta sheets of the fibril. It is also observed that there is dynamical exchange between bulk water and bound water.¹⁴⁸

ICT based probes





Molecular rotor based Probes



Aggregation based Probes

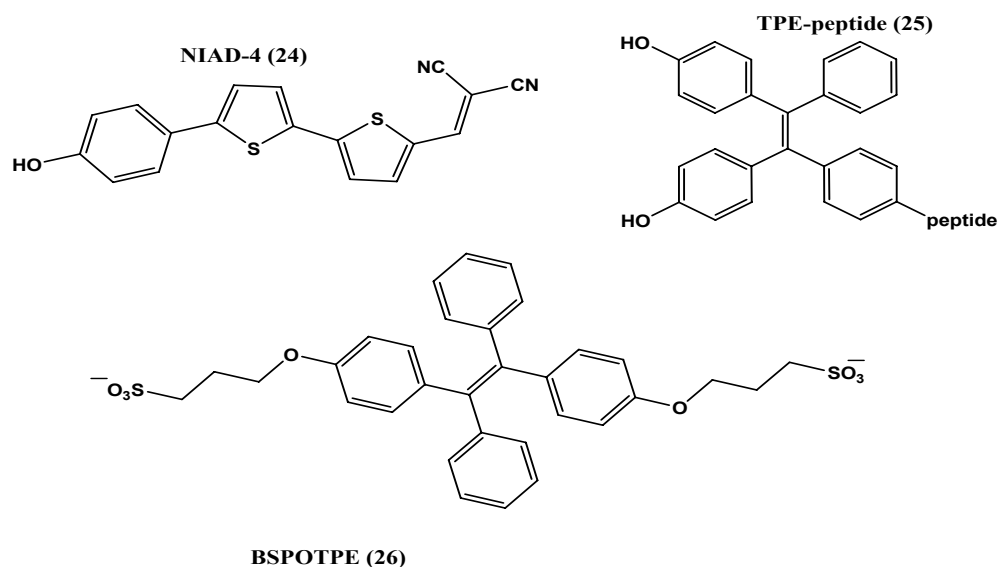


Figure 1.5 Structures of selected extrinsic fluorescence probes employed in amyloid fibrils detection.

1.3.2 Fluorescence resonance energy transfer

Fluorescence resonance energy transfer (FRET) is distance dependent interaction between two molecules where the energy absorbed by a fluorescent molecule (donor) will be transferred to second molecule (acceptor) non-radiatively through long range dipole-dipole interactions.¹²⁵ This energy transfer can be experimentally monitored by the quenching of donor fluorescence with a concomitant increase in acceptor fluorescence with increase in acceptor concentration.¹²⁵ As the theory of FRET has been explained by Forster, FRET is also known as Forster resonance energy transfer.¹⁵⁸ FRET is insensitive to the surrounding solvent shell of a fluorophore, and thus, produces molecular information unique to that revealed by other solvent-dependent events, such as fluorescence quenching, solvent relaxation, or anisotropic measurements. According to Forster's theory,¹⁵⁸ FRET efficiency (E)

exclusively depends on the following factors: (i) Spectral overlap between the donor emission and the acceptor absorption (ii) orientation of the transition dipoles of the donor and acceptor (iii) emission quantum yield of the donor (iv) extinction coefficient of acceptor and (v) distance between the donor and acceptor. Main advantage of FRET is its ability to find the distance between the donor-acceptor in Å level by knowing FRET efficiency. The FRET efficiency (E) has been calculated by the following equation.¹²⁵

$$E = 1 - \frac{F_{DA}}{F_D} = 1 - \frac{\tau_{DA}}{\tau_D} \quad (1.4)$$

where F_{DA} , F_D , are the emission intensity of donor in the presence and absence of acceptor respectively. However, the measuring emission intensity with reliability is difficult due to the spectral overlap between emission spectra of donor and acceptor (common in many cases). For that purpose, lifetime of the donor in the presence (τ_{DA}) and absence of acceptor (τ_D) have been used to calculate FRET efficiency. The mean relative distance (R) between the donor and acceptor dyes is calculated by the following equation

$$R = R_0 \sqrt[6]{\frac{1-E}{E}} \quad (1.5)$$

where R_0 is known as Forster distance, a distance at which there is 50% energy transfer is achieved. R_0 is estimated by using the following equation.¹⁵⁸

$$R_0 = 0.211[\kappa^2 n^{-4} Q_D J(\lambda)]^{1/6} \quad (1.6)$$

where, κ^2 is the orientation factor which is considered as 2/3 for the random orientation of donor and acceptor. n is the refractive index i.e., 1.4 for macro molecules in water. Q_D is the quantum yield of the donor and $J(\lambda)$ is the overlap integral which takes care of the spectral overlapping between emission spectrum of donor and absorption spectrum of acceptor and calculated by following equation.¹⁵⁸

$$J(\lambda) = \frac{\int_0^{\infty} F_D(\lambda) \varepsilon_A(\lambda) \lambda^4 d\lambda}{\int_0^{\infty} F_D(\lambda) d\lambda} \quad (1.7)$$

where ε_A is the molar extinction coefficient of the acceptor, $F_D(\lambda)$ is the peak normalized fluorescence intensity of donor at the wavelength, λ . Thus we can measure the distance between the FRET pair as close as $\sim 10\text{\AA}$ up to 10 nm.¹⁵⁹ Such advantage of FRET has been explored by several research groups to identify the relative location of new amyloid probe either with respect to intrinsic fluorophore such as tryptophan or extrinsic fluorophores.^{46, 160, 161}

Besides that, FRET has also been utilized to monitor or distinguish distinct features of amyloid fibrils. A FRET sensor has been developed to follow fibrillation process by fusing yellow fluorescent protein (YFP, donor) to α -synuclein protein aggregates (acceptor) by monitoring the lifetime of YFP by fluorescence lifetime imaging (FLIM) technique.¹⁶² It is observed that the decrease in the lifetime can be very good probe to monitor the dynamics compared to the emission intensity. In fact, this strategy has been utilized to monitor the fibrillation kinetics inside living cells.¹⁶² Moore and his co-workers developed a methodology based on FRET between two curcumin derivatives, CRANAD-2 & 5 (**8**, **9**, figure 1.5) to differentiate A β monomers

from higher molecular weight aggregates, even dimers. Monomers could not facilitate FRET between these two probes while in dimers and higher A β aggregates these two probes come close to each other resulting FRET between them. It is also shown that by combining thioflavin T (ThT) (**20**, figure 1.5) assay and this FRET assay, oligomers can also be distinguished from matured fibrils.¹⁶³ Deng et al reported that through dansyl-tryptophan FRET in Transthyretin (105-115), inter peptide arrangements can be studied.⁴⁶ Same group has also proved that the dansyl-tryptophan FRET is versatile tool for distinguishing the arrangements of beta sheets in the amyloid core. They have shown that dansyl-tryptophan FRET efficiency in parallel β -sheets is much higher than that in anti-parallel β -sheets.¹⁶¹

1.3.3 Aggregation induced quenching (AIQ) and enhancement (AIE)

The quenching of fluorescence with increase in the concentration of fluorophore is a well known phenomenon. This concentration quenching is due to the formation of aggregates, which is also known as ‘Aggregation induced quenching’ (AIQ).¹⁶⁴ In general such aggregation process is unwanted in most of the application of these fluorophores.¹⁶⁵ Most of the fluorophores are organic in nature and they tend to aggregate in aqueous solution due to their limited solubility in water resulting their fluorescence quenching.¹⁶⁴ Recently, it has been shown such fluorescence quenching due to the aggregation of probes is advantageous in detecting hydrophobic species such as amyloid aggregates.^{140, 166} These probes generally exist as aggregates in aqueous solution. However, on addition of amyloid fibrils to their aqueous solution, their aggregates breaks and the monomeric probes binds to the hydrophobic region of the fibril. Such de-aggregation of the probe due to the addition of fibril results in large increase in their emission intensity. At present, probes based on this principle, known

as ‘disaggregation induced fluorescence probes’, are used regularly to detect the fibril and to follow the kinetics of the fibril formation.¹⁶⁶

Swager et al designed and synthesized new fluorescent probe, NIAD-4 (**24**, figure 1.5), based on bithiophene molecular structure.¹⁴⁰ This dye shows strong affinity towards the amyloid fibrils and shows large fluorescence enhancement (~400 fold) upon binding with fibrils. Such large enhancement along with BBB (Blood brain barrier) penetrating power makes it very sensitive probe for fibrils.¹⁴⁰ Sodupe and coworkers has established through detail photophysics in different environment and computational studies that NIAD-4 primarily present in the aggregated form in the aqueous solution and disaggregates in the presence of amyloid fibrils.¹⁶⁶

However, there are several fluorescent probes has been discovered which on aggregation shows much higher emission yield compared to their monomers in the solution. The formation of aggregates in such class of molecules results in the retardation in the non-radiative torsional motion in their excited state and results in large fluorescent enhancement.¹⁶⁷ Fluorescent probes based on this principle, commonly known as “aggregation induced enhancement” (AIE),¹⁶⁷ has also been used for the detection of amyloid fibrils. For example, Pradhan et al designed an AIE based fluorescence probe, tetraphenylethene (TPE, **25**, figure 1.5) linked to an amyloid binding peptide, for monitoring the fibrillation process.¹⁶⁸ This probe doesn’t show any fluorescence in aqueous solution while it shows large fluorescence enhancement due to the formation of aggregates on the fibrillar surface.¹⁶⁸ Another interesting example of AIE based probe is 1,2-bis[4-(3-sulfonatopropoxy) phenyl]-1,2-diphenylethene (BSPOTPE, **26**, figure 1.5).⁸¹ This dye shows very low fluorescence in the presence of monomeric insulin protein while shows enhanced fluorescence in the

presence of preformed fibrils. However, surprisingly, prior mixing of this probe with insulin inhibits its fibrillation. This is due to the fact that BSPOTPE binds with partially unfolded insulin through hydrophobic interaction and obstructs further progress of the fibrillation process. Thus, BSPOTPE can also serve as ex-situ monitor and in-situ inhibitor for the fibrillation process.⁸¹ Similar strategy has been applied by other research groups also but could not able to reach significant sensitivity.¹⁶⁹

1.3.4 Ultrafast molecular rotors (UMR)

Ultrafast molecular rotors are characterized by the ultrafast torsional motion around a single bond connecting electron donor and acceptor moieties of a molecule in their excited state.¹⁷⁰⁻¹⁷⁷ Strictly speaking, these are subclass of ICT based probes but their emission properties are mostly governed by the rate of formation of twisted intramolecular charge transfer state (TICT) from locally excited state (LE).¹⁷⁰⁻¹⁷⁷ These molecules possess extremely low quantum yield in low viscous solvents. This is due to the existence of barrier less large amplitude torsional motion which creates efficient non-radiative channel for the depopulation of the photo excited state.^{128, 130, 178, 179} The retardation in such non-radiative torsional motion in the excited state will show high impact in its fluorescence properties. For example, in viscous solvents, due to the frictional force offered by the solvent, the rate of bond twisting decreases which leads to increase possibility of radiative emission from the LE state and thus increase in their emission yield.^{128, 130, 178, 179} Because of such property, the emission yield of UMRs is very sensitive to viscosity of the surrounding medium.^{170, 180-183}

Thioflavin T (ThT, **20**, figure 1.5), a gold standard amyloid probe, belongs to the class of UMR.^{129, 184-186} On photoexcitation, non-radiative twisting around the

central C-C single bond takes resulting very low emission yield in aqueous solution. However, in confined environment, like amyloid fibrils such bond twisting process retarded and shows large increase in its emission yield.^{128, 130, 179, 181, 187} Apart from ThT, several other UMR based probes have been explored for the sensitive detection of amyloid fibrils. Auramine-O (AuO, **21**, figure 1.5) is another classic example of UMR in which rotation about two amino phenyl groups leads to very low fluorescence in aqueous solution.^{188, 189} However, the binding of AuO to amyloid fibrils leads to large enhancement in its emission yield.¹⁹⁰ Interestingly, in the presence of insulin fibrils, AuO gives a new emission band at 560 nm in addition to its normal emission band at 500 nm.¹⁹⁰ Through detail spectroscopic studies, it has been showed that the long wavelength emission band arises due to formation of emissive H-aggregates of AuO in amyloid fibrils.¹⁹¹ As this aggregate band appears only in insulin fibrils and not in fibrils from other proteins like lysozyme, β -lactoglobulin and HSA, such properties of AuO can be used to distinguish insulin fibrils from other fibrils.¹⁹¹ However, strong fluorescence enhancement observed in the presence of native BSA protein questions the applicability of AuO as amyloid marker.¹⁹² Di-cyano vinyl julolidine (DCVJ, **22**, figure 1.5) is another UMR which is also been employed to detect amyloid fibrils.^{193, 194} DCVJ shows increase in its emission intensity on association with amyloid fibrils. Nonetheless, in contrast to ThT, it has been shown that DCVJ can detect the prefibrillar aggregates in solution. However, the sensitivity of DCVJ to amyloid fibrils is not as good as ThT.¹⁹⁴

Apart from the intensity based measurements, fluorescence lifetime of the molecular rotor is also sensitive to aggregation of proteins. Thompson et al reported that through fluorescence lifetime imaging (FLIM) of molecular rotor DISC₂ (**23**,

figure 1.5), multiple stages in the aggregation of lysozyme and insulin can be detected.¹⁹⁵ Same group introduced cyanine-based and BODIPY-based viscosity sensitive fluorescent molecular rotors to monitor the supramolecular assembly of various proteins.¹⁹⁶ The molecular rotors were covalently linked to the aggregating proteins to provided a unique possibility to monitor the aggregation process in amyloid fibrils both in-vitro and ex-vivo. Such approach offers opportunity to observe increased molecular crowding during protein aggregation in vitro and ex-vivo.¹⁹⁶

Hence, to develop and design an efficient molecular probe for amyloid fibrils, one should consider following points.^{102, 112, 117, 119, 120, 123, 139}

1. High sensitivity and binding affinity for amyloid fibrils.
2. Significant changes in the fluorescence properties upon binding to fibrils
3. Suitable emission wavelength to minimize the interference from background fluorescence
4. Ability to cross blood brain barrier (BBB)
5. High metabolic stability
6. Fast washout kinetics from normal brain regions
7. Low toxicity
8. Easy synthesis or availability.

Various classes of extrinsic fluorophores have been developed for assessing amyloid fibrils formation. However, the exact mechanism by which these probes recognize the misfolded and fibrillar state of amyloidogenic proteins is not well understood. It is believed that probe intercalation due to the similarity in the structure with the inner grooves present in the fibrillar structure is responsible for their sensing activity.^{184, 197, 198} Energy lowering by the hydrophobic contacts and hydrogen bonding

interactions of the side chain of the amino acids with aromatic moieties of the probe molecule is also playing important role in the binding of these probes in amyloid fibrils.^{21, 129}

1.4 Classification based on Molecular structure

Most of the existing fluorescence probes possess common structural features, a push-pull structure with donor and acceptor moieties at the two ends of the structure and are connected by polarizable bridge. This structural feature makes the probe molecules polar.¹⁹⁹ Due to the difference in the excited state and ground state dipole moments, their fluorescence properties are very sensitive to the surrounding polarity.²⁰⁰ Most of the research on developing amyloid probes adopted a strategy of making derivatives of existing standard amyloid probes instead of going for new molecular scaffold. Hence, we will further discuss about the advances in designing molecular probes for the detection of amyloid fibrils in the view of different molecular scaffolds.

1.4.1 Congo Red based molecules

Congo Red (CR, **1**, figure 1.5) is an aromatic sulfonated azo dye, was introduced in 1920 by Benhold²⁰¹ and Divry²⁰² and demonstrated its characteristic blue-green birefringence under cross polarizers in the presence of amyloid fibrils. Since then, it is one of the standard assays for identification of amyloid fibrils. Despite such usage, CR binding to collagen and cytoskeletal proteins also gives characteristic birefringence leads to false positive signals.²⁰³ Further, Fink and his co workers showed that CR can also bind to native and partially folded α -proteins, such as interleukin 2 and citrate synthase.²⁰⁴ Through small angle X-ray scattering it has been shown that CR can induce oligomerization of native proteins.²⁰⁴ Due to these reasons,

large number of derivatives of CR has been synthesized to overcome the limitation shown by CR. Klunk and his coworkers showed that the main structural feature that defines CR binding to fibrils is two acidic groups and the separation between them. They have synthesized fluorescent and lipophilic derivative of CR, Chrysamine-G (**3**, figure 1.5), which has two acidic groups having similar space between them.¹¹⁹ Chrysamine-G retained the amyloid affinity of its parent molecule, CR. However, due to its large size, the brain uptake of Chrysamine-G is very less. This limits its usage as *in-vivo* imaging agent.²⁰⁵ Consequently, intense efforts made to develop derivatives with high BBB permeability. BSB, K114 (**12**, **13** figure 1.5) are analogs of CR showed very good brain pharmacokinetics.²⁰⁶⁻²⁰⁸ As BSB has short wavelength emission, the interference from the autofluorescence from the cells is serious problem for the fluorescence imaging.²⁰⁷ But radiolabelled BSB has been used as PET imaging agent.²⁰⁹ K114 is also suffers from the interference from cellular auto fluorescence but to a lesser extent than BSB.²⁰⁸ Another CR derivative is methoxy-X04 (**11**, figure 1.5), which has shown to be a good candidate for *in-vivo* imaging of amyloid plaques.²¹⁰ However, the fluorescence properties and the brain uptake of methoxy-X04 is reported to be insufficient for *in-vivo* imaging of protein aggregates in transgenic mice models.²¹⁰ Hence, the derivatives of CR are less ideal for the imaging of fibrils. Further structural modifications are limited as the molecular frameworks of these dyes are quite rigid. As a result, attention has been shifted to develop probes on different molecular scaffold.

1.4.2 Thioflavin T based molecules

Another molecular dye for the histological staining of amyloid plaques is Thioflavin T (ThT). ThT is used for the detection of amyloid fibrils since 1959 and

remains unchallenged for decades.¹⁹⁸ ThT, a benzothiazole based UMR, is non fluorescent in the aqueous solution and shows large enhancement in its fluorescence intensity upon binding to amyloid fibrils.^{129, 186} Due to such large enhancement and lack of protein specificity makes it a gold standard for detection of amyloid fibrils *in-vitro*.²¹¹ Large enhancement in the presence of fibrils is attributed to the retardation of ultrafast non-radiative torsional relaxation around its central C-C bond in the excited state.^{128, 178, 212} However, several recent studies show that ThT can promote fibrillation through stabilizing β sheet conformations²¹³ and its sensitivity towards the fibrils is largely affected by the solution pH and ionic strength.^{194, 214} Such limitations of ThT question its usage as gold standard amyloid probe. Furthermore, positive charge on ThT decreases its permeability through BBB which limits its usage in *in-vivo* imaging.²¹⁵ Intense efforts have been made to modify the molecular scaffold of ThT to have lipophilic derivatives with better brain permeability. Among them, 2-(4-(4-methylamino)phenyl) benzothiazole (BTA-1, **14**, figure 1.5) shows nanomolar affinity towards amyloid fibrils with better brain uptake.²¹⁵ However, most of the derivatives don't retain the fluorescent properties of parent ThT.²¹⁵ Thus, some of them are radiolabelled with ¹¹C and used as PET / SPECT agents.^{106, 140, 216} Out of them, ¹¹C-PIB (**15**, figure 1.5) is successful *in-vivo* PET imaging agent which has been recently undergone clinical trials.^{217, 218}

Nonetheless, some of the fluorescent derivatives of ThT have shown affinity towards amyloid fibrils. Jung et al synthesized several ThT analogues which show micromolar affinity towards amyloid fibrils but the modulation in their fluorescence intensity upon bind with amyloid fibrils is limited (~36 fold).²¹⁹ Saji and coworkers have synthesized two push-pull benzothiazole based derivatives PP-BTA-1 and PP-

BTA-2 (**5, 6** figure 1.5) with benzothiazole moiety as electron donor and dicyanovinyl moiety as electron acceptor.¹²⁴ These derivatives also show very good affinity to fibrils in postmortem AD brain. From the inhibition studies, it has been shown that these dyes occupy same fibril site as ThT indicating both dyes are detecting similar fibrillar structure.¹²⁴ However, fluorescence enhancement observed for these dyes due to their association with fibrils is low and not suitable for imaging of fibrils.¹²⁴

1.4.3 Curcumin based molecules

Curcumin (**7**, figure 1.5), a common ingredient in Indian spices, is one of the histo-pathological amyloid staining dye for the senile plaques.^{220, 221} It has also been shown that curcumin can easily penetrate through BBB. Curcumin is being used in multiphoton imaging of amyloid fibrils in transgenic mice.^{220, 221} However, number of efficacy and safety studies revealed its instability in aqueous solution and its low bioavailability. Furthermore, it is also reported that curcumin can bind to native proteins and affect the fibrillation process. For example, Hafner-Bratovic et. al. showed that curcumin binds to α -helical intermediate of prion protein and inhibits its aggregation.²²² It is also shown, through SEM technique, that insulin forms smaller fibrils in the presence of curcumin.²²³ Thus, curcumin might give false positive signals during the evaluation of the efficiency of therapeutic drugs.²²⁰

Curcumin has also been derivatized to give better fluorescence amyloid specific probe. In the curcumin structure, a difluoroboronate moiety and two dimethyl anilino groups have been attached to create a donor-acceptor-donor architecture. Among such derivatives, CRANAD -2 (**9**, figure 1.5) shows significant fluorescence enhancement (~70 fold) and large blue shift (~90 nm) in its emission spectrum in

presence of A β aggregates.²²⁴ Unfortunately, low brain uptake and slow clearance from non specific regions of brain makes it unsuitable for the *in-vivo* imaging.²²⁴ Same group have developed several other curcumin derivatives like CRANAD-58, CRANAD-17 etc.²²⁵ However, all these probes interact with soluble A β monomers leads to fluorescence changes but to a lesser extent compared to insoluble fibrillar species.²²⁵

1.4.4 Luminescent conjugated polymers (LCP)

The optical properties of conjugated polymers are highly affected by the conformation of polymer framework and separation of different parts of polymer and aggregation of polymer chains.²²⁶ The distinctive conformational sensitive optical properties offer a great advantage for studying protein aggregation as binding of LCPs to different structural intermediates give different emission characteristics.²²⁷ For example, Polythiophene acetic acid (**4**, PTAA, figure 1.5) exhibits different spectral properties in the presence of native and fibrillar states of protein.²²⁷ PTAA emits strong emission at 550 nm in the presence of native insulin and quenched emission at 580 nm in the presence of insulin fibril.²²⁷ Although the different protein forms are easily distinguishable due to its distinctive emission properties, LCPs that are selective to fibrils are preferred. Further, a zwitterionic polymers t-POWT and PONT has shown fluorescence enhancement (~6 fold), contrasting to PTAA, in the presence of insulin fibrils.²²⁸ Like ThT, PONT can also follow the fibrillation kinetics.²²⁸ Due to the low fluorescence enhancement further chemical modification is required to enhance the optical properties. The conformation induced change in optical properties has been used to identify different structural intermediates during amyloid formation in transgenic mice. LCPs exhibit emission of different colours which are attributed to

different kind of aggregated species. This property has been utilized to understand the pathways involved in fibrillation as well as polydispersity/heterogeneity of fibrils.¹³⁹

Swager et al designed new fluorescent probe, NIAD-4 (**23**, figure 1.5) based on bithiophene molecular scaffold.¹⁴⁰ This dye shows strong fluorescence enhancement (~400 fold) along with large affinity to fibrils.¹⁴⁰ Further, some more derivatives such as NIAD-11 and NIAD-16 have been evaluated for *in-vivo* imaging. NIAD-16 can distinguish vascular and non-vascular A β plaques from background signal through fluorescence lifetime imaging studies.¹¹⁸

1.4.5 Cyanine based molecules

Yarmoluk and his coworkers have studied the fluorescence properties of a series of polymethine cyanine containing benzothiazole and benzimidazole end groups in presence of β -microglobulin fibrils.²²⁹ Out of all the dyes screened, molecules containing small polymethine chain (mono and trimethine) have shown higher contrast to amyloid fibrils to native proteins. Cyanine dyes with long methine chain are sensitive to spherical oligomers.²²⁹ Meso-substituted symmetric cyanine dyes such as T-49, SH-516, etc. also show a promising fluorescence response towards fibrillar aggregates.²²⁹ A fluorescent benzothiazole based meso substituted cyanine dye, 7519, has been used for the study of fibrillation inhibitory properties of zirconium metal complexes.²³⁰ Volkova et al introduced several cyanine based dyes for the amyloid detection. These probes have spectral properties, unlike ThT, suitable for the *in-vivo* amyloid imaging and their presence doesn't affect the fibrillation process. But these probes show quite limited sensitivity.²³¹ THK-265 (**16**, figure 1.5) is another cyanine based probe with two pyrimidine rings at the two ends of molecule.²³² THK-265

shows strong affinity to fibrils than Thioflavin-T but less than BTA-1. But large fluorescence yield (38.5%) in the free form and low Log P value (~1.8) restricts its practical applicability.²³²

1.4.6 BODIPY based molecules

Boron-dipyrromethene, BODIPY, based dyes found extensive applications in variety of fields due to its photo stability, high extinction and fluorescence yields, wide tunability and ease of synthesis.²³³ One of the derivative, BODIPY-7 (**19**, figure 1.5), has been synthesized and its dual SPECT/fluorescence imaging properties.¹¹⁶ Unfortunately, radiolabelled one doesn't meet requirement of the SPECT imaging agent. High emission yield in its free form and small Stokes' shift limits in further usage in optical imaging.¹¹⁶ Saji and his coworkers synthesized series of BODIPY derivatives known as BAP-1(**18**, figure 1.5) to BAP-5.^{234, 235} All these derivatives show very strong affinity to amyloid deposits *ex-vivo*. But these probes show nonspecific binding i.e., showed large accumulation in the scalp than in the brain.²³⁵ These results suggest that further chemical modifications of BODIPY derivatives are required for future imaging applications.

1.4.7 Other probes

Extensive effort has been made to develop amyloid probes based on several other chemical scaffolds. Hintersteiner et al have synthesized a series of oxazine core based probes and have been assayed for their affinity to the amyloid structures.²³⁶ Among these probes, AOI-987 (**17**, figure 1.5) shows absorption and emission at 650 nm, 670 nm respectively, shows bright images and good affinity to fibrils. It also displaced ThT bound to A β suggests both dye occupies same binding site.²³⁶

Nonetheless, the signal contrast between the wild-type and transgenic mice were not significant. Small Stokes shift and low fluorescence enhancement makes it as inefficient in imaging applications. Structurally, AOI-987 belongs to a donor–acceptor structure but with a rigidified bridge. This might be the reason for non optimal properties of this probe.²³⁶

Recently, Cui et al reported a series of probes called DANIR probes which are having dimethyl aniline group as donor and dicyano vinyl group as acceptor with conjugated double bonds as bridge.¹²² Among them, DANIR 2c (**10**, figure 1.5) shows strong affinity towards fibrils but the fluorescence enhancement is very low (~12 fold).¹²² To improve this aspect same group has introduced second generation of DANIR probes by replacing benzene group with naphthalene group leading to the increase in the π - conjugation length in the system.²³⁷ These dyes show strong fluorescence enhancement in the presence of fibrils both *in-vitro* and *in-vivo*. However, these dyes exhibit poor brain kinetics such as low brain uptake and show slow washout kinetics from normal brain regions.²³⁷ Besides, DANIR 3c is shown to be unstable in mice.²³⁷ Further chemical modifications are needed to have proper balance between hydrophilic and hydrophobic properties of DANIR probes for better contrast and proper brain kinetics.

Research on the fluorescence based detection of amyloid self assembly has taken a great leap in the last few years. Several classes of dyes have been explored for the efficient detection of protein aggregates *in-vitro*, *ex-vivo* and *in-vivo*. Despite such intense efforts, still ThT has been used extensively for the regular detection of amyloid fibrils *in-vitro* and for histological staining of postmortem AD brains. This is due to the fact that except a few, most of the dyes developed doesn't show better

fluorescence enhancement than ThT even though they have better binding affinity.^{215, 238, 239} Thus, there is still lot of scope for developing fluorescence probes for amyloid fibrils with better sensitivity. Recently, our group showed that, through ultrafast fluorescence spectroscopy, only small part of (~10%) of amyloid bound ThT population is contributed to the observed fluorescence enhancement.²¹⁴ The major part of bound ThT i.e., surface bound ThT, which are driven by electrostatic forces, are not contributing to its fluorescence enhancement in amyloid fibrils. Only those ThT molecules which are bound in the inner grooves of the fibrils give the enhanced fluorescence.²¹⁴ Thus, strategy for developing better amyloid probes is to reduce surface bound population. This can be achieved by designing probes with better hydrophobic character in their molecular structure. By doing this, we can increase the percentage of dye population bound in the inner grooves of the fibrillar structure. In this dissertation, we have explored three electronically different probes, cationic (chapter 3), neutral (chapter 4) and zwitterionic probes(chapter 5) for the efficient detection of amyloid fibrils through monitoring their modulation in the fluorescence properties such as band position, intensity and excited state lifetime. The relative location of these probes with respect to ThT has been identified by employing energy transfer phenomenon. AutoDock studies also have been performed to understand the nature and kind of interactions that leads to efficient binding of these probes to amyloid fibrils.²⁴⁰ Beside the detection of amyloid fibrils, understanding the dynamical aspects which govern the fibrillation also has utmost importance in determining their activity. In the chapter 6, we have attempted to understand the fate of dynamics of water in Human serum albumin (HSA) fibrils and compared with that of native protein.

Chapter-2

Instruments and Methods

2.1 Introduction:

This chapter gives a brief overview of the various experimental techniques that have been used to pursue the research work pertaining to the present thesis. To understand the dynamical processes in different probes in amyloid fibrils, both steady-state and time-resolved photophysical measurements were carried out using absorption and fluorescence techniques. Time-resolved fluorescence anisotropy measurements have been performed to understand the rotational diffusion of the probes in amyloid fibrils. Fluorescence imaging techniques such as epi-fluorescence as well as confocal microscopy have been used to image dye stained amyloid fibrils. Ultrafast processes like, charge transfer, solvent relaxation, intramolecular relaxation, etc in the excited state of the probe molecules have been investigated using state-of-the-art femtosecond time-resolved fluorescence up-conversion technique. Brief description of different instrumental techniques used in this work was presented below.

2.2. Ground-State Absorption Measurements

The knowledge on the absorption and emission properties of systems under investigation will help in better understanding the effect of light on the chromophoric systems. Optical absorption (ultraviolet-visible; UV-vis) spectroscopy is an

extensively utilized technique to obtain information about the ground-state absorption characteristics of the chemical systems (the wavelengths of the absorption bands, the extinction coefficients at different wavelengths). UV-vis absorption spectrum, being dependent on the electronic structure and the environment of the absorbing chromophore, allows the characterization or the identification of different chromophoric systems and their micro-environments. Changes in the solvent polarity, polarizability and hydrogen bonding characteristics often induce significant changes in the absorption spectra.^{125, 241-243} Hence, this simple spectroscopic technique can provide much useful information regarding the nature of interactions between the ground-state of a chromophoric molecule and its surrounding environment. Measurements of the optical absorption spectra is very essential to maintain the concentration of the absorbing species for the purpose of their investigations using different other spectroscopic techniques.

The working principle of the spectrophotometer is based on the Beer-Lambert's law (*cf.* equation 2.1). According to this law the absorbance (A) of a chromophore is directly proportional to the concentration (C) of the species, its molar extinction coefficient (ϵ_λ) at the measuring wavelength λ and the optical path length (l).²⁴¹

$$A = \log\left(\frac{I_0}{I}\right) = \epsilon_\lambda Cl \quad (2.1)$$

where I_0 and I are the intensities of the incident and transmitted light, respectively. In present work, absorbance of the chemical systems has been measured in a quartz cuvette of 1 cm path length.

Ground-state optical absorption measurements have been carried out using a JASCO (Model #V-650) UV-visible spectrophotometer. It is a double-beam spectrophotometer with a photomultiplier tube (PMT) detector. Typical operating wavelength range is 200-900 nm. The light sources used in this instrument are deuterium lamp (range: 190 to 350 nm) and a tungsten (W) lamp (range: 330 to 900 nm).

2.3. Steady-State Fluorescence Measurements

Fluorescence spectroscopy is the most sensitive and extremely powerful technique to investigate various photophysical and photochemical processes that occur in the excited state of the chromophoric molecules. The intensity of the fluorescence band, the fluorescence peak position, as well as the shape of the fluorescence spectrum is in general very sensitive to the environment.^{125, 241-243} In the present study steady-state fluorescence measurements (fluorescence intensity, excitation spectra or emission spectra) have been carried out using a Hitachi spectrofluorometer (model F-4500), which uses a 150 W continuous powered high pressure xenon lamp as the excitation source and R-928F PMT (Hamamatsu) as the photo detector. The spectral range covered in the present instrument is 220 to 800 nm. Liquid sample in a 1 cm x 1 cm suprasil quartz cuvette is excited and the fluorescence is measured in a perpendicular direction with respect to the direction of the excitation beam in order to minimize the excitation background.

The quantum yield of fluorophores has been measured by comparative method using a known standard as reference.¹²⁵ The fluorescence quantum yield of the sample

(ϕ_{sample}) can be expressed with respect to the quantum yield of the reference ($\phi_{\text{reference}}$) according to equation 2.2.¹²⁵

$$\phi_{\text{sample}} = \frac{OD_{\text{reference}}}{OD_{\text{sample}}} \times \frac{A_{\text{sample}}}{A_{\text{reference}}} \times \frac{n_{\text{sample}}^2}{n_{\text{reference}}^2} \times \phi_{\text{reference}} \quad (2.2)$$

where $OD_{\text{reference}}$ and OD_{sample} are the absorbances at the excitation wavelength, $A_{\text{reference}}$ and A_{sample} are integrated fluorescence intensities and $n_{\text{reference}}$ and n_{sample} are the refractive indices for the reference and the sample solutions, respectively.

2.4. Fluorescence Lifetime Measurements

Time-dependent fluorescence studies are extremely important to understand the details of the photoprocesses taking place in the excited state of the molecules. The most versatile technique for the time-dependent fluorescence measurement is based on the Time-Correlated Single Photon Counting (TCSPC) principle and is widely used to measure fluorescence lifetimes in the nanosecond to millisecond time scales.^{125, 241-247} In fact, the development of various ultrashort light sources like the nanosecond flash lamps, nanosecond LEDs, picosecond laser diodes, picosecond/sub-picosecond pulsed lasers, etc. has made the TCSPC technique as the most demanded technique for time-dependent fluorescence measurements.^{125, 241-247} In the present work a TCSPC spectrometer from Horiba Jobin Yvon IBH, UK (model Data Station Hub) was used to measure the fluorescence lifetimes of the samples under investigation. The important aspects related to the present TCSPC spectrometer are described in the following sections.

2.4.1. Basic Principles of TCSPC Technique

The time dependent fluorescence measurement by TCSPC technique relies on the principle that the probability distribution of a single photon emission is equivalent to actual intensity versus time distribution for all photons detected.^{125, 244-247} The schematic diagram of TCSPC has been presented in figure 2.1. The overall fluorescence decay measurement is carried out in the following sequence. The excitation pulse is splitted into two parts. One part is used for the excitation of the sample and other is synchronously fed into the start PMT. The output electrical signal from start PMT is routed through constant fraction discriminator (CFD) to a time to amplitude converter (TAC). On receiving the start pulse, the charging of TAC is initiated and continues with time. A STOP signal is generated on receiving first emission photon from the sample at the stop PMT. The STOP signal is fed to the stop input of TAC after passing through another CFD and variable delay line. On receiving the STOP signal, the charging of TAC stops and generates an electrical output with amplitude proportional to the time difference between the START and STOP pulses. The TAC output pulse is then fed into the Multichannel Analyzer (MCA) through an Analog-to-Digital Converter (ADC). The ADC generates a numerical value proportional to the amplitude of the TAC output pulse and thus selects the corresponding memory channel in the MCA, where a single count is added up.

The above START and STOP cycle is repeated for exceedingly large number of times to generate histogram of counts in the MCA channels. In TCSPC measurements, the emission count rate is kept very low (not exceeding 2% of the excitation rate) by adjusting the excitation and emission slits.^{125, 244-247} Under such

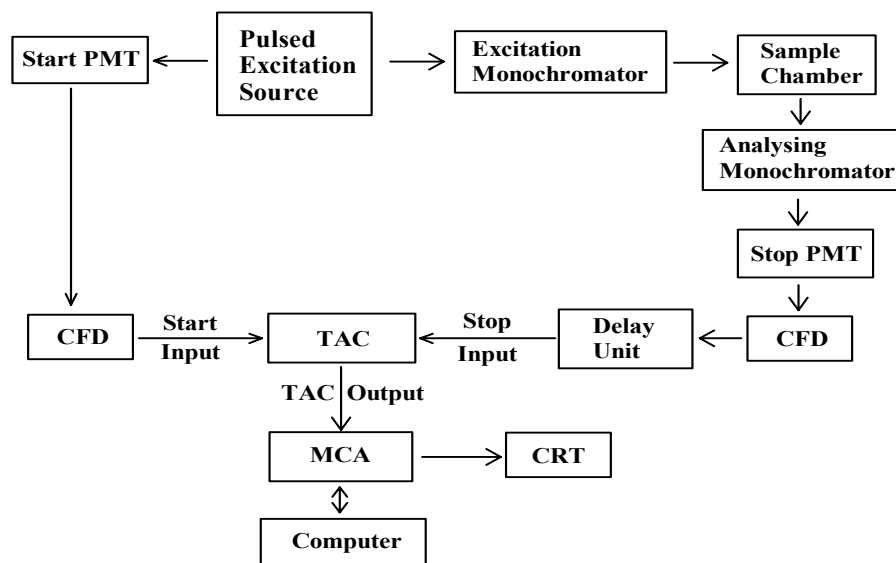


Figure 2.1 Schematic diagram of a Time-Correlated Single Photon Counting (TCSPC) Spectrometer.

situation, the distribution of counts recorded in MCA channels should represent the time dependent probability distribution of single photon emitted from the sample and thus the fluorescence decay.^{125, 244-248}

2.4.2. Important components of a TCSPC spectrometer

The important components of the present TCSPC instrument are briefly described below.

(a) **Pulsed excitation source:** Various light emitting diodes (LED's) and diode lasers, having different emission wavelengths between 292 nm to 490 nm have been used as the excitation sources. With diode laser excitation sources (405 and 445 nm) and using a special fast stop PMT (vide infra), the instrument response function (IRF) for the spectrometer is about 170 ps (FWHM). With the LED excitation sources, the

IRF is about 1.2 ns (FWHM). The repetition rate for excitation sources is usually kept at 1 MHz.

(b) Constant Fraction Discriminator (CFD): CFD offers two advantages in TCSPC setup one is to improve signal to noise ratio and other is to give well defined timing information to TAC from the START and STOP pulses. Since the other simple leading edge discriminators are always possess significant timing errors, the CFDs are known to be the best-suited discriminators for the TCSPC measurements to obtain accurate timing information for TAC.

(c) Variable Delay Line: A variable delay line is introduced in the path of STOP signal immediately after CFD to ensure that the entire stop signal should arrive at TAC after receiving the respective START signal. An optimum delay is always required to be introduced in the variable delay line to place the recorded fluorescence decay trace, histogram in the MCA, properly within the MCA channels.

(d) Time-to-Amplitude Converter (TAC): TAC is the heart of a TCSPC instrument.^{244-246, 249-251} The time-correlation between excitation and emission events (START & STOP signals) is in fact carried out by this unit and its function is conceptually shown in figure 2.2. The electrical signal received from START PMT initiates the charging process of timing capacitor in TAC and the charging is terminated upon receiving STOP signal. This generates the electrical output pulse whose amplitude is proportional to time difference between start and stop events. If the stop event is not registered within preset time, TAC range, the charging automatically stops without recording an event and gets reset for the next collection cycle. In the present TCSPC instrument the TAC range can be varied from 50 ns to

200 μs . A suitable TAC range is judiciously selected to make the complete fluorescence decay of the sample to be collected within the appropriate channels of the MCA used.

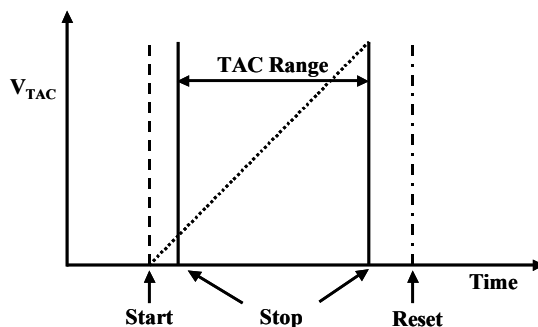


Figure 2.2 Functioning of a TAC unit used in a TCSPC instrument. Start indicates the initiation of the charging process. Stop signal can arrive at TAC unit at any time within the TAC range following the arrival of the start pulse.

(e) Multichannel Analyzer (MCA) and its calibration: The MCA used in TCSPC instrument have an analog to digital convertor (ADC) and a memory having large number of channels for storing the time correlated data. The MCA used in a TCSPC instrument can be operated either in the Pulse Height Analysis (PHA) mode (for measuring fluorescence decays) or in the Multichannel Scaling (MCS) mode (for measuring time-resolved emission spectra). The time calibration of MCA channels (*time/channel*) can be carried out by using a number of precisely calibrated delay lines in the path of the STOP pulse.^{244-246, 249-252} Here, the STOP signal is divided into two paths, one is fed to the START input of the TAC and the other is routed through the precisely calibrated delay lines to the STOP input of the TAC. As the same signal is fed into the START and STOP input of the TAC, count will be collected at a single channel of the MCA, determined by the known delay introduced in the path of the STOP pulse. For different known delays, the counts are thus collected at different

channels of the MCA. The MCA data thus obtained are then transferred to a computer and the time calibration is calculated using a suitable analysis program. The calibration process should be independently carried out for different TAC ranges to be used in the measurements.

(f) The Start PMT: As the light intensity detected by the Start PMT is quite high, an ordinary PMT with medium gain and reasonably low transit time (the time difference between the emission of a photoelectron and its arrival to the anode) can be used to generate the START signals for the TAC unit.

(g) The Stop PMT: The transit time spread of the PMT has a prominent effect on the time resolution of a TCSPC instrument. Reduction in the transit time will also reduce the transit time spread resulting in better time resolution of a TCSPC measurement. Hence, a fast PMT is always preferable for the TCSPC measurements. It is important to mention that due to the inherent low level of light in TCSPC measurement, stop PMT should have high gain which in turn needs large number of dynodes. In general use of large number of dynodes results in the increase in the transit time as well as its spread and thus, reduces the time resolution significantly. The detector used in this instrument is a special Hamamatsu PMT, used in combination with a TBX4 module provided by IBH, UK, and is used with a Peltier cooling. The spectral response of the detector is from ~300 to 800 nm. To increase the time resolution below 100 ps, a multi channel plate (MCP) PMT has been coupled with the IBH TCSPC instrument. For faster data collection, the START and STOP signals are reversed in this setup. The electrical pulses synchronized with excitation light source are directly used as the STOP pulses for the TAC unit while the electrical pulses generated due to the emitted photon in the STOP PMT is actually used as the START pulse for the TAC unit. Such

reverse order in the START and STOP signal (commonly known as “reverse mode”) is used to avoid unnecessary charging of the TAC unit while using excitation source with high repetition rate. To be mentioned, a PC based card that incorporates both TAC and MCA is used for the data collection. PC monitor is directly used to display the measured decay curve. DAS6.0 software (IBH, UK) is used to analyze the measured decay curves to obtain the fluorescence decay parameters of the samples.

2.4.3. Analysis of the fluorescence decay curves measured in a TCSPC instrument

In the absence of any complex photochemical processes, the emission decay of excited state molecules follows single-exponential decay kinetics (equation 2.3). However, the decay often becomes more complicated due to the presence of complex processes in their excited state and needs a complex decay functions for its representation. In general, most of the complex decay kinetics can be fitted with the multi-exponential decay function (equation 2.3).^{244-246, 248, 252-255}

$$I(t) = \sum A_i \exp(-t / \tau_i) \quad (2.3)$$

where A_i is the pre-exponential factor and τ_i is the fluorescence lifetime of the i^{th} decay component of the measured decay. If the sample is excited with an unusually short excitation pulse (δ -pulse) and the response time of the detection system is very fast compared to the fluorescence lifetime of the sample, the fluorescence lifetime can be directly obtained from the observed fluorescence decay either by noting the time at which the fluorescence intensity decreases to $1/e$ of its initial value or from the slope of the plot of $\log I(t)$ versus t .^{244-246, 248, 252-255}

However, when the fluorescence lifetime is short and comparable to the instrument response function, the decay traces will get distorted due to the finite width of the excitation profile. Under such circumstance, it is not possible to apply the above procedures to obtain the fluorescence lifetime of the sample. In such cases, the observed fluorescence decays are analyzed following a reconvolution and compare procedure as described below. Since the excitation pulses used do have a finite time width and also the detection system has its finite response time, the observed decay curve $I(t)$ would actually be a convolution of the true decay curve $G(t)$ and the effective instrument response function $P(t)$. From a simple consideration it can be shown that the function $I(t)$, $G(t)$ and $P(t)$ can be correlated by the following convolution integral.^{244-246, 248, 252-255}

$$I(t) = \int_0^t P(t') G(t - t') dt' \quad (2.4)$$

Both $I(t)$ and $P(t)$ can be measured experimentally. The measurement of emission from the sample produces $I(t)$. To record $P(t)$, an ideal scatterer is placed in place of the sample and the scattered light is collected under similar condition. During analysis, a decay function $G(t)$ is first assumed for the sample and is convoluted with the observed $P(t)$ according to equation 2.4 to obtain a calculated decay curve $Y(t)$, which is then compared with the experimentally observed decay curve, $I(t)$. This procedure is repeated by changing fitting parameters iteratively until a proper representation of true decay curve is obtained. The success of an analysis and accordingly the acceptance of a fit is determined from the judgment of the following statistical parameters.

(a) Reduced Chi-square (χ_r^2) values: An important statistical parameter to judge the goodness of a reconvolution analysis of an observed fluorescence decay curve using TCSPC measurement is the reduced chi square (χ_r^2) value which is defined by the following equation.²⁴⁴⁻²⁴⁶

$$\chi_r^2 = \frac{\sum_i W_i \{Y(i) - I(i)\}^2}{(n - p)} \quad (2.5)$$

where $Y(i)$ is the count at the i^{th} channel of the calculated curve, $I(i)$ is the count at the i^{th} channel of the experimentally measured curve, $W_i [=1/I(i)]$, is the weighting factor of the counts in the i^{th} channel, n is the number of channels used for the decay to be analyzed and p is the number of degrees of freedom in the decay function considered for the analysis (equals to the number of variables in the function $G(t)$). For a good fit, the χ_r^2 value should be very close to unity.²⁴⁴⁻²⁴⁶

(b) Distribution of weighted residuals: Another important statistical function that is widely used in combination with χ_r^2 values to judge the goodness of a re-convolution analysis of an observed decay is the distribution of the weighted residuals among the data channels used. The weighted residual for the i^{th} channel, r_i , is defined by equation 2.6.

$$r_i = \sqrt{W_i} \{Y(i) - I(i)\} \quad (2.6)$$

where W_i , $Y(i)$ and $I(i)$ are as defined earlier. For a good fit, the weighted residuals should be randomly distributed about the zero line for the whole range of the data channels used in the decay analysis.²⁴⁴⁻²⁴⁶

2.5. Fluorescence Anisotropy Measurements

In a homogeneous solution, where all fluorophores are randomly oriented, excitation with a polarized light results in an anisotropic distribution in the ground state due to photoselective excitation. Each chromophore has, within its molecular framework, a fixed absorption and emission transition dipole with a definite orientation with respect to the molecular axis. The probability of absorption of the incident light is determined by the angle between the absorption transition dipole and the electric field vector of the incident light. Chromophores with absorption transition moment oriented parallel to the electric field of the incident light preferentially absorb the photon.^{164, 244, 246, 256} Thus, due to such photoselection, the excited state population is not randomly oriented. Instead, there will be somewhat larger number of excited molecules, which have their absorption transition dipole moment aligned to the polarization of the excitation light. This preferential excitation of molecules creates anisotropy in excited electronic state and a mirror image of this anisotropy in the ground-state (see Figure 2.3).¹²⁵

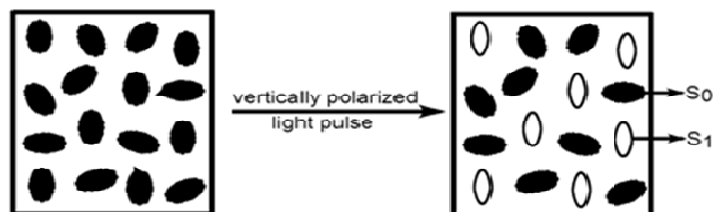


Figure 2.3 Creation of ground-state and excited state anisotropies from an isotropic distribution of molecules due to photoselective absorption of photons.

In dilute solutions, where intermolecular energy transfer is negligible, depolarization in the ground-state anisotropy is primarily due to the rotational motion

and electronic relaxation of the fluorophores. However, depolarization in the excited state takes place only due to the rotational relaxation process. The anisotropy measurements reveal the average angular displacement of the fluorophore that occurs between the absorption and the subsequent emission of a photon. This angular displacement is dependent upon the rate and extent of rotational diffusion during the lifetime of the excited state. Such diffusive motions are largely dependent on the size and shape of the molecules and the frictional forces due to the surrounding environment. Such frictional force could be due to merely shearing force (viscosity) or due to any solute-solvent interaction, like H-bonding, etc. Thus, the anisotropy measurements provide us the knowledge about the frictional force exerted on the fluorophore by surrounding media.^{125, 244, 254, 256}

Fluorescence anisotropy can be measured using both steady-state and time-resolved techniques. In a steady-state measurement, the sample is illuminated with a continuous beam of plane polarized light while in time-resolved technique the excitation is performed with a pulsed polarized light. The schematic for the measurement of the fluorescence anisotropy (both steady-state and time-resolved) is illustrated in figure 2.4. The sample is excited with the vertically polarized light, i.e. the electric vector of the excitation light is oriented along the z -axis. In steady-state measurements, the emission intensity the sample is measured through a polarizer oriented either parallel (I_{\parallel}) or perpendicular (I_{\perp}) with respect to the excitation polarization and the anisotropy ($\langle r \rangle$) is calculated using following equation.^{125, 244, 254,}

256

$$\langle r \rangle = \frac{I_{\parallel} - GI_{\perp}}{I_{\parallel} + 2GI_{\perp}} \quad (2.7)$$

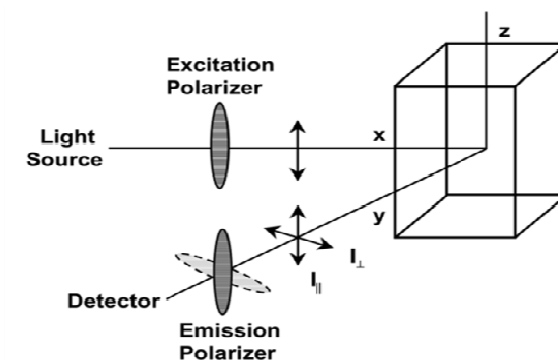


Figure 2.4 Schematic diagram for the measurement of fluorescence anisotropy.

The factor G in equation 2.7 arises to correct the polarization dependent sensitivity of the detection system. The G -factor is experimentally measured independently by exciting the sample with horizontally polarized light and measuring the fluorescence intensities at perpendicular (I_{HV}) and parallel (I_{HH}) polarization with respect to excitation polarization. The ratio of emission intensity at these two polarization, I_{HV}/I_{HH} , gives the value of the G factor at respective emission wavelength.^{125, 244, 254, 256}

Similar to steady-state anisotropy, the time-resolved fluorescence anisotropy is expressed as

$$r(t) = \frac{I_{\parallel}(t) - GI_{\perp}(t)}{I_{\parallel}(t) + 2GI_{\perp}(t)} \quad (2.8)$$

where $I_{\parallel}(t)$ and $I_{\perp}(t)$ are the two polarized fluorescence decays with emission polarizations parallel and perpendicular with respect to the vertically polarized excitation light.^{125, 244, 254, 256}

2.6. Fluorescence up-conversion Measurements

The maximum time resolution that can be achieved with the TCSPC technique is ~ 40 ps using a MCP-PMT as the detector. Further improvement in the time resolution in TCSPC techniques could not be archived due to lack of fast detector system.^{125, 244, 254, 257} Hence, any excited state processes that happens in the sub-picosecond time-scale cannot be measured by TCSPC technique. However, to record the emission transient in the sub-picosecond time scale, non-linear optical gating technique is introduced by Mahr and Hirsch.²⁵⁸ Such technique can provide the time resolution comparable to the excitation pulse width. In optical gating technique, the emission from the sample is mixed with the femtosecond laser pulse (gate) in a nonlinear medium to generate the sum or difference frequency light. Such optical mixing technique can provide time resolution close to the width of gate pulse. Optical gating technique, where the mixing of the gate pulse and the fluorescence generates sum frequency, commonly known as fluorescence upconversion technique, is widely used for measuring the fluorescence decays in the ultrafast time scales.

2.6.1. Basic principle of fluorescence up-conversion

2.6.1.1. Sum-frequency generation

The basic principle of fluorescence upconversion is based on the generation of sum frequency of incident gate beam of frequency (ω_g) and the emission frequency

(ω_{fl}) in a thin nonlinear crystal. The generation of sum frequency (ω_s) is schematically shown in figure 2.5. Due to the pulsed nature of the gate pulse, the sum-frequency is generated only during the temporal overlap of the gate pulse and the emission light in the upconversion crystal. Thus, despite longer temporal width of the emission light, only a thin slice of it will be upconverted by the gate pulse and hence, providing time-resolution quite comparable to the width of the gate pulses used.²⁵⁸⁻²⁶²

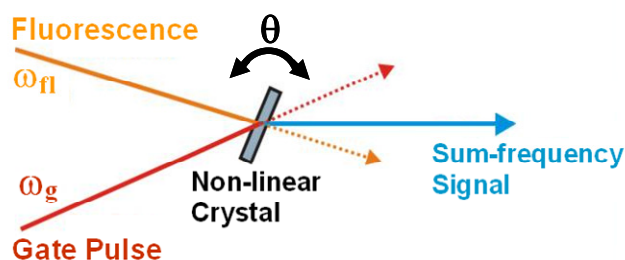


Figure 2.5 Schematic representation of sum frequency generation in a non-linear crystal.

The up-conversion efficiency of gate and emission pulses are mainly governed by the phase matching condition among the wave vectors (\vec{k}) of the different lights (ω_g , ω_{fl} , and ω_s) that interact in the nonlinear crystal.²⁵⁸⁻²⁶² For the efficient sum-frequency generation, two important criteria that needs to be satisfied are the “energy conservation” and the “momentum conservation” phase (matching condition) among the interacting lights in the nonlinear crystal. The conservation of energy implies following relation among the frequencies of the different light involved.

$$\omega_g + \omega_{fl} = \omega_s \quad (2.9)$$

Similarly, the momentum conservation (phase matching) condition gives the following relation

$$\vec{k}_s = \vec{k}_g + \vec{k}_f \quad (2.10)$$

where \vec{k}_g , \vec{k}_f and \vec{k}_s are the wave vectors for the gate, fluorescence and the sum frequency lights. The closeness of the phase matching condition for the sum frequency generation has been related to a parameter called phase mismatch, $\Delta\vec{k}$, and is expressed by the following equation.

$$\Delta\vec{k} = \vec{k}_s - (\vec{k}_g + \vec{k}_f) \quad (2.11)$$

For the collinear propagation of the gate and the fluorescence beams, the expression for phase mismatch can be simplified as,

$$\Delta\vec{k} = \vec{k}_s - (\vec{k}_g + \vec{k}_f) = \frac{1}{c} (n_s \omega_s - n_g \omega_g - n_f \omega_f) \quad (2.12)$$

where c is the velocity of light in vacuum and n_s , n_g and n_f are the refractive indices of the lights ω_s , ω_g and ω_f , respectively, in the non-linear medium. It is trivial that for the true phase matching condition, the $\Delta\vec{k}$ value should be equal to zero. Thus, smaller is the $\Delta\vec{k}$ value, better is the phase matching condition and hence better is the upconversion efficiency. However, achieving zero value for $\Delta\vec{k}$ is not practically possible as none of the interacting lights are monochromatic in nature. Thus, practically, efforts are made to achieve minimum phase match condition to attain maximum intensity for the sum frequency light.²⁵⁸⁻²⁶² To achieve this, the optical axis of the non-linear crystal is rotated with respect to the polarization direction and the

direction of propagation of the gate and the fluorescence light pulses until the intensity of the sum-frequency light becomes maximum for a selected ω_{fl} value. The monitoring emission wavelength (ω_{fl}) can be easily achieved by setting the wavelength of the monochromator at the sum-frequency light ω_s , that is expected according to equation 2.21. Thus, fluorescence decays at different emission wavelengths can be measured by simply tuning the optic axis of nonlinear crystal for the maximum generation of sum frequency. Due to high transparency over a wide spectral range (190-2500) and a reasonably high non-linear efficiency for the sum-frequency generation process, β -barium borate (BBO) is considered to be the best suited nonlinear crystal for the fluorescence up-conversion measurements.²⁵⁸⁻²⁶²

2.6.1.2. Time resolution

The fluorescence decay in the upconversion measurements has been obtained by the measuring the integrated intensity at different time delay of the gate pulse at the nonlinear crystal with respect to the excitation pulse and thereby scanning the whole fluorescence decay of the sample as shown in Figure 2.8. At any delay of the gate pulse, the intensity of the sum frequency light (I_s) is proportional to the correlation function of the fluorescence intensity (I_{fl}) and the intensity of the gate light (I_g), and is given by the following equation.²⁵⁸⁻²⁶²

$$I_s(\tau) = \int_{-\infty}^{+\infty} I_{fl}(t)I_g(t - \tau)dt \quad (2.13)$$

where τ is the time delay between the excitation and the gate pulses. Since the intensity of the gate pulse, I_g , unchanged at all the delays, the intensity of the sum frequency light at each delay position is directly proportional to the intensity of the

fluorescence light at that delay. Thus, pictorially, the value of the integral in equation 2.13 at any delay position can be represented by the shaded area under the fluorescence curve as shown in Figure 2.6. The entire fluorescence decay trace can be obtained by scanning the delay for the gate pulse and recording the integrated intensity of the sum frequency light at each delay.²⁵⁸⁻²⁶²

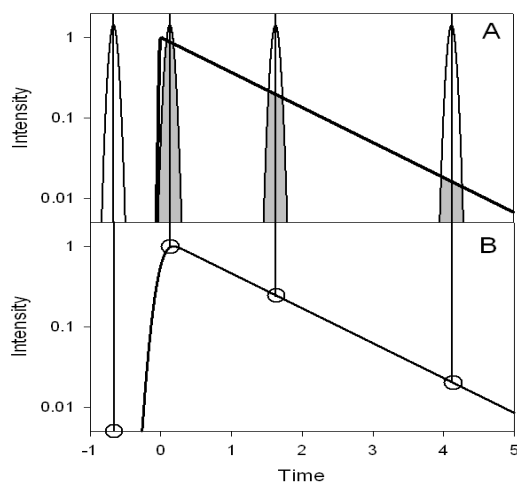


Figure 2.6 Schematic representation of fluorescence decay measurement using fluorescence up-conversion technique.

The block diagram of femtosecond fluorescence upconversion instrument used in the present work is shown in figure 2.7. A diode pumped solid state (DPSS) laser pumped mode locked Ti-Sapphire laser has been used to produce ultrashort laser pulses for the wavelength around 800 nm. The pulse duration of the present Ti:sapphire laser system is ~ 50 fs and it operates with a repetition rate of 82 MHz with a wavelength tunability over 720-900 nm. For the work presented in this thesis, 880 nm laser pulse from the oscillator is used. The second harmonic pulse at 440 nm is generated by passing the fundamental 880 nm light from the oscillator through a nonlinear BBO crystal. The second harmonic light (440 nm) thus produced is

separated from the residual fundamental light (880 nm) using a dichroic mirror and further used for the excitation of the samples. The intensity of the 440 nm light is normally kept reasonably low to ensure that the fluorescence intensity remains linearly dependent on the excitation laser intensity and to minimize the photo-degradation of the samples.

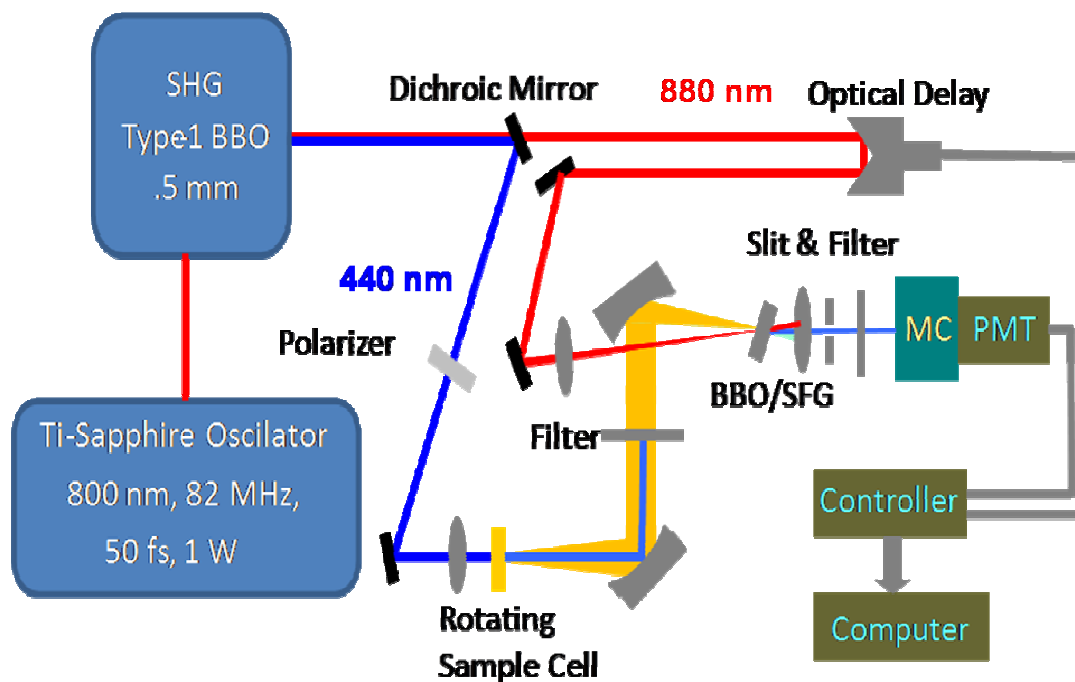


Figure 2.7 The Schematic diagram of the femtosecond fluorescence up-conversion instrument.

For the upconversion experiments, the sample solution is kept in a rotating quartz cell of 1 mm thickness. The sample cell is rotated continuously during the measurement to minimize the photo-decomposition. A long pass filter is used immediately after the sample cell to block the excitation light and transmit the emission light. The transient fluorescence originating from the sample is then focused onto an up-conversion crystal (0.5 mm thick BBO crystal), using two parabolic

mirrors. The residual fundamental beam, the gate pulse, is initially directed to an optical delay line and subsequently focused onto the up-conversion crystal. A translational stage, driven by a stepper motor with a step size of 0.1 μm , is used to change the delay between the gate pulse and the emission light. The gate pulse is focused onto the up-conversion crystal using a lens to mix with the fluorescence signal and thus to generate the sum-frequency or the up-converted signal. The upconverted light is focused onto a slit of a double monochromator after passing through a band pass filter that eliminates the gate and the unused fluorescence light but transmits the up-converted light. This up-converted light is finally detected by using a photomultiplier tube connected to a photon counting system (CDP Inc. Russia). A variable wave plate (Berek compensator) in the path of the excitation beam is used to control the polarization direction of the excitation pulses relative to the horizontally polarized gate pulses. Fluorescence up-conversion measurements are normally carried out under magic angle condition to avoid the rotational depolarization effect of the probe molecules on the observed fluorescence decays.

2.6.1.3. Instrument response function

As the excitation pulses are having considerable pulse width, the fluorescence decay measured at a particular wavelength using this technique is a convolution of the sample response with that of the instrument response function. Thus, the measured fluorescence decay should be deconvoluted with that of instrument response function (IRF) in order to get true sample response or the exact decay parameters. Thus, it is very essential to measure IRF of the up-conversion setup to analyze the observed fluorescence decays, and this can be easily obtained by mixing the residual excitation light that passes through the sample with the gate pulse in the up-conversion crystal

and measuring the sum-frequency light, which is commonly referred as the cross-correlation light. The changes in the cross-correlation light intensity with the delay time of the gate pulse can be easily recorded similar to the measurements of the fluorescence decays and the temporal profile thus obtained for the cross-correlation light represents the IRF of the fluorescence up-conversion instrument. A typical IRF of the present setup is shown in Figure 2.8, which is found to be Gaussian in shape. The FWHM of the IRF for the present instrument is found to be ~ 175 fs

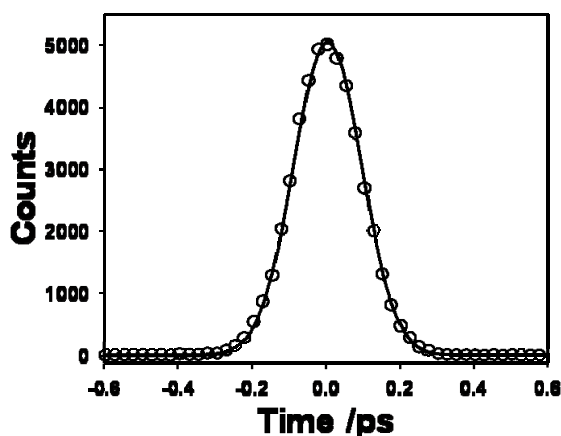


Figure 2.8 A typical instrument response function of the present fluorescence up-conversion instrument measured for 440 nm excitation light. The full-width at half maximum of the instrument response function is ~ 175 fs.

2.7 Fluorescence Microscopy

Fluorescence microscopy is a versatile technique, which has been used widely in the field of life sciences, material sciences and in medical sciences to visualize different targets stained with fluorescence probes.²⁶³ Fluorescence microscope basically images different classes of substrates through the fluorescence or phosphorescence emanating from the fluorophores after photoexcitation. Since the

wavelength of emission from the probes is quite separated from the excitation light, fluorescence microscope provides images with much better contrast over the other conventional optical microscope. Fluorescence images give information about the physical and chemical environments around the fluorophores and thus the specific attached targets. The development of variety of organelle specific fluorescent probes enhances the ability of fluorescence microscopy to identify different components in the cell such as nucleus, mitochondria, cell membranes etc.^{263, 264} Such use of array of fluorophores also helps us to understand the function of different cellular components simultaneously. Further, polarized fluorescence microscopy can provide information about the orientation of fluorophores with respect to the orientation of its targets.²²⁷ Recent advances in this field such as fluorescence lifetime imaging (FLIM) and single molecule fluorescence microscopy will help us not only to record the images but also to understand the dynamics, even in the live cells.^{118, 162}

2.7.1 Principle

The basic design of the fluorescence microscope consists of a light source to illuminate the sample, an excitation filter to choose the wavelength of excitation, a dichroic mirror to reflect the excitation light and transmit the emission light and an emission filter to cut any residual excitation light and a detector to record the image.²⁶³ Thus, only the fluorescence light emitted only reaches the detector to give the image of the fluorescence structures of the specimen. In general, the light sources used are broad band sources like Xenon arc lamp or mercury vapour lamp. Nowadays, high power tunable laser sources or LEDs are also being used. The excitation filter, emission filter and dichroic mirror should be selected according to the excitation and

emission profiles of the fluorophores of interest. CCD array is commonly used as detector for recording the fluorescence images.

2.7.2 Epifluorescence microscope

The majority of the fluorescence microscope used in the biological science is based on epi-fluorescence microscope.^{263, 265} A schematic representation of the epi-fluorescence microscope is shown in figure 2.9. In general, in epi-fluorescence microscopic design, vertical illumination from the top of the sample is preferred. The collimated excitation light is focused on the sample by using an objective lens and fluorescence emitting from the specimen is collected with the same objective lens and detected with the CCD camera after passing through the dichroic mirror and emission filter. In this configuration, most of the excitation light, except scattered from the sample, is transmitted through the sample. Thus, vertical excitation helps to enhance the signal to noise ratio. For our studies, Axioskop II mot plus (Zeiss) microscope equipped with 40x objective has been used for the imaging of PicoGreen stained insulin fibrils (chapter 3).

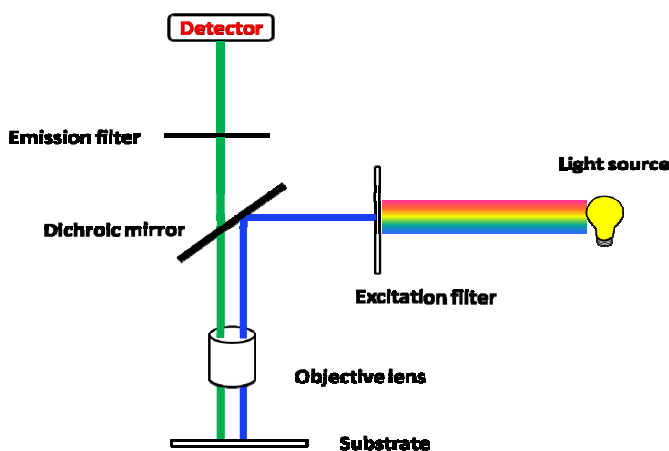


Figure 2.9 The schematic diagram of a typical epi-fluorescence microscope.

2.7.3 Confocal microscope

Confocal microscopy has been developed to overcome some limitations of wide field fluorescence microscopes such as low optical resolution, image distortion etc.²⁶⁵ In epi-fluorescence microscope the sample is excited uniformly with the light from the excitation source and records its fluorescence images. The schematics of a confocal microscope are shown in figure 2.10.

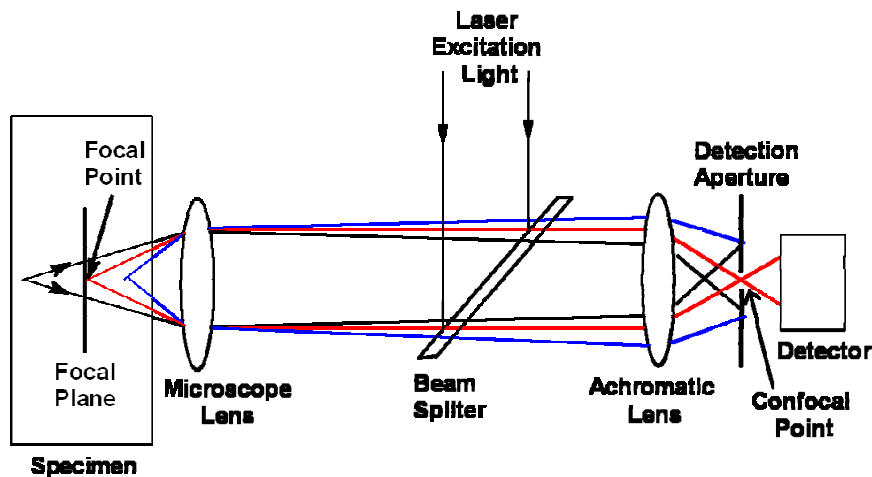


Figure 2.10 Schematic diagram of typical confocal fluorescence microscope

Confocal design of focal point and the pinhole eliminates light from out of focus planes or points away from the optic axis. This is known as optical sectioning. Thus, the detector receives the light mostly from the focal point. This records a fluorescence image of a point object which is free from out of focus blur. By scanning through the entire specimen, we can get the total fluorescence image with a better resolution. But the increased resolution is at the cost of decreased signal intensity and hence long exposures are needed, which can cause photo bleaching of the samples. To

avoid this, very sensitive detectors such as high gain PMTs or avalanche photodiodes have been used in confocal microscopes. Through confocal microscopy, three dimensional images can be reconstructed by collecting the images at different depths of a thick object.^{238, 266} For imaging of 2Me-DABT and SYPRO Orange stained insulin fibrils, LSM 780 meta laser scanning confocal microscope (Zeiss) has been used.

2.8 Quantum Chemical Calculations

Density functional theory (DFT) is a quite powerful method to evaluate the ground state properties of molecular systems with an appreciable accuracy.²⁶⁷ The time dependent DFT approach (TDDFT) has become a routine method for the evaluation of vertical electronic excitation spectra and excited state geometry. Although, TDDFT calculated energy parameters do not provide quantitative accuracy, qualitative information regarding the electronic and geometric structures and energetic are reasonably good. The ground state geometries of all the molecules were optimized using the density functional theory (DFT) without imposing any symmetry restriction. Becke's three parameter hybrid exchange function with the Lee-Yang-Parr gradient corrected correlated functional (B3LYP)^{267, 268} was used in conjunction with 6-311++g(d,p) basis set as implemented in Gaussian 03 software package.²⁶⁹

2.9 Molecular Docking Studies

Autodock suite (version 4.2) implemented in the autodock tools (version 1.5.6) was used for the molecular docking studies of amyloid probes with fibril structure to detect the binding site, best direction and binding energy.^{240, 270} The structure of A β 1-

42 fibril was obtained from Protein database (PDB) with PDB id: 2MXU.²⁷¹ The structures of probes have been optimized using DFT and further used for blind molecular docking studies. To be mentioned, in Autodock experiment, the host molecules are considered to be structurally rigid and do not allow any structural reorganization due to the incorporation of the guest molecules. In spite of such limitation, the prediction of the autodock on the binding sites of small molecules in different biomolecules, like protein, DNA, is found to be quite reasonable. Hence, for our studies, fibril was considered as a rigid host molecule and probe molecules as a flexible ligand allowing all torsional motions in the molecule. Mullikan charges obtained from quantum chemical calculations have been used in docking studies. Molecular docking was initiated with several initial positions of the ligand with respect to the fibril. The size of the grid was made in such that the ligand can access all possible binding sites in fibrils. Each docking involved 200 independent runs with a maximum number of 5×10^6 energy evaluation and 27000 generations. The Lamarckian genetic algorithm (LGA) method was applied to find the docked conformations of the ligand with the lowest energy.²⁷⁰ Results of all 1000 runs were clustered with root mean square deviation (RMSD) $< 2 \text{ \AA}$ and ranked according to their binding energies. The highest binding energy conformations have been reported. To identify relative location one probe with respect to other, docking with multiple ligands has been performed. In this procedure, already docked molecule-fibril complex is treated as rigid host and the additional probe is treated as the ligand and above procedure has been applied to get the final docking conformation.

Chapter-3

PicoGreen as amyloid fibril sensor and deciphering its ultrafast dynamics

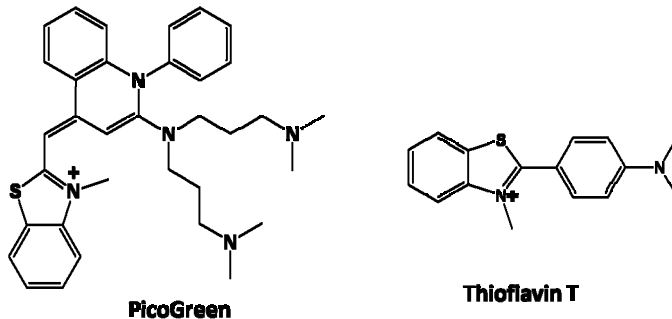
3.1. Introduction

As discussed in chapter 2, among the several techniques available for the detection of fibrils, optical imaging using fluorescent amyloid markers has received a lot of attention.¹¹² Thus, developing new sensitive probes for amyloid fibrils is an active field of research. Among the developed fluorophores, Thioflavin T, belongs to class of ultrafast molecular rotors (UMR), has been utilized extensively for staining amyloid fibrils both *in-vitro* and *ex-vivo* due to its large fluorescence enhancement in the presence of fibrils.¹⁹⁸ Such large emission enhancement of ThT is due to the retardation of ultrafast non-radiative torsional relaxation around its central C-C bond upon binding with amyloid fibrils.²¹² ThT has become a gold standard for amyloid detection and in use for several decades. Additionally, its selective binding with amyloid fibril and lack of interaction with native, unfolded proteins, oligomers, and protofibrils makes it a suitable probe to monitor the fibrillation kinetics.¹²⁹ Thus, ThT has also been used to evaluate the anti amyloid activity of several drugs. Despite having lot of advantages, use of ThT for the detection of amyloid is also suffered from several drawbacks. ThT has shown to promote the fibrillation process through the

preferential stabilization of the beta sheet conformations in amyloid fibrils.²¹³ The fluorescence intensity of Thioflavin T in fibril is highly sensitive to the external conditions such as ionic strength and pH and also on the structural morphology of the fibrils.^{194, 214} Thus, it is difficult to assign the activity of the drugs just based on the ThT fluorescence. Recently, we have shown through ultrafast fluorescence spectroscopy that, only small part of the amyloid bound ThT is contributing to the enhanced fluorescence while the other major part does not contribute much to the observed emission.²¹⁴ Further, the excitation and emission spectral positions of ThT are not compatible with standard laboratory instruments, like fluorescence microscope, flow cytometer, plate readers etc. Thus, there is a need for an efficient, sensitive fluorescent amyloid probes.

In the search of such probes, recently it has been reported that molecular rotor based probes are promising for the amyloid staining. Recently, two UMR based fluorophore, namely, Auramine O (AuO)¹⁹⁰ and, di-cyano vinyl julolidine (DCVJ)¹⁹⁴ has been shown to have good sensitivity towards amyloid fibrils compared to native protein. It has been shown that the restriction of their internal rotation upon binding to fibrils cause the observed enhanced fluorescence for both UMR dyes. However, the sensitivity achieved with these UMRs is either comparable to or less than that of ThT.^{190, 194} In recent past, Volkova et. al. shows that cyanine based probes can also able to detect amyloid fibrils. These cyanine dyes has spectral properties suitable for the use of common laboratory instruments to detect amyloid fibrils and their presence does not affect the fibrillation process. However, such cyanine dyes suffers from low sensitivity.^{229, 231}

From all these reported results it is expected that a cyanine based UMR may provide suitable spectral properties, like cyanine dyes, as well as high sensitivity, like UMRs, for the efficient detection of amyloid fibrils. PicoGreen (PG) is one of the recently reported cyanine based molecular rotor whose structure is shown in scheme 1. This dye shows very weak fluorescence in water.²⁷² Dragan et. al proposed that the ultrafast internal dynamics of the probe are responsible for such high quenching of the excited state in low viscous solvents.²⁷² Through quantum chemical calculations, Okishi et. al. showed that rotation of benzothiazole group is responsible for such efficient quenching of the excited state of PG in low viscous solvents.²⁷³ It has also been proposed that restriction on such rotation can improve the emission yield to a significant extent. Thus, the emission quantum yield of PG is reported to be increases with the increase in the viscosity of surrounding medium.²⁷⁴



Scheme 3.1 Molecular structures of PicoGreen (PG) and Thioflavin T (ThT).

From the molecular structures, it is evident that like ThT, PG has a benzothiazole group and also shows the properties of a molecular rotor where the benzothiazole rotation is playing a key role.²⁷⁵ Inspired from these facts, we have explored the possibility of the use of PG as amyloid strain and investigated its photophysical properties in insulin fibril through steady state and time-resolved

fluorescence techniques. It has been shown that large enhancement of PG fluorescence is observed upon its interaction with insulin amyloid fibrils. Fluorescence resonance energy transfer and molecular docking studies has also been carried out to determine the probable location of PG in fibril.

Apart from the detection point of view, the dynamics of molecular rotor probes give a detailed understanding about the mechanism of its sensing activity. For example, in case of ThT, it has been shown that the restriction of excited state torsional dynamics in amyloid fibrils is responsible for the observed large fluorescence enhancement compared to water.^{128, 130} The knowledge about the detailed excited state dynamics will help us to understand the molecular level details of the binding and helps us to design new molecules with suitable excited state properties that can result in better amyloid sensitivity. For this purpose, we have studied the excited state dynamics of PG in molecular solvents with different polarity as well as viscosity. We have also correlated the dynamics of PG in fibril with the dynamics in molecular solvents.

3.2. Experimental Methods

Bovine insulin, ThT, NaCl have been purchased from Sigma-Aldrich. ThT has been recrystallized twice from water and its purity has been checked by NMR. PicoGreen (20X in DMSO) has been purchased from Invitrogen and used as received. Acetonitrile (ACN), ethyl acetate (EA) were purchased from Spectrochem, India and ethylene glycol (EG) was purchased from Sigma-Aldrich. Triple distilled water has been used for all the experiments. The fluorescence quantum yield of PG in molecular

solvents were determined by comparative method using Nile red in dioxane ($\phi_f=0.7$) as the reference.

The ground state absorption and steady state emission spectra were obtained from Jasco spectrophotometer (model # V-650) and Hitachi spectrofluorometer (model # F4500). Nanosecond time-resolved emission measurements have been carried out using a time-correlated single photon counting (TCSPC) based instrument from IBH, UK. All the samples were excited with 451 nm delta diode laser with instrument response of 170 ps. Except anisotropy measurements, all emission measurements were carried out with the emission polarizer at magic angle with respect to the vertical polarization of the excitation light. All measurements were carried out at ambient temperature (25⁰C).

The time weighted average lifetime has been calculated according to the following equation.¹²⁵

$$\tau_{avg} = \frac{\sum a_i \tau_i^2}{\sum a_i \tau_i} \quad (3.1)$$

For the calculation of FRET efficiency the amplitude weighted average lifetime has been estimated using following equation.¹²⁵

$$\tau_{avg} = \frac{\sum a_i \tau_i}{\sum a_i} \quad (3.2)$$

Insulin fibrils has been prepared by following method proposed by Manno et al.²⁷⁶ Briefly, 2 mg/ ml of insulin has been dissolved in 20% acetic acid and heated at 70⁰C for about 24 hours with constant stirring. The formation of fibril has been

confirmed by standard ThT fluorescence assay. The fibrils were diluted 12 times with Tris buffer and the pH of the fibril has been adjusted to 7.4 by using dilute NaOH solution. For the fibrillation kinetics experiments, the insulin fibrils have been prepared by another method reported by Heldt et al.⁷⁵ Insulin (2mg/ ml) has been dissolved in 25 mM HCl, 100 mM NaCl (pH 1.6) and heated at 60⁰C for 4 hours. The aliquots of the fibril have been taken every 15 minutes and required amount of dyes have been added and subsequently their fluorescence has been measured. The kinetic profiles were fitted with the following sigmoidal equation

$$I_f = \frac{I_f^0 - I_f^\infty}{1 + e^{(t-t_0)/\sigma}} + I_f^\infty \quad (3.3)$$

where I_f is observed intensity of fluorescence, I_f^0 , I_f^∞ is the fluorescence intensity in the absence of fibril and at the completion of fibrillation, t_0 is the time at which 50% of the maximal fluorescence has been achieved. Lag time is given by $t_0 - \sigma$.²⁷⁷

Femtosecond time-resolved fluorescence measurements were carried out using a fluorescence upconversion instrument discussed earlier (*cf.* Chapter 2). In the present study the second harmonic of Ti-Sapphire laser pulses (440 nm, 50 fs, 82 MHz) was used for the sample excitation. For the construction of the time-resolved emission spectra (TRES), the fluorescence transients were recorded at 10 nm intervals across the steady-state emission spectrum of PG. All these fluorescence transients were fitted with a tri-exponential function using an iterative convolution method. Time-resolved emission spectra (TRES) were reconstructed using the best fitting parameters of the fluorescence decays measured at different wavelengths following the method proposed by Maroncelli and Fleming.¹³⁸ In the present study, the

experimental data points for the each reconstructed TRES were fitted using the lognormal function of the following form.¹³⁸

$$I(\nu) = a \exp \left[-\ln(2) \left\{ \frac{1}{b} \ln \left(1 + \frac{2b(\nu - \nu_p)}{w} \right) \right\}^2 \right] \quad \text{if } \frac{2b(\nu - \nu_p)}{w} > -1$$

$$= 0 \quad \text{if } \frac{2b(\nu - \nu_p)}{w} \leq -1 \quad (3.4)$$

where, the amplitude, a , the peak frequency, ν_p , the width parameter, w , and the asymmetry parameter, b , are the adjustable parameters. The full width at half maximum (FWHM) of the emission spectra were calculated from width parameter, w , and the asymmetry parameter, b , by using the following equation.¹³⁸

$$FWHM = w \frac{\sinh(b)}{b} \quad (3.5)$$

Autodock suite (version 4.2) implemented in the autodock tools (version 1.5.6) was used for the molecular docking studies.²⁴⁰ The structure of A β ₁₋₄₂ fibril was obtained from Protein database (PDB) with PDB id: 2MXU. The geometry of PG and ThT were optimized by quantum chemical calculations using Gaussian 03 package.²⁶⁹ B3LYP functional^{267, 268} and 6-31++g(d,p) basis function were used to optimize the chemical structures by DFT method. The energy optimized structure of PG has been used for blind molecular docking studies. For docking studies, fibril was considered as rigid host molecule and PG as a flexible ligand allowing all torsional motions in the molecule. For docking with ThT, fibril with a docked PG was used as a host molecule and a similar procedure as used for the docking of PG with fibril was followed.

3.3. Results and Discussion

3.3.1 Steady state emission measurements

The emission properties of PG are reported to be highly sensitive towards its immediate surroundings.^{272, 274} The emission spectra of PG in water and in the presence of insulin fibrils of different concentrations have been recorded by exciting the sample at 485 nm and presented in figure 3.1. The emission spectrum of PG in water shows a very weak and broad emission with a maximum at 540 nm. Extremely low quantum yield of PG in water has been reported to be due to the high frequency rotation and stretching C-C bond of benzothiazole and quinolinium coupled system.^{272, 273} From figure 3.1 it is clear that there is a spectacular enhancement of ~1000 fold in the fluorescence intensity of PG due to the addition of insulin fibrils. Such increase in the emission yield clearly indicates that PG binds very strongly with insulin fibrils. Dragan et. al, showed that the fluorescence intensity of PG is very sensitive to viscosity rather than the polarity of the media.²⁷² This means that PG experiences a larger microviscosity at the binding site of the fibril leading to large fluorescence enhancement. This result indicates the internal dynamics of PG are being restricted due its binding to insulin fibrils. The variation in the emission intensity at 540 nm for PG due to the addition of amyloid fibril is shown in the inset of Figure 3.1. Such low background fluorescence in water and remarkable fluorescence enhancement (~1000 fold) in fibrillar media makes PG a very good fluorescence probe for the detection of amyloid fibrils.

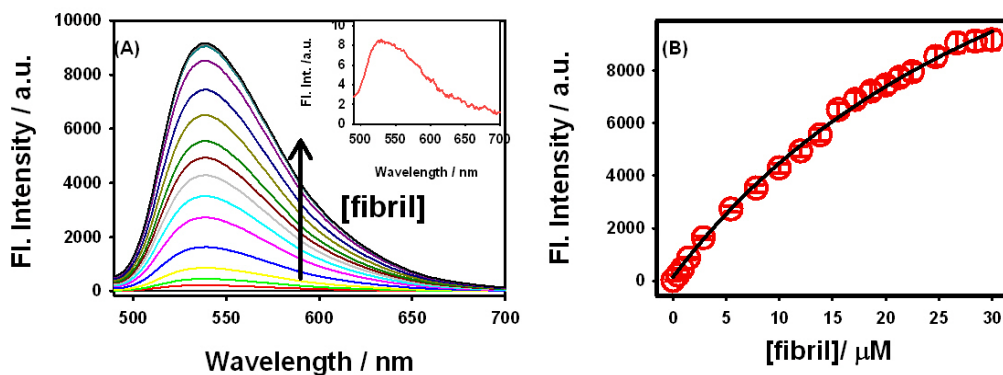


Figure 3.1 (A) The fluorescence spectra of PG in water in the presence of different concentrations of insulin fibril. Arrow indicates the increase in insulin fibril concentration, 0-30 μM . Concentration of PG is 130nM. The excitation wavelength is 480 nm. Inset: The fluorescence Spectra of PG in water (B) Variation in the emission intensity of PG at 540 nm with the fibril concentration. Circles represent the experimental data points and the solid line represents the fitted line according to Equation 3.6.

In order to quantify the propensity of PG towards insulin amyloid fibrils, the changes in the emission intensity due to the addition of amyloid fibrils were fitted with following modified Benesi-Hildebrand equation.²⁷⁸

$$I_f = \frac{I_f^0 + I_f^\infty K_b [\text{fibril}]}{1 + K_b [\text{fibril}]} \quad (3.6)$$

where I_f is the observed fluorescence intensity, I_f^0 , I_f^∞ are the fluorescence intensity of free and completely bound PG, respectively. K_b is the binding constant. The solid line in the inset of figure 3.1 represents the fitting of the experimental data with equation 3.4. A nice correlation ($R^2=0.997$) clearly indicates that there is 1:1 binding is

operating between PG and fibril and the estimated binding constant is found to be $2.45 \times 10^4 \text{ M}^{-1}$.

3.3.2. Time resolved emission measurements

Steady state measurements show that the internal dynamics of PG has been restricted upon binding with insulin fibrils. The excited state lifetime is reported to be a measure of internal dynamics of PG.²⁷² To understand the effect of the interaction of insulin fibrils on the internal dynamics of PG, we have measured the fluorescence lifetime of PG in fibrillar solution using TCSPC method and the results are presented in figure 3.2. Black curve represents the decay trace of PG in water. It is clear that the lifetime of PG is IRF limited. It has been reported that the excited state lifetime of PG in buffer is ~ 4 ps.²⁷² Such short lifetime is due to the internal dynamics such as rotation, isomerization etc., of the molecule. Recently, Nakai and his coworkers showed theoretically that there exist two conical intersections between the ground and excited states in the free PG molecule. The rotation of benzothiazole and stretching of C-C bond adjacent to benzothiazole group are the requirements for the formation of conical intersections. This gives the additional non-radiative channel for the deactivation of the excited state leading to very low quantum yield for PG in solution.²⁷³

The excited state decay of PG is gradually slower with increase in the concentration of insulin amyloid fibrils which is evident from figure 3.2A. All the decays were fitted with tri exponential function and fitted parameters are presented in table 3.1. The excited state lifetime of molecular rotors is, in general, represented by the average lifetime due to the existence of barrier less potential energy surface.^{128, 130,}

^{178, 279} Drawing an analogy, for PG also the average lifetime will be representative for the whole process. The variation in the average lifetime of PG with the addition of insulin fibrils have been displayed in figure 3.2 B. It is evident from figure 3.2B that in the presence of insulin fibrils, the excited state lifetime increased from 4 ps in neat water²⁷² to 3.45 ns in 30 μM insulin fibril solution. Increase in the excited state lifetime by three orders of magnitude clearly indicates the presence of strong interaction between PG and insulin fibrils. Dragan et. al. measured the excited state lifetime of PG with different solution conditions such as different polarity and viscosity and concluded that the excited state lifetime of PG is very sensitive to the solution viscosity rather than the polarity.²⁷² They have also shown that PG can serve as very good viscosity sensor and has been used estimate the viscosity inside collagen fibers.²⁷⁴ Thus, in case of insulin fibrils, PG is experiencing a higher microviscosity at the binding location where its internal rotation is restricted.

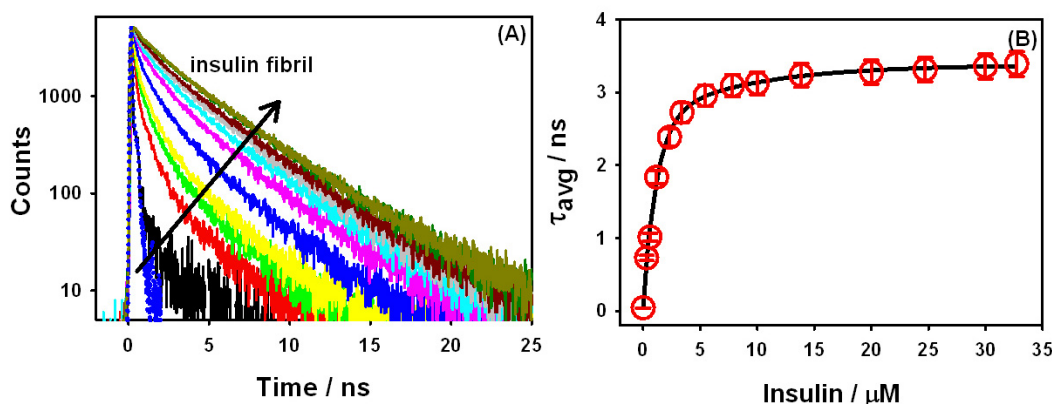


Figure 3.2 (A) Time-resolved fluorescence decays of PG (130 nM) in insulin fibril of different concentrations (0-30 μM). Excitation wavelength 445 nm and the emission were monitored at 540 nm. The dotted line represents lamp profile. **(B)** The variation in the average lifetime of PG with the concentration of insulin fibrils.

Table 3.1 Fitting parameters for transient emission decays and average lifetime of PG in amyloid fibril solutions.

[Fibril]	A ₁	τ_1 / ns	A ₂	τ_2 / ns	A ₃	τ_3 / ns	τ_{avg} / ns
0.30	41	0.05	33	0.40	26	2.24	0.73
0.60	28	0.06	36	0.47	36	2.26	1.00
1.18	13	0.06	35	0.77	52	2.99	1.83
2.31	7	0.07	29	0.94	64	3.30	2.39
5.45	5	0.14	26	1.32	69	3.75	2.94
10.0	4	0.15	22	1.31	74	3.79	3.10
13.8	3	0.17	23	1.45	74	3.93	3.25
20.0	4	0.24	23	1.58	73	3.96	3.26
24.7	3	0.25	23	1.63	74	3.99	3.34
32.7	3	0.25	23	1.65	74	4.05	3.38

3.3.3. Time-resolved anisotropy studies

Fluorescence anisotropy technique is extensively used to understand the binding pattern for dye-bio-supramolecular assemblies.^{280, 281} To understand the rotational dynamics of PG upon interacting with insulin fibrils, time-resolved anisotropy measurements of PG in water with the addition of different concentrations of insulin fibril have been performed and the results are presented in figure 3.3. From figure 3.3, it is seen that the anisotropy decay for PG in water is very fast which yields a time constant of ~ 100 ps. The addition of insulin fibril to aqueous solution of PG causes a drastic decrease in the rate of decay in anisotropy. This result indicates that the rotation of PG is getting restricted upon binding to insulin fibril. This implies that fibril bound PG experiences a larger rigidity compared to free molecule in water. The time-resolved anisotropy data also corroborates with the results from both steady state and time-resolved fluorescence measurements. All anisotropy decays were fitted with bi-exponential function and the fitted parameters are presented in table 3.2. The fast

rotational time constant (~ 100 ps) can be assigned to the unbound PG molecules and the longer decay component can be assigned to PG bound to fibril. At the highest concentration of fibril used in this study, fluorescence anisotropy of PG does not decay completely within the lifespan of the fluorophore and yields a residual anisotropy of 0.36 at 10 ps. Anisotropy decay parameters presented in table 3.2 suggests that the residual anisotropy of PG increases with increase in the fibril concentration.

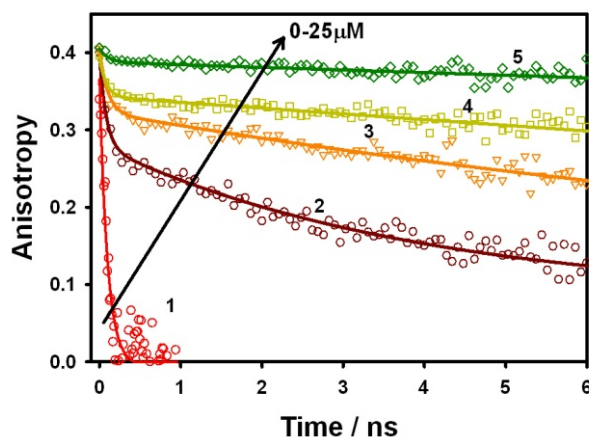


Figure 3.3 Time resolved fluorescence anisotropy of PG with varying concentration of insulin fibril (1) water (2) 0.30 (3) 1.18 (4) 5.21 and (5) 25.62 μM .

Table 3.2 Fitting parameters for anisotropy decays of PG in fibrillar solutions

[fibril] / μM	a_1	r_1 / ns	a_2	r_2 / ns	$r_{\infty}\#$
0	100	0.12*			0
0.3	47.2	0.08	53.78	3.91	0.079
1.2	39.3	0.10	61.69	9.87	0.227
2.6	24.2	0.10	75.76	13.72	0.284
5.2	100.0	0.09	----	----	0.295
11.8	100.0	0.11	----	----	0.366
19.9	100.0	0.11	----	----	0.353
25.6	100.0	0.11	----	----	0.348

limiting anisotropy is represented by the value of anisotropy at 10 ps. * subjected to errors due to small lifetime of ~ 4 ps

3.3.4. Effect of ionic strength

As PicoGreen is positively charged and at neutral pH some of the amino acids such as glutamic acid ($pK_a=4.07$), in the fibril are expected to be in anionic form, it is highly expected that the electrostatic forces might play a role in the binding of PG to the amyloid fibril. To evaluate the role of electrostatic interaction in the binding of PG to insulin fibrils, we have studied the emission properties of PG in amyloid fibrils in the presence of varying amounts of salt and results are presented in figure 3.4. In contrary to our expectation, no change in the fluorescence intensity as well as the lifetime of PG has been observed even in the presence of salt of $\sim 10^6$ times more concentrated than the probe concentration in amyloid fibrils. This result clearly indicates that despite of charges on the host and guest molecules, electrostatic interaction does not have any role in the association of PG with amyloid fibrils. Hence, hydrophobic interaction is the most probable forces operating between PG and insulin fibrils. From the molecular structure of PG we can observe three molecular groups benzothiazole, quinolinium and aminopropyl chains. Comparison of molecular structure of PG with standard amyloid staining dye, ThT, indicates the presence of common benzothiazole moiety in both molecules. It is believed that the size of the benzothiazole moiety is such that it can nicely fit in the amyloid grooves and leads to strong binding of ThT with fibrils.¹⁹⁸ Thus, it can be inferred that like ThT, the benzothiazole unit of PG can fit tightly into the amyloid grooves. Such binding of the benzothiazole unit hinder its non-radiative torsional motion resulting large increase in its emission yield.

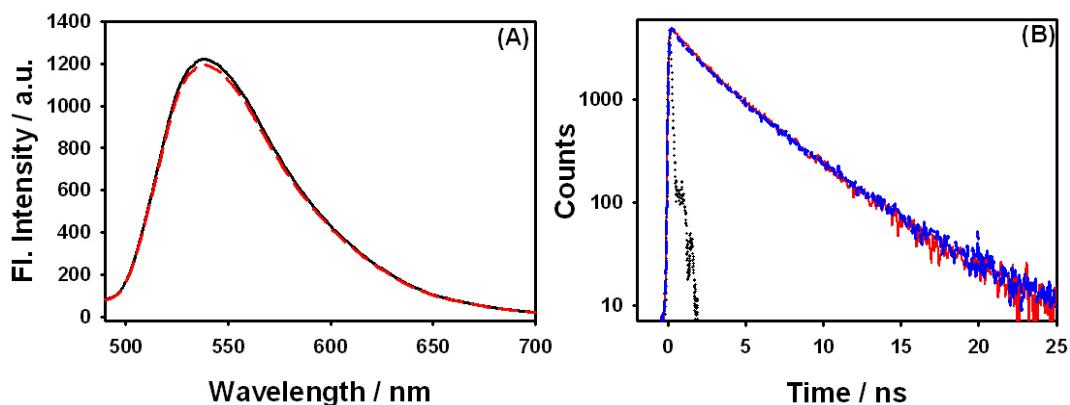


Figure 3.4 (A) Fluorescence spectrum of PG in insulin fibril without salt (solid curve) and with 500 mM NaCl (dashed curve). (B) Fluorescence decays of PG fibril with (solid) and without salt (dashed). Dotted curve represents IRF.

3.3.5. Comparison with standard amyloid staining dye, Thioflavin T

As mentioned earlier that ThT is most widely used amyloid staining dye whose fluorescence is greatly enhanced when bound to amyloid fibrils.¹⁹⁸ Hence, to compare the sensitivity of PG in comparison to ThT, fluorescence spectra of both dyes were recorded in water and amyloid fibril under similar experimental condition and the results are displayed in figure 3.5 A. From figure 3.5A, it is observed that the fluorescence intensity of PG is enhanced by a factor of ~ 1000 while under the same conditions, ThT shows only 400 fold increase in its emission intensity. Thus, the present results suggest that PG has 2.5 times more sensitivity towards insulin fibrils as compared to the gold standard amyloid probe, ThT. However, besides higher sensitivity, an amyloid probe should also capable to follow the kinetics of the amyloid formation. To check such characteristics for PG, we have also monitors the changes in the emission intensity of PG during the fibrillation process and the results are

compared with ThT. The changes in the emission intensity of PG and ThT during fibrillation process are shown in 3.5 B. It is evident from the figure that both PG and ThT can follow the process of fibrillation with equal capability. The fibrillation kinetics has been analyzed according to the equation 3.1. The lag times thus estimated are 96.5 and 95.5 min for PG and ThT respectively. Similar fibrillation lag time with these two probes, further confirms that both these dyes are equally potential to monitor the amyloidosis process. Thus, all these results clearly indicate that due to higher sensitivity towards the amyloid fibrils, PG is a superior amyloid probe than ThT. Further, the longer excitation and emission wavelength for PG as compared to ThT, make it possible to use the common laboratory instrument for the detection of amyloid fibrils. The longer emission wavelength of PG (540 nm) as compared to ThT (490 nm) would also be advantageous due to low interference from the cell auto fluorescence.²⁸² It is important to be mention that the binding strength of PG ($2.45 \times 10^4 \text{ M}^{-1}$) is smaller than ThT ($K_{b1} \sim 1 \times 10^7 \text{ M}^{-1}$ and $K_{b2} \sim 3.6 \times 10^4 \text{ M}^{-1}$).¹⁸⁶ Recently, our group showed that only minor population of fibril bound ThT is contributing to its characteristic fluorescence through ultrafast fluorescence spectroscopy. However, in the case of PG we have observed ionic strength independent single mode of binding exists for PG to fibrils. Hence, although the fibril binding affinity of ThT is higher than PG, all the fibril bound PG is contributing to the observed fluorescence which leads to give large sensitivity over ThT.

Fluorescence microscopy is a versatile tool which has been extensively utilized to visualize the protein fibrils using fluorescent dyes.²⁶³ ThT has been widely used to see the fibrils under optical microscope since years.²⁸³ To check whether PG can also be used for microscopic studies, we have recorded the fluorescence microscopic

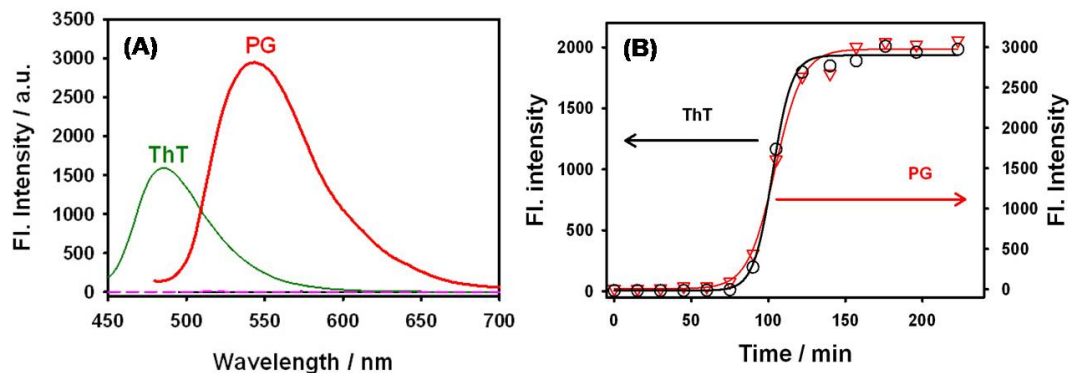


Figure 3.5 (A) The emission spectra of ThT and PG (0.1 μ M) in the presence of 30 μ M of insulin fibril. Dotted curves represent the emission spectra in water for both dyes. (B) Fibrillation kinetics of Insulin fibril with both ThT (○) and PG (▽). Solid lines represent their fits with equation 3.1.

images of amyloid fibril strained with same concentration of PG and ThT and the results are shown in Figure 3.6. From the figure, it can be clearly observed that PG gives brighter images compared to ThT. This result is in corroboration with the results obtained from the steady state emission studies. Thus, brighter microscopic images indicate that PG can serve as a better alternative to ThT for in-vitro imaging of amyloid fibrils.

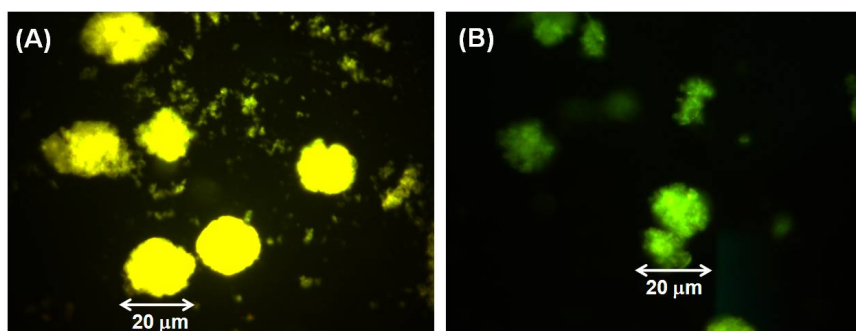


Figure 3.6 Microscopic images of insulin fibrils strained with (A) PG and (B) ThT. Concentration of dye and fibrils are same in both measurements.

3.3.6. Competitive binding and energy transfer studies

As PG and ThT have similar benzothiazole moiety in their molecular structure and the rotation of benzothiazole is restricted due to the binding interaction in both the cases, it might be possible that they may have similar binding location in the amyloid fibrils. In order to verify such possibility, we have carried out competitive binding with PG and ThT in fibrillar media. As binding constant of ThT is much higher compared to PG, it is expected that ThT can replace PG if they have same binding sites in amyloid fibrils. To check such possibility, we have gradually added ThT to the PG-fibril solution and the emission spectra have been recorded and shown in figure 3.7. The figure shows that there is no change in the emission intensity of PG even after addition of excess amount of ThT to the fibril solution. This implies that the added ThT does not affect the binding of PG in the amyloid fibril indicating that these two amyloid probes have distinct binding location in the amyloid fibrils.

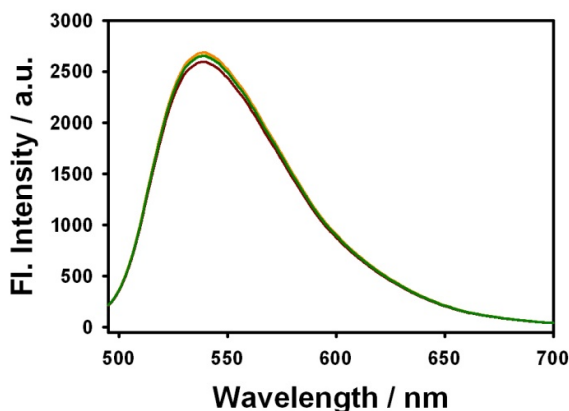


Figure 3.7 Emission spectra of PG (0.1 μM) in 30 μM fibril in the presence of different concentrations (0-3 μM) of ThT.

To understand the relative location of these two amyloid probes, energy

transfer between these two probes has been investigated. The normalized absorption and emission spectra of PG and ThT in insulin fibrils are presented in figure 3.8. It is observed that the emission spectrum of ThT and absorption spectrum of PG have significant spectral overlap which makes them a very good fluorescence resonance energy transfer (FRET) pair.¹²⁵ Thus, we can use FRET to find the relative location of PG and ThT in amyloid fibrils.

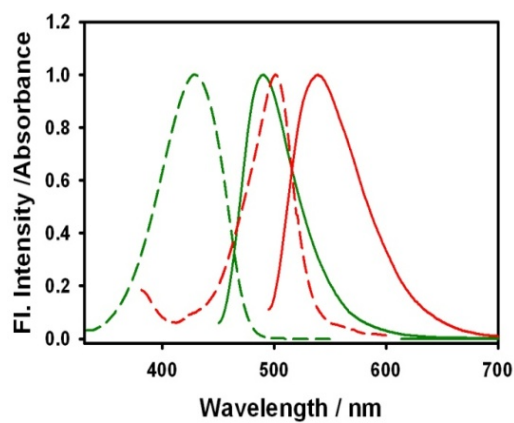


Figure 3.8 Normalized absorption (dashed) and emission (solid) spectra of ThT (green) and PG (red) in Insulin fibrils.

The emission spectra of ThT-fibril solution in the presence of different concentrations of added PG are recorded and shown in figure 3.9A. From figure 3.9A it is observed that due to addition of PG to ThT-fibril solution, the emission intensity at 490 nm due to ThT gradually decreases with concomitant increase in the emission of PG at 540 nm. Additionally, due to addition of PG, an iso-emissive point at 560 nm has also been observed. The increase in the emission intensity of PG is clearly evident from the intensity normalized emission spectra as shown in the inset of figure 3.9 A. The appearance of an iso-emissive point clearly indicates that the decrease in ThT emission and increase in PG emission are interconnected. This result can be explained

from the fact that due to significant spectral overlapping between emission spectrum of ThT and absorption spectra of PG, the energy can easily flow from the photoexcited ThT to a ground state PG bound to amyloid fibril. As a control experiment, we have also measured the emission spectrum of PG (final concentration used in the experiment) in fibril by exciting at 440 nm and shown as dashed line in figure 3.9 A. Such low emission intensity of PG in amyloid fibril on photoexcitation with 440 nm clearly indicates that the large emission observed at 540 nm due to the addition of PG to ThT-fibril solution is not from the direct excitation of PG. Rather, such large emission of PG arises due to the efficient energy transfer from the photoexcited ThT to PG.

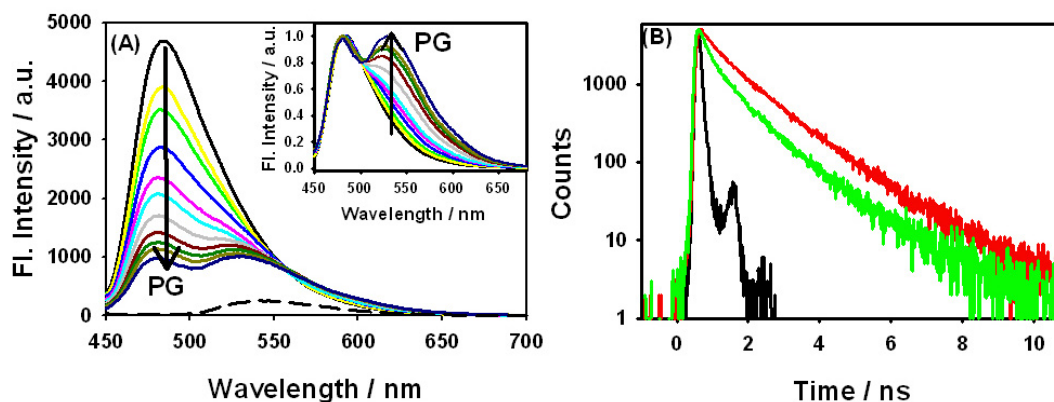


Figure 3.9 (A) Emission spectra of ThT ($0.1 \mu\text{M}$) in fibrils in presence of different concentrations of PG ($0\text{-}1\mu\text{M}$). Dashed line represents the emission spectra of $1\mu\text{M}$ PG on excitation with 440 nm light. **Inset:** Intensity normalized emission spectra of ThT-fibril solution with different PG concentrations. **(B)** Emission decays traces for ThT in fibrillar solution in the absence (red) and presence (green) of PG. Excitation wavelength is 440 nm.

Time-resolved emission studies have also been conducted to confirm the energy transfer between ThT and PG in amyloid fibrils. The energy transfer creates an additional deactivation channel for the donor excited state resulting decrease in its fluorescence lifetime.¹²⁵ In order to check such possibility we have measured emission transients of ThT in fibril in the absence and presence of PG. The fluorescence decay of ThT in fibril follows non exponential kinetics which is fitted with tri exponential function. The average lifetime of ThT in amyloid fibrils decreases from 0.67 ns to 0.34 ns in the presence of PG. Such large reduction in the fluorescence lifetime clearly indicates that efficient energy transfer takes place between photoexcited ThT and ground state PG in amyloid fibrils. Time-resolved fluorescence data have been used to estimate the energy transfer efficiency using following equation.²⁸⁴

$$E = 1 - \frac{\tau_{DA}}{\tau_D} \quad (3.7)$$

where, τ_{DA} , τ_D are the amplitude weighted average lifetimes of the donor in the presence and absence of acceptor respectively. So efficiency of FRET is estimated to be ~50.1%. From Forster theory of resonance energy transfer, the Forster distance (R_0) has been calculated using the following equation²⁸⁴

$$R = R_0 \sqrt[6]{\frac{1-E}{E}} \quad (3.8)$$

$$R_0 = 0.211 [\kappa^2 n^{-4} Q_D J(\lambda)]^{1/6} \quad (3.9)$$

Where κ^2 is the orientation factor which is 0.67 for random orientation of donor and acceptor, n is refractive index = 1.4 for macromolecules in water, Q_D is quantum yield of donor (0.43 for ThT in fibril), $J(\lambda)$ is overlap integral which is given as

$$J(\lambda) = \frac{\int_0^{\infty} F_D(\lambda) \varepsilon_A(\lambda) \lambda^4 d\lambda}{\int_0^{\infty} F_D(\lambda) d\lambda} \quad (3.10)$$

ε_A is extinction coefficient of the acceptor, F_D is fluorescence intensity of donor. Thus, R_0 is calculated as 52.7 Å. The mean relative distance has been estimated as 53.3 Å.

3.3.7. Quantum chemical calculations and Molecular docking studies

The structures of PG and ThT were optimized by quantum chemical calculations using a Gaussian 03 package.²⁶⁹ B3LYP functional^{267, 268} and 6-31++g(d,p) basis function was used to optimize the chemical structures by DFT. The minimum energy configurations of ThT and PG were shown in figure 3.10 and are used further in docking studies.

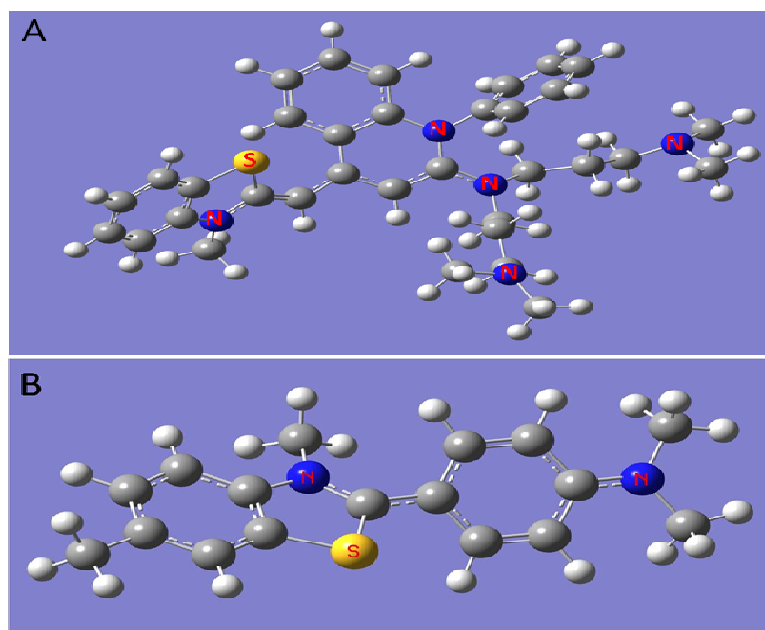


Figure 3.10 Optimized structures of (A) PG and (B) ThT.

In order to further determine the preferred binding location and the nature of interactions between PG and fibril we have performed blind molecular docking studies for PG with fibrils using Autodock 4.0. As the crystal structure of insulin fibril is not available we have carried out docking studies with A β 1-42 fibril (pdb ID: 2MXU) structure which is closely associated with Alzheimer's disease.²⁷¹ Out of several initial positions of PG used for docking, the most energetically stable configuration has been obtained and shown in figure 3.11. From the figure it is seen that PG binds in the inner core of the amyloid fibrils. From the detailed analysis of the several possible molecular interactions, we found that hydrophobic forces are the main reason for the binding of PG to fibrils. There is also π - π Interaction between quinonoid group of PG and aromatic side chains of amino acids in the fibril exists in PG-fibril complex.

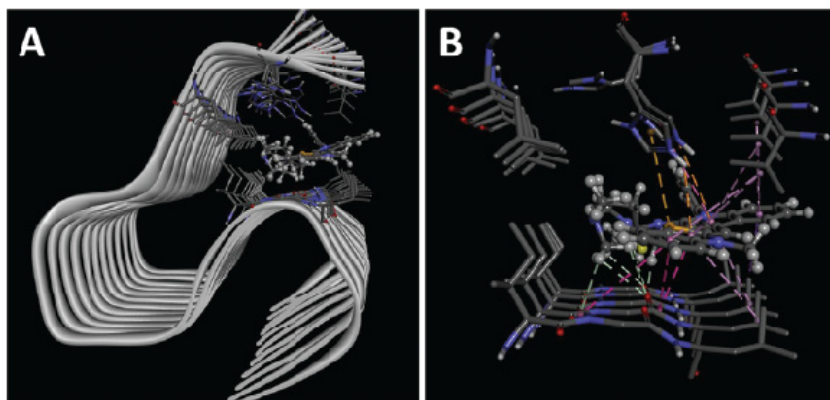


Figure 3.11 (A) The most stable configuration of PG in fibril obtained from molecular docking studies. (B) Closer look at the interactions between PG and amino acids of fibril at the binding pocket. For clarity, PG is shown by ball- stick model and amino acids are shown by sticks.

In order to identify the relative locations of PG and ThT in amyloid fibrils, we have further carried out docking studies of ThT with already docked PG-fibril

complex. The most energetically stabilized ThT conformation is in the inner core of amyloid fibrils. The docked conformation of PG and ThT in amyloid fibrils has been shown in figure 3.12. The docking studies show that PG and ThT are separated by a distance of 42 Å. These results are consistent with the results obtained from steady state and time-resolved fluorescence measurements. Molecular docking studies also supports that ThT and PG are having situated in different binding sites in amyloid fibrils as shown by the experiments.

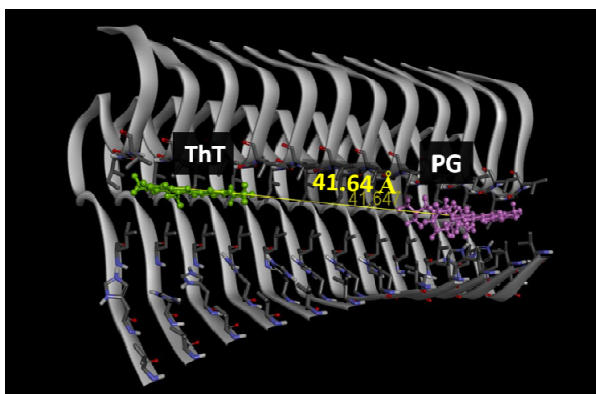


Figure 3.12 Binding pose of ThT in the fibril incorporated with PG.

Thus, our detail studies clearly indicate that PG is a very sensitive probe for the detection of amyloid fibrils. Such high sensitivity is primarily due to its extremely low emission yield in bulk water and its subsequent increase in its emission yield in amyloid fibrils. Unfortunately, at this juncture, we do not have any knowledge of the fundamental processes that is responsible for the low emission yield of PG in water. It is expected that such fundamental processes will be inhibited in the amyloid fibrils to show large emission yield. Hence, it is of utter importance to understand the fundamental processes that takes place in the excited state of PG in water and in other low viscous solvents. Hence, we have investigated the photophysical properties of PG

in different molecular solvents, including water, using steady-state and femtosecond time-resolved fluorescence techniques.

3.3.8. Photophysical studies of PG

3.3.8.1. Steady state fluorescence measurements

Steady state fluorescence spectra have been recorded to evaluate the effect of viscosity of the medium on the emission quantum yield (ϕ_f) of PG. Being a member of UMR, the emission intensity of PG is expected to be influenced by the solvent viscosity. We have recorded the emission spectra of PG in acetonitrile (ACN)-ethylene glycol (EG) solvent mixtures with different compositions. The selection of ACN-EG solvent mixtures is based on the fact that they have very similar polarity (ϵ for ACN is 37 and ϵ for EG is 37.5) but quite different viscosity (η for ACN is 0.34 cp and η for EG is 16 cp).²⁸⁵ Hence, due to the change in solvent composition of the mixed solvent, there will be hardly any change in the solvent polarity and thus only the effect of viscosity will be observed in the emission spectra. The fluorescence spectra of PG in ACN-EG solvent mixtures with different compositions are shown in figure 3.13A. It is evident from figure 3.12A that the emission intensity increases with increase in the viscosity of the solvent medium. The quantum yield of PG in mixed solvents have been measured by comparative method using Nile red in dioxane ($\phi_f=0.7$) as a reference²⁸⁶ and the values are presented in table 3.3. Thus, the emission quantum yield of PG increases from 2.13×10^{-4} in ACN to 33.7×10^{-4} in EG. Variation in the ϕ_f values with the solvent viscosity is represented in figure 3.13B. Thus, there is more than 15 fold increase in the emission yield due to change in solvent from ACN to EG. Nakai et al suggested that large quenching of PG in non-viscous solvents is due

to the non-radiative torsional motion in the excited state of PG.²⁷³ Such efficient torsional motion has been restricted in viscous medium which leads to increase in the emission yield.

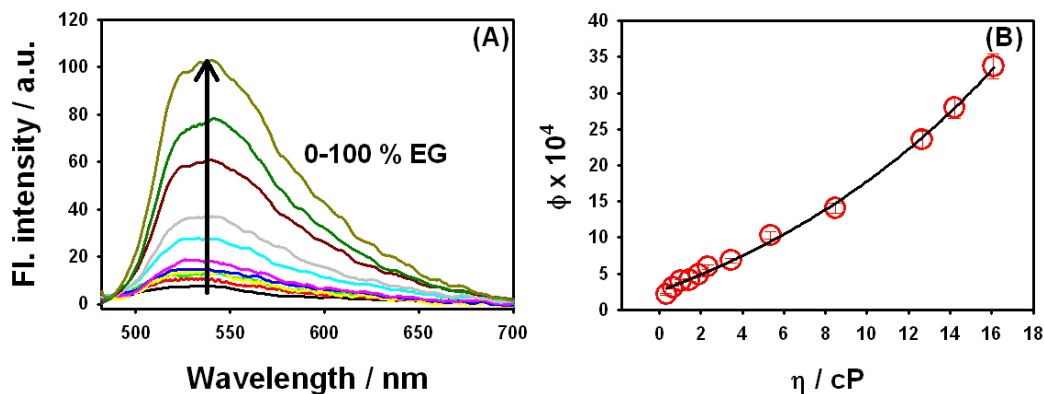


Figure 3.13 (A) The fluorescence spectra of PG in ACN-EG solvent mixtures with different compositions. (B) The variation of emission quantum yield of PG with viscosity of the solvent medium.

Table 3.3 The emission quantum yield of PG in ACN-EG solvent mixtures.

Volume % of EG	viscosity(η)/cP*	$\phi_f \times 10^4$
0	0.34	2.13
17	0.65	3.08
19	1.03	3.99
37	1.45	4.11
44	1.90	4.88
50	2.35	5.95
60	3.45	6.84
71	5.36	10.33
83	8.48	14.06
93	12.66	23.57
96	14.22	27.94
100	16.10	33.70

*Viscosity of mixtures has been calculated according to $\ln(\eta_{mix}) = \sum w_i \ln \eta_i$ η_{mix} is the viscosity of mixture, η_i is the viscosity of i^{th} component and w_i is the weighting factor of the i^{th} component²⁸⁷

The quantitative assessment of viscosity probe has been performed using following Forster-Hoffmann.²⁸⁸

$$\log(\phi_f) = \log(A) + \alpha \log(\eta) \quad (3.11)$$

where ϕ_f is the emission quantum yield and η is the viscosity of the medium. 'A' is constant which depends on the radiative rate of dye and properties of solvent and α is a constant which relies on the chromophore properties like intra molecular dynamics such as rotation and isomerization.²⁸⁸ Figure 3.14 shows the variation of $\log(\phi)$ with $\log(\eta)$ and fitted with the equation 3.8. The ' α ' parameter has been estimated from the fitting and found to be 0.7. The value of α determined by us is very close to the value reported in the literature for PG.²⁷⁴ Such a high value of α signifies the ability of PG as viscosity sensor.

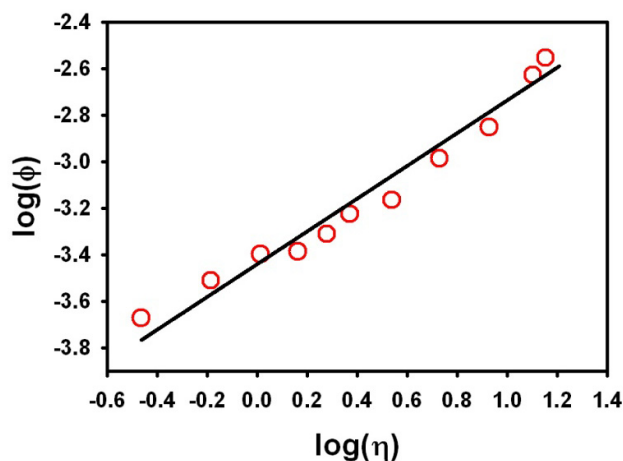


Figure 3.14 Variation of $\log(\phi)$ with $\log(\eta)$. The solid line is the fitting of the experimental data by Forster-Hoffmann equation.

3.3.8.2. Time-resolved fluorescence studies

Molecular rotors are family of molecules which are characterized by the ultrafast torsional motion around a single chemical bond in their excited state.^{170, 173} Such torsional motion is generally non-radiative and mainly responsible for extremely low emission yield of molecular rotors in low viscous solvents.^{128, 170, 173} The excited state lifetimes of this class of molecules are very sensitive to the rigidity offered by the surrounding medium.¹³⁰ To get a better insight into the excited state processes with viscosity, time-resolved fluorescence measurements were carried out for PG in ACN, EG and their solvent mixtures. Emission transient decays recorded for PG in these solvents are shown in figure 3.15. In low viscous ACN, the fluorescence decay is very fast. Drawing analogy to the molecular rotors,¹³⁰ the observed ultrafast excited state decay of PG in ACN is assigned due to the excited state non-radiative bond twisting process. The emission transient decay becomes slower with the increase in the EG content, i.e. with the increase in the viscosity of the medium. All transient decays thus recorded have been fitted with multi exponential decay function according to equation 3.1 and the fitted parameters are shown in table 3.4. It is evident from the table and figure 3.15 that irrespective of the solvent viscosity, the fastest decay component in all solvents is very similar. This result clearly indicates that PG is characterized by a fast decay component with time constant ~ 180 fs which is independent of the solvent viscosity. Following such viscosity independent decay components, decays traces of PG in all solvent are characterized by two viscosity dependent relatively longer decay components. Thus, the absence of effect of viscosity on the fastest decay components indicates that no diffusional motion of the molecules is responsible for such fast decay processes. The faster decay components is assigned to the formation of intramolecular

charge transfer (ICT) state prior to the twisting process in PG. Formation of such ICT prior to bond twisting has already been reported for other molecular rotors.²⁸⁹⁻²⁹¹ Formation of such ICT in the ultrafast timescale has also been supported from the polarity dependent studies (vide infra). However, viscosity dependence of two longer decay components indicating large amplitude diffusional motion in PG is involved in its excited state. Drawing analogy with the other molecular rotors,¹³⁰ the two long decay components has been assigned to the torsional motion in the excited state of PG. Thus, the average lifetime (calculated according to equation 3.1) of PG has increase from 1.36 ps in ACN to 19.71 ps in EG indicating extensive retardation in the non-radiative torsional motion in relatively viscous EG.

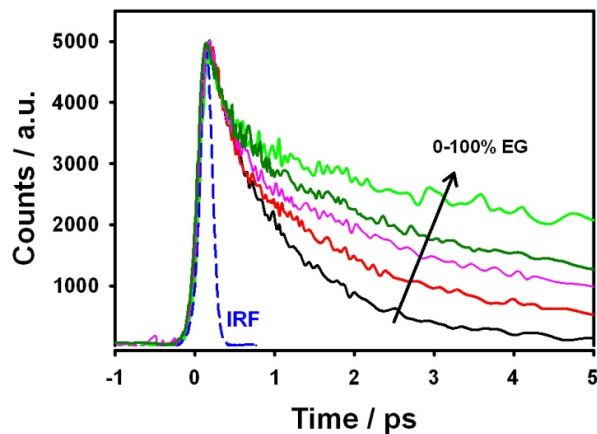


Figure 3.15 Fluorescence transients decay traces for PG in ACN-EG solvent mixtures: (1) 0, (2) 50, (3) 70, (4) 80 and (5) 100 % EG. The dashed line represents instrument response function (IRF).

Table 3.4 Fitted parameters for transient emission decay of PG in ACN-EG solvent mixtures.

% of EG	a_1	τ_1/ps	a_2	τ_2/ps	a_3	τ_3/ps	$\tau_{\text{avg}}/\text{ps}$
---------	-------	--------------------	-------	--------------------	-------	--------------------	-------------------------------

0	3.5	0.18	58.2	0.84	38.3	2.27	1.36
50	5.8	0.17	43.8	1.57	50.4	7.55	4.51
70	3.3	0.19	22.9	1.80	73.8	11.22	8.70
80	1.9	0.17	18.4	1.94	79.8	14.48	11.90
100	1.1	0.16	6.8	2.68	92.1	21.19	19.71

It is also possible that the fast decay observed in ACN-EG solvent mixtures may arise due to the formation of PG aggregates. Such molecular aggregates are known to show ultrafast decay component which is unaffected by the solvent viscosity.^{292, 293} However, as the extent of aggregation is largely depends on the molecular concentration, such fast decay due to aggregates is expected to be affected by the solute concentration. To check the possibility of the formation of aggregates, emission transient decays have been recorded in ACN at different concentration of PG and the results are shown in figure 3.16. It is clearly evident from figure 3.16 that the excited decay kinetics for PG in ACN does not depend on its concentration. This result discounts the possibility of aggregation of PG in ACN-EG solvent mixtures.

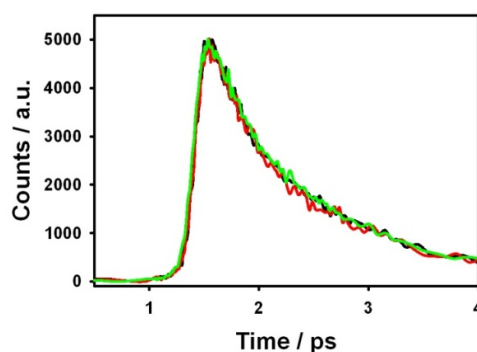


Figure 3.16 Fluorescence transient decays in ACN for different concentrations of PG: 4 μM (black), 7.8 μM (red) and 13.3 μM (green).

In order to get better understanding on the excited state dynamics of PG, wavelength dependent time-resolved fluorescence measurements have been carried

out using fluorescence upconversion spectroscopy. Emission transient decays of PG in ACN recorded at different emission wavelengths are shown in figure 3.17. It is apparent from the figure that the excited state dynamics of PG largely depends on the monitoring emission wavelength. Thus, the emission decay becomes faster on the blue edge of the emission spectra while the decay becomes slower at the red edge of the emission spectrum. It is also evident from the figure that emission transient decays recorded at the blue edge of the emission spectrum is characterized by an ultrafast decay component followed by a relatively slow decay. The faster decay observed at the blue edge of the emission spectrum might arise from the vibrational decay of PG in the excited state.²⁹² To confirm the presence of such vibrational relaxation in the measured emission transient decay, we have recorded the emission transient decays at the blue edge of the emission spectrum for different excitation wavelengths. However, we have not seen any effect of the excitation wavelength on the measured emission transient decays. This result eliminates the possibility of the contribution of intramolecular vibrational relaxation in the measured emission decay traces.

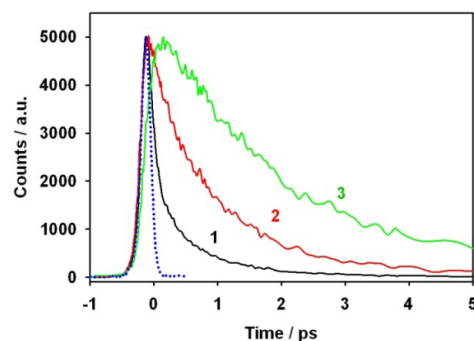


Figure 3.17 Fluorescence decay traces of PG in ACN at different emission wavelengths: (1) 500 nm, (2) 540 nm and (3) 620 nm. The dashed line represents the IRF.

To unravel the underlying mechanism for the observed wavelength dependent emission decay traces, time-resolved emission spectra (TRES) have been constructed following the procedure proposed by Maroncelli and Fleming.¹³⁸ Figure 3.18A represents the constructed TRES at different time for PG in ACN. It is evident from figure 3.18A that the emission intensity of PG decreases drastically with time. Further, a substantial temporal shift in the emission spectra ($\sim 1220\text{ cm}^{-1}$) has also been observed which can be seen from peak normalized TRES (*cf.* figure 3.18B). Such observed time-dependent fluorescence Stokes' shift (TDFSS) is generally assigned to the solvent relaxation process.²⁹⁴ However, in the present case the observed TDFSS is not due to the solvent relaxation can be explained from the following facts. Solvent relaxation is the process where the stabilization of the excited state takes place due to the solvent reorientation. During such solvent relaxation, the excited state population is more or less maintained and thus there will not be much changes in the emission intensity with time. However, in the present case, we have seen that TDFSS is accompanied with almost $\sim 95\%$ reduction in the emission intensity (*cf.* inset of figure 3.17). Such large reduction in the excited state population cannot be explained by the solvent relaxation process. Absence of any effect of solvent relaxation process on the observed TDFSS is also supported by the fact that PG does not show any significant solvatochromism. For example, PG shows similar emission peak position in nonpolar ethyl acetate (EA) and polar ACN. However, such TDFSS has been reported for the UMR class of molecules.^{178, 279, 295} For example, despite the lack of solvatochromism, ThT shows large extent of TDFSS in several molecular solvents and assigned due to the torsional motion in its excited state.^{128, 130} Drawing an analogy, the observed

TDFSS for PG can also be assigned to the intramolecular torsional process in its excited state.

Careful examination of peak normalized TRES (*cf.* figure 3.18B) also reveals that apart from the large TDFSS, there is a significant broadening of the emission spectra especially in the red edge. Such broadening in red edge has been observed for chromophoric coumaric acid in photoactive yellow protein.²⁹⁶ The change in the mean

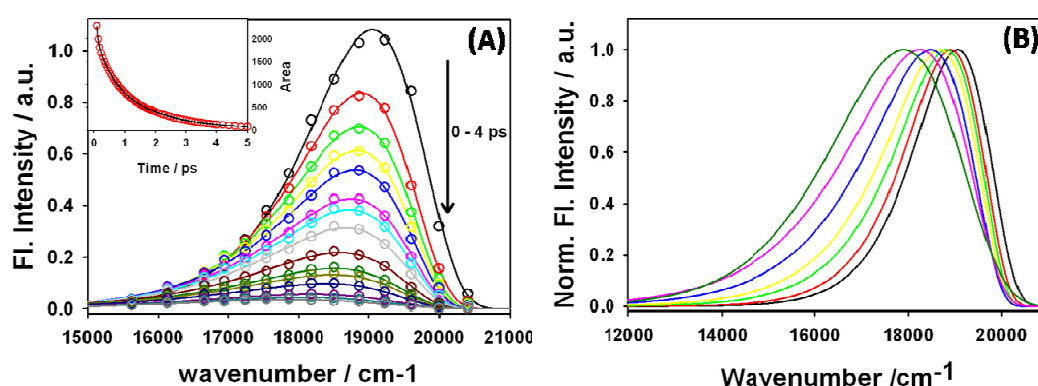


Figure 3.18 (A) Time-resolved emission spectra (TRES) of PG in ACN. Circles denote the experimental points and solid lines are their respective log-normal fits **Inset:** Variation of integrated area under the emission spectra with time. **(B)** Peak intensity normalized (TRES) of PG in ACN at 0.1 ps (black), 0.2 ps (red), 0.5 ps (green), 1 ps (yellow), 2 ps (blue), 3 ps (magenta) and 4 ps (olive green).

frequency and spectral width (FWHM) with time has been displayed in figure 3.19. The changes in the mean frequency with time follow bi-exponential decay with time constants of 0.12 ps and 3.74 ps. It is also evident from figure 3.18 that the spectral width increases with time and could be fitted with bi-exponential decay function with time constant of 0.13 ps and 4.35 ps. Similar temporal behaviour of peak position and spectral width with similar time constant clearly indicates that same process in the

excited state of PG is responsible for the observed changes in the peak position and spectral width. Further, the present results also support that the observed changes in the peak position with time is not due to the solvent relaxation process. If the solvent relaxation process takes place, spectral width, normally, does not change.²⁹⁴ However, in the present case, we observed large increase in spectral width with time indicating that there is some intramolecular process occurs which is responsible for the changes in TDFSS and FWHM. The significant increase in the spectral width along with large TDFSS clearly indicates the formation of a new emissive species following the photoexcitation of PG in ACN. This can be either ICT state or TICT state and will be confirmed through the effect of solvent viscosity on the excited state dynamics of PG (vide infra).

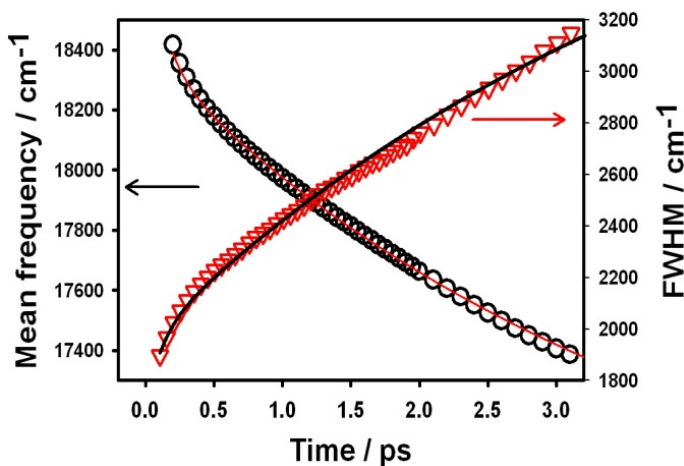


Figure 3.19 The change in the emission peak position (○) and FWHM (▽) with time for PG in ACN. Solid lines represent their bi-exponential fits.

To resolve the changes in the spectral shape, along with variation in TDFSS, the areas under the spectra at different times were normalized and plotted in figure 3.20. Figure 3.20 reveals that there is significant red shift in the emission spectra

which is evident from the constructed time-resolved area normalized emission spectra (TRANES). It is to be mentioned that two isoemissive points have been observed in TRANES. It is to be mentioned that two isoemissive points have been observed in TRANES in the time windows of 0.1-1.3 ps and 2-4 ps. Appearance of iso-emissive points in TRANES indicates that there are three emissive species exist in equilibrium.²⁹⁷⁻²⁹⁹ For the class of UMR, for example ThT, such isoemissive point is observed earlier and assigned to the conversion of LE to TICT state.¹²⁸ However, in the present case, first isoemissive point appears in the time window (0.1-1.3 ps) where the excited state decay is independent on the solvent viscosity. Thus, unlike ThT, the first isoemissive point does not arise due to torsional motion in PG. As proposed earlier, the first isoemissive point appears probably due to the LE-ICT conversion (vide infra) process. As the other isoemissive point has been observed in the time scale where viscosity dependent excited state dynamics has been observed, second isoemissive points has been assigned due to the excited state ICT to TICT process.

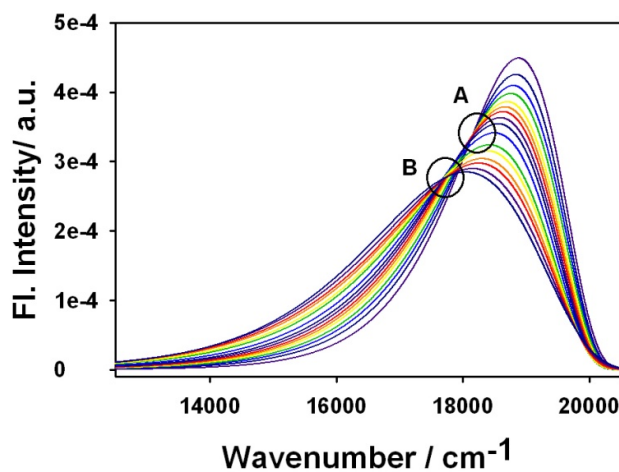


Figure 3.20 Time-resolved area normalized emission spectra (TRANES) for PG in ACN: (A) 0.1-1.3 ps (B) 2-4 ps.

3.3.8.3. Effect of viscosity on the ultrafast dynamics of PG

In order to get deep understanding on the nature of states involved in the excited state decay of PG, the ultrafast dynamics of PG in solvents with different viscosity have been investigated in detail. As mentioned earlier, due to the possibility of the charge transfer in the excited state of PG, polarity can also affect the excited state dynamics. As mentioned earlier, ACN-EG solvent mixtures are suitable to see the effect of viscosity on the excited state dynamics keeping the solvent polarity same. Hence, we have investigated the excited state dynamics of PG in EG and 1:1 ACN-EG mixtures and the results are compared with ACN. Like ACN, PG in both EG and EG-ACN mixture, shows strong emission wavelength dependent excited state decay dynamics. Faster decay in blue edge and ultrafast growth in red edge are characteristic of the dynamics of PG in both of these solvents. The decays at all emission wavelengths become slow with the increase in the solvent viscosity. For both solvents, wavelength dependent decays were fitted with multi exponential function and all the fitted parameters are utilized in constructing TRES. To get better comparison, from this point onwards, we will compare the spectral changes for all three solvents investigated. The variation in the integrated area with time is presented in figure 3.21. It is apparent from the figure that there is large reduction in the emission intensity with time. Thus, the integrated emission intensity is decreases to ~ 95% in ACN, ~85% in 1:1 ACN-EG mixture, and ~55% in EG within 4 ps following photoexcitation. Such large reduction in integrated intensity in short time supports that there is minimal influence of solvent relaxation process on observed TDFSS. In all the three solvents, the observed TDFSS can be assigned for the excited state intramolecular process of PG. It is also observed from figure 3.21 that the decrease in the emission intensity up

to 1 ps is unaffected by the solvent viscosity. However, at longer time the rate of decrease in the emission intensity largely influenced by the solvent viscosity. Thus, rate of decay in the emission intensity decreases with the increase in the solvent viscosity. Thus, the intensity decay dynamics can be divided into two time regions. One is viscosity independent region, where there is no intermolecular motion is involved. Other is viscosity dependent region, which involves the ultrafast torsional motion in the excited state, probably TICT formation.

The changes in the mean frequency of fluorescence spectra along with FWHM

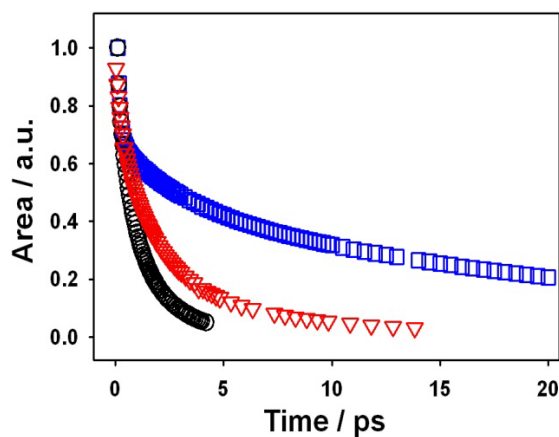


Figure 3.21 The variation of integrated area under the emission curve with time for PG in ACN (O), 1:1 ACN: EG mixture (∇), and EG (\square)

for all three solvents are presented in figure 3.22. The variations in the mean frequency and FWHM with time were fitted with the multi-exponential decay function and fitted parameters are presented in table 3.5. From fitted parameters it is quite evident that like ACN, same excited state process is responsible for the observed temporal changes in the mean frequency and FWHM in EG and in 1:1 EG-ACN mixture. It is also evident from figure 3.22 and fitted parameter shown in table 3.5,

that like ACN, the changes in mean frequency and FWHM with time in EG and 1:1 EG-ACN mixture is independent of solvent viscosity in early time scale (up to ~ 1 ps). These results also invariably suggest that the friction independent process occurs in the excited state which corresponds to the decrease of ~ 400 cm^{-1} in mean frequency and 400 cm^{-1} increase in the FWHM. As mentioned earlier, such dynamics in early time scale is assigned to the transition of LE state to ICT state. As no diffusional motion is involved in LE to ICT transition, such process is viscosity independent. In recent studies of well known TICT molecule DMABN, through detailed time-resolved fluorescence studies, it has been shown that there is ultrafast ICT formation which precedes the TICT formation.³⁰⁰ Myeongkee et al showed that, by comparing DMABN with its rigid derivative NTC6 (1-tert-Butyl-6-cyano-1,2,3,4-tetrahydroquinoline), ICT process is clearly involved with partial twisting before completely twisted TICT formation.²⁸⁹ By comparing with all these studies, we can propose the observed ultrafast dynamic in the first time region (< 1 ps) corresponds to the formation of ICT state from LE state.

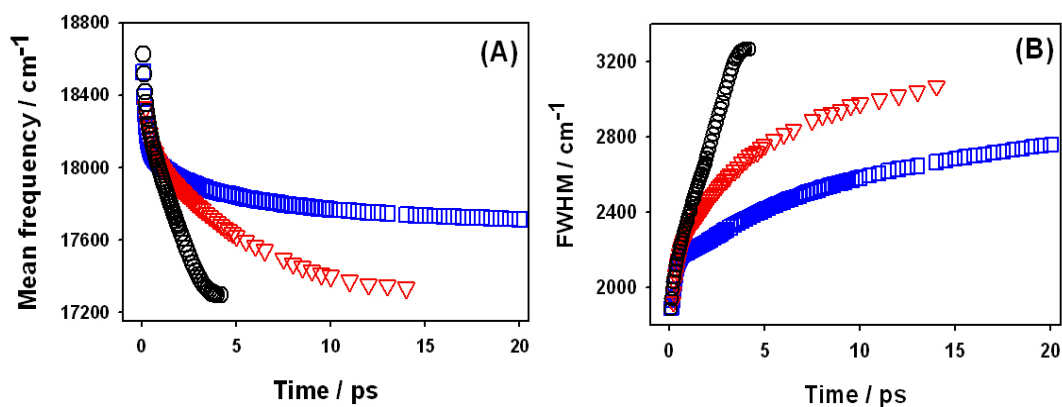


Figure 3.22 The variation of (A) mean frequency and (B) FWHM with time for PG in different solvents: ACN (O), 1:1 EG: ACN (∇), and EG (\square).

Table.3.5 Fitting parameters of mean frequency decay and FWM growth of PG in ACN-EG solvent mixtures and EA

Solvents	a ₁	τ ₁ / ps	a ₂	τ ₂ / ps	a ₃	τ ₃ / ps
Mean frequency						
ACN	1.0	0.12	99.0	3.74	----	----
ACN:EG(1:1)	1.0	0.19	99.0	6.69	----	----
EG	0.8	0.18	3.2	4.49	96.0	38.00
EA	1.0	0.32	99.0	5.88	----	----
FWHM						
ACN	-0.3	0.11	-99.7	4.35	----	----
ACN:EG(1:1)	-0.6	0.16	-98.4	6.96	----	----
EG	-0.5	0.12	-7.7	3.22	-91.8	39.12
EA	-0.2	0.33	-99.8	6.52	----	----

Large influence of the solvent viscosity on the rate of change in mean frequency and FWHM in the later time scale clearly indicates that some diffusional motion in photoexcited PG are responsible for such dynamics. Comparing with other molecular rotors,^{128, 178, 279} we have assigned such viscosity dependent process to the formation of TICT through ultrafast non-radiative twisting in the excited state. From table 3.5 it is clear that the time constant corresponding to the TICT formation increases with the frictional force offered by the solvent medium. The viscosity dependent dynamics in this region clearly supports such proposition.

TRANES is well established method that can used to identify the number of emissive species exist in equilibrium in the excited state.²⁹⁷⁻²⁹⁹ Like PG in ACN, we have observed two isoemissive points in other two compositions also. The case of PG in ACN:EG(1:1) mixture has been presented in figure 3.23. It is evident from the figure that first isoemissive point is observed in the similar frequency range during similar time scales (0.1-1.5 ps). This suggests that the conversion of locally excited

state to ICT formation happens during these time scales. Like PG in ACN, another isoemissive point also observed for PG in other two solvents. However, the time scale for the observation of such second isoemissive point depends on the solvent viscosity. Thus, in ACN-EG mixture, isoemissive point appears at 8 ps and remains up to 24 ps while in EG it starts at 12 ps and remains up to 60 ps. Thus, the large dependence of the time scale for the appearance of the isoemissive point on the solvent viscosity indicates the formation of emissive TICT state in the excited PG molecules. Thus, following photo-excitation, PG undergoes stepwise process of conversion from LE to ICT and then to TICT.

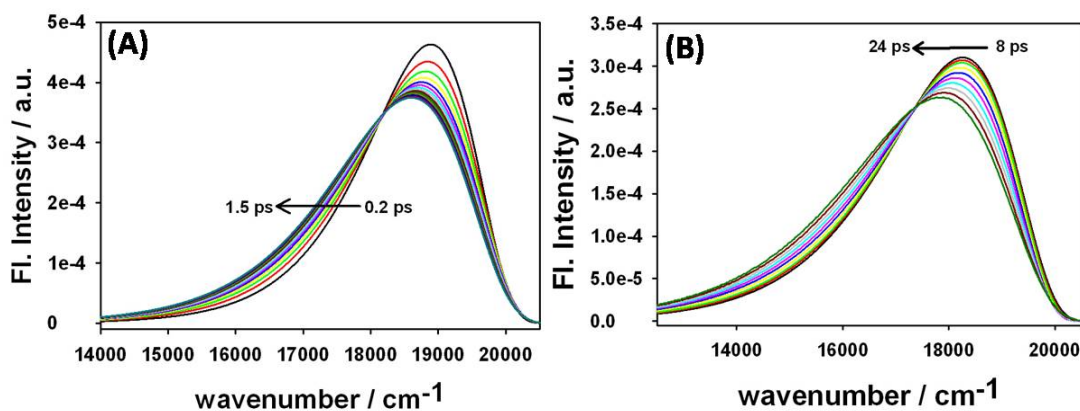


Figure 3.23 TRANES of PG in 1:1 ACN: EG mixture at (A) 0.2-1.5 ps and (B) 8-24 ps.

3.3.8.4. Effect of polarity on the ultrafast dynamics of PG

The formation of ICT involves the distribution of charge in the molecule leading the change in electronic distribution and thus the molecular dipole moment. Hence, ICT process should depend on the polarity of the surrounding medium.¹²⁵ High polarity of the solvent facilitates the formation of ICT compared to low polar solvent.

To confirm the hypothesis of ICT formation, we have studied the ultrafast dynamics of PG in relatively low polar solvent, ethyl acetate (EA, $\epsilon=6.02$), and the results are compared with the dynamics in acetonitrile. The emission transient for PG in EA at 540 nm is measured and shown in figure 3.24 along with the decay measured in ACN for comparison. It is evident from the figure that the excited state population decay got slowed down in ethyl acetate as compared to ACN. As the viscosity of EA ($\eta=0.45\text{cp}$) which is similar to the viscosity of ACN ($\eta=0.34\text{ cp}$), the observed changes in the decay were not due to the change in viscosity. Thus, it is in line with proposition of ICT formation in the earlier time scales. Less polar EA unable to facilitate the ICT formation leads to slow emission intensity decay compared to PG in high polar ACN.

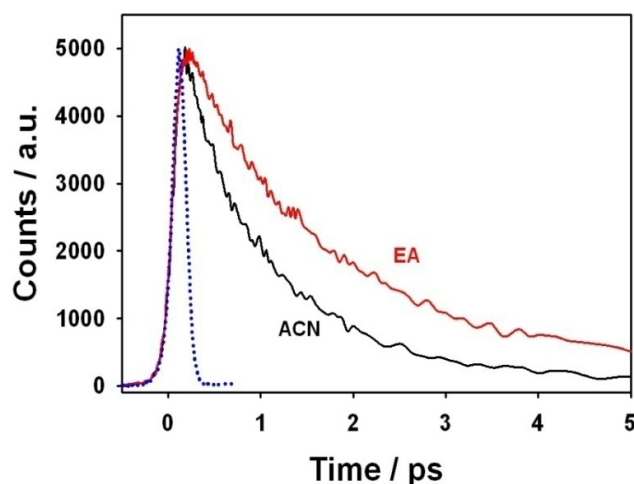


Figure 3.24 The fluorescence transient decays of PG in ACN and EA. The dotted curve is the IRF.

Table.3.6 Fitting parameters of intensity decay of PG in ACN and EA.

Solvents	a_1	τ_1 / ps	a_2	τ_2 / ps	a_3	τ_2 / ps
ACN	0.07	0.14	0.93	1.16	--	--
EA	0.02	0.27	0.40	1.42	0.58	5.45

Wavelength dependent decays for PG in EA were measured using upconversion method. PG in EA also shows similar kind of dynamics as in ACN and other solvent mixtures. These decays were fitted with tri-exponential function and the fitted parameters are used to construct TRES and TRANES. The variation in the integrated area with time for PG in ACN and EA were shown in figure 3.25A. In EA also there is large reduction in the fluorescence intensity ($\sim 85\%$) within 4 ps suggests that there is minimal contribution from solvent relaxation in observed dynamics. It is evident from figure 3.25A that the rate of decay of area of PG in EA is slower compared to ACN which is in agreement with the lifetime measurements. The temporal variation of mean frequency has been presented in figure 3.25B. It is clear from the figure that the mean frequency decay of PG in EA is slower than PG in ACN. Thus the observed dynamics of PG are very much dependent on polarity especially at the earlier time scales. The mean frequency decay has been fitted with bi-exponential function and the decay parameters have been tabulated in table 3.5. PG in EA shows a short component of 0.32 ps which is higher than the observed fast time constant for PG in ACN-EG mixtures (~ 0.18 ps). This result suggests that the ultrafast dynamics in sub ps time scales, assigned for LE-ICT conversion, are dependent on the polarity rather than viscosity of the surrounding medium.

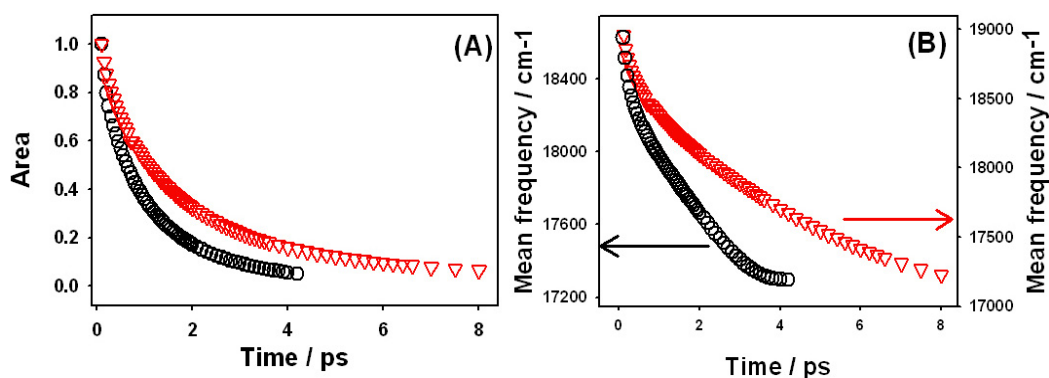


Figure 3.25 Variation in (A) integrated area and (B) mean frequency of PG in EA (O) and ACN (∇).

TRANES has been constructed for PG in EA and presented in figure 3.26. Careful examination of TRANES of PG in EA reveals that the isoemissive point appears at 3 ps after photo excitation at 17700 cm^{-1} . This indicates the conversion of LE-ICT conversion got slowed down due to decrease in polarity of the surroundings. These results indicate that ICT formation precedes TICT formation in PG. Proposed mechanism is shown in scheme 3.1.

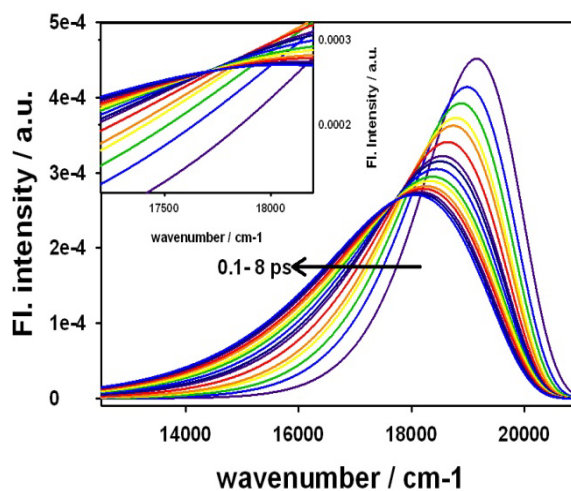
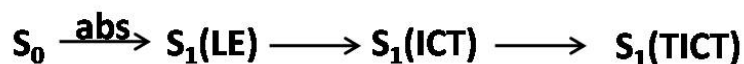


Figure 3.26 TRANES of PG in EA at different times. Inset: magnified figure of TRANES of PG in EA.

Scheme 3.2 Proposed mechanism of excited state relaxation processes involved in PG



3.3.8.5. Dynamics of PG in insulin fibril:

Our primary aim is to resolve the change in excited state dynamics of PG which are responsible for the observed large enhancement in the fluorescence. As the lifetime of PG in fibrillar solution extends over nanosecond time scales, we have studied the dynamics of PG in fibril using TCSPC method in nanosecond regime. To understand the fate of the excited state dynamics we have studied wavelength dependent decay dynamics for PG in 30 μM insulin fibril and are presented in figure 3.27A. From the figure it is clear that the intensity decay gets slower on going to the red side of the emission spectra. The decays were fitted with tri-exponential function and the fitted parameters are utilized for the making TRES and TRANES. It is evident from figure 3.27B that there is substantial red shift as well as broadening in the emission spectra with time. This is similar to the dynamics observed for PG in molecular solvents.

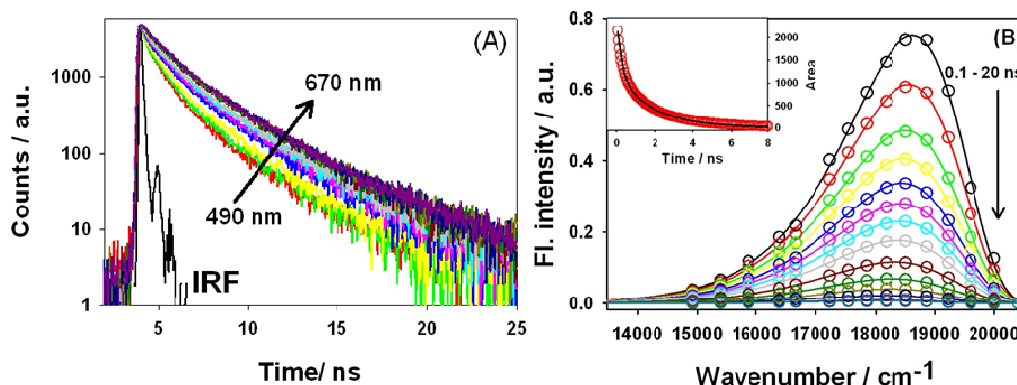


Figure 3.27 (A) Wavelength dependent decay traces of PG in 30 μM insulin fibril. (B) TRES of PG in 30 μM fibril. Circles represent experimental data points and solid curves represent their lognormal fits **Inset:** variation in the integrated area of PG in fibril.

The variations in mean frequency and FWHM with time for PG in amyloid fibrils are shown in figure 3.28A. The mean frequency decay was fitted with bi-exponential function and yielded the time constants of 0.23 ns and 2.85 ns. The FWHM growth also shows similar variation as the mean frequency with time constants of 0.19 ns and 2.29 ns indicates that they are accompanied by one another. Drawing an analogy from the observed dynamics in PG in molecular solvents, we can assign the observed dynamics to be the formation of TICT formation of PG in excited state. In the observed time scales, the formation of ICT is negligible as evident from the previous results of PG in ACN and EA. TRANES (*cf.* figure 3.28B) shows a single isoemissive point at 18200 cm^{-1} suggests that the formation of TICT is restricted due to the binding of PG in fibril. In fibril, the non-radiative torsional motion is restricted in the excited state leading to large enhancement in the dye's fluorescence.

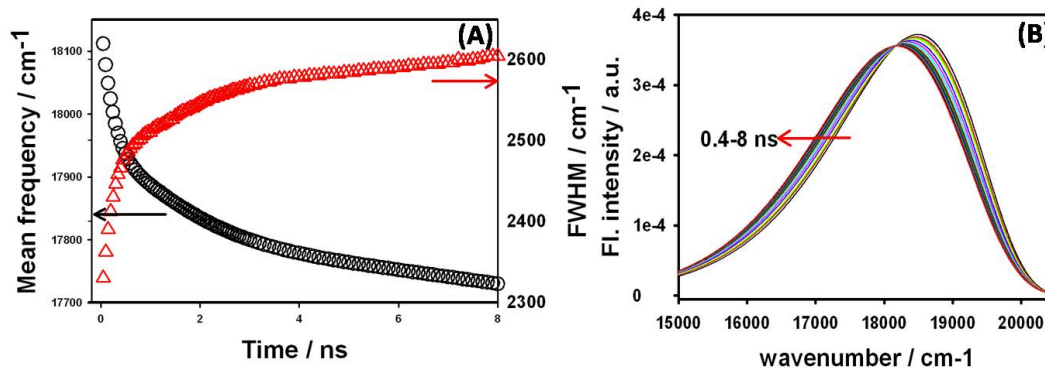


Figure 3.28 (A) Variation of mean frequency (○) and spectral width (△) with time. **(B)** TRANES of PG in fibril at different times.

Table 3.7 Fitting parameters for the temporal changes in mean frequency and FWHM of PG in fibril

	a_1	τ_1 / ns	a_2	τ_2 / ns
Mean frequency	0.52	0.23	0.48	2.85
FWHM	0.57	0.19	0.43	2.29

3.5. Conclusions:

In this chapter, we have explored the suitability of PG as amyloid fibril sensor. PG shows remarkable fluorescence enhancement of ~ 1000 fold in the presence of insulin fibrils. The fluorescence intensity as well as lifetime indicates that dye experiences larger micro viscosity at the binding location in insulin fibril. PG fibril binding is independent of ionic strength indicates that hydrophobic interactions are playing a major role in the binding mechanism. PG shows similar fibrillation kinetics and better fluorescence enhancement factor compared to the standard amyloid stain, ThT. From the detailed energy transfer studies from ThT to PG gives an estimation of binding location of these two dyes in amyloid fibrils. The spatial separation between these two dyes has been estimated from Forster theory as 52 Å. Such experimental results are also supported by molecular docking studies. Thus, PG can be better alternative to ThT for the detection of amyloid fibrils in vitro.

In order to understand the fate of excited state processes of PG in fibril, we have also studied the ultrafast excited state dynamics of PG, in ACN, EA, EG and 1:1 mixture of ACN and EG. From the detail time-resolved emission measurements we have seen that there is large reduction in fluorescence intensity in all solvents within 4 ps following photoexcitation along with large shift in mean frequency suggesting no

contribution from the solvent relaxation towards the observed dynamics. TDFSS decay and FWHM growth follows similar trend with time indicating that a single process is responsible for the changes in mean frequency and spectral width. We have observed two processes occur in the excited state of PG in these solvents. First is the ICT formation which happens within 4 ps and depends on the polarity of the surrounding medium. Secondly, TICT formation which happens after ICT formation and depends on the frictional force offered by the solvent medium. Finally, in insulin fibril, the torsional motion has been restricted and the dynamics were extends up to nanosecond region. The restriction in the torsional motion of PG is responsible for the observed large fluorescence enhancement in the fibril

Chapter-4

Synthesis, Photophysics and interaction with amyloid fibrils of neutral benzothiazole derivative

4.1. Introduction:

As discussed in chapter 3, PicoGreen is an efficient sensor than Thioflavin T but both dyes are positively charged. Due to their ionic character and low lipophilicity, they doesn't able to penetrate through Blood brain barrier (BBB). In this chapter we have synthesized a neutral analogue of ThT, a benzothiazole based molecule in order to develop a fluorescent probe for the in-vivo detection of fibrils. The remarkable fluorescence enhancement of ThT in the presence of amyloid fibrils makes it a promising diagnostic agent for amyloid deposits in vitro.¹⁹⁸ The characteristic fluorescence enhancement of ThT has been attributed to the restriction in the nonradiative torsional motion around its central C-C bond between dimethyl aniline and benzothiazole groups upon binding to fibrils.²¹² The free rotation about central C-C bond leads to the conversion of emissive locally excited (LE) state to non-emissive twisted intramolecular charge transfer (TICT) state resulting extremely low emission yield in low viscous solvents.^{128, 181, 301} Upon binding to fibrils, the hindrance in the bond rotation leads to decrease in the population of non-emissive TICT state and

results in a large increase in its emission yield.^{128, 181, 301} Although, ThT doesn't have protein specificity and binds to fibrils from all classes of proteins, it has been used for several decades for its strong affinity towards amyloid fibrils and large sensitivity due to its remarkable fluorescence enhancement on binding with amyloid fibrils.^{129, 184} Despite such extensive usage of ThT, the actual mechanism of interaction with amyloid fibrils is not clearly understood. It has been proposed that molecular structure of ThT matches with structure of inner grooves of its fibrillar channel. Such shape matching between ThT and fibrillar structure along with hydrophobic stabilization is believed to be mainly responsible for the strong association of ThT with amyloid fibrils.³⁰²

For in-vivo imaging of amyloid plaques, the probe should cross the blood brain barrier (BBB). For an efficient crossing of BBB, the probe with smaller size and higher lipophilicity is preferred.¹¹² Being a positively charged molecule, ThT is unable to cross the BBB and hence cannot be used for the in-vivo detection of amyloid plaques.²¹⁵ Further, emission spectral position of ThT is largely remains unchanged due to association with amyloid fibrils.^{198, 303} Hence, spectral distinction between amyloid bound ThT and free ThT in water cannot be done. This results in large background signal for imaging studies leading to low S/N values. Further, it has been shown recently that ThT also promotes A β fibrillation by preferential stabilization β -sheet conformation over the native form of the protein.²¹³ Such limitations of ThT encourage us to develop a neutral fluorescent probe for amyloid fibrils which can have different spectral properties in water and in amyloid fibrils. Due to structural complementarity between ThT and fibrils, the neutral probes with similar molecular shape as ThT are anticipated to have stronger association with the amyloid fibrils.^{215,}

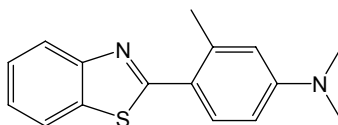
^{216, 304, 305} Thus, researchers have synthesized lipophilic analogues of ThT by removing its positive charge on quaternary heterocyclic nitrogen and attaching different substituents at various positions in ThT and analysed their affinity for fibrils. Among several such probes investigated, Klunk et. al. showed that more lipophilic 2-[4'-(methylamino)phenyl]-6-methylbenzothiazole (6-Me-BTA-1) bind to Amyloid β fibrils and has higher affinity than their parent molecule ThT under physiological conditions.²¹⁵ Further, 6-Me-BTA-1 has shown great efficiency in crossing BBB and used for the first time for in-vivo PET imaging of amyloid plaques after radio labelling.²¹⁵ Based on the success of 6-Me-BTA-1, researchers have explored different neutral derivatives of ThT and evaluated them for the detection of amyloid fibrils.^{106, 140, 216} To date ¹¹C-Pittsburgh compound (¹¹C-[PIB]) is one of the most studied radio labeled ThT derivative for the detection of amyloid plaques.^{106, 217, 218 306}

Most of the studies on neutral derivatives of ThT focussed on radiochemical imaging like PET and single photon emission computed tomography (SPECT) by tagging a radioactive nuclide. As the radiochemical imaging possess inherent difficulties like handling, disposal of radioactive chemicals and the preparation of reagent should be just prior to the diagnosis, we need a technique with ease to do the imaging like fluorescence imaging.^{101, 112, 122, 139} Klunk et al showed that BTA derivatives doesn't show any change in their emission spectrum on association with amyloid fibrils.²¹⁵ Instead, emission intensity of one of the BTA derivatives, which has been extensively utilized for PET imaging, was reduced in presence of amyloid fibrils.³⁰⁴ Hence, a neutral ThT derivative, which can show a significant increase in the emission intensity as well as a change in the spectral position on association with

amyloid fibrils, need to be developed for efficient detection of these neurotoxic protein aggregates.

Herein, we have synthesized a new neutral fluorescent analogue of ThT, 2-[2Me,4'-(dimethyl amino)phenyl]benzothiazole (2Me-DABT, see scheme 1 for chemical structure). In order to understand how this molecule behaves in the presence of amyloid fibrils, we first explored the photophysical properties of this molecule in molecular solvents and their mixtures with different environments such as polarity, viscosity etc. Finally, the changes in the spectral properties of 2MeDABT due to the interaction with insulin fibrils at physiological pH have been discussed.

Scheme 4.1 Molecular structure of 2-[2Me, 4'-(dimethylamino) phenyl] benzothiazole (2Me-DABT)



4.2. Materials and methods

All the organic solvents used in the experiments were of spectroscopic grade and obtained from either Spectrochem (India) or S.D. Fine Chemicals (Mumbai, India) and used as received. Double distilled water was used for the experiments. Solvent polarities were estimated using the dielectric constants (ϵ) and refractive indices (n) obtained from the literature. The dielectric constants and refractive indices of mixed solvents were estimated using the following relations.³⁰⁷⁻³⁰⁹

$$\epsilon_{ms} = f_A \epsilon_A + f_B \epsilon_B \quad (4.1)$$

$$n_{ms} = f_A n_A^2 + f_B n_B^2 \quad (4.2)$$

where ms represents mixed solvent, subscripts A and B represents the co-solvents of the mixture and f_A and f_B represents the respective volume fractions. The solvent polarity function, Δf , is defined as,^{135, 310-312}

$$\Delta f = \frac{\varepsilon - 1}{2\varepsilon + 1} - \frac{n^2 - 1}{2n^2 + 1} \quad (4.3)$$

Absorption spectra were recorded using JASCO UV-Visible spectrometer (Model V630, Japan). Steady-state fluorescence measurements were carried out using Hitachi spectrofluorimeter (Model F-4500, Japan). Fluorescence quantum yield (ϕ_f) measurements were estimated by comparative method using 4',6-diamidino-2-phenylindole (DAPI) in dimethyl sulphoxide as reference ($\Phi_f \sim 0.58$).³¹³ The fluorescence and absorption measurements were carried out at ambient temperature (25 ± 1 °C). For the studies in insulin fibril the samples were excited at 340 nm to avoid any interference from the protein itself. Time-resolved fluorescence measurements were carried out using IBH (Scotland, UK) spectrometer based on time-correlated single-photon-counting (TCSPC) technique. Emission transients were collected at their respective peak positions by exciting the probe in molecular solvents with 292 nm, LED. The instrument response function (IRF) of such measurements was ~ 700 ps. However, the probes in amyloid fibril were excited with 340 nm LED with IRF of ~ 1.3 ns. Fluorescence from the sample was detected at right angle to the excitation direction using a photomultiplier tube based detection module (model TBX4; IBH). All these measurements were carried out with an emission polarizer set at magic angle orientation with respect to the vertically polarized excitation pulse to

eliminate the effect of rotational reorientation of the dye on the observed fluorescence decays.¹²⁵ All decays were analysed using non-linear least square method to obtain time constants.¹²⁵

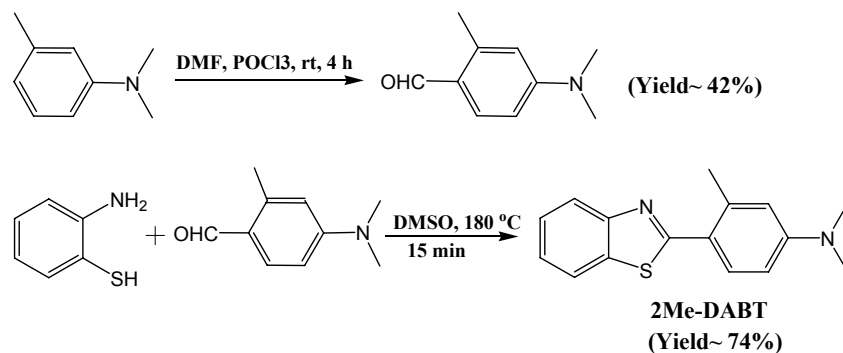
Insulin fibrils were prepared by heating 2mg/ml insulin protein solution in 20% acetic acid (pH 1.6) at 70 °C for 24 hours.^{128, 314} The formation of fibrils was confirmed by the enhanced fluorescence of ThT. The fibrils were diluted 12 times by Tris-HCl buffer (pH 7.4) and the pH was adjusted with NaOH to 7.4.

The molecular structures of 2Me-DABT and ThT were optimized by quantum chemical calculations using a Gaussian 03 package.²⁶⁹ DFT method was adopted along with the use of B3LYP functional^{267, 268} and 6-311++g(d,p) basis function to optimize the chemical structures. These optimized structures were used for the blind molecular docking. For docking studies the fibril was considered as a rigid host molecules and the ligand (2Me-DABT) as flexible ligand allowing all torsional motion in the ligand. Molecular docking was performed with five different initial location of the ligand with respect to the fibril. A cubical box with dimension of 100x100x100 Å³ with 0.6 Å grid spacing was created at the centre of the fibril. The size of the grid box was made such a way that the ligand can access all possible binding sites in the fibril. Each docking involved 200 independent runs with maximum number of 5x10⁶ energy evaluation and 27000 generations. The Lamarckian Genetic Algorithm (LGA) method has been applied to find the docked conformations of the ligand with lowest energy.²⁷⁰ Results of all 1000 runs was clustered with root mean square deviation (RMSD) <2Å and ranked according to their binding energy. For docking with ThT, the fibril with a docked 2Me-DABT was used

as the host molecules and followed similar procedure as used for docking of 2Me-DABT with fibril.

4.3. Synthesis and Characterization of 2Me-DABT

Scheme 4.2 Reaction scheme for the synthesis of 2Me-DABT.



4.3.1. Synthesis of 4-(dimethyl amino)-2 methyl benzaldehyde:

To the mixture of 1.1 ml of N,N-3-trimethylaniline (7.395 mmol) and 0.7 mL of N,N-dimethyl formamide (8.875 mmol) in 40 mL dichloromethane maintained at -10 °C; 0.78 mL (8.135 mmol) phosphorous oxychloride was added drop wise under argon gas atmosphere. The reaction mixture was allowed to stir for four hours at room temperature. The reaction mixture was then treated with aqueous solution of 2M sodium hydroxide and stirred for four hours. It was extracted with ethyl acetate. The organic layer was concentrated under vacuum by removing excess solvent and dried over magnesium sulfate. The resulting residue was purified by chromatography to obtain desired aldehyde. (0.5 g, 41.6%) ^1H NMR (200 MHz, CDCl_3): δ = 2.36 (s, 3H), 2.9 (s, 6H), 6.80-6.84 (d, 2H, J = 8 Hz), 7.63-7.67 (d, 1H, J = 8 Hz), 10.14 (s, 1H) ppm.

4.3.2 Synthesis of 2Me-DABT

To the stirring solution of 4-(dimethyl amino)-2 methyl benzaldehyde (3.063 mmol) in 25 mL of dimethyl sulfoxide, 0.49 g of 2-aminothiophenol (3.982 mmol) was added and the reaction mixture was allowed to heat at 180 °C for 15 minute. The solution was then cooled to room temperature and poured into water. The organic layer was extracted with ethyl acetate. Removal of the solvent under reduced pressure gave the yellow crude solid that was purified by column chromatography. (0.61 g, 74%) ¹H NMR (200 MHz, CDCl₃): d = 2.39 (*s*, 3H), 2.73 (*s*, 6H), 7.02-7.10 (*m*, 2H, *J* = 16 Hz), 7.29-7.33 (*m*, 1H, *J* = 8 Hz), 7.36-7.48 (*m*, 1H, *J* = 24 Hz), 7.85-7.89 (*d*, 1H, *J* = 8 Hz), 8.01-8.05 (*d*, 1H, *J* = 8 Hz), 8.22-8.26 (*d*, 1H, *J* = 8 Hz) ppm.

4.4. Results and discussion

4.4.1. Photophysical studies of 2Me-DABT

4.4.1.1. Ground state absorption studies

The absorption and emission spectra of 2Me-DABT have been measured in different solvents and solvent mixtures of different polarity. Table 4.1 lists all photophysical parameters of 2Me-DABT in different solvents along with their solvent polarity function, Δf . Figure 4.1 shows the absorption spectra of 2Me-DABT in 3-methylpentane (3MP) and water (2%Methanol). The absorption maximum of 2Me-DABT is 293 nm in 3MP and 302 nm in water(2%Methanol). The present result indicates that the absorption spectra of 2Me-DABT is sensitive to the solvent polarity and shows bathochromic shift with the increase in the solvent polarity. This implies that ground state of 2Me-DABT has been stabilized with increase in surrounding

Table 4.1 Photophysical parameters of 2Me-DABT dye as estimated in different solvents and solvent mixtures. Subscripts indicate their corresponding percentage volume fractions.

solvent	Δf	$\lambda_{\text{abs}}/\text{nm}$	$\lambda_{\text{em}}/\text{nm}$	$\bar{\Delta\nu}/\text{cm}^{-1}$	ϕ	τ_f/ns	$k_r/10^8\text{s}^{-1}$	$k_{nr}/10^9\text{s}^{-1}$
Aprotic solvents								
MP	0.000	292.5	424.0	10603	0.10	1.59	0.63	0.57
MP ₉₈ EA ₂	0.011	293.5	427.0	10652	0.11	1.72	0.65	0.52
MP ₉₅ EA ₅	0.025	296.0	428.0	10419	0.12	2.02	0.61	0.44
MP ₉₀ EA ₁₀	0.046	297.0	431.0	10468	0.13	2.39	0.54	0.36
MP ₈₀ EA ₂₀	0.081	298.0	436.0	10621	0.16	2.86	0.57	0.29
MP ₆₀ EA ₄₀	0.128	298.0	438.0	10741	0.19	3.34	0.58	0.24
MP ₅₀ EA ₅₀	0.146	298.0	440.0	10834	0.23	3.58	0.64	0.22
MP ₄₀ EA ₆₀	0.160	298.5	443.5	10953	0.24	3.88	0.58	0.20
MP ₂₀ EA ₈₀	0.183	299.5	445.0	10917	0.26	4.18	0.62	0.18
EA	0.200	299.5	447.0	11012	0.28	4.26	0.65	0.17
EA ₉₈ ACN ₂	0.210	299.5	448.0	11052	0.32	4.29	0.75	0.16
EA ₉₅ ACN ₅	0.223	299.5	449.0	11127	0.29	4.32	0.66	0.17
EA ₉₀ ACN ₁₀	0.238	299.5	451.0	11250	0.28	4.35	0.64	0.17
EA ₈₀ ACN ₂₀	0.258	299.5	452.0	11260	0.28	4.38	0.62	0.17
EA ₆₀ ACN ₄₀	0.280	299.5	462.0	11744	0.27	4.45	0.60	0.17
EA ₄₀ ACN ₆₀	0.291	299.5	464.0	11837	0.26	4.51	0.57	0.17
EA ₂₀ ACN ₈₀	0.299	299.5	465.0	11911	0.24	4.51	0.52	0.17
ACN	0.305	299.5	469.0	12048	0.25	4.52	0.50	0.17
Protic solvents								
Decanol	0.205	300.0	461.2	11650	0.32	4.96	0.64	0.14
D ₉₅ M ₅	0.218	300.0	462.2	11697	0.31	4.80	0.65	0.14
D ₉₀ M ₁₀	0.228	300.0	464.1	11786	0.32	4.82	0.66	0.14
D ₈₀ M ₂₀	0.244	300.0	466.2	11883	0.29	4.70	0.63	0.15
D ₅₀ M ₅₀	0.275	300.0	473.0	12191	0.23	4.56	0.58	0.17
D ₃₀ M ₇₀	0.290	300.0	476.0	12324	0.21	4.29	0.55	0.18
Methanol	0.309	300.0	485.0	12714	0.18	4.17	0.44	0.20
M ₉₀ W ₁₀	0.311	300.0	487.0	12799	0.18	4.23	0.42	0.20
M ₈₀ W ₂₀	0.313	300.0	488.0	12841	0.17	4.26	0.40	0.20
M ₇₀ W ₃₀	0.315	300.0	488.2	12849	0.16	4.12	0.39	0.20
M ₆₀ W ₄₀	0.316	300.4	489.0	12839	0.15	4.05	0.37	0.21
M ₅₀ W ₅₀	0.317	300.6	490.0	12858	0.14	4.03	0.34	0.21
M ₄₀ W ₆₀	0.318	301.0	491.0	12856	0.13	3.85	0.38	0.22
M ₃₀ W ₇₀	0.319	301.2	496.0	13039	0.11	3.71	0.35	0.24
M ₂₀ W ₈₀	0.319	301.4	498.0	13098	0.09	3.54	0.31	0.254
M ₁₀ W ₉₀	0.320	301.6	500.0	13156	0.07	3.39	0.26	0.27

Abbreviation- MP - 3-methylpentane; EA - ethylacetate; ACN - acetonitrile; D - Decanol; M - methanol; W - water

solvent polarity. This suggests that the ground state of 2Me-DABT is polar in nature. The polarity of such neutral derivatives has been reported earlier in the literature which has been attributed to partial intramolecular charge transfer character in its ground state.^{136-138, 200, 241} The ground state structure has been optimized by using quantum chemical calculations and the dipole moment has been estimated to be 5.45 D which supports the bathochromic shift in the absorption spectra with polarity.

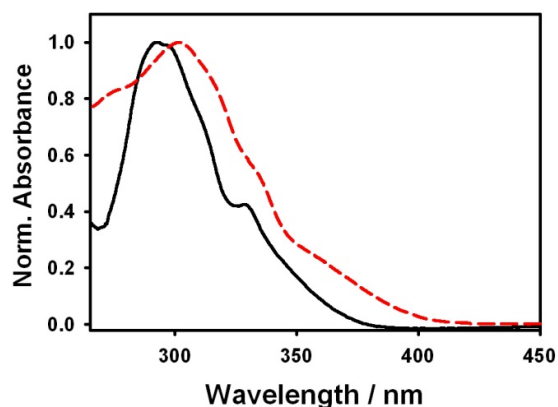


Figure 4.1 Ground state absorption spectra of 2Me-DABT in 3MP (solid) and water (dashed).

4.4.1.2. Steady state fluorescence measurements

Emission spectra of 2Me-DABT have been recorded in different solvents and solvents mixtures and different emission characteristics are presented in table 4.1. The intensity normalized emission spectra of 2Me-DABT with varying polarity are plotted in figure 4.2. It is evident from figure 4.2 that unlike ThT, 2Me-DABT shows a strong solvatochromism. The emission maxima of 2Me-DABT thus changes from 424 nm in MP to 500 nm in water. This result suggests that there is a large change in the dipole moment of 2Me-DABT upon photoexcitation. 2Me-DABT shows very large Stokes' shift of $\sim 3585 \text{ cm}^{-1}$ in the emission spectra in changing the solvent from non-polar MP

to polar water. The solvatochromism observed for 2Me-DABT is quite large as compared to most commonly used solvatochromic dyes, coumarins.^{308,315} Thus, it can be inferred that 2Me-DABT can be a potential candidate to probe the micropolarity of different complex chemical and biological environments. Further, large Stokes' shift shown by 2Me-DABT in all solvents studied indicates very low or no overlap of excitation and emission spectrum. Such property of a fluorescent probe has advantages in fluorescence imaging studies. Common molecular probe used for fluorescence imaging of biomolecules such as Alexafluor 488, fluorescein isothiocyanate (FITC), etc. has very low value of Stokes' shift and suffers from large excitation background during imaging studies. But the imaging agents with large Stokes' shift reduces the excitation background to a significant extent and increases their detection limits significantly. Thus, large Stokes' shift of 2Me-DABT can be useful for sensitive fluorescence imaging of biological samples.

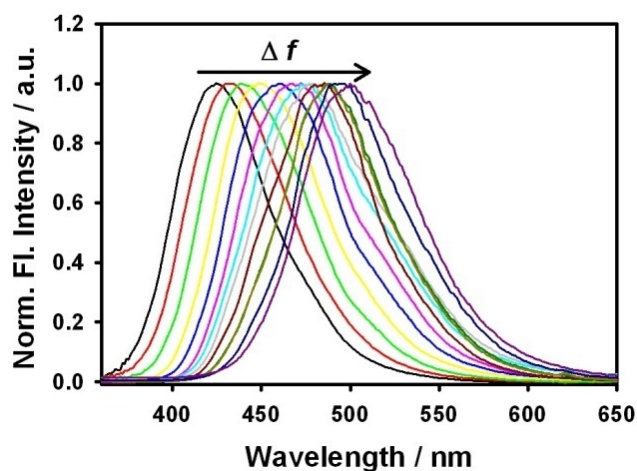


Figure 4.2 Normalized emission spectra of 2Me-DABT in solvents with different polarity.

For molecules where absorption and fluorescence spectra are due to transitions

between same ground and excited electronic states, Stokes' shift is expected to vary linearly with Δf following the Lippert–Mataga equation.¹³⁵

$$\Delta\bar{\nu} = \Delta\bar{\nu}_0 + \frac{2\Delta\mu^2}{hcr^3} \Delta f \quad (4.4)$$

where $\Delta\mu$ is the difference between the ground state and the excited state dipole moments of the molecule, h is the Planck's constant, c is the light velocity and r is the Onsager radius of interaction. The slope of linear plot of Stokes' shift with Δf gives the $\Delta\mu$ values for the molecules.¹³⁵ The variation of Stokes' shift with solvent polarity function Δf is plotted in figure 4.3. From the figure, it has been observed that Stokes' shift varies linearly with Δf in aprotic solvents. This behavior indicates that the nature of ground and excited states remain same in the case of aprotic solvents. From Lippert-Mataga relation,¹³⁵ the difference in the dipole moments of ground and excited state of 2Me-DABT in aprotic solvents is estimated to be 5.39 D. From the quantum chemical calculations, the ground state dipole moment of 2Me-DABT is estimated to be 5.45 D. Thus, the excited state dipole moment of 2Me-DABT in aprotic solvents is 10.84 D. Thus, the large dipole moment in the excited state is indicative of the charge separation in the excited state of 2Me-DABT. From the molecular structure of 2Me-DABT, it is clear that an electron accepting benzothiazole group is connected to an electron donating dimethylanilino group. As both electron donating and electron accepting groups are present in the same molecule, there is a high probability of partial charge transfer and may result in the formation of intramolecular charge transfer (ICT) state which leads to the increase in the dipole moment in the excited state of 2Me-DABT.

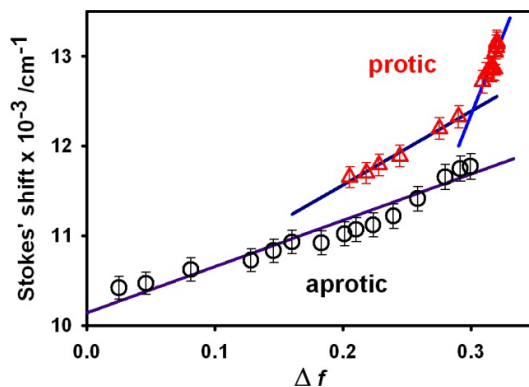


Figure 4.3 Variation of Stokes' shift of 2Me-DABT with Δf in aprotic (O) and protic (∇) solvents. Solid lines represent the fitting of the experimental data with Lippert-Mataga equation (cf. equation 4.4).

However, the Stokes' shift of 2Me-DABT in protic solvents varies linearly with Δf parameter, there are two distinct regions. In the low polar region (< 0.31), Stokes' shift varies relatively slowly with Δf as compared to the highly polar ($\Delta f > 0.31$) protic solvents. A noteworthy observation is that the slope of Lippert-Mataga plot for protic solvents, irrespective of the solvent polarity, is always higher than the aprotic solvents. This indicates that the nature of electronic states involved is different in these two classes of solvents. The fitting of the experimental data with equation 4.4 results in $\Delta\mu$ values of 6.64 D and 13.65 D for protic solvents with $\Delta f \leq 0.31$ and $\Delta f > 0.31$, respectively. Thus, the estimated dipole moments for the excited state of 2Me-DABT are 12.09 D and 19.1 D in low polar ($\Delta f \leq 0.31$) and high polar ($\Delta f > 0.31$) protic solvents, respectively. Such significant difference in the dipole moments in protic and aprotic solvents suggests that there is involvement of hydrogen bonding between 2Me-DABT and solvents which leads to the increase in the dipole moment in protic solvents. Such unusual behaviour in protic solvents with high hydrogen bond

donating abilities (α) have been reported for several fluorophores, like coumarin, etc.³¹⁶⁻³¹⁹ Due to high α value (1.17), electronic states of solute substantially stabilized in water than other protic solvents, like alcohols ($\alpha=0.78 - 0.98$).^{318, 319} Further, among alcohols, methanol has highest H-bond donating ability ($\alpha=0.98$).^{318, 319} It is to be noted that the steeper slope in the variation in Stokes' shift with Δf arises in MeOH-water mixture. To confirm the role H-bonding with solvent, we have plotted the Stokes's shift with Kamlet-Taft ' α ' parameter of the protic solvents and the results are shown in figure 4.4. The α values for the mixed solvents are calculated using following equation.

$$\alpha_{ms} = \sum f_i \alpha_i \quad (4.5)$$

where α_{ms} is α for the mixed solvent, α_i is the α value for i^{th} component and f_i is the volume fraction of i^{th} component.

It is quite evident from figure 4.4 that the Stokes' shift of 2Me-DABT varies linearly with α value in protic solvents. This result further confirms that the unusual trend in Stokes' shift with Δf values shown in figure 4.3 is due to the solute-solvent hydrogen bonding. The presence of solute-solvent H-bonding will be further supported by the isotopic effect (*vide infra*). Thus, the increase in the excited state dipole moment of 2Me-DABT in protic solvents is due to the formation of solute-solvent H-bonding. Further, increase in the dipole moment in protic solvents also indicates that H-bonding occurs at electron acceptor center i.e., benzothiazolic nitrogen. Due to H-bonding, there might be more charge transfer takes place which leads to large increase in the dipole moment of the excited state.

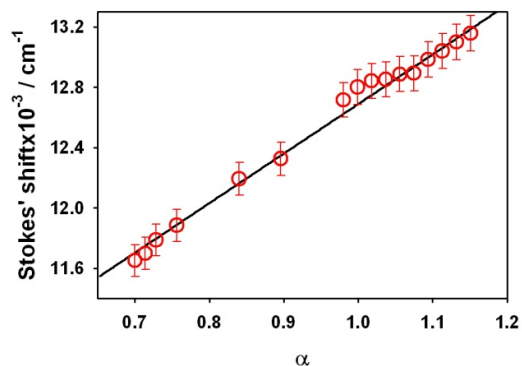


Figure 4.4 Variation in Stokes' shift of 2Me-DABT with α value in protic solvents.

In order to get detailed information on the excited state processes, fluorescence quantum yield (ϕ) of 2Me-DABT have been measured in different solvents and listed in table 4.1. Figure 4.5 shows the variation of emission quantum yield with Δf of solvents. From the figure it is clear that in case of aprotic solvents, the ϕ increases with increase in the polarity up to $\Delta f \sim 0.2$. Further increase in the polarity doesn't cause any change in its emission yield.

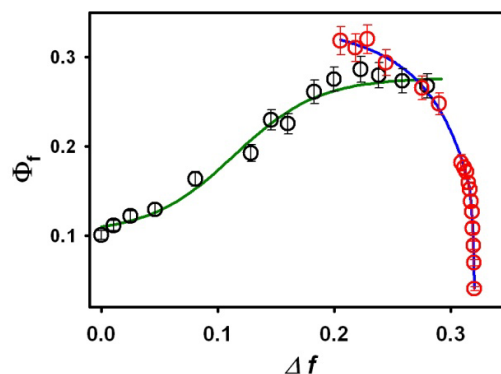


Figure 4.5 Variation in the emission yield of 2Me-DABT with Δf in aprotic (\circ) and protic (∇) solvents.

However, in protic solvents, the quantum yield shows contrasting behavior as compared to aprotic solvents. The emission quantum yield decreases slowly in low

polar solvents ($\Delta f \leq 0.31$) and decreases sharply in high polar solvents ($\Delta f > 0.31$). To be mentioned, similar behavior is observed for Stokes' shift (*cf.* figure 4.4). These results suggest that solute-solvent hydrogen bonding is involved in excited state process which leads to decrease in the emission yield in highly polar protic solvents.

As the charged analogue of 2Me-DABT, ThT is well known viscosity probe. The fluorescence properties of ThT are largely dependent on the surrounding viscosity, we have studied the emission properties of 2Me-DABT as a function of viscosity. Surprisingly, the fluorescence properties are insensitive to the frictional force offered by the solvent. This indicates there is no internal dynamics such as twisting are taking place in the excited state of 2Me-DABT.

4.4.1.3. Time-resolved studies

To substantiate the variation in quantum yield of 2Me-DABT in different solvents, we have carried out time-resolved fluorescence measurements using TCSPC technique. The results have been shown in figure 4.6. All fluorescence decays follow the mono-exponential decay kinetics. The lifetimes thus measured are tabulated in table 4.1. The variations in the lifetime with Δf for both protic and aprotic solvents are shown in figure 4.7. From the figure it is evident that the lifetime in aprotic solvents increases with increase in polarity and remain constant in high polar aprotic solvents. In contrast to aprotic solvents, the lifetime in protic solvents decreases slowly with solvent polarity for solvents with $\Delta f \leq 0.31$. However, the lifetime changes much faster with polarity for highly polar ($\Delta f > 0.31$) protic solvents. This result also clearly tells that H-bonding between solute and solvent leads to the decrease in the fluorescence lifetime of 2Me-DABT. This is in agreement with the steady state results.

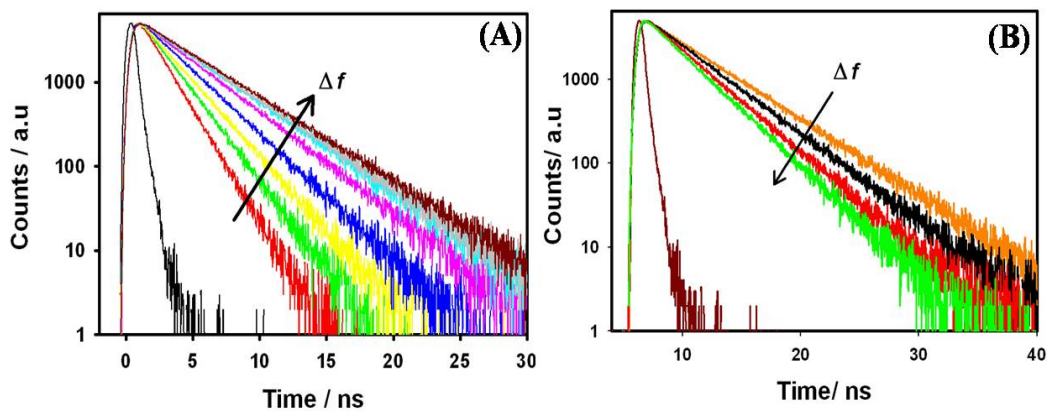


Figure 4.6 Transient fluorescence decays of 2Me-DABT in (A) aprotic and (B) protic solvents.

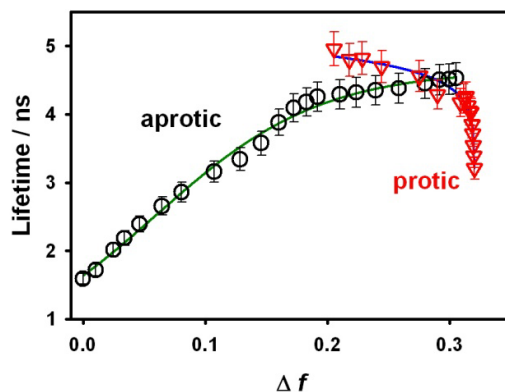


Figure 4.7 The variation of the fluorescence lifetime of 2Me-DABT with Δf for aprotic (○) and protic (▽) solvents.

Since the ϕ_f and τ_f values arise due to the combined effect of the radiative (k_r) and non-radiative (k_{nr}) decay processes in the S_1 state, for a better understanding on the excited state processes, it is very important to understand the effect of solvent polarity on k_r and k_{nr} . The k_r and k_{nr} values for the dye in different solvents have been calculated using following equations and presented in table 4.1.^{308, 309}

$$k_r = \frac{\phi_f}{\tau_f} \quad (4.6)$$

$$k_{nr} = \frac{1 - \phi_f}{\tau_f} \quad (4.7)$$

Figure 4.8 shows the plot of radiative (k_r) and non-radiative (k_{nr}) decay rate constants with Δf for all solvents used. It is seen from the figure that in case of aprotic solvents, radiative decay rate remains almost invariable with solvent polarity while the non-radiative decay rate decreases with polarity. Such decrease in the non-radiative rate results in the increase in the emission quantum yield with polarity in aprotic solvents. As radiative process is directly related to the transition probability between the two electronic states involved in the emission process, the k_f value is not expected to be affected that significantly by the solvent polarity if the nature of the two electronic states of the dye remains unchanged in different solvents.

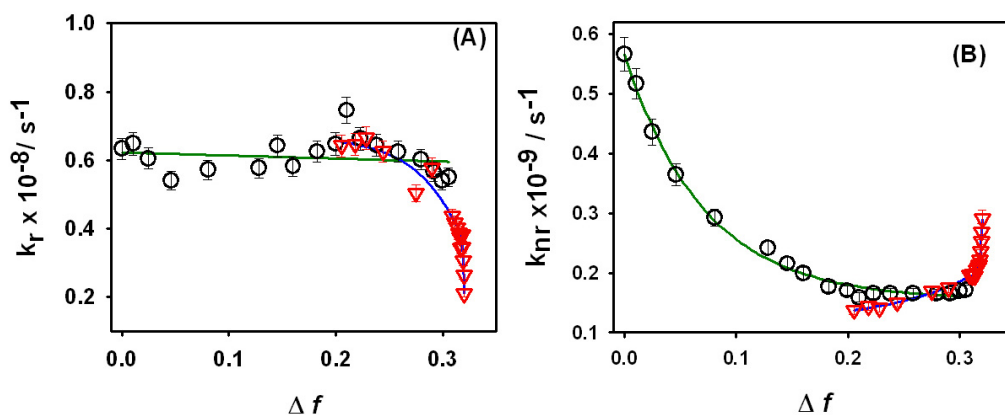


Figure 4.8 Variation of (A) k_r and (B) k_{nr} with Δf in aprotic (○) and protic (▽) solvents.

However, in protic solvents, there is slight decrease in the radiative rate with concomitant increase in the non-radiative decay rate. It is also evident from figure 4.8

that variation in k_r and k_{nr} with Δf is more steeper in case of highly polar ($\Delta f > 0.31$) protic solvents suggesting that intermolecular hydrogen bond assisted additional non-radiative process is involved in protic solvents. It is well established that due to solute-solvent H-bonding, a large number of solvent states are available for the solute to transfer its excited state energy to the solvent molecules. Thus, a faster non-radiative process is observed for the excited state molecules in strong H-bond donating solvents.^{316, 317, 320} Thus, the observed changes in the photophysical properties of 2Me-DABT in protic solvents can be attributed to the intermolecular hydrogen bonding with solvent molecules.

4.4.1.4 Isotope effect

To confirm the involvement of intermolecular hydrogen bonding, isotope effect on the photophysical properties has been investigated. The emission spectra of 2Me-DABT in D₂O and H₂O have been measured and shown in figure 4.9. Thus, the emission spectrum of 2Me-DABT in D₂O is relatively blue shifted as compared to H₂O. The emission maxima of 2Me-DABT are 498 nm and 500 nm in D₂O and H₂O, respectively. Such difference in emission spectra in D₂O and H₂O clearly indicates the role of solute-solvent hydrogen bonding on the photophysics of 2Me-DABT.

To see the deuterium effect on the lifetime of 2Me-DABT, we performed the time resolved fluorescence measurements in MeOH-D₂O mixed solvents and the results are compared with MeOH-H₂O solvent mixtures. Figure 4.10A represents the fluorescence intensity decays of 2Me-DABT in D₂O and H₂O. It is clear from the

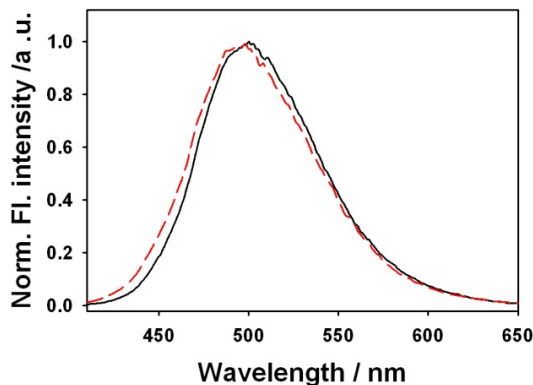


Figure 4.9 Normalized emission spectra of 2Me-DABT in H₂O (solid) and D₂O (dashed).

figure that the transient decay is relatively slower in D₂O compared to H₂O. The variation in the fluorescence lifetimes with Δf for MeOH-D₂O and MeOH-H₂O mixed solvents are presented in figure 4.10B. Thus, the emission lifetime of 2Me-DABT is always relatively longer in MeOH-D₂O than in MeOH-H₂O solvent mixtures. Thus, the intermolecular hydrogen bonding assisted non radiative decay process has been relatively restricted in D₂O.³²¹⁻³²³ This result confirms the role of solute-solvent H-

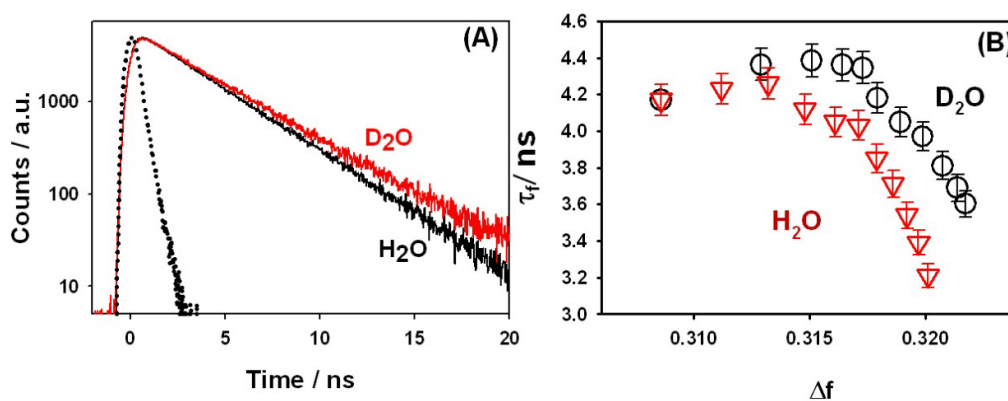
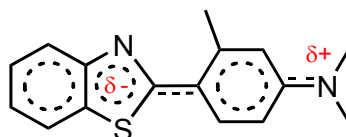


Figure 4.10 (A) Transient fluorescence decays of 2Me-DABT in H₂O (black) and D₂O (red). The dotted curve represents IRF. (B) The variation in fluorescence lifetime of 2Me-DABT in MeOH-D₂O (O) and MeOH-H₂O (∇) solvent mixtures.

bonding on the photophysical properties of 2Me-DABT.

Thus, the presence of electron accepting benzothiazole and electron donating dimethyl aniline in the 2Me-DABT facilitates partial charge transfer between them and leads to the formation of polar intramolecular charge transfer state. The increase in the quantum yield with polarity in aprotic solvents indicates that ICT state is emissive. Due to the formation of ICT, the nitrogen in the benzothiazole becomes electron rich (*cf.* scheme 4.3). This makes it favorable for the hydrogen bonding with protic solvents. Due to the H-bonding there will be a decrease in the electron density on the benzothiazole moiety which favors the charge transfer process. This is in consistency with increased dipole moment of 2Me-DABT in protic solvents. Such effect of solute-solvent H-bonding on the non-radiative process is well reported for different classes of molecules.^{309, 310, 316, 317, 320, 324}

Scheme 4.3 The plausible intramolecular charge transfer (ICT) state of 2Me-DABT



4.4.2. Interaction with Insulin fibrils

4.4.2.1. Steady state fluorescence measurements

As mentioned earlier, due to structural similarity with gold standard amyloid stain, ThT, 2Me-DABT is expected to have strong affinity towards the amyloid fibrils. Hence, we have investigated photophysical properties of 2Me-DABT in insulin amyloid fibrils. It is seen that insulin fibrils does not have any observable effect on the absorption spectra of 2Me-DABT. However, the emission spectral properties of 2Me-

DABT in aqueous solution changes significantly due to the addition of amyloid fibrils. The emission spectra of 2MeDABT have been recorded in aqueous solution in presence of different concentrations of insulin fibrils and the results are shown in figure 4.11A. Aqueous solution of 2Me-DABT shows broad emission spectra with a maximum of ~500 nm. It is clear from the figure 4.11 that the addition of insulin fibrils led to a significant enhancement of ~65 fold in the emission intensity (at 445 nm) along with large hypsochromic shift in the emission spectrum. Figure 4.11B depicts the peak normalized emission spectra of 2Me-DABT in fibril solution. It is evident from the figure that the fluorescence maxima changes from 500 nm in water to 445 nm in amyloid fibrils. Such a large enhancement in the emission intensity along with a large blue shift indicates that 2Me-DABT interacts strongly with amyloid fibrils. Thus, large increase in the fluorescence intensity upon binding with insulin fibrils indicates that 2Me-DABT can be used as a potential amyloid probe. Considering the emission maxima of 2Me-DABT in fibrils (445 nm), it can be inferred that the micropolarity at the site of binding in amyloid fibrils is significantly low as compared to the bulk water. As shown earlier the emission quantum yields in protic solvents increase with the decrease in the polarity and with the decrease in the extent of H-bond formation with solvents. Thus, the observed increase in the emission intensity of 2Me-DABT in fibril is due to both, decrease in the micropolarity as well as due to the decrease in the extent of H-bond formation with solvent owing to lack of availability of water at the site of binding. Thus, from present studies, we can infer that 2Me-DABT is located in hydrophobic pocket in the fibrillar structure. Moreover, such a large shift in the emission spectra due to the presence of amyloid fibrils can

make 2Me-DABT a better ratiometric probe for amyloid fibrils. A noteworthy observation is that the emission spectrum of ThT is largely unchanged in the presence

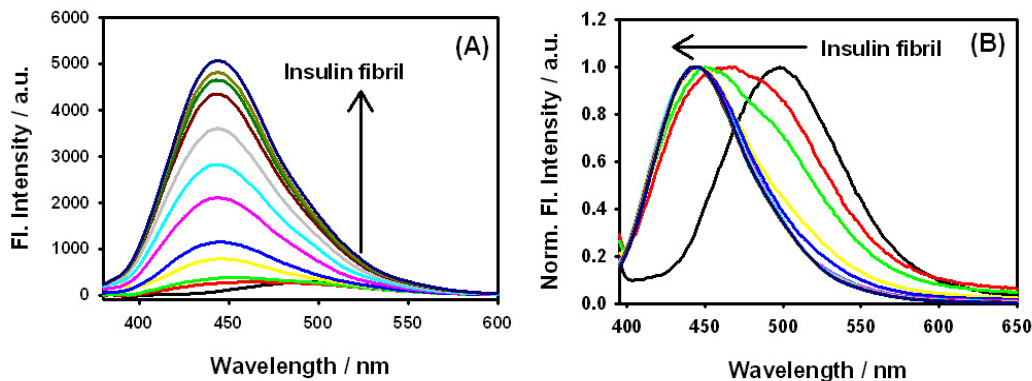


Figure 4.11 (A) The emission spectra ($\lambda_{\text{ex}}=340$ nm) of 2Me-DABT in the presence of different concentrations of insulin fibrils (0-30 μM). (B) Peak intensity normalized emission spectra of 2Me-DABT in amyloid fibrils.

of amyloid fibrils.^{128, 325} Therefore, ThT can act only as single intensity based sensor. Such single intensity based sensors are prone to give false positive signals due to different fluctuations such as probe concentration, intensity of excitation source etc, during the measurement.¹³² Nonetheless, fluorescence intensity ratio at two different wavelengths of emission spectrum of the probe is less prone to such errors during the measurement. The ratiometric measurements are especially helpful in the fluorescence imaging studies of live cells, for which the concentration of the probe, environment of probes as well as optical path length changes during the time of the measurement. It is worth mentioning that, UV excitation (340 nm), used for the excitation of 2Me-DABT, can cause auto fluorescence from the cells and can interfere with the fluorescence measurements.²⁸² But it should be noted that the emission yield of 2Me-DABT in the presence of amyloid fibrils is very high, ~68%. Therefore, the emission

intensity generated by the 2Me-DABT will be significantly higher than the cellular auto fluorescence. Hence, the interference from cell auto fluorescence will be negligible during the course of imaging fibrils with 2Me-DABT.

The quantification of binding is necessary to assess the efficacy of 2Me-DABT as amyloid probes. The binding constant for the association of fibrils with 2Me-DABT is estimated using Benesi-Hildebrand equation assuming 1:1 complexation.^{278, 326}

$$\frac{1}{\Delta I_f} = \frac{1}{K_b(I_c - I_o)} \frac{1}{[Insulin]} + \frac{1}{(I_c - I_o)} \quad (4.8)$$

where ΔI_f is the change in fluorescence intensity on addition of fibrils. K_b is the binding constant. I_o and I_c are the fluorescence intensity of the dye when it is completely free and completely bound with amyloid fibrils, respectively. The double reciprocal plot for the variation in the fluorescence intensity with the insulin fibril concentration has been plotted and presented in figure 4.12. From the figure, it can be seen that there is nonlinearity in double reciprocal plot which indicates that there are two modes of binding for 2Me-DABT with amyloid fibrils. The experimental data were fitted in two regions of fibril concentration as shown in figure 4.12. The binding constants thus estimated are $1.0 \times 10^6 \text{ M}^{-1}$ and $4.1 \times 10^4 \text{ M}^{-1}$. Previously, it has been reported that there are two modes of binding for ThT in insulin fibrils.^{186, 214, 327} Strong binding corresponds to the binding in the inner grooves of the fibril and the weaker binding is due to its association on fibrillar surface.^{186, 214, 327} Due to structural similarity between ThT and 2Me-DABT, we propose similar type of binding do exists for 2Me-DABT also. Stronger binding mode corresponds to the inner core of amyloid fibrils and weaker mode is due to binding on the fibrillar surface. As 2Me-DABT is

small, neutral and have a higher affinity towards the fibrils, it could be a potential drug for *in-vivo* detection of amyloid fibrils.

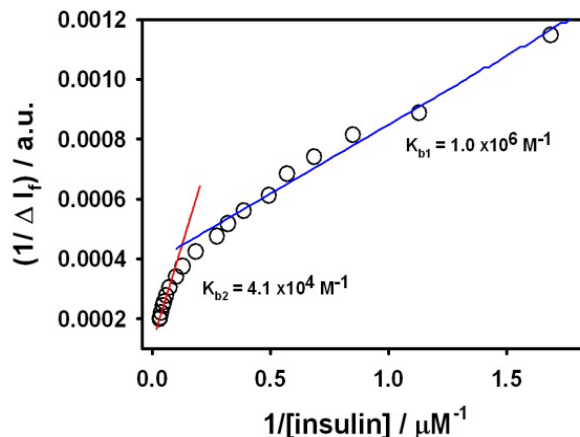


Figure 4.12 Double reciprocal Benesi-Hildebrand plot for the variation in emission intensity of 2Me-DABT with the concentration of insulin amyloid fibrils. Straight lines are fitted data following equation 4.8.

4.4.2.2. Time-resolved measurements

To get a better insight on the effect of fibril on the excited state processes, we have recorded emission transients of 2Me-DABT in presence of different concentrations of insulin fibrils and presented in figure 4.13A. It is evident from the figure that the transient decays become slower due to the addition of fibrils. All transient decay traces have been fitted with bi-exponential decay function and the fitted parameters are shown in table 4.2. The variation in the average lifetime of 2Me-DABT with fibril concentrations are displayed in figure 4.13B. The average lifetime (τ_{avg}) changes from 2.9 ns in water to 4.2 ns in the presence of 25 μM insulin fibril. Such changes in the lifetime also suggest that there is very strong interaction between 2Me-DABT with amyloid fibrils. The observed changes in the excited state lifetime

can be attributed to the changes in the environment around the probe at the binding location. Correlation with the lifetime data of 2Me-DABT in protic solvents suggests that the decrease in polarity along with decrease in the probability of formation of H-bonding at the binding site might results in the increase in excited state lifetime of the probe. Time-resolved data is in agreement with the results obtained from the steady state measurements. Thus, 2Me-DABT is located in hydrophobic environment where the probability of H-bond formation with solvent water molecules is less.

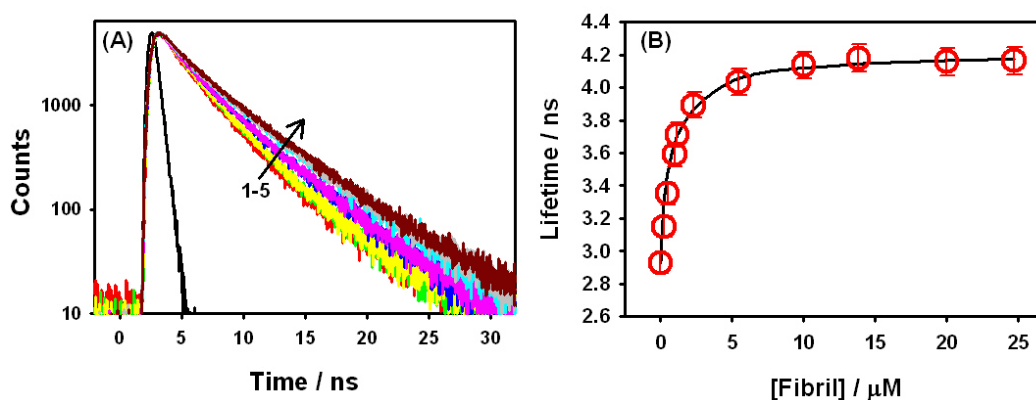


Figure 4.13 (A) The fluorescence transient decays for 2Me-DABT in the presence of different concentrations of insulin fibrils (1) 0, (2) 0.30, (3) 1.17, (4) 4.44 and (5) 15.56 μM . The black curve represents the IRF of the TCSPC instrument. (B) Variation in the average lifetime of 2Me-DABT with insulin fibril concentration.

Table 4.2 Fitting parameters for the emission decay traces of 2Me-DABT in presence of different concentrations of fibril.

[fibril] / μM	a_1	τ_1 / ns	a_2	τ_2 / ns	τ_{avg} / ns
0.00	0.20	0.98	0.80	3.48	2.96
0.25	0.19	1.06	0.80	3.67	3.16
0.51	0.18	1.22	0.81	3.82	3.33
0.95	0.22	1.26	0.77	4.28	3.61
1.18	0.23	1.18	0.77	4.47	3.72
2.31	0.19	1.20	0.81	4.52	3.88
5.45	0.19	1.23	0.80	4.58	3.92

10.00	0.18	1.21	0.82	4.63	4.01
13.84	0.17	1.20	0.82	4.71	4.09
20.00	0.19	1.23	0.81	4.83	4.12
24.71	0.19	1.41	0.81	4.96	4.29

4.4.2.3 Fluorescence microscopic studies

A fluorescence microscope has also been used for in-vitro imaging of amyloid fibrils stained with 2Me-DABT and compared with native protein. The fluorescence images are presented in figure 4.14. It is evident from the figure that 2Me-DABT stained fibrils shows bright blue images and could be detected under fluorescence microscope while there is no such fluorescence has been observed for native protein.

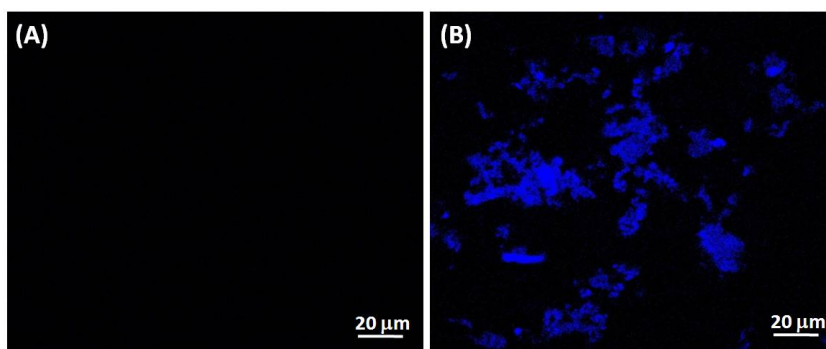


Figure 4.14 Fluorescence microscopic images of 2Me-DABT with (A) native insulin and (B) fibrils.

4.4.2.4 Energy transfer studies

As the molecular structure of 2Me-DABT and ThT are similar, it would be interesting to know whether both dyes are having same or independent binding sites in the fibril. For this purpose, we have studied the emission properties of 2Me-DABT in the presence of fibrils with addition of different concentrations of ThT and the results are shown in figure 4.15A. There is a significant decrease in the emission intensity of

amyloid bound 2Me-DABT at 445 nm along with concomitant increase emission at 490 nm due to addition of ThT. The emission spectrum of only ThT in fibrillar solution is also presented for comparison. It is clear from figure 4.15A that the emission intensity of ThT bound to amyloid fibrils in the absence of 2Me-DABT is quite low when excited with 340 nm light. However, the fluorescence intensity at 490 nm is significantly enhanced (~9 fold) in presence of 2Me-DABT in the fibrillar solution. The variation in the fluorescence intensities at the 445 nm and 490 nm with the concentration of ThT has also been shown in figure 4.15B. It is apparent from the figure that there is large increase in fluorescence intensity of ThT at the expense of the fluorescence of 2Me-DABT. This clearly indicates that there is energy transfer takes place from 2Me-DABT to ThT in the presence of amyloid fibrils.

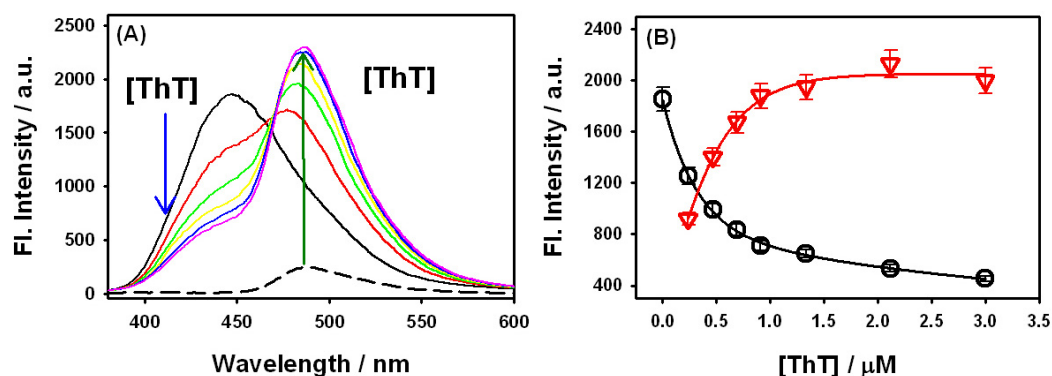


Figure 4.15 (A) The emission spectra ($\lambda_{\text{ex}}=340$ nm) of 2Me-DABT in fibrillar solution in the presence of different concentrations of ThT (0-3 μ M). The dashed curve shows the emission spectrum ($\lambda_{\text{ex}}=340$ nm) of 3 μ M ThT in the fibrillar solution. (B) Variation in the emission intensity at (O) 445 nm and (∇) 490 nm with the ThT concentration in the fibrillar solution.

Energy transfer between photoexcited 2Me-DABT and ThT is also supported from the absorption and emission spectra of both dyes in fibrillar solution (cf. figure 4.16). From the figure it is clear that there is substantial overlap in the emission spectra of 2Me-DABT and the absorption spectrum of ThT in fibrillar medium. Such a large overlap facilitates the observed energy transfer between 2Me-DABT and ThT in amyloid fibrils.

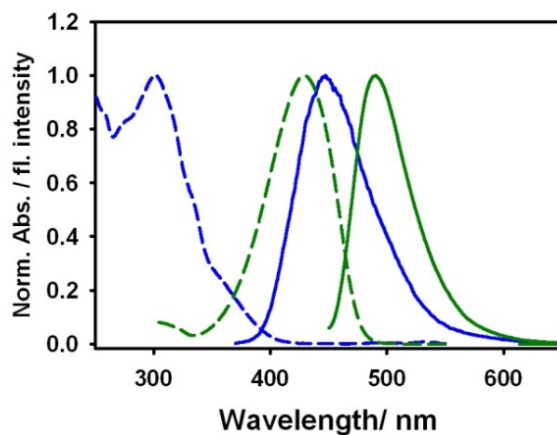


Figure 4.16 Normalized absorption (dashed curves) and emission spectra (solid curves) of 2Me-DABT (blue) and ThT (green) in insulin fibrils.

The observed energy transfer also indicated that there is no replacement of 2Me-DABT by ThT in amyloid fibrils. Rather, ThT occupies some other binding site available in fibrils. It is worth mentioning that fibrils formed from bigger proteins such as insulin can offer different binding locations depending on the property of the molecule. Besides that, our studies showed that both dyes are close enough for efficient Forster resonance energy transfer (FRET) to take place. This is also supported by molecular docking studies which will be described in the next sections of this chapter.

The energy transfer from 2Me-DABT to ThT in fibrillar solution is also studied through time-resolved fluorescence measurements. Emission transients for 2Me-DABT in amyloid fibrils in the presence and absence of ThT are shown in figure 4.17. It is evident from the figure that the emission decays of 2Me-DABT become faster due to the addition of ThT. Further, it is important to mention that no emission is observed at 445 nm for ThT in the presence of fibrils due to its excitation with 340 nm light. Thus, the emission decays observed at 445 nm is contributed only from photo excited 2Me-DABT. The presence of ThT creates an additional decay channel for the excited state of 2Me-DABT through energy transfer. The average lifetime of 2Me-DABT decreases from 4.3 ns to 1.7 ns due to presence of 3 μ M ThT. The efficiency for the FRET (E) has been calculated from the following equation and it is found to be 60.5 %.¹²⁵

$$E = 1 - \frac{\langle \tau_{DA} \rangle}{\langle \tau_D \rangle} \quad (4.9)$$

$\langle \tau_{DA} \rangle$ and $\langle \tau_D \rangle$ represents the average fluorescence lifetimes of 2Me-DABT in the presence and absence of ThT, respectively. From the Forster theory of resonance energy transfer, the Forster distance has been calculated as 45.5 Å (*cf* eqn. 3.9) using κ^2 as 0.67 for random orientation of donor and acceptor and Q_D as 0.68. From the efficiency, the mean separation distance between 2Me-DABT and ThT has been estimated to be 41.2 Å. This result also supports that both dyes doesn't share same binding location in fibrils.

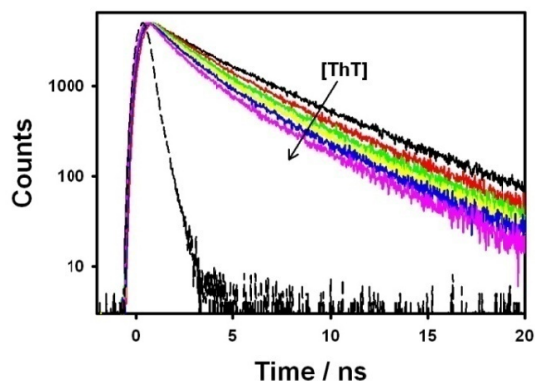


Figure 4.17 Emission transient decays for fibril bound 2Me-DABT in the presence of different concentrations of ThT (0-3 μM). The dashed curve represents the IRF.

4.4.2.5 Quantum chemical calculations and molecular docking studies:

The structures of 2Me-DABT and ThT were optimized by quantum chemical calculations using a Gaussian 03 package.²⁶⁹ B3LYP^{267, 268} functional and 6-31++g(d,p) basis function was used to optimize the chemical structures by DFT. The minimum energy configuration 2-Me-DABT is shown in figure 4.18 and used further in docking studies.

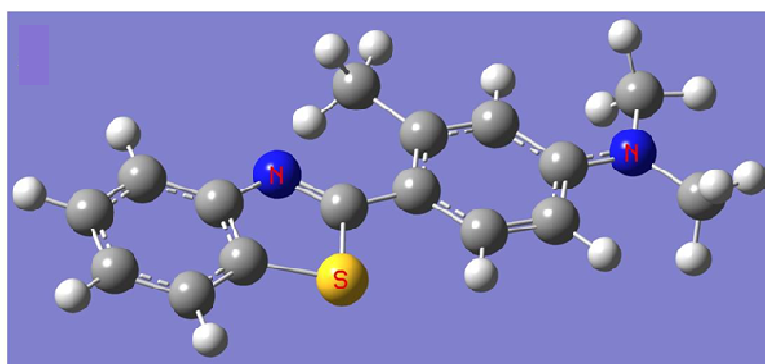


Figure 4.18 The Optimized structure of 2Me-DABT

Molecular docking experiments have been performed for 2Me-DABT with fibrils in order to understand the nature of binding between them. Such understanding will help us in developing amyloid probes with better sensitivity. As there is no proper detailed structural information on insulin fibrils, we have used fibrillar structure reported for amyloid β_{1-42} (PDB ID: 2MXU) for the molecular docking experiments.²⁷¹ The use of $A\beta_{1-42}$ fibril is preferred over the most abundant 40 residue amyloid- β protein ($A\beta_{1-40}$) for the docking studies due to the fact that recently it has been shown that protofibril of $A\beta_{1-42}$ is much more toxic and shows more propensity towards the aggregation as compared to its 40 residue analogue.^{328, 329} Docking of 2Me-DABT in $A\beta_{1-42}$ fibril is performed with several initial position of the ligand with respect to the host fibril. The initial docking consists of 1000 runs and all the results were clustered with RMSD value of 2Å. After clustering two primary binding sites for 2Me-DABT in $A\beta_{1-42}$ fibril have been identified. The two most energetically stable configurations have been shown in figure 4.19A. The lowest energy configuration (Mode 1) involves the localization of 2Me-DABT in the inner channel for the fibril. The binding energy for the mode-1 (with population 750 out of 1000) and mode-2 (with population 180 out of 1000) was estimated to be 6.87 and 6.39 kcal mol⁻¹ respectively. Different interactions operating between 2Me-DABT and amino acids of amyloid fibril for most populated mode of binding (mode-1) is also shown in figure 4.18B. It is found that the binding of 2Me-DABT in the amyloid fibril is mainly supported by the π - π stacking interaction between the aromatic rings of 2Me-DABT and the nearby histidine moiety (His14*). Further, the π - π interaction between the aromatic rings of 2Me-DABT with the amide bonds of the amyloid fibril also operative in the binding process. Beside such π - π interaction, hydrophobic interaction with the CH₂ groups of the peptide chain

also favour the incorporation of 2Me-DABT in the inner core region of the fibril. However, besides the binding in the inner core of the fibril, binding at the external grooves of the fibrils has also been observed in the present system. The population of such groove binding is found to be extremely low (6 out of 1000) with considerably low binding energy ($5.45 \text{ kcal mol}^{-1}$). It is important to mention that unlike ThT, binding of 2Me-DABT at the two end of the fibril could not be observed in our docking studies.³³⁰ This result is in agreement with the results reported by Wu et al, who have shown that unlike charged ThT, neutral ThT analogues does not bind to the end of the beta sheet structure.²³⁹

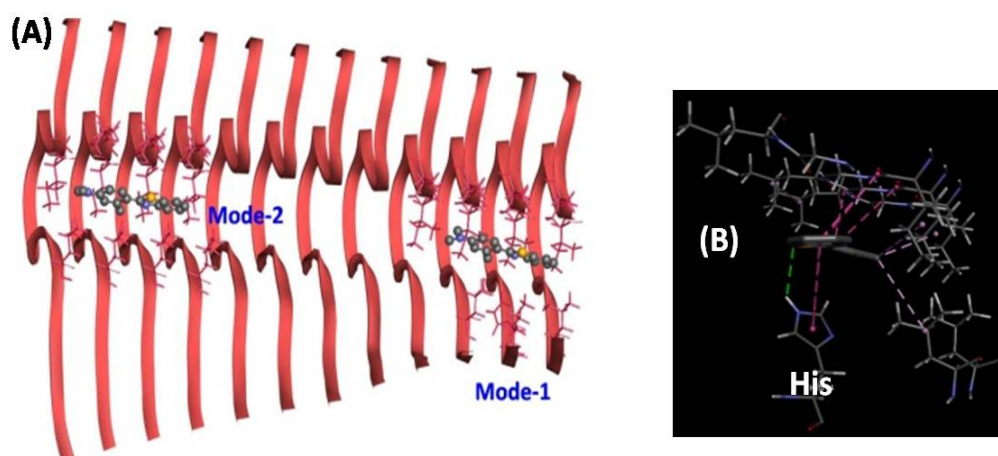


Figure 4.19 (A) Two most probable binding sites for 2Me-DABT in amyloid fibril. The mode 1 is the most energetically stable binding mode. (B) Close look of the binding pocket for the mode 1. The dashed lines indicate the different types of interaction between 2Me-DABT and fibril.

To further identify the relative location of 2Me-DABT and ThT in amyloid fibrils, we have performed the molecular docking using the fibril with docked 2Me-DABT (mode-1) as initial host structure. The most populated and the strongest mode

of binding shows that the added ThT also localized in the inner core of the fibril. The relative position of ThT with respect to 2Me-DABT in the amyloid fibril is shown in figure 4.20. Our docking studies show that the mean relative distance between ThT and 2Me-DABT is ~ 40.2 Å. The distance between 2Me-DABT and ThT obtained from the molecular docking studies is very close to the values obtained from the FRET studies. Our docking studies further support the fact that the site of localization of 2Me-DABT and ThT are quite distinct.

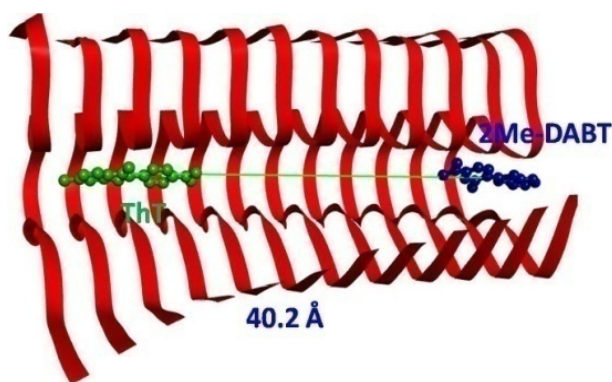


Figure 4.20 Binding pose of the ThT in the amyloid fibril with incorporated 2Me-DABT. The solid lines indicate the distance between 2Me-DABT and docked ThT.

4.4. Conclusions

Photophysical properties of newly synthesized neutral benzothiazole derivative, 2Me-DABT, has been investigated in solvents with different polarity. 2Me-DABT shows very strong solvatochromic behavior that is in contrast to its charged analogue, ThT. The variation in Stokes' shift and the quantum yield in aprotic solvents are due to the reduction in non-radiative channel in the excited state. In the case of protic solvents, due to solute-solvent H-bonding at thiazolic nitrogen, increase in the excited state dipole moment as well as strong quenching of the excited state has

been observed. Deuterium isotope effect confirms the involvement of H-bonding in the excited state of 2Me-DABT.

2Me-DABT binds strongly with the amyloid fibril resulting large increase in its emission intensity along with a large spectral shift. Thus, unlike ThT, large shift in the emission wavelength of 2Me-DABT on binding with amyloid fibril makes it potential ratiometric sensor and hence can provide high sensitivity in detection of amyloid fibril by fluorescence imaging techniques. Correlation with the photophysical properties suggest that large change in the emission properties of 2Me-DABT in amyloid fibril is due to low polarity of the hydrophobic pocket in the amyloid fibril where 2Me-DABT resides. FRET and molecular docking studies confirm that the binding location for ThT and 2Me-DABT is distinct and separated from each other by average distance of ~ 40 Å. Thus, our studies show that 2Me-DABT will be an efficient fluorescent sensor than ThT for the detection of the amyloid fibrils. Further, due to lack of any charge, 2Me-DABT will be more efficient for the *in-vivo* imaging of amyloid fibrils. The knowledge on the binding site and mode of interaction between probe and fibril obtained from the present study will assist in more rational design of benzothiazole based small molecule for the detection of amyloid fibril.

Chapter-5

Zwitterionic SYPRO Orange as sensitive amyloid probe

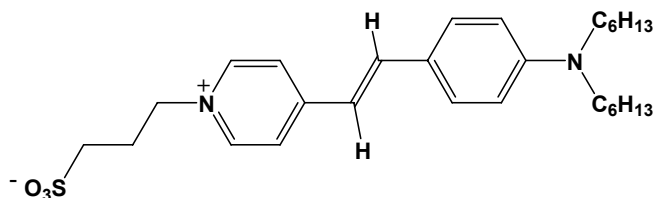
5.1. Introduction

In the earlier chapters, we have explored cationic probe, PG and a neutral probe, 2Me-DABT for the efficient detection of amyloid fibrils. Both probes showed great sensitivity towards amyloid fibrils. However, the advantage of 2Me-DABT over PG is its lipophilicity, which is prerequisite for efficient transport through BBB. This is the factor which decides the applicability of probe for the efficient in-vivo detection of brain related diseases.³³¹⁻³³⁶ Researchers have developed large number of probes with different structural characteristics for the in-vitro detection of amyloid fibrils but failed in in-vivo imaging due to lack of their BBB penetration.¹¹² Generally, for an efficient BBB crossing, the molecules should have proper lipophilicity.³³¹⁻³³⁶ It has been shown that for an efficient BBB crossing, molecules should have logP value (octanol-water partition coefficient) of 2-3.5.^{335, 336} Further, smaller size (<500 Da) of the molecules also favors the crossing of the tight junction in the endothelial cells of BBB.³³⁷ For cationic/anionic drugs, low lipophilicity is the primary reason for their lack of BBB penetrability.³³⁵⁻³³⁷ Mostly, small uncharged molecules have been successfully transported through BBB.³³⁸ Apart from the neutral molecules, there are few zwitterionic compounds such as phosphotidyl choline derivatives,³³⁹

methotexrate³⁴⁰ also have been shown to cross BBB. Recently, Mazak et. al. showed that the zwitterions have better membrane penetration power compared to cationic/anionic and neutral molecules at wide range of pH.³⁴¹ It is also shown that zwitterionic polymer coated nanoparticles can penetrate through BBB and also have long retention times.³⁴² Hence, zwitterionic fluorescent molecules have been explored as amyloid sensors with the aim of development of in-vivo amyloid imaging agent. For example, Konradsson and his coworkers demonstrated that a polythiophene based zwitterionic molecule could detect amyloid fibrils at acidic pH.²²⁸ However, such probes shows only limited sensitivity. Considering the higher permeability of zwitterions, it is necessary to search for efficient zwitterionic fluorescent molecules which can have potential application in amyloid imaging.

SYPRO Orange is a zwitterionic dye developed by Invitrogen Corp, USA. The molecular structure of SO, which is proposed by Yarmoluk and his workers³⁴³ and further confirmed by Kroeger et al.³⁴⁴ through liquid chromatography-mass spectrometry (LCMS) and NMR spectroscopy, is shown in scheme 5.1. It is a zwitterionic merocyanine based dye which has two hexyl groups attached to the anilino N-atom at one end and propyl sulphonate group is attached to pyridinium nitrogen at other end. The negative charge on the sulphonate group is electronically isolated from the stilbazolium moiety. However, the positive charge in SYPRO Orange is delocalized over entire stilbazolium moiety.

SYPRO Orange is a fluorescent dye, which is extensively used to study the unfolding of protein molecules using differential scanning fluorimetry (DSF). SYPRO Orange has extremely low emission yield in aqueous solution ($< 1 \times 10^{-3}$). Further, SYPRO Orange does not show any affinity towards the native proteins. However,

Scheme 5.1: Molecular structure of SYPRO Orange.³⁴⁴

SYPRO Orange shows strong non-specific binding to the unfolded protein resulting large increase in its emission yield.³⁴⁵⁻³⁴⁸ Thus, with the increase in the temperature of protein solution, the emission yield increases substantially neat the melting point of the protein. However, on further increase in the temperature, SYPRO Orange dissociates from the protein and results in decrease in its emission intensity.³⁴⁵⁻³⁴⁸ Due to such contrasting fluorescence behavior before and after melting temperatures, it has been extensively used to measure the melting temperatures of proteins with much higher sensitivity and reliability.³⁴⁵⁻³⁴⁸ Such fluorescence behaviour of SYPRO Orange has also been utilized for the understanding of the inter protein interactions.^{345, 348} Although it has been extensively used to study the protein melting, the fundamental mechanism which is responsible for such fluorescence behavior of SYPRO Orange is not yet understood. It has been proposed that due to the unfolding the hydrophobic part of the protein becomes accessible and SYPRO Orange binds specifically to these hydrophobic parts of protein resulting large increase in the emission yield.^{344, 345, 348} However, experimental proof of such proposition is still lacking.

As the protein unfolding is the initial step in the fibrillation process, it is possible that the fibrillation process may be monitored through the fluorescence of SYPRO Orange. Indeed, SYPRO Orange has been used for the detection of fibrils from amylin.³⁴⁹ SYPRO Orange shows only limited increase in its emission yield (~6

fold) due to its binding with amylin fibril. Further, it has been shown that like gold standard amyloid probe, ThT, SYPRO Orange can also follow the fibrillation kinetics.³⁴⁹ However, detail studies on the binding of SYPRO Orange with fibril and the mechanism for the increase in its emission upon binding with fibril is not fully investigated.

In this chapter, we explored the binding characteristics of SYPRO Orange to insulin fibrils and compared with standard amyloid probe, ThT. The mechanism of interaction has been explained on the basis of detailed photophysics of SYPRO Orange in different solvents of varying properties such as polarity, viscosity etc.

5.2. Materials and Methods

SYPRO Orange dye is purchased from Sigma-Aldrich as 5000X concentrated solution in DMSO. In all experiments, 1X SYPRO Orange has been used. The source of bovine insulin, Thioflavin T and all the solvents have been mentioned in chapters 3 and 4. The preparation of insulin fibrils is described in chapter 3. The fluorescence quantum yield of SYPRO Orange in molecular solvents were determined by comparative method using Nile red in dioxane ($\phi=0.7$) as the reference.²⁸⁶ The calculation of the solvent polarity function (Δf) has been described in chapter 4 (*cf.* equation 4.3).

The ground state absorption and steady state emission spectra were obtained from Jasco spectrophotometer (model# V-650) and Hitachi fluorimeter (model # F4500) whose details have been discussed in chapter 2. Nanosecond time-resolved emission measurements have been carried out using a time-correlated single photon counting (TCSPC) method based instrument from IBH, UK. All the samples were

excited with 445 nm laser diode with instrument response of 160 ps. For all measurements the emission polarizer was kept at magic angle with respect to vertical excitation pulse. All the measurements were carried out at $25\pm 1^\circ\text{C}$. Molecular docking studies have been carried out using Autodock 4.0 as described in chapter 2. The fibril structure has been taken from Protein databank (PDB id 2MXU). The structure of SYPRO Orange has been optimized by quantum chemical calculations using Gaussian 03 package. B3LYP functional and 6-31++g (d, p) basis function were used to optimize the chemical structures by DFT. The optimized structure of SYPRO Orange was used for the docking with fibril.

5.3. Results and discussion

5.3.1. Ground state absorption studies

To understand the effect of fibril on the photophysical properties of SYPRO Orange, ground state absorption measurements have been performed and the results are presented in figure 5.1. SYPRO Orange in water shows broad absorption band with a peak at 487 nm. It is evident from figure 5.1A that the absorption spectra show large blue shift due to the addition of insulin fibrils up to $1\ \mu\text{M}$. Thus, the absorption maxima of SYPRO Orange change from 487 nm in water to 474 nm in $1\ \mu\text{M}$ fibril solution. Such a large blue shift with very low concentration of fibril ($1\ \mu\text{M}$) indicates the presence of strong interaction between SYPRO Orange and fibrils. However, further addition of fibril leads to a red shift in the absorption spectrum of SYPRO Orange which is evident from figure 5.1B. Thus, in presence of $30\ \mu\text{M}$ of insulin fibril, the absorption spectrum shows its peak at $\sim 500\ \text{nm}$ which is about $\sim 26\ \text{nm}$ red shifted compared to its spectrum in $1\ \mu\text{M}$ fibril solution. Therefore, there is an overall

red shift of ~ 13 nm in fibril compared to aqueous solution of SYPRO Orange. Such contrasting shift in the absorption spectra at low and high concentrations of fibrils indicates that there are different kinds of interactions taking place in these two concentration regions. Thus, we can infer that there might be two different binding modes exists for SYPRO Orange in fibril. Such two types of binding modes for the amyloid probes have been reported earlier in the literature for several fibril binding dyes.^{184, 186, 214, 239, 327, 330, 350} Two modes of binding in fibril for cationic probes, such as ThT, are surface binding governed by the electrostatic forces and inner channel binding governed by hydrophobic interactions.²¹⁴ However, for the neutral probes, it has been reported that both the binding modes are mainly governed by hydrophobic interaction and also have some contribution from π - π stacking interactions for probes with aromatic moieties.^{239, 330} As amyloid fibrils are highly heterogeneous and also can offer variety of interactions,^{21, 351} further studies are required to understand the nature of the interaction between SYPRO Orange and fibrils.

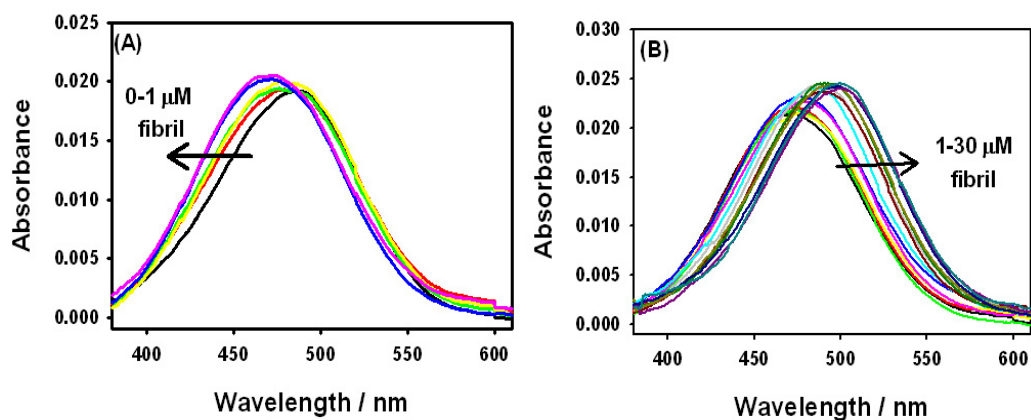


Figure 5.1 Ground state absorption spectra of SYPRO Orange in insulin fibril: (A) at 0-1 μM and (B) 1-30 μM insulin fibrils.

5.3.2. Steady state fluorescence measurements

In order to get better insight into the effect of fibril on photophysical properties of SYPRO Orange, the steady state fluorescence spectra of SYPRO Orange in water and in fibril solutions have been measured and the results are presented in figure 5.2A. Aqueous solution of SYPRO Orange shows very weak and broad fluorescence band with maximum at ~620 nm. Addition of the fibril causes large blue shift in the emission spectrum. Thus, the emission maxima of SYPRO Orange in 30 μ M insulin fibril solution is 580 nm, which is ~40 nm blue shifted as compared to water. Most importantly, along with the change in the emission peak position, the addition of amyloid fibrils results in a significant increase in the emission intensity. Thus, the emission intensity of SYPRO Orange in presence of 30 μ M insulin fibril increases by ~1200 fold as compared to water. Such large fluorescence enhancement indicates that the non-radiative excited state depopulation pathways might be restricted due to the association with amyloid fibrils. Large blue shift of ~40 nm along with high fluorescence enhancement signifies that there is very strong interaction of SYPRO Orange with the fibril. The shift in the emission maxima along with a large increase in the emission intensity upon binding with amyloid fibrils is very advantageous for the optical imaging of amyloid plaques.²⁶³ Large shift in the emission maximum ensures the reduced background emission and high fluorescence enhancement with the fibril helps to get brighter images with better contrast.²⁶³ A noteworthy observation is that unlike the absorption spectra, the fluorescence spectra of SYPRO Orange always show hypsochromic shift with the increase in the concentration of fibrils. Figure 5.2B shows the intensity normalized emission spectra of SYPRO Orange in amyloid fibrils. It is evident from the figure that the shift in the emission spectral position is more

prominent in the low concentration region of amyloid fibrils. This result indicates that strong interaction between SYPRO Orange and insulin fibrils takes place in the low concentration region of amyloid fibrils.

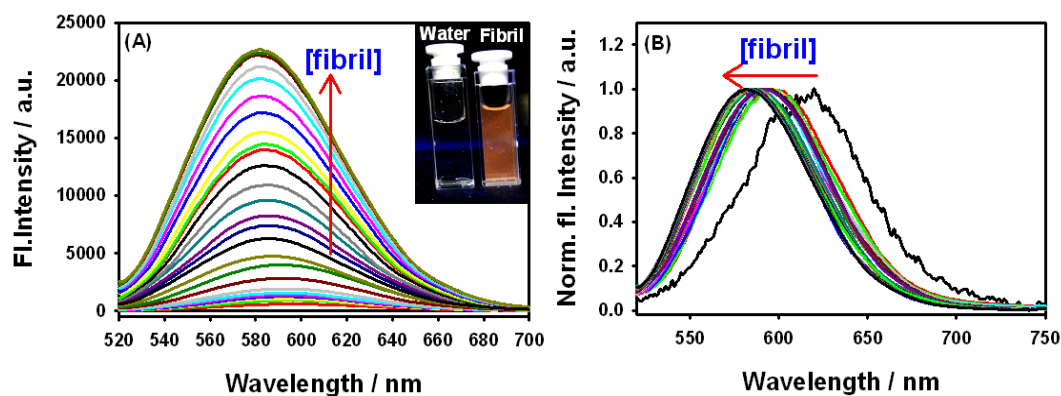


Figure 5.2 (A) Fluorescence spectra of SYPRO Orange in water in the presence of different concentrations (0-30 μM) of addition of fibril. **Inset:** Photograph of SYPRO Orange in water (left) and 30 μM insulin fibril (right) under UV irradiation. (B) Intensity normalized emission spectra of SYPRO Orange in water in presence of fibrils (0-30 μM).

Large enhancement in the fluorescence provokes us to check whether naked eye detection of fibrils, even at little higher concentration, is possible under UV irradiation. The inset of figure 5.2A shows the photographic image of aqueous solution of SYPRO Orange in the absence and presence of 30 μM insulin fibrils. SYPRO Orange in fibril solution shows bright orange fluorescence emitted from fibrillar aggregates while no such emission has been observed from the aqueous solutions. Thus, SYPRO Orange can be used for the naked eye detection of fibrils under UV irradiation.

The quantitative assessment of the binding strength is required to know the efficacy of SYPRO Orange as diagnosing agent. For that purpose, the binding strength has been estimated using modified Benesi-Hildebrand equation.^{278, 326}

$$\frac{1}{\Delta I_f} = \frac{1}{K(I_c - I_o)} \frac{1}{[Insulin]} + \frac{1}{(I_c - I_o)} \quad (5.1)$$

where ΔI_f is the change in fluorescent intensity with the addition of the fibril and I_c and I_o are the fluorescence intensity of SYPRO Orange when completely bound with fibril and free in water, respectively. K is the binding constant. $1/\Delta I_f$ vs. $1/[fibril]$ plot is shown in figure 5.3. It has been observed from the figure that there is nonlinearity in the double reciprocal plot. Due to the non-linearity, the experimental data have been fitted with Benesi-Hildebrand equation (equation 5.1) separately in the low and high fibril concentration regions and the fitted data are shown as straight lines in figure 5.3. Such fitting results in two binding constants of $6.8 \times 10^6 \text{ M}^{-1}$ and $1.47 \times 10^5 \text{ M}^{-1}$ in the low and high fibril concentration region, respectively. Thus, like ground state absorption studies, the steady state emission measurements further confirms the presence of two mode of binding for SYPRO Orange in fibril. Such high value of binding constant along with large fluorescence enhancement of SYPRO Orange upon binding with fibrils notifies that SYPRO Orange can be a promising probe for the detection of amyloid fibrils.

5.3.3. Time-resolved fluorescence measurements

Large enhancement in the fluorescence intensity indicates that there is definite modulation in the excited state relaxation pathways.¹²⁵ To get better insight into the fate of excited state processes due to the association with fibrils, time-resolved

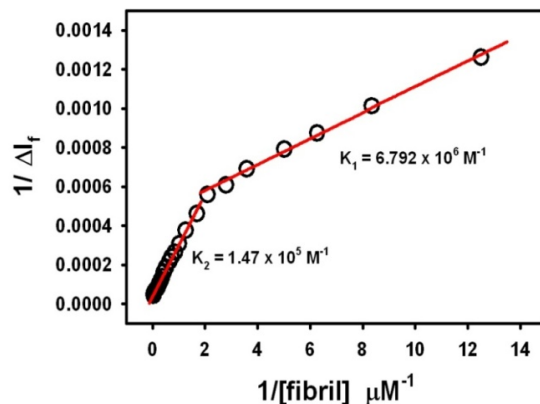


Figure 5.3 Modified Benesi-Hildebrand plot for the fluorescence changes due to SYPRO Orange-fibril complexation. Open circles represent experimental data points while solid lines represent fit to the experimental data according to equation 5.1.

fluorescence measurements were carried out using TCSPC technique and the results are shown in figure 5.4. It is evident from figure 5.4A that SYPRO Orange in water shows very fast fluorescence intensity decay whose lifetime could not be estimated due to limited time resolution of TCSPC instrument. This result indicates that there are some ultrafast non-radiative excited state depopulation channels exist for SYPRO Orange in aqueous solution. Presence of such ultrafast non-radiative decay channel might be responsible for the observed low emission yield of SYPRO Orange in water. It is also evident from figure 5.4A that the emission transient decay becomes slower with the addition of fibrils. All emission transient decays of SYPRO Orange are non-exponential in nature and fitted with tri-exponential decay function. Fitting parameters for transient emission have been presented in table 5.1. Thus, the average lifetime of SYPRO Orange increases from IRF limited lifetime in water to 2 ns in 25 μM insulin fibril. Such large increase in the excited state lifetime of SYPRO Orange indicates that the non-radiative excited state depopulation processes, which are responsible for low

emission yield in aqueous solution, has been restricted due to its binding with fibrils. The variation in the average lifetime of SYPRO Orange has been plotted as a function of the fibril concentration and is shown in figure 5.4B. It is quite apparent from the figure that the changes in the average lifetime are much more at the initial concentrations of fibrils as compared to higher fibril concentration. Such distinct rate of change in the lifetime in two fibril concentration regions, further support the existence of two modes of binding for SYPRO Orange in fibrils.

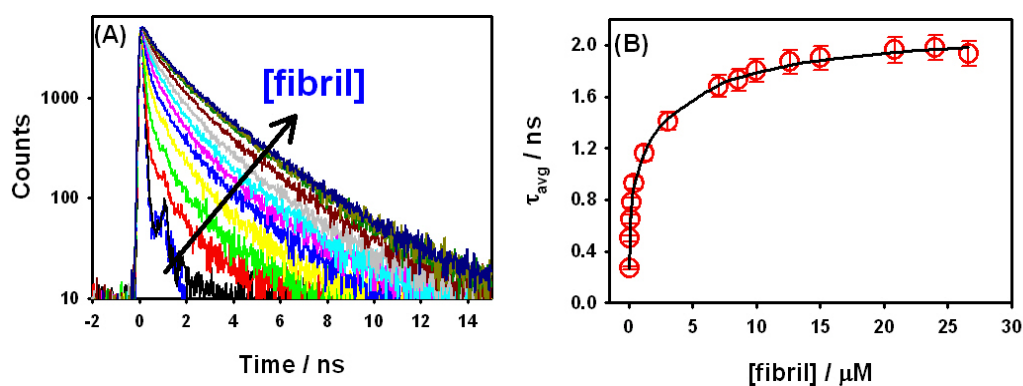


Figure 5.4 (A) Fluorescence transients of SYPRO Orange in water with addition of fibril. Blue dashed curve represents IRF (B) Variation in the average lifetime of SYPRO Orange with fibril concentration.

5.3.4. Comparison of SYPRO Orange with Thioflavin T

5.3.4.1 Steady-state fluorescence spectra

Strong binding affinity, large fluorescence enhancement (~ 1200 fold) along with large blue shift (~ 40 nm) in the emission spectra makes SYPRO Orange a better fluorescence marker for amyloid fibrils. Nevertheless, the question arises is whether SYPRO Orange can be better than gold standard amyloid stain, ThT. In order to answer this question, the fluorescence spectrum of ThT and SYPRO Orange have

Table 5.1 Fitting parameters of fluorescence decay traces of SYPRO Orange in presence of at different concentrations of fibrils.

[fibril]/ μM	a_1	τ_1 / ns	a_2	τ_2 / ns	a_3	τ_3 / ns	τ_{avg} / ns
0.04	78.4	0.03	10.1	0.31	11.5	1.90	0.27
0.08	54.7	0.03	23.1	0.32	22.2	1.83	0.50
0.12	41.0	0.04	31.2	0.36	27.8	1.86	0.65
0.24	31.8	0.05	34.9	0.37	33.3	1.91	0.78
0.40	26.9	0.07	35.1	0.41	38.0	2.00	0.93
1.18	16.1	0.09	40.1	0.51	43.9	2.15	1.16
3.04	11.7	0.14	38.9	0.66	49.4	2.31	1.41
7.06	5.8	0.12	33.9	0.71	60.2	2.38	1.68
8.57	7.5	0.17	34.7	0.84	57.8	2.47	1.73
10.00	6.9	0.18	32.9	0.85	60.2	2.50	1.80
12.63	8.2	0.23	34.1	0.97	57.7	2.63	1.87
15.00	5.4	0.17	32.6	0.89	62.0	2.58	1.90
20.87	6.3	0.24	28.5	0.94	65.3	2.58	1.96
24.00	4.3	0.17	31.4	0.91	64.2	2.63	1.98
26.66	5.5	0.21	32.1	0.94	62.4	2.60	1.93

been measured under similar condition and compared. The emission spectra of ThT and SYPRO Orange in the presence of 30 μM insulin fibril are shown in figure 5.5. The absorbance values at the excitation wavelength (440 nm for ThT and 490 nm for SYPRO Orange) for both dyes are kept same. It is quite obvious from the figure that the fluorescence enhancement due to the interaction with amyloid fibrils is ~ 3 times more for SYPRO Orange than ThT. Such large difference in the enhancement factor makes SYPRO Orange a better amyloid staining agent than gold standard amyloid probe, ThT. It should be mentioned that ThT doesn't show any change in emission wavelength upon interaction with fibrils leading to large background signal during fluorescence imaging of amyloid fibrils.^{128, 198} However, SYPRO Orange gives large blue shift of ~ 40 nm in the presence of fibrils. This will reduce the background signal to a significant extent and can improve the detection limits remarkably. Another important advantage of SYPRO Orange over ThT is its emission wavelength, 580 nm,

in fibrillar solution. In the view point of fluorescence imaging of fibrils in the biological matrix such as brain cell lines, orange emission helps not only in reducing the interference from the auto fluorescence from cells but also in increasing in the tissue penetration power.^{263, 352} Further, as mentioned earlier, the zwitterionic SYPRO Orange may also have much better penetrability through BBB over the positively charged ThT. All these factors make SYPRO Orange as a potential candidate for the efficient detection of fibrils in both *in-vitro* and *in-vivo*. It has already been showed that SYPRO Orange can bind specifically to amyloid aggregates but not the oligomers, prefibrillar aggregates.³⁴⁹ SYPRO Orange can also monitor the progress of fibrillation process. Hence, the aggregation of proteins and inhibition assays can also be studied using SYPRO Orange to evaluate the therapeutic efficiency of drugs.³⁴⁹

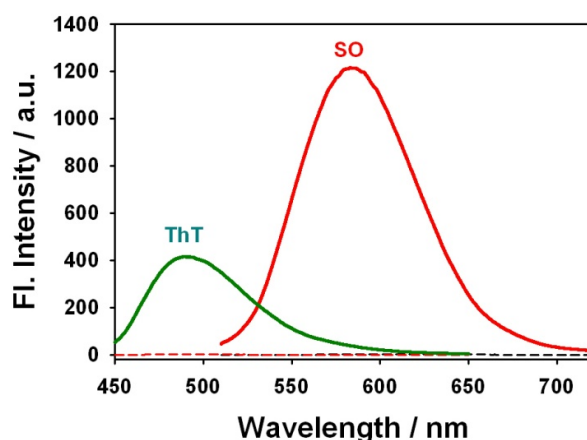


Figure 5.5 Fluorescence spectra of ThT (λ_{ex} is 440 nm) and SYPRO Orange (λ_{ex} is 500 nm) in water (dashed) and in presence of 30 μ M insulin fibril (solid).

5.3.4.2. Fluorescence microscopic studies

Fluorescence microscopy is versatile tool which has been extensively utilized to visualize the protein fibrils using amyloid specific fluorescent markers.²⁶³ ThT has been widely used to see the fibril under optical microscope since years.¹⁹⁸ In order to

assess the possibility of usage of SYPRO Orange to visualize fibrils, we have recorded microscopic images of insulin fibrils stained with SYPRO Orange and compared with images of ThT. Figure 5.6 shows the microscopic images of fibrils stained with both SYPRO Orange and ThT. It has been observed that images obtained for SYPRO Orange are brighter than ThT. Thus, it is inferred that SYPRO Orange can be a better candidate for the in-vitro optical imaging of amyloid fibrils.

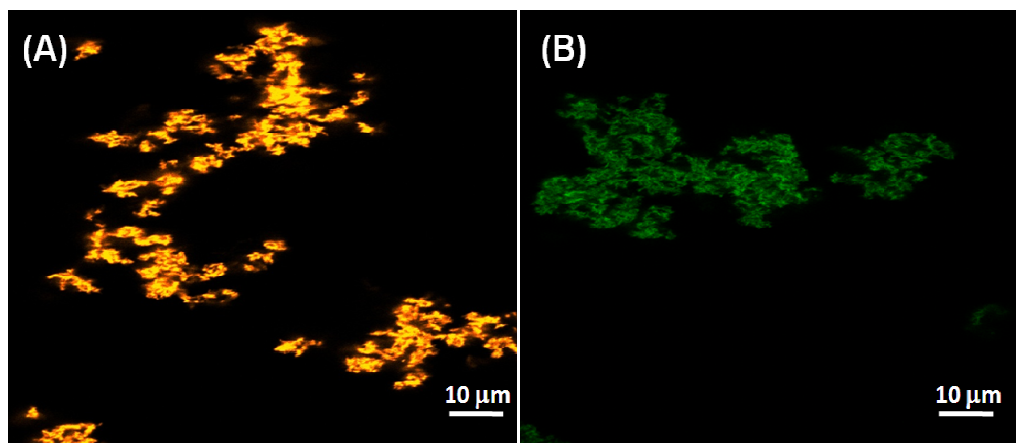


Figure 5.6 Fluorescence microscopic images of insulin fibril stained with (A) SYPRO Orange and (B) ThT.

5.3.4.3. Limit of detection

Another criterion of a sensitive probe for any biological system is its detection limit. Lower the detection limit, better probe it is. To determine the limit of detection (LOD) emission spectra of SYPRO Orange and ThT has been recorded in presence of low concentrations (in nM regime) of amyloid fibrils. The calibration curves are generated by plotting the emission intensity of the dye with fibril concentrations. Such calibration curves for SYPRO Orange and ThT are shown in figure 5.7. The experimental data are fitted with linear equation with slope values of 16.25 nM^{-1} for

SYPRO Orange and 0.38 nM^{-1} for ThT. Larger slope of the calibration curve for SYPRO Orange compared to ThT clearly indicates that former probe has better sensitivity than latter probe. Quantification of the sensitivity for these two probes has been done by the calculation of limit of detection (LOD) using following equation.^{353,}

354

$$LOD = \frac{3.3 * \sigma}{S} \quad (5.2)$$

where σ is standard deviation of the measurement and S is the slope of calibration curve. LOD has been estimated to be 0.42 nM for SYPRO Orange while 13.5 nM for ThT. Thus, the detection limit for SYPRO Orange is ~ 34 times lower than that of ThT. The LOD values clearly suggested that SYPRO Orange is very sensitive probe compared to ThT. Thus, SYPRO Orange can be employed to detect very small concentration of fibrils where ThT is unable to detect them.

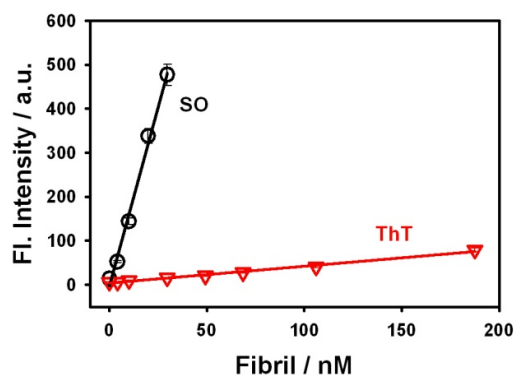


Figure 5.7 The variation in the fluorescence intensity of SYPRO Orange (○) and ThT (▽) with the concentration of insulin fibril. Solid line represents their linear fits.

5.3.5. Mechanistic investigation of binding modes of SYPRO Orange with fibril

5.3.5.1. Effect of ionic strength

Now, it is understood that SYPRO Orange is very sensitive probe towards fibrils. However, the question remains is that what makes it more sensitive. To answer this query, we have investigated the detailed photophysics of this molecule under different environmental conditions. From the proposed molecular structure, SYPRO Orange is in zwitterionic form in which the negative charge on the sulphonate group is electronically isolated from the remaining fluorophore unit by a propyl chain while the positive charge can be delocalized over the entire stilbazolium moiety. As the amino acids can be both negatively and positively charged in fibril at the experimental pH value, electrostatic force may play an important role in the binding of SYPRO Orange with amyloid fibrils. Role of such electrostatic force has been demonstrated for the binding of cationic ThT with the amyloid fibrils.^{214, 327} The electrostatic interaction facilitates the surface binding which leads to the binding of the probe in the inner grooves of the fibril. To check the existence of the electrostatic force in the binding process, effect of strong electrolyte on the emission characteristics of SYPRO Orange in fibril solution has been investigated. The emission spectrum and the emission transient of SYPRO Orange in fibril solution has been recorded in the presence of 0.5M NaCl and the results are shown in figure 5.8. Surprisingly, despite having charge centre, the emission characteristics of SYPRO Orange in fibril solution remains unaffected in the presence of large amount of strong electrolyte. This result suggests that electrostatic force does not have any role in the binding of SYPRO Orange with

amyloid fibrils. Hence, it can be proposed that the interaction between SYPRO Orange and amyloid fibrils primarily hydrophobic in nature.

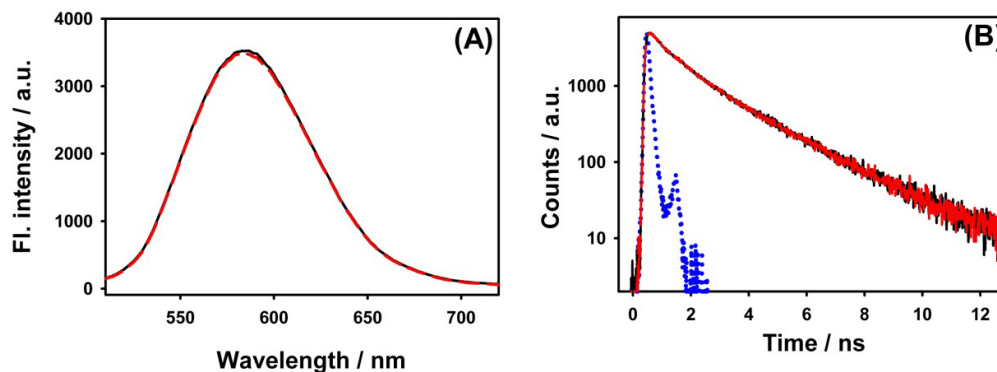


Figure 5.8 (A) Emission spectra and (B) emission transient decays of SYPRO Orange in fibril solution in the absence (—) and presence of 500 mM NaCl (- - -). The dotted curve in panel B represents IRF.

In order to understand the kind of interactions that takes place between SYPRO Orange and amino acids of the fibril at the respective binding location, the effect of different environmental conditions such as polarity, viscosity, hydrogen bonding etc, on the photophysics of SYPRO Orange has been investigated through ground state absorption, steady state and time-resolved emission measurements.

5.3.5.2. Effect of solvent polarity

To assess the effect of polarity on photophysical properties of SYPRO Orange, absorption and emission spectra in homogeneous molecular solvents and their mixtures with varying polarity have been measured. The normalized absorption spectra of SYPRO Orange in different solvents are displayed in figure 5.9A. It is evident from the figure that the absorption spectra is continuously red shifted with increase in the solvent polarity. This indicates that the ground state getting stabilized

with increase in polarity of the surrounding medium, which is quite expected due to zwitterionic nature of SYPRO Orange. In figure 5.9B, normalized fluorescence spectra with varying Δf have been presented. From the figure it is clear that the emission spectra also shows continuous bathochromic shift with increase in the solvent polarity. Such behavior suggests that the dipole moment of the excited state is larger than the ground state which is characteristic of a solvatochromic dye.^{125, 138}

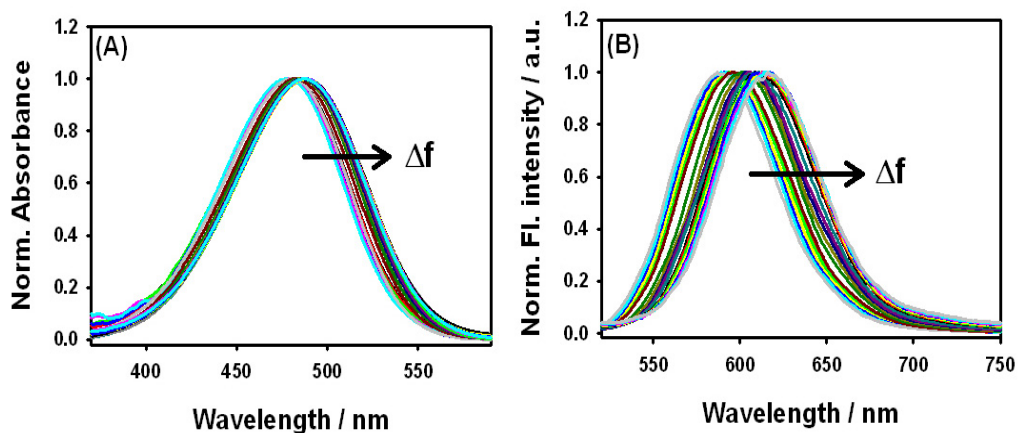


Figure 5.9 Normalized absorption (A) and emission (B) spectra of SYPRO Orange in solvents with different Δf values.

The variation of Stokes' shift with solvent polarity function Δf is plotted in figure 5.10. From the figure it has been observed that Stokes' shift varies linearly with Δf in aprotic solvents. This behavior indicates that the nature of ground and excited states remain same in the case of aprotic solvents. From Lippert-Mataga relation (see equation 4.4), the difference in the dipole moments of ground and excited state of SYPRO Orange in aprotic solvents is estimated to be 5.19 D. From the quantum chemical calculations, the ground state dipole moment of SYPRO Orange is estimated to be ~ 20.2 D. Thus, the excited state dipole moment of SO is ~ 25.4 D. Such a large

Table 5.2 Photophysical parameters of SYPRO Orange dye as estimated in different solvents and solvent mixtures.. Subscripts indicate their corresponding percentage volume fractions.

Solvent composition	Δf	$\lambda_{abs}^{max} / \text{nm}$	$\lambda_{ems}^{max} / \text{nm}$	ϕ	τ_{avg} / ns
CH ₄₅ EA ₅₅	0.158	476.5	587.0	0.45	0.82
CH ₆₈ EA ₃₂	0.166	477.0	588.0	0.40	0.78
CH ₇₅ EA ₂₅	0.174	477.5	589.0	0.34	0.72
CH ₈₃ EA ₁₇	0.183	478.0	590.0	0.30	0.65
CH ₈₈ EA ₁₂	0.188	478.0	591.0	0.29	0.6
CH ₉₄ EA ₀₆	0.194	478.5	592.0	0.25	0.55
CH ₉₇ EA ₀₃	0.197	479.0	593.0	0.24	0.52
EA	0.200	479.5	595.0	0.22	0.5
EA ₉₇ ACN ₀₃	0.211	481.0	597.0	0.19	0.42
EA ₉₄ ACN ₀₆	0.227	482.0	600.0	0.15	0.32
EA ₈₈ ACN ₁₂	0.243	483.0	602.5	0.11	0.25
EA ₈₃ ACN ₁₇	0.253	484.0	604.5	0.09	0.2
EA ₇₉ ACN ₂₁	0.260	484.5	606.5	0.08	0.18
EA ₇₁ ACN ₂₉	0.269	485.0	608.0	0.06	0.15
EA ₆₅ ACN ₃₅	0.275	485.5	610.0	0.05	0.13
EA ₅₈ ACN ₄₂	0.281	485.5	612.0	0.05	0.11
EA ₅₀ ACN ₅₀	0.286	486.0	614.0	0.04	0.11
EA ₄₄ ACN ₅₆	0.289	486.0	615.0	0.04	0.1
EA ₃₈ ACN ₆₂	0.293	486.0	615.0	0.03	0.09
EA ₂₉ ACN ₇₁	0.296	486.0	615.0	0.03	0.09
EA ₂₁ ACN ₇₉	0.299	486.0	615.0	0.03	0.07
EA ₁₁ ACN ₈₉	0.302	486.0	615.0	0.02	0.07
ACN	0.305	486.0	615.0	0.02	0.06

change in dipole moment indicates that there is increased charge distribution takes place in the photoexcited state of SYPRO Orange. It is quite possible that upon photoexcitation, there is significant charge transfer from the aniline group to pyridinium moiety which results in large separation between negatively charged sulphonate group and the positive charge results in large dipole moment in the excited

state. Such charge transfer over a long distance might be responsible for the observed strong solvatochromism behaviour of SYPRO Orange. Such strong solvatochromism has already been reported for stilbazolium based molecules.³⁵⁵⁻³⁵⁸

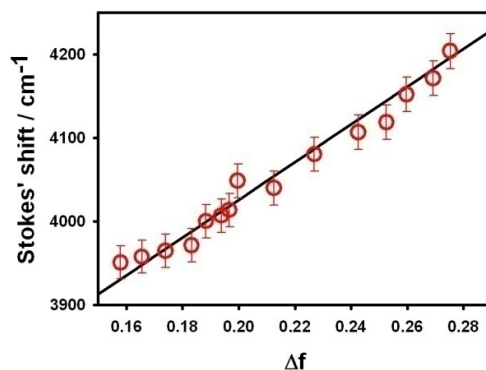


Figure 5.10 Variation of Stokes' shift of 2Me-DABT with Δf . \circ represents the experimental data. Solid lines represent the fitting of the experimental data with Lippert-Mataga equation (equation 4.4).

Besides the spectral position, the emission quantum yield is an important parameter which will be governed by the surrounding environmental conditions. The fluorescence quantum yield of SYPRO Orange has been estimated in different solvents and solvent mixtures and the data is presented in table 5.2. The variation in the emission quantum yield of SYPRO Orange with the solvent polarity function, Δf , is shown in figure 5.11. It can be seen from the figure that the emission yield of SYPRO Orange decreases with the increase in the solvent polarity. This result indicates that there might be an increase in the efficiency of non-radiative decay pathways of photoexcited SYPRO Orange with increase in the solvent polarity. Thus, it can be inferred that the fluorescence intensity of SYPRO Orange enhances along with the blue shift in both absorption and emission when it is bound in hydrophobic environments. This is in line with the observed hypsochromic shift in the absorption

as well as emission of SYPRO Orange in the low concentration region of fibril. Thus, mode I could be due to binding of SYPRO Orange in hydrophobic location in the fibril. From the studies with other amyloid probes mentioned in previous chapters, we may assume that SYPRO Orange might be situated in the inner core of the amyloid fibrils just like PG and 2Me-DABT.

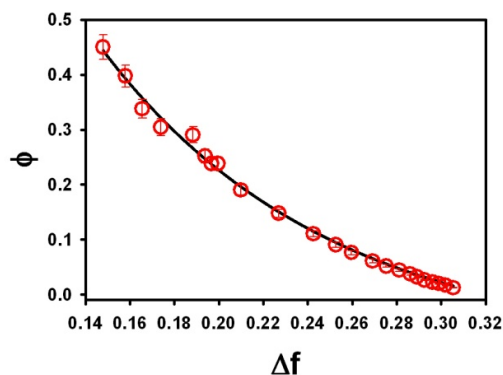


Figure 5.11 Variation in the fluorescence quantum yield of SYPRO Orange with Δf values of solvents.

The emission transients have also been recorded for SYPRO Orange to understand the fate of excited state relaxation pathways with change in the surrounding polarity and the results are presented in figure 5.12A. It is apparent from the figure that the fluorescence intensity decays becomes faster with increase in the solvent polarity. This suggests that there is an increase in the rate of excited state decay with increase in the solvent polarity. All emission transients follow non exponential decay kinetics and are best fitted with bi-exponential decay function. The variation in the average lifetime of SYPRO Orange with solvent polarity function, Δf , is shown in figure 5.12B. It is evident from the figure that the average fluorescence lifetime also follows the same trend as the emission quantum yield. This indicates that the rate of non-radiative pathways increase with the increase in the solvent polarity.

Thus, it can be inferred that the fluorescence intensity as well as the lifetime increases when SYPRO Orange is situated in low polar site in fibrils. However, even at the lowest polarity ($\epsilon = 3.3$) used in these experiments lifetime only reaches to about 0.8 ns while in the fibril, the lifetime is about 2 ns. As the fibrils comprises of charged amino acids, it is not possible to have a dielectric constant below 3 at the binding location. Thus, difference in the lifetime in molecular solvents and fibril suggests that the polarity alone cannot be made responsible for the observed fluorescence enhancement in the fibril.

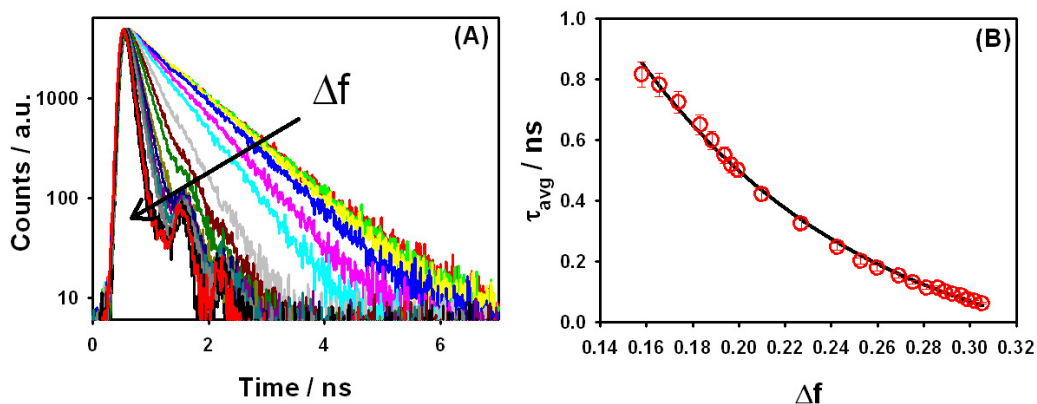


Figure 5.12 (A) Transient fluorescence decays of SYPRO Orange in solvent mixtures with different polarity. (B) Variation in the average lifetime of SYPRO Orange with solvent polarity.

5.3.5.3 Effect of solvent viscosity

Another important factor that can alter the photophysical parameters of a fluorophore is the viscosity of the surrounding medium.^{130, 274, 288, 359, 360} To unravel the effect of viscosity, all photophysical parameters have been measured with SYPRO Orange in glycerol by varying its temperature from 15-70 °C. It is well known that the viscosity rather than the polarity of glycerol is very sensitive to the change in

temperature. Thus, the viscosity of glycerol changes from 1970 cP at 15 °C to 47 cP at 70 °C.³⁶¹ The absorption spectra of SYPRO Orange in glycerol at different temperatures have been recorded and displayed in figure 5.13. It is evident from the figure that there is no shift in the absorption maxima with the change in the viscosity of the solvent. However there is definite change in the absorbance with temperature. This might be due to the change in refractive index of glycerol with temperature. Thus, the observed spectral shift in the absorption spectra of SYPRO Orange in the presence of fibril is not due to the change in rigidity of the surrounding medium.

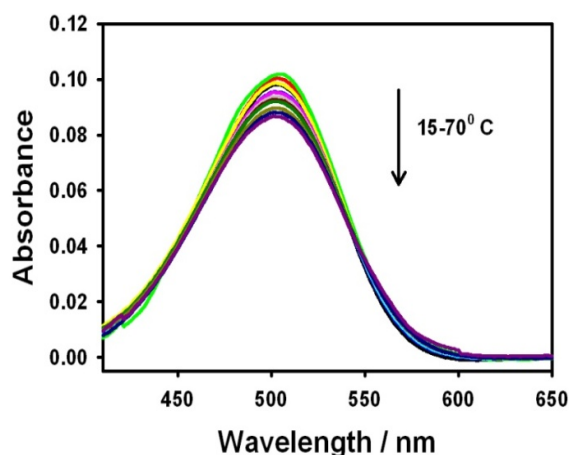


Figure 5.13 The absorption spectra of SYPRO Orange in glycerol at different temperatures (15- 70 °C)

Figure 5.14A depicts the variation in fluorescence spectra with the change in the viscosity of the medium. The fluorescence intensity of SYPRO Orange in glycerol gradually decreases with increase in temperature. This suggests that there are some internal dynamics which are being more efficient and leads to decrease in its fluorescence yield with decrease in the viscosity of the medium. From the molecular structure, it can be seen that there are two possibilities for such intramolecular

dynamics in SYPRO Orange. One is cis-trans isomerization of stilbene group³⁶² and the other is the rotation of dihexyl amino group.^{355, 363} It has been reported that both of these processes are viscosity dependent.^{355, 362, 363} But, which process is responsible for the observed fluorescence enhancement with the viscosity is still not understood. The normalized emission spectra of SYPRO Orange in glycerol at different temperatures have been shown in figure 5.14B, which reveals that the emission maxima shows red shift with decrease in the viscosity.

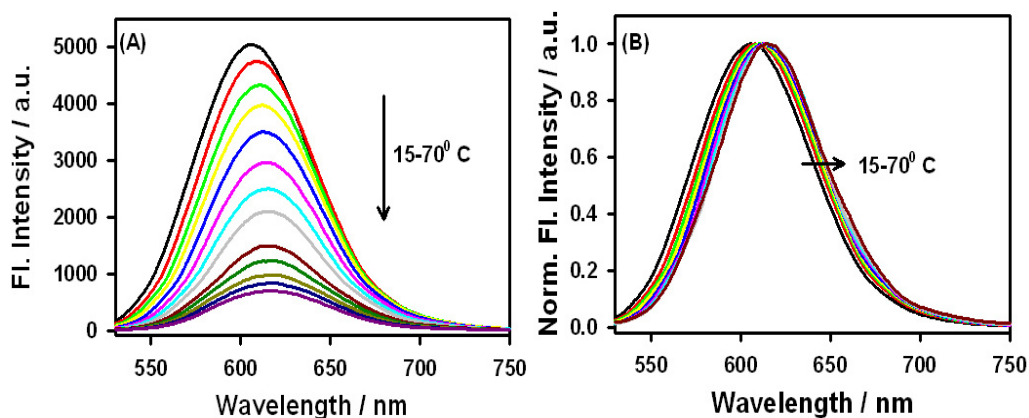


Figure 5.14 (A) Fluorescence spectra and (B) intensity normalized fluorescence spectra of SYPRO Orange in glycerol at different temperatures.

The quantum yield has been estimated for SYPRO Orange in glycerol at different temperatures and presented in table 5.3. It is evident from the table 5.3 that the emission yield of SYPRO Orange decreases with increase in temperature of glycerol solution. The viscosity dependence of quantum yield of fluorescence probe

Table 5.3 Photophysical parameters of SYPRO Orange dye in glycerol solution at different temperatures.

Temperature / °C	Viscosity / cP	ϕ	$\tau_{\text{avg}} / \text{ns}$
15.0	1970.1	0.68	2.05
17.8	1574.0	0.63	1.87
21.8	1150.7	0.56	1.67
25.1	894.2	0.53	1.47
29.9	625.8	0.48	1.26
35.1	430.5	0.40	1.09
40.0	306.1	0.34	0.92
44.7	222.8	0.29	0.87
50.3	154.5	0.21	0.76
55.0	114.8	0.17	0.64
60.1	83.9	0.14	0.54
65.0	62.6	0.13	0.43
70.0	46.9	0.11	0.38

has been related to the viscosity of surrounding medium by following Forster-Hoffmann equation.^{172, 288}

$$\log(\phi) = \log(A) + \alpha \log(\eta/T) \quad (5.3)$$

The ‘ α ’ parameter in the above equation is reported to be the measure of strength of viscosity probe.^{172, 274} The variation in $\log(\phi)$ with $\log(\eta/T)$ has been presented in figure 5.15. The data has been fitted with equation 5.3 resulting α of 0.54. Such large value of ‘ α ’ indicates SYPRO Orange can be a very good viscosity probe. Thus, the fluorescence intensity of SYPRO Orange is also very sensitive to frictional force offered by the surrounding medium.

In order to get deep insight on the rate of excited state depopulation due to the variation in the viscosity of the surrounding medium, the fluorescence intensity decays of SYPRO Orange in glycerol at different temperatures have been recorded and

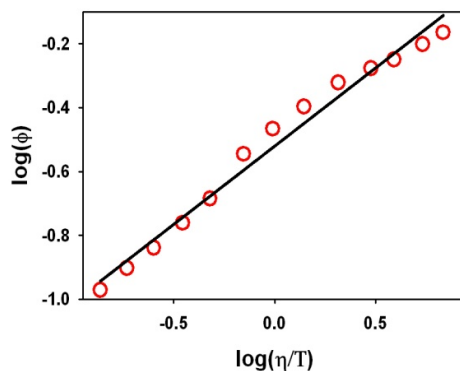


Figure 5.15 Forster-Hoffmann plot for SYPRO Orange in glycerol. Circles represent the data points and solid line represents their linear fit by equation 5.3.

presented in figure 5.16A. The transient fluorescence decays of SYPRO Orange gets faster with increase in temperature of the glycerol solution, i.e., decreasing the viscosity of the surrounding medium. All decays follow bi-exponential decay kinetics. The average fluorescence lifetime of SYPRO Orange in glycerol decreases from 2.3 ns at 15 °C to 0.2 ns at 70 °C. The ‘ α ’ parameter also have been obtained from $\log \tau_{\text{avg}}$ vs. $\log(\eta/T)$ plot (figure 5.16B) which is about 0.49. The ‘ α ’ value thus estimated from time-resolved measurements is very similar to that estimated by steady state emission experiments. Therefore, with increase in the viscosity of the surrounding medium, there is an enhancement in the emission intensity as well as the emission lifetime accompanied by blue shifted emission spectrum. Hence, we can infer that increased micro viscosity at the binding location also contributes towards the enhanced fluorescence obtained for SYPRO Orange in the presence of fibrils.

However, emission maximum observed for SYPRO Orange in glycerol at highest viscosity in this experiment is still 605 nm along with no shift in the

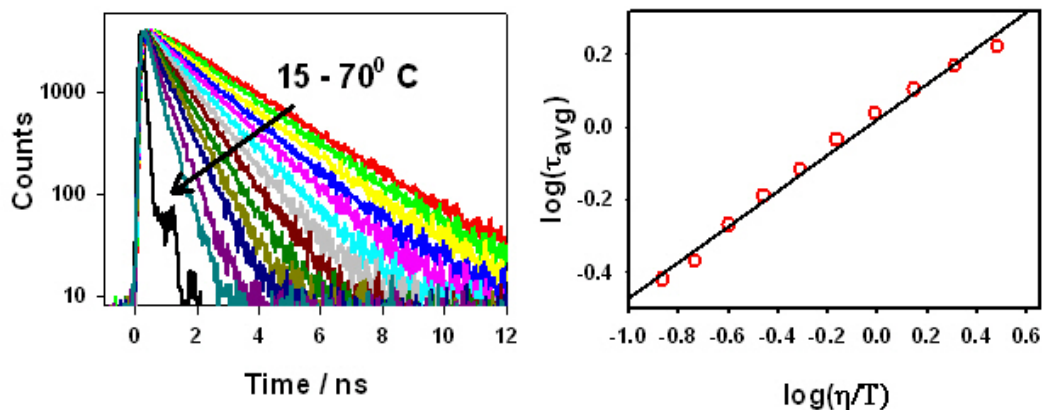


Figure 5.16 (A) The fluorescence decay traces of SYPRO Orange in glycerol at different temperatures. (B) Plot for the changes in the average lifetime of SYPRO Orange with solvent viscosity.

absorption peak. The ‘ α ’ value obtained for SYPRO Orange (0.54) is smaller compared to the ‘ α ’ value for ThT (0.98).¹⁷² This suggests viscosity is not the only reason for the observed spectral changes of SYPRO Orange in insulin fibril. Rather, both decrease in polarity and increase in rigidity around the binding site of SYPRO Orange in fibril is responsible for the observed spectral behaviour.

5.3.5.4 Effect of hydrogen bonding

Even after the detail photophysical studies in solvents with different polarity and viscosity, the reason for the observed bathochromic shift in the absorption spectra of SYPRO Orange in presence of high concentration of fibril remains unanswered. Considering the molecular structure of SYPRO Orange, there might be some sort of special interactions, such as hydrogen bonding, might be operating between SYPRO Orange and amino acids of the fibrils. Amino acids, such as glutamic acid, histidine etc., with side chains containing proton can form H-bond with the SYPRO Orange in amyloid fibrils. To understand the role of H-bonding in the photophysical properties,

the absorption and emission spectra of SYPRO Orange have been recorded in acetonitrile (ACN)-methanol (MeOH) solvent mixtures and shown in figure 5.17. Due to the similar dielectric constant of ACN ($\epsilon=37.5$) and MeOH ($\epsilon=34$) and similar viscosity ($\eta_{\text{MeOH}} = 0.45$ cP and $\eta_{\text{ACN}} = 0.34$ cP²⁸⁵), the polarity and viscosity will remain same for ACN-MeOH mixtures for all compositions. However, increase in the MeOH fraction in the solvent mixture will increase the intermolecular H-bond forming ability of the solvent mixtures. It is evident from figure 5.16A that increase in the MeOH fraction in the solvent mixtures results in a bathochromic shift in the absorption spectra of SYPRO Orange. Thus, the absorption maxima for SYPRO Orange are 486 nm in ACN and 496 nm in MeOH. However, it is evident from figure 5.17B that there is no change in either emission peak position or emission intensity of SYPRO Orange due to change in the composition of solvents. This result indicates that H-bonding doesn't affect the excited state while it is only stabilizing the ground state of SYPRO Orange. From the molecular structure of SYPRO Orange it can be intriguing that isolated sulphonate group may form H-bond with side chains of amino

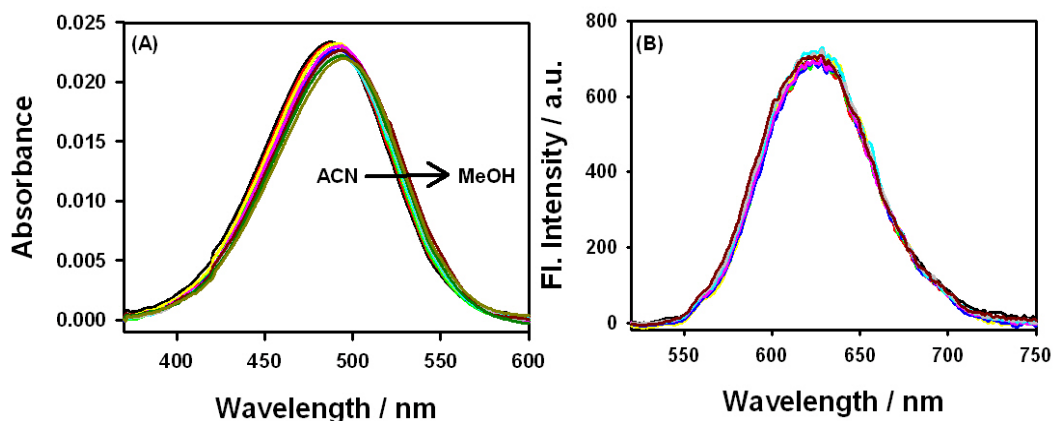


Figure 5.17 (A) Absorption spectra and (B) Emission spectra of SYPRO Orange in ACN-MeOH solvent mixtures.

acid while the main fluorophoric unit, amino stilbazolium group, is not interacting. These results revealed that the observed red shifted absorption is high concentration region of fibril bound SYPRO Orange is due to H-bonding effect at the binding location.

5.3.5.5 Effect of aggregation

As water is more polar and having strong H-bonding ability than MeOH,^{285, 318} we would expect aqueous solution of SYPRO Orange should show absorption maximum at much longer wavelength as compared to other solvent studied. Unexpectedly, the absorption peak of SYPRO Orange in water is 487 nm which is ~9 nm blue shifted compared to that in MeOH. To investigate such unusual behaviour, we have studied the photophysical properties of SYPRO Orange in MeOH-water mixtures. Absorption and emission spectra of SYPRO Orange recorded in MeOH-water mixtures at different compositions are presented in figure 5.18 and 5.19. Based on the spectral behaviour SYPRO Orange in MeOH-water mixtures, results are divided into three regions: (a) 0-50% H₂O (b) 50-80 % H₂O (c) 80- 100% H₂O. In the first region the absorption as well as emission properties doesn't change due to the addition of water to the methanolic solution of SYPRO Orange. This result indicates that even in the presence of 50% water in the solvent mixture, there is no specific interaction between solvent and SYPRO Orange. However, in the second region, i.e. 50-80% H₂O, there is continuous blue shift of absorption maxima due to the increase in the water content. Thus, the absorption maxima changes from 495 nm in presence of 50% water to 481 nm in presence of 80% water in the MeOH-water solvent mixtures. Along with the spectral shift, there is also a significant increase in the spectral width of the absorption spectra due to increase in the water content. It is also

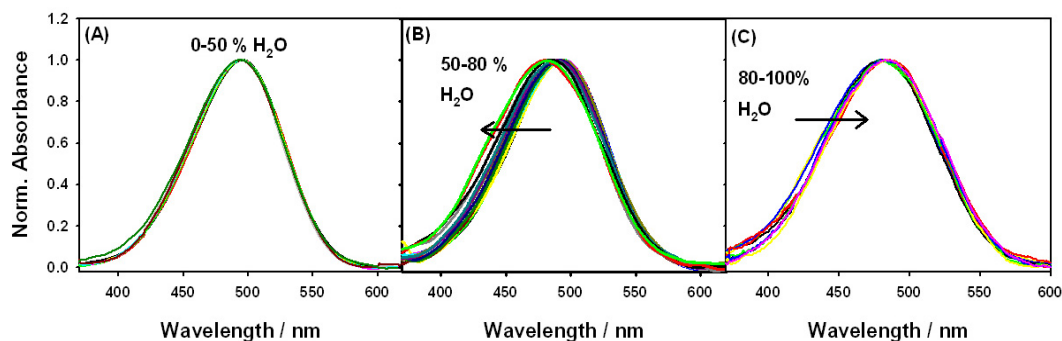


Figure 5.18 Normalized absorption spectra of SYPRO Orange in MeOH-H₂O mixtures with different compositions. (A) 0-50% H₂O. (B) 50-80% H₂O. (C) 80-100% H₂O.

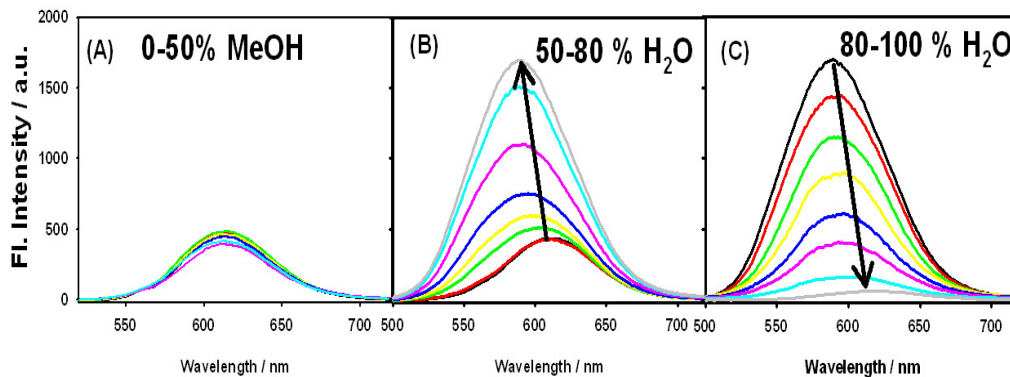


Figure 5.19 Fluorescence spectra of SYPRO Orange in MeOH-H₂O mixtures with different compositions. (A) 0-50% H₂O. (B) 50-75% H₂O. (C) 75-100% H₂O.

evident from figure 5.18B that due to the addition of water a new emission band at ~590 nm which is ~30 nm blue shifted from emission spectra of SYPRO Orange in MeOH, has been observed. Such changes in emission spectra have been reported to be due to aggregate formation for several classes of molecules.^{191, 364, 365} Drawing analogy, we propose that there is some sort of aggregate formation occurs in this solvent mixture. The nature of these aggregates is not yet understood.

In the third region, i.e., 80-100 % H₂O the absorption spectra shows bathochromic shift of ~7 nm which makes the absorption spectral peak at ~487 nm in

water. In this region, the emission spectra shifted back to 620 nm along with large reduction in the emission intensity. This might be possible that SYPRO Orange is aggregating to larger aggregates, which lead to drastic quenching in the emission yield.

The ratio of absorbance at 450 nm (close to aggregate absorption) and 500 nm (close to monomer absorption) has been calculated and plotted as a function of percentage of water and presented in figure 5.20A. It is obvious from the figure that up to 50% water, there is no change in ratio indicating absence of any aggregation till 50% of water. Further addition of water, i.e., up to 80% water, causes rise in absorbance ratio indicates the formation of aggregates of SYPRO Orange. However, above 80% water, the absorbance ratio started decreasing. This effect is clearly visible from the ratio of fluorescence intensity at 575 nm (predominantly aggregate emission) and 610 nm (predominantly monomer emission) which is shown in figure 5.20B. Such changes might be possible due to the formation of higher degree of aggregates when water content exceeds 80% in water-MeOH mixtures. However, if the former case is true, then the fluorescence intensity of SYPRO Orange should be recovered to level of intensity in MeOH. Contrastingly, the fluorescence has been significantly quenched in third region of MeOH-water mixtures. The formation of higher aggregates might be the possible case for SYPRO Orange in this region in which exciton quenching can take place leads to low fluorescence in water.

Increase in the fluorescence lifetime along with the rise of new emission band is shown to be one of the evidence for aggregate formation.^{191, 364, 365} In order to check such possibility, emission transients were recorded for SYPRO Orange in MeOH-water mixtures using TCSPC technique and the results are displayed in figure 5.21.

The emission decays are also follows the same trend as fluorescence intensity. Upto 50% of water there is no change in the rate of emission decay which yields a lifetime

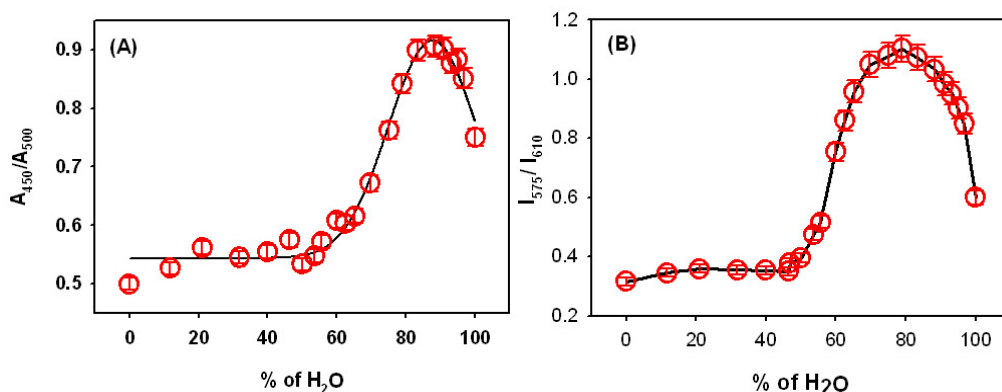


Figure 5.20 The variation in the ratio of (A) absorbance ratio of 450 nm to 500 nm and (B) fluorescence intensity ratio of 575 nm to 610 nm for SYPRO Orange as a function of percentage of water in MeOH.

of ~100 ps (data not shown). However, in the second region, it is observed that the decay of excited state becomes slower with increase in the percentage of water. However, on further addition of water results in the significant increase in the rate of emission decay of SYPRO Orange.

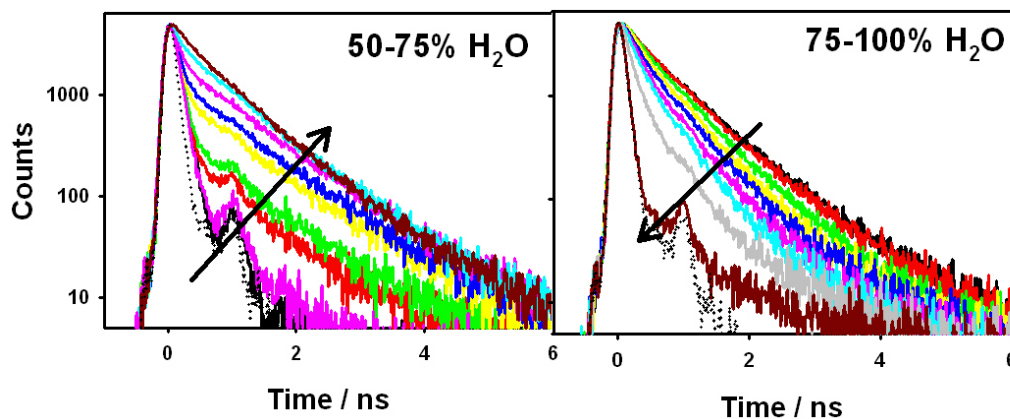


Figure 5.21 Fluorescence transient decays for SYPRO Orange in MeOH-H₂O mixtures with different compositions. (A) 50-80 % water (B) 80-100 % water

All decays were fitted with tri-exponential decay function. The variation in the average lifetime of SYPRO Orange with water content in MeOH-water mixtures is presented in figure 5.22. It is clear that there is no change in the average lifetime up to 50% water but the rise in lifetime on further addition of water up to 80% water clearly indicates the aggregate formation. However, for more than 80% water, there is drastic reduction in the excited state lifetime of SYPRO Orange.

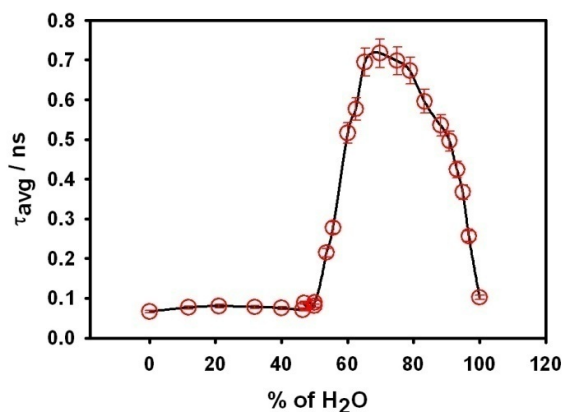


Figure 5.22 The variation in the average lifetime of SYPRO Orange with the water content in MeOH-H₂O mixtures. Solid line is guide to eye.

5.3.5.6 Mechanism of Binding of SYPRO Orange to insulin fibril.

The absorption and emission measurements suggested that there are two binding modes exist between SYPRO Orange and fibril. One mode of binding at the low concentration region (<1 μM) of fibril and other is at high concentration region (1-30 μM) region of the fibril. In the first mode of binding we have observed there is blue shift in the absorption accompanied by blue shift in the emission. From the detail spectroscopic studies in molecular solvents, we may infer that in aqueous solution SYPRO Orange exist as large aggregates. Thus, on initial addition of fibril to aqueous solution of SYPRO Orange causes disaggregation of dye followed by its binding in

the hydrophobic site of amyloid fibrils. This can explain observed hypsochromic shift in both absorption and emission along with the large enhancement in the fluorescence intensity.

Further addition of fibril causes bathochromic shift in the absorption along with hypsochromic shift in the emission. Therefore, we are proposing that in the second weaker binding mode, SYPRO Orange binds to fibril at location where there is strong hydrogen bonding interaction between SYPRO Orange and side chains amino acids like glutamic acid, histidine etc., which explains the red shifted absorption. At this location SYPRO Orange also experiences higher micro viscosity which explains the enhanced emission along with the blue shift in the emission spectrum.

5.3.6 Quantum chemical calculations and Molecular docking studies

The structures of 2Me-DABT and ThT were optimized by quantum chemical calculations using a Gaussian 03 package.²⁶⁹ B3LYP^{267, 268} functional and 6-31++g(d,p) basis function was used to optimize the chemical structures by DFT. The minimum energy configuration of SYPRO Orange was shown in figure 5.23 and is used further in docking studies.

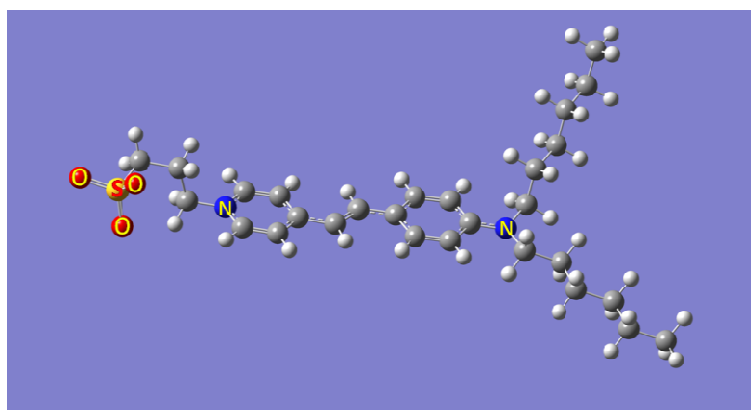


Figure 5.23 Minimum energy configuration of SYPRO Orange

To further acquire the knowledge of nature of binding between SYPRO Orange and fibril, blind molecular docking studies has been performed. As there is no detail structural information on insulin fibrils, in docking studies we have used the fibrillar structure (PDB ID: 2MXU) of A β ₁₋₄₂ as host.²⁷¹ The molecular structure of SYPRO Orange has been optimized using quantum chemical calculations and has been used in docking studies. Docking has been executed with various initial positions of SYPRO Orange with respect to the host fibril. Most energetically stable configuration of SYPRO Orange-fibril has been shown in figure 5.24A as mode I. The figure shows that the dye molecule located in the inner groove of fibrils which is in close agreement with the first mode of proposed binding. Close look on this mode has been shown in figure 5.24B. From this figure, we can see that there is no special interactions have been observed which indicates that hydrophobic stabilization is the main reason for the observed binding of SYPRO Orange to fibril. The binding energy calculated is about 4.74 kcal / mole. To understand the other mode of binding, docking of another SYPRO Orange molecule was carried out using most stable docked SYPRO Orange-fibril complex as host which has been shown in figure 5.24A as mode II. Figure 5.23 C shows a close look at the second mode of binding. The estimated binding energy is about 3.93 kcal/ mole. Thus, docking results supports the experimental results.

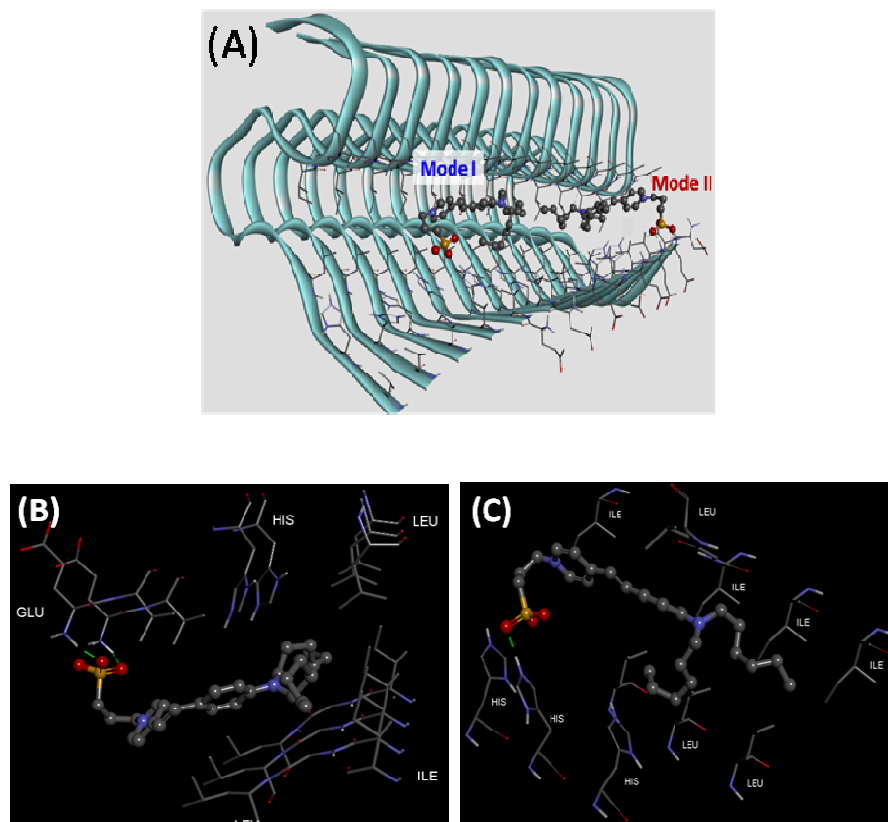


Figure 5.24 (A) Two most probable binding sites for SYPRO Orange in amyloid fibrils obtained from molecular docking studies. Close look of (B) mode I (C) mode II. The dashed lines indicate that H-bonding interactions between SYPRO Orange and side chain of glutamic acid.

Conclusions

Thus, we have demonstrated that SYPRO Orange, a zwitterionic probe, can be a sensitive probe for the amyloid fibrils. SYPRO Orange shows better fluorescence properties in the presence of fibril and brighter images compared to standard amyloid stain, Thioflavin T. SYPRO Orange shows ~34 times lower detection limit compared to ThT makes SYPRO Orange a more sensitive amyloid probe than ThT. From the detailed photophysical studies in fibril, it has been understood that there are two

modes of binding of SYPRO Orange to fibril exists. Detailed photophysical studies of SYPRO Orange in molecular solvents helps in elucidating the mechanism of interaction of SYPRO Orange to fibrils. One mode of binding is involved in disaggregation process of aqueous dye solution accompanied by the binding in inner core of the fibrils stabilized by hydrophobic forces. Second mode of binding involves the hydrogen bonding interaction of sulphonate group with side chains of amino acids in fibril and increased micro viscosity around the probe which leads to large fluorescence enhancement. Such a large fluorescence enhancement, ionic strength independence, orange fluorescence makes SYPRO Orange as better probe for amyloid fibrils.

Chapter-6

Solvent relaxation dynamics in amyloid fibrils

6.1 Introduction

The mechanistic understanding of protein's self assembly and its relation to amyloidosis is still a matter of debate as there is very limited experimental means by which the detailed dynamics of protein aggregation can be monitored in real time.^{21, 34, 61, 366, 367} Moreover, the recent evidences suggest that the diffusible intermediate species appear during the aggregation pathway and are involved in pathology of amyloid related diseases.^{21, 34, 61, 366, 367} Besides that, the fibrillar structure can be disintegrated and dissolved by a number of small molecules indicates that the amyloid structure is dynamical in nature.³⁶⁸⁻³⁷⁰ In fact, there are cases where the disaggregation of fibrils leads to reduction in the symptoms of the corresponding diseases.^{371, 372} This highlights the importance of elucidation of high resolution dynamics along aggregation pathways for a comprehensive understanding of the molecular basis of amyloid diseases.

Studies on amyloid fibrils is mostly focused on the effect of protein conformation⁴⁹, amino acid sequence,^{20, 36, 48} and environmental conditions like pH,^{194, 373} ionic strength³⁷⁴ etc., to understand protein-protein interactions. But water is

treated as spectator even it is an important constituent in biological system.³⁷⁵ As a matter of fact, the solubility of proteins and the inter protein interactions are highly rely on the neighboring water molecules which hydrate them.³⁷⁵ Recently Chong et. al studied the role of surrounding water in determining the proneness of proteins to undergo aggregation.¹⁵⁰ They have correlated hydrophobicity of different amyloid forming proteins with their prone towards the aggregation.³⁷⁶ A good correlation even with the proteins with large variation in their native structures and amino acid sequences has been shown. These results indicate that it is the surrounding water which controls the propensity of protein's aggregation in aqueous solutions rather the protein itself. They have further shown that the electrostatic interaction between water and protein molecules plays an important role in the protein aggregation process.¹⁵⁰ The long range order of water structure is accountable for two protein molecules to come closer to aggregate. Once protein molecules come in contact, the inter-protein interactions control the aggregation process. Thus, water molecules around the protein plays vital role in the formation of amyloid fibrils.^{150, 376}

De Simone and co-workers investigated the role of hydration on the amyloid fibril formation of Ribonuclease A using molecular dynamics simulations.^{50, 377} They found that there are two types of water exist in fibrillar structure, buried and surface water. Buried water guides the structural dynamics of proteins, while the surface water plays an important role in protein aggregation.³⁷⁷ They have shown that surface water is always in dynamical exchange with the bulk water. Such exchange process is highly entropically favorable and reduces the activation energy for the protein unfolding. It is further shown that the residence time of surface water is very short.³⁷⁷ Thus, all these

studies indicate that the dynamics of water in and around the protein molecules play a crucial role in the formation of amyloid fibril.

Recently, fibrillation of human serum albumin (HSA) has been studied by several research groups.^{17, 18, 378, 379} HSA plays a key role in transporting fatty acids, and other physiologically essential molecules.³⁸⁰ It regulates osmotic pressure of blood. HSA is a single poly peptide chain containing 585 amino acid molecules with α -helix as major structural motif. More importantly, it contains a tryptophan (W214), a valuable environment sensitive fluorescence probe which can be used to probe the local dynamics around it. Its emission maximum, intensity, fluorescence lifetime and depolarization time are the most useful information that have been used to reveal the structural information of proteins.³⁸¹⁻³⁸⁴ Native HSA protein has very less β -sheet content (~5%), and hence the possibility for preformed fibrils is negligible. The formation of unfolded / misfolded protein is requisite for the fibril formation and hence heating at elevated temperatures leads to formation of HSA fibril.³⁸⁵

To understand the solvent interaction in the fibrillation process of HSA, recently Juarez et. al. studied the effect of alcohol on the fibrillation of HSA at different pH.³⁸⁶ They found that the electrostatic interaction of solvent with the protein changes the fibrillation kinetics, its morphology and the extent of fibril formation. Hydrogen bonding by solvent with the β -sheets changes the fibrillar structure from curly fibers to straight long fibrils. It is very interesting that pre and post addition of alcohols to the fibrils has contradictory behavior. Pre addition enhances the fibrillation and post addition dissolves the fibrils.³⁸⁷ Thus, it is clear that solvent interaction with proteins has a very crucial role in HSA fibrillation.^{385, 387} Though the interaction of

water with protein depicts its biological activity but the water interaction with amyloid fibrils are not well known.

Herein we have tried to elucidate and understand the local structural flexibility of protein and the nature of water in the fibrillar state by monitoring time dependent spectral changes of the sole tryptophan (W214) in HSA. By investigating the tryptophan fluorescence dynamics we can elucidate the local structural flexibility and nature of water in the fibrillar state.

6.2. Materials and Methods:

HSA, Tris(hydroxymethyl) aminomethane) (Tris) were purchased from Sigma Aldrich and used without further purification. Nanopure water (conductivity less than 0.1 mScm^{-1}), from a Millipore Milli Q system, was used for all sample preparations. All the samples are freshly prepared before the prior experiments. Fibrils were prepared by dissolving HSA (2mg/ml) in Tris-HCl buffer (pH~7.4) and heated at 65°C for 4 hours.³⁸⁵

Steady-state fluorescence spectra were measured with Hitachi F-4500 spectrofluorimeter whose details were discussed in chapter 2. The emission spectra were corrected for the wavelength-dependent instrument responses using the spectrum of standard aqueous tryptophan solution. The measured wavelength domain spectra, $I(\lambda)$, were converted into the frequency domain spectra, $I(\nu)$, by using the following equation.

$$I(\nu) = \lambda^2 I(\lambda) \quad (6.1)$$

The fluorescence transients were collected at wavelengths with 10 nm interval over the entire emission spectrum using time-correlated single-photon counting (TCSPC) instrument from IBH, UK. The samples were excited with 295 nm, 1MHz LED. The instrument response function for these time-resolved measurements was \sim 780 ps. All the fluorescence decays were fitted with tri-exponential decay function using an iterative convolution method. Time-resolved emission spectra (TRES) were constructed according to the method explained in chapter 3.

Time dependent fluorescence anisotropy was calculated by using the following equation.¹²⁵

$$r(t) = \frac{I_{\parallel}(t) - GI_{\perp}(t)}{I_{\parallel}(t) + 2GI_{\perp}(t)} \quad (6.2)$$

$$r(t) = r_0 \exp(-t / \tau_r) \quad (6.3)$$

where, I_{\parallel} and I_{\perp} are the two polarized fluorescence decays with emission polarizations parallel and perpendicular to the vertically polarized excitation light, respectively. To correct the polarization dependent instrumental sensitivity, G factor was measured separately.

6.3. Results and Discussion:

6.3.1. HSA fibril formation

The fibril formation of HSA has been monitored through standard Thioflavin T fluorescence assay.²³⁸ The comparison of the ThT fluorescence intensity before and after fibrillation is presented in figure 6.1A. The increase in the ThT fluorescence by \sim 15 fold indicates the formation of HSA fibril. The changes in the ThT emission

intensity during fibrillation is presented in inset of figure 6.1 A. It is evident from the figure that there is no lag phase in HSA fibrillation process suggesting that the formation of HSA fibril is thermodynamically feasible process.³⁸⁸ No further change in the emission intensity of ThT at longer fibrillation time indicates the completion of the fibrillation process. Thus, in present work fibrils formed after heating the protein sample for 4 hours are used for further experiments.

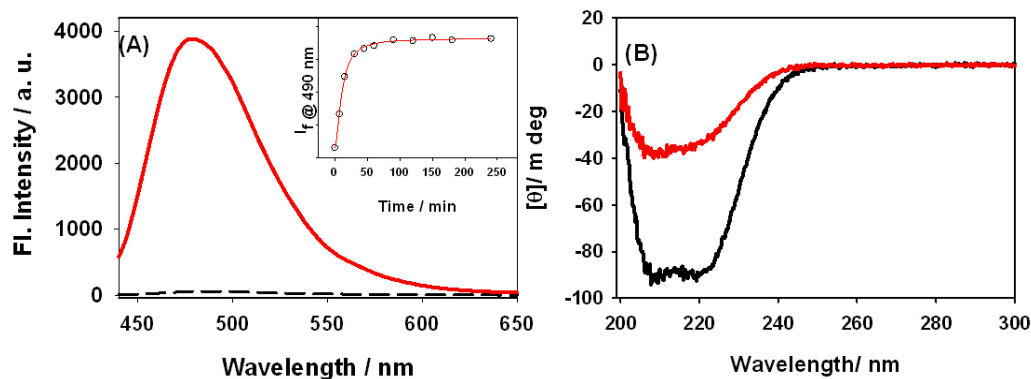


Figure 6.1 (A) Fluorescence spectra of ThT in HSA protein (dashed) and fibril (solid).

Inset: Variation in the ThT fluorescence intensity during HSA fibrillation. **(B)** Far-UV circular dichroism spectra of (a) HSA protein and b) HSA fibril.

Figure 6.1B shows far UV circular dichroism (CD) spectra of HSA protein and fibril. Native HSA protein shows negative peaks at 208 nm and 220 nm which are characteristic of α helical structure.^{18, 388-390} The intensity of CD signal at both these peak positions reduces substantially in the amyloid fibrils. Such large changes in the CD spectra clearly indicates that in the fibril the α helical content is drastically reduced and consequently the β -sheet or coiled structures is increased. The strong reduction in the intensity of 220 nm peak clearly indicates the increase of β -sheet structure at the expense of helical content.^{18, 388, 390}

6.3.2. Steady state fluorescence measurements

Steady state fluorescence spectra of W214 in HSA protein and fibril have been recorded by exciting at 295nm and results are presented in figure 6.2. The excitation wavelength is chosen in such a way that only tryptophan residue will be excited preferentially.¹²⁵ HSA in its native form shows emission maximum at 345nm.³⁹¹ However, HSA fibril shows a fluorescence peak at 337 nm showing a blue shift of ~8nm compared to its native form. Such a blue shift in the fluorescence spectra of W214 in HSA due to fibrillation has been reported in the literature.³⁸⁷ Such blue shift in the emission spectra indicates that the micro environment around W214 changes substantially due to the fibrillation process.¹²⁵ Further, preferential quenching of red side of tryptophan emission spectrum by charged amino acid residues can also cause blue shift in HSA fibril. Sometimes even exposure to water can also cause blue shift of the tryptophan emission spectra.³⁹² Such blue shift explicitly depends on the orientation of water molecules with respect to indole ring of tryptophan.³⁹³

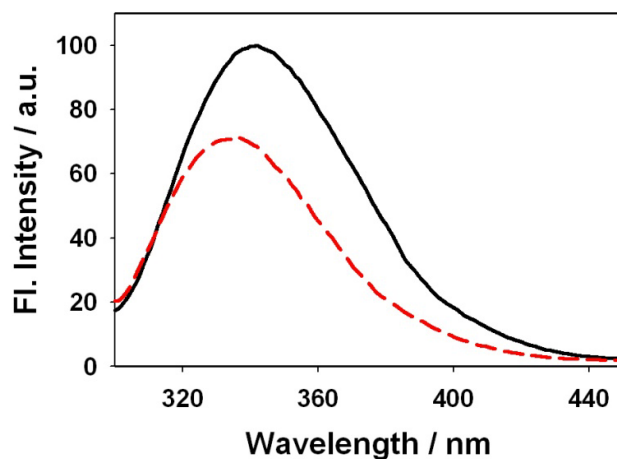


Figure 6.2 Steady state emission spectra ($\lambda_{\text{ex}}=295$ nm) of HSA native protein (solid) and fibril (dashed).

It can also be seen from figure 6.2 that there is reduction in the fluorescence intensity of tryptophan during the fibrillation process. This indicates in the fibrillar phase W214 may be situated closer proximity to charged amino acid residues like arginine etc.³⁸⁴ From the crystal structure of HSA, it is shown that polar amino acid residues like R218, K199 and E450 are in the nearby region of W214.³⁹⁴ Bhagavan and his co workers showed that R218 is mainly responsible for the electronic quenching of W214 by site directed mutagenesis.³⁸⁴ X-Ray structure of HSA shows that R218 is apart from W214 by 3.14 Å. Fluorescence quenching might also be due to the exposure of tryptophan to water molecules.³⁹⁵ Water can stabilize the charge transfer state and increases the rate of electron transfer reaction thus decreases the fluorescence yield. There are several reports showing the quenching of indole derivatives due to the involvement of hydrogen bonding in protic solvents.¹²⁵

6.3.3 Time resolved measurements

In order to understand the changes in the environment of W214 due to the fibrillation, detail time resolved fluorescence studies have been carried out. Fluorescence transients recorded for W214 in native protein and fibrils are shown in figure 6.3. It is evident from the figure that fluorescence intensity of W214 decays faster in fibril compared to native protein. Both transient decays have been fitted with tri-exponential decay function and the average lifetime estimated to be 5.85 ns for native protein and 4.06 ns for amyloid fibrils. Such decrease in the excited state lifetime also supports that the tryptophan fluorescence has been quenched due to more close proximity of polar amino acids in fibril as compared to native protein.³⁹²

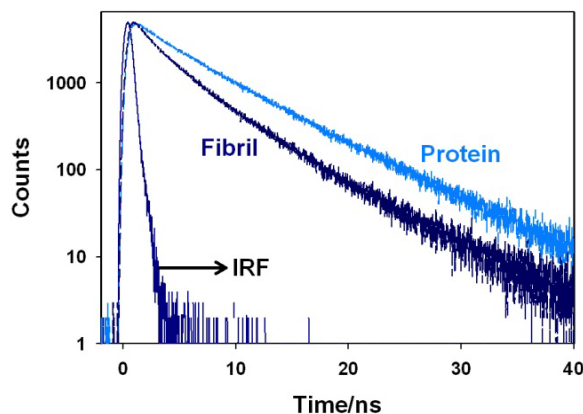


Figure 6.3 Fluorescence transients of tryptophan in HSA protein and fibril at their corresponding emission peak wavelength.

Table 6.1 Fitting parameters of fluorescence decay traces of HSA protein and fibril

HSA	a_1	τ_1 / ns	a_2	τ_2 / ns	a_3	τ_3 / ns	$\tau_{\text{avg}} / \text{ns}$
Protein	0.014	0.49	0.316	3.71	0.670	6.98	5.85
Fibril	0.060	0.41	0.425	2.44	0.515	5.85	4.06

To explore the excited state dynamics of W214 in the fibrillar state, we have carried out detail wavelength dependent fluorescence measurements of HSA fibril and the results are shown in figure 6.4. It is clear from the figure that the emission transient decays are strongly dependent on the emission wavelength. The fluorescence transient in the blue edge of the spectrum decays relatively faster than the decay at the red edge of the spectrum. Similar wavelength dependent emission transient decays have also been observed for native HSA. However, transient decays at all emission wavelengths are relatively faster for amyloid fibril than native protein.

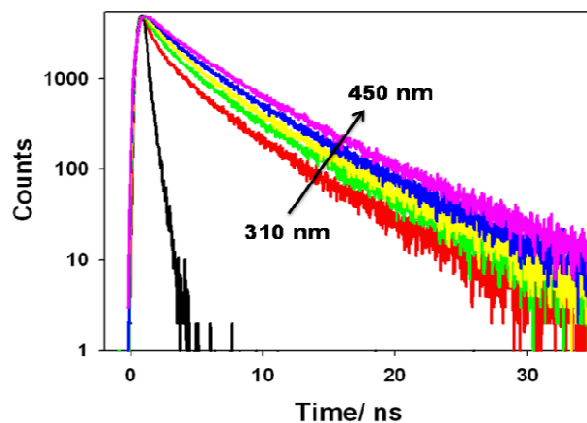


Figure 6.4 Fluorescence transients for W214 in HSA fibril at different emission wavelengths. The black curve represents the IRF.

To understand the excited state dynamics of W214 in fibril, time-resolved emission spectra (TRES) have been constructed by the method proposed by Maroncelli and Fleming.¹³⁸ The TRES thus constructed has been shown in figure 6.5A. TRES was constructed for HSA native protein also and the results are compared with the fibril. From figure 6.5A, it is evident that the intensity of the transient fluo-

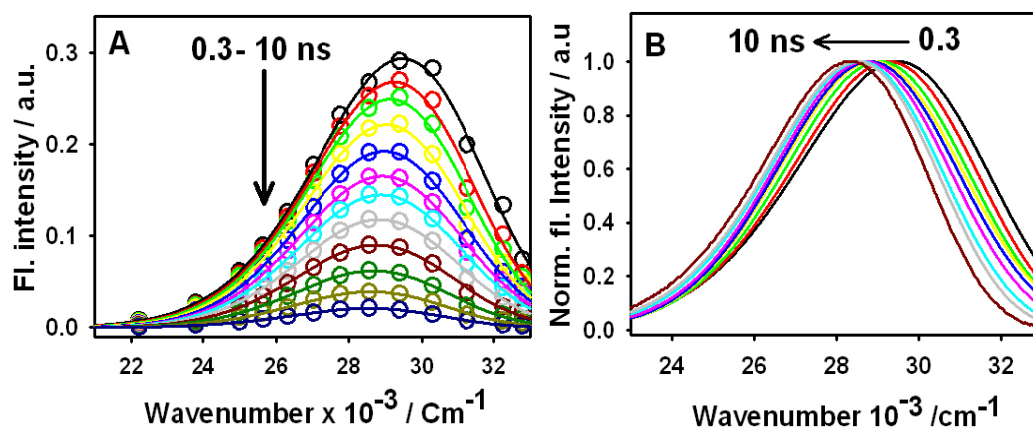


Figure 6.5 (A) Time-resolved emission spectra (TRES) of HSA fibril. Circles show the data points and solid lines represents corresponding log-normal fits. **(B)** Peak normalized TRES of HSA fibril from 0.3 to 10 ns.

cence spectra decreases with time. In addition to the decrease in intensity, a significant time dependent fluorescence Stokes' shift has also been observed (cf. figure 6.5B). Thus, emission maximum shifts from $29,474 \text{ cm}^{-1}$ at 0.3 ns to $28,576 \text{ cm}^{-1}$ at 10 ns.

Figure 6.6 represents the variation in the area under the emission spectra with time for native and fibrillar protein. Note that the emission intensity decay is relatively faster in fibrillar medium than the native protein. The decay of area under the emission curve has been fitted with multi exponential function and the average decay times were estimated to be 5.91 ns and 4.1 ns for protein in native and fibrillar form, respectively. This result is in agreement with the fluorescence lifetime obtained from the decay at their respective emission maxima.

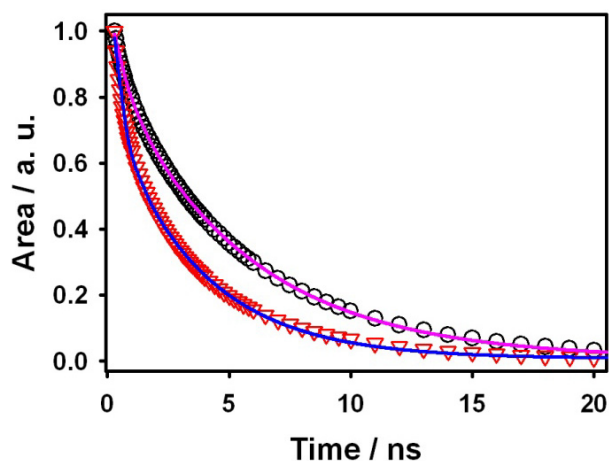


Figure 6.6 The variation in the area under the emission spectrum of fibril (∇) and native protein (\circ). The solid line represents their multi exponential fits.

To get more detailed information on the excited state dynamics, we examined the variation of peak of the transient emission spectra with time. The temporal peak profile for fibril and protein are shown in figure 6.7. It is evident from the figure that

extent of change in the peak frequency is more and faster for the fibril compared to that in the native HSA. The variations of the emission peak position with time were fitted with a bi-exponential function and the time constants obtained are 180 ps (79%) and 5.35 ns (21%) for fibril and 470 ps (46%) and 12.8 ns (54%) for the native protein. Thus, the average time constant for the rate of change in emission peak position is estimated to be 1.26 ns & 7.12 ns for the fibrillar & native protein, respectively. The change in emission peak of W214 in native protein is reported to be due to the solvent relaxation process.³⁹⁶ Drawing analogy with protein, the observed dynamic Stokes' shift in fibrillar solution is also assigned to the solvent relaxation process.

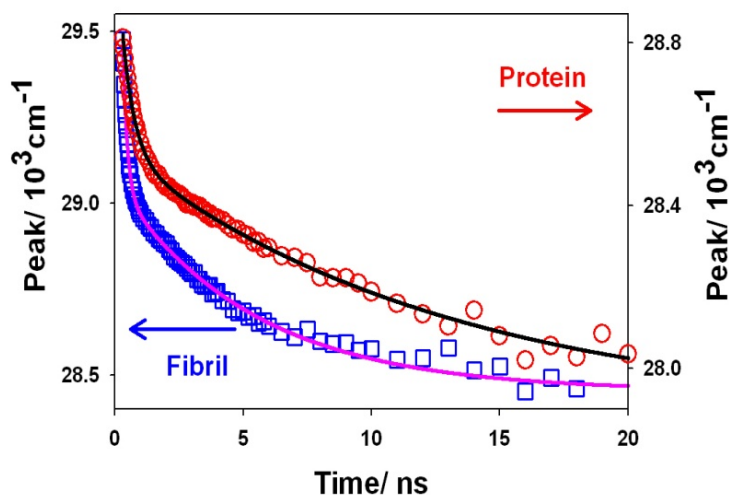


Figure 6.7 Variation in the emission maxima with time for protein (○) and fibril (□).

The solid lines represent the bi-exponential fits

Thus, from the present result, it is quite evident that the solvent relaxation process becomes much faster in fibrillar phase as compared to that in native protein despite having more ordered structure in the fibril. Crystallographic data of HSA suggests that there is some bound water molecules are available near tryptophan

residues which can solvate W214 in nanosecond time scales.³⁹⁴ Hence, faster solvent relaxation in fibril eventually suggests that in fibrillation W214 gets more exposed to more mobile water. As the protein unfolding is the initial step in the fibril formation,¹⁶ it is quite possible that during the unfolding process the region where tryptophan resides getting more exposure to the bulk water or some water channels which are more labile than the native protein. These results suggest that even though the amyloid fibril structure is highly ordered, there are solvent accessible regions and have a faster hydration dynamics than the protein.

Recently Schiro and his coworkers have studied nanosecond dynamics of Concanavalin A (Con A) amyloid fibrils using neutron scattering experiments at different temperatures.^{397, 398} They observed that the fibrils have more mobile H-atoms compared to the native protein and amorphous aggregates. But FTIR and circular dichroism spectroscopic studies suggest the formation of ordered amyloid structures. In the fibril structure, the side chains are extended towards the fibril surface and reducing the steric hindrance from the other amino acids and allowing the water interactions easier.^{397, 398} MD simulation studies of amyloid β protein also suggest that there are hydrated cavities in the fibrillar structure.³⁹⁹ Hochstrasser and co-workers also showed that the mobile water molecules are present in the amyloid structures of A β (1-40) using two-dimensional infrared (2DIR) spectroscopy.¹⁴⁹ Based on spectral diffusion studies they inferred that there are channels that contain energetic water molecules between two beta sheets. Therefore, in HSA fibril, W214 may be situated and exposed to water in such hydrated cavities which leads to the faster solvation dynamics.

It is evident from figure 6.5B that apart from change in the peak frequency and area under the emission spectrum, there are substantial changes in the spectral width, especially towards the blue edge of the emission spectrum. To understand such changes in the shape of the emission spectrum, the temporal variation in the FWHM of the emission spectrum has been plotted in figure 6.8 for native protein and fibril.

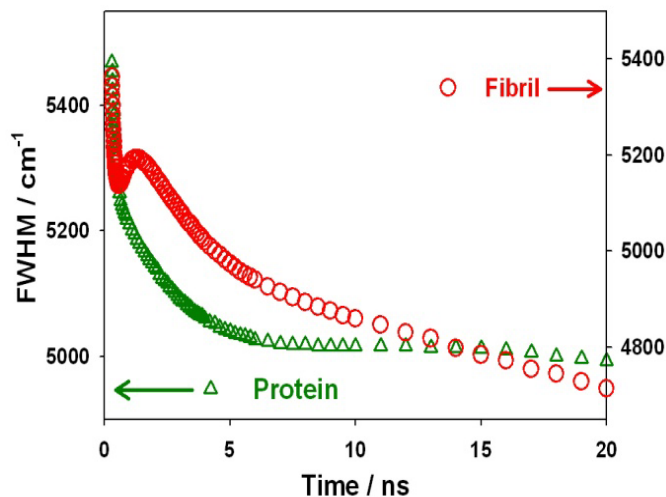


Figure 6.8 Time dependent variation of FWHM for HSA protein (\triangle) and fibril (\circ).

The evolution of spectral width is a very useful in understanding the heterogeneity of the medium around the fluorophore.⁴⁰⁰ It is evident from figure 6.8 that in both native and fibrillar HSA, there is $\sim 10\%$ decrease in the FWHM with time. Such decrease in spectral width, due to solvent relaxation, is well established for the homogeneous and micro heterogeneous systems and assigned to the change in solvent environment of the probe due to photoexcitation.^{138, 401-403} It is evident from figure 6.8 that unlike native protein, the time course of FWHM for the fibril shows a distinct maximum. Such kind of behavior is observed in highly heterogeneous media like supercooled liquids,⁴⁰⁴ lipid bilayers,⁴⁰³ etc. In such heterogeneous systems, the

fluorophore resides in spatially different micro environments which respond to the excitation light separately. Some of the molecules relax faster and some relax slower which causes broadening in the transient emission spectra. This leads to maximum in TRES width at intermediate times. The amount of broadening is measure of heterogeneity of the system. Qui et. al reported that HSA protein shows FWHM broadening in the picosecond regime,¹⁴³ while in fibril we have observed the peak in the nanosecond regime which indicates the increase in the heterogeneity of the system. This indicates fibrils are more heterogeneous than the native protein. It is reported that even at the same growth conditions amyloid fibrils can form different morphologies.^{405, 406} Sometimes even the external appearance is same, but the internal cross beta structure differs.^{266, 407} There are reports showing that same protein under similar conditions forms fibrils with difference in the number of protofibrils comprising them.⁴² Actually, structural heterogeneity is itself exists in the partially folded conformers which are initial precursors for the fibril formation.⁴⁰⁸ But protein has a distinct secondary structure. Structural heterogeneity is not expected in protein in its native form unless there is any external perturbation. 2DIR spectra of A β 1-40 fibrils also support the presence of the microscopic heterogeneity in the individual fibrils which leads to appearance of multiple diagonal peaks and corresponding cross peaks.¹⁴⁹ 2DIR spectra is expected to give a single diagonal peak for amide II band, but in the experiments shows there are multiple diagonal peaks appeared along with the corresponding cross peaks. This indicates the peaks appearing from a single fibril and they are coupled.¹⁴⁹ This indicates microscopic heterogeneity exists in the individual fibrils. All these observations suggest that fibrils are intrinsically heterogeneous.

6.3.4. Time resolved anisotropy studies:

For the better understanding on the local flexibility of HSA in the fibrillar form, time-resolved fluorescence depolarization experiments have been carried out and the results are shown in figure 6.9. The anisotropy decays were fitted with bi-exponential decay function and the fitting parameters are tabulated in table 6.1. HSA protein is known to show two rotational reorientation times, one is in the sub nanosecond regime which is assigned to be tryptophan segmental motion and another time constant is in the order of few tens of nanoseconds which is assigned to be the whole rotation of the protein.⁴⁰⁹ From table 6.1 it is evident that in fibril segmental rotational reorientation time of W214 is slightly faster compared to native protein indicates the tryptophan resides in the softer core of the ordered amyloid fibrils. It is evident that the fibril shows large residual anisotropy (~ 0.15) compared to that of native protein (~ 0.05). The large size of the amyloid fibril results in long correlation times leads to large residual anisotropy.

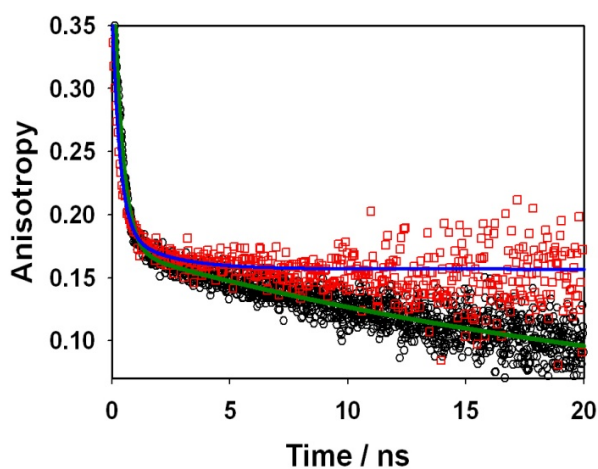


Figure 6.9 Time-resolved anisotropy of HSA protein (O) and fibril (□). The solid lines represent the bi-exponential fits to the experimental data.

Table 6.2 Fitting parameters for the time-resolved anisotropy decay of HSA protein and fibrils.

HSA	a_1	τ_1 / ns	a_2	τ_2 / ns	Residual anisotropy at 30 ns
Protein	0.42	0.386	0.58	26.46	0.05
Fibril	1.00	0.338			0.15

6.4. Conclusions:

Excited state dynamics of HSA fibril has been investigated by using its intrinsic tryptophan (W214) as a fluorescence probe by employing time-resolved fluorescence technique. The dynamics of water molecules around the tryptophan molecules have been studied through TDFSS studies. This study shows that in spite of having more ordered structure, tryptophan in fibril experiencing an environment with more labile water as compared to the native protein. The faster hydration dynamics in fibril suggests that the fibrillation of HSA causes the exposure of the tryptophan moiety to either bulk water or some water channels where water is more mobile than in the interior of the native protein.

To get more detailed information on the structural and dynamical aspects in fibrils, one should study the dynamics using spectroscopic technique with much shorter time resolution. These studies will provide results about short range fluctuations in the dynamics of the solvents as well as nearby amino acid residues around tryptophan during the fibrillation. Besides that the probing the dynamics of proteins at different stages of fibrillation, like nucleation, elongation and saturation, will give a brief description about the step by step changes in protein conformation

and role of hydration during the fibrillation. Further, incorporation fluorescent amino acid at different location of protein will help us to understand the site specific structure and dynamics of water molecules. Such information will help us to understand the specific contribution of each sites of protein towards fibrillogenesis. In future, we are planning to do such experiments in our lab to unravel the mechanism of fibrils as well as the changes in the hydration dynamics during fibrillation using time-resolved spectroscopy with sub-picosecond time resolution.

Chapter-7

Summary and Outlook

In the present thesis, we have explored the applicability of three classes of dyes cationic PicoGreen (PG), neutral derivative of Thioflavin T, 2Me-DABT and zwitterionic SYPRO Orange (SO) for the amyloid fibril detection. All the three dyes show very distinct changes in their photophysical properties in the presence of amyloid fibrils.

Cationic PicoGreen shows large enhancement in the fluorescence intensity as well as lifetime due to binding with insulin fibrils. It has been shown that PG is better amyloid probe than standard amyloid stain Thioflavin T (ThT). By employing ultrafast fluorescence spectroscopy, it has been identified that the large retardation in the internal torsional motion of PG upon binding with fibrils is primarily responsible for the observed large fluorescence enhancement in the presence of amyloid fibrils.

Neutral benzothiazole derivative, 2Me-DABT, has been synthesized in order to overcome the problem of low blood brain barrier penetrating power of its parent ThT. Unlike ThT, 2Me-DABT shows strong solvatochromic behavior due to its existence of emissive intramolecular charge transfer state. Very low quantum yield of 2Me-DABT in water is proven to be due to solute-solvent hydrogen bonding with solvents. The binding with insulin fibrils cause large enhancement in the fluorescence intensity

along with the large blue shift which makes this dye as efficient ratiometric sensor for the amyloid fibrils.

Zwitterionic SYPRO Orange is another probe which shows promising changes in its spectral properties due to the interaction with amyloid fibrils. SYPRO Orange shows large fluorescence enhancement, strong blue shift in the presence of insulin fibrils. SYPRO Orange gives brighter images of amyloid fibrils compared to ThT. It has also been shown to be ~35 times more sensitive than ThT. From the detailed photophysical studies in different molecular solvents, it has been understood that the breaking of preformed aggregates in aqueous SYPRO Orange solution along with special effects of hydrophobic binding, restriction in its internal dynamics and hydrogen bonding of SYPRO Orange with insulin fibrils as a whole give such a huge enhancement in its emission intensity upon binding with amyloid fibrils.

Apart from the detection of fibrils, it has also been tried to elucidate the dynamics of fibrils of well known blood plasma protein, Human Serum albumin(HSA), using its internal fluorescence probe Tryptophan(W214) and compared with the native protein. From detailed time-resolved fluorescence measurements, it has been shown that the dynamics are faster in the fibril compared to protein due to the presence of some labile water pocket in amyloid fibrils.

There is always a scope to develop new and better probes for the detection of amyloid fibrils. In recent days, NIR probes are found to be better alternative compared to standard PET probes in terms of ease of use, fast processing and non radioactive.^{122, 232, 237, 410, 411} In our lab, we are currently focus on the developing and understanding new NIR probes for the sensitive detection of amyloid fibrils both in-vitro and in-vivo. We have also initiated ultrafast spectroscopic studies on dynamics in amyloid fibrils

using both extrinsic fluorescence probes as well as intrinsic probes such as tryptophan. Such studies will elucidate the dynamics in the fibril in greater detail.

References

1. Chiti, F.; Dobson, C. M., *Annu. Rev. Biochem.* **2006**, 75, 333.
2. Fandrich, M., *Cell. Mol. Life Sci.* **2007**, 64, 2066.
3. Harper, J. D.; Lansbury, P. T., *Annu. Rev. Biochem.* **1997**, 66, 385.
4. Koo, E. H.; Jr., P. T. L.; Kelly, J. W., *Proc. Natl. Acad. Sci. USA* **1999**, 96, 9989.
5. Murphy, R. M., *Annu. Rev. Biochem.* **2002**, 4, 155.
6. Shahi, P.; Sharma, R.; Sanger, S.; Kumar, I.; Jolly, R. S., *Biochemistry* **2007**, 46, 7365.
7. Vander Linden, E.; Venema, P., *Curr. Opin. Colloid Interface Sci.* **2007**, 12, 158.
8. Wang, W., *Int. J. Biopharmaceutics* **2005**, 289, 1.
9. Bellotti, V.; Mangione, P.; Stoppini, M., *Cell. Mol. Life Sci.* **1999**, 55, 977.
10. Dobson, C. M., *Biochem. Soc. Symp.* **2001**, (1), 1.
11. Kelly, J. W., *Curr. Opin. Struct. Biol.* **1998**, 8, 101.
12. Uversky, V. N.; Talapatra, A.; Gillespie, J. R.; Fink, A. L., *Med. Sci. Monit.* **1999**, 5, 1001.
13. Uversky, V. N.; Talapatra, A.; Gillespie, J. R.; Fink, A. L., *Med. Sci. Monit.* **1999**, 5, 1238.
14. Francis, P. T., *J. Qual. Res. Dement* **2015**, 383, 4.
15. Dobson, C. M., *Nature* **2003**, 426, 884.
16. Uversky, V. N.; Fink, A. L., *Biochim. Biophys. Acta* **2004**, 1698, 131.
17. Sancataldo, G.; mail, V. V.; Foderà, V.; Cara, G. D.; Militello, V.; Leone, M., *PLOS One* **2014**, 9, e84552.
18. Pandey, N. K.; Ghosh, S.; Tripathy, D. R.; Dasgupta, S., *Protein Peptide Letts.* **2014**, DOI: 10.2174/0929866521666140320104409.
19. Buchanan, L. E.; Dunkelberger, E. B.; Tran, H. Q.; Cheng, P.-N.; Chiu, C.-C.; Cao, P.; Raleigh, D. P.; Pablo, J. J. d.; Nowick, J. S.; Zanni, M. T., *Proc. Natl. Acad. Sci. USA* **2013** 110 19285.
20. Yoon, G.; Lee, M.; Kim, J. I.; Na, S.; Eom, K., *Plos One* **2014**, 9, 1.
21. Kumar, S.; Udgaonkar, J. B., *Curr. Sci.* **2010**, 98, 639.
22. Zhou, Z.; Yan, X.; Pan, K.; Chen, J.; Xie, Z.-S.; Xiao, G.-F.; Yang, F.-Q.; Liang, Y., *Biophys. J.* **2011**, 101, 1483.
23. Tompa, P., *Trends Biochem. Sci.* **2002**, 27, 527.
24. Uversky, V. N., *Eur. J. Biochem.* **2002**, 269, 2.
25. Serpell, L. C., *Biochim. Biophys. Acta* **2000**, 1502, 16.
26. Serpell, L. C.; Sunde, M.; Benson, M. D.; Tennent, G. A.; Pepys, M. B.; Fraser, P. E., *J. Mol. Biol.* **2000**, 300, 1033.
27. Sunde, M.; Blake, C., *Adv. Protein Chem.* **1997**, 50, 123.
28. Sunde, M.; Serpell, L. C.; Bartlam, M.; Fraser, P. E.; Pepys, M. B.; Blake, C. C., *J. Mol. Biol.* **1997**, 273, 729.
29. Mali, K. S.; Dutt, G. B., *J. Chem. Sci.* **2007**, 119, 147.
30. Pertinhez, T. A.; Bouchard, M.; Tomlinson, E. J.; R.Wain; Ferguson, S. J.; Dobson, C. M.; Smith, L. J., *FEBS Lett.* **2001**, 495, 184.
31. Dobson, C. M., *Trends Biochem. Sci.* **1999**, 24, (329-332).

32. Lansbury Jr, P. T., *Proc. Natl. Acad. Sci. U. S. A.* **1999**, 96, 3342.
33. Rochet, C.; Lansbury, P. T., *Curr. Opin. Struct. Biol.* **2000**, 10, 60.
34. Zerovnik, E., *Eur. J. Biochem* **2002**, 269, 3362.
35. Fink, A. L., *Fold. Des.* **1998**, 3, 9.
36. Harper, J. D.; Lansbury, P. T. J., *Annu. Rev. Biochem.* **1997**, 66, 385.
37. Okamura, N.; Harada, R.; Furumoto, S.; Arai, H.; Yanai, K.; Kudo, Y., *Curr. Neurol. Neurosci. Rep.* **2014**, 14, 500.
38. Camus, V.; Payoux, P.; Barré, L.; Desgranges, B.; Voisin, T.; Tauber, C., *Eur J. Nucl. Med. Mol. Imaging* **2012**, 39, 621.
39. Winner, B.; Jappelli, R.; Maji, S. K.; Desplats, P. A.; Boyer, L.; Aigner, S.; Hetzer, C.; Loher, T.; Vilar, M.; Campioni, S.; Tzitzilonis, C.; Soragni, A.; Jessberger, S.; Mira, H.; Consiglio, A.; Pham, E.; Masliah, E.; Gage, F. H.; Riek, R., *Proc. Natl. Acad. Sci. U.S.A.* **2011**, 108, 4194.
40. Stefanis, L., *Cold Spring Harb Perspect Med* **2012**, 4, a009399.
41. Paslawski, W.; Andreasen, M.; Nielsen, S. B.; Lorenzen, N.; Thomsen, K.; Kaspersen, J. D.; Pedersen, J. S.; Otzen, D. E., *Biochemistry* **2014**, 53, 6252.
42. Kad, N. M.; Thomson, N. H.; Smith, D. P.; Smith, D. A.; Radford, S. E., *J. Mol. Biol.* **2001**, 313, 559.
43. Brange, J.; Andersen, L.; Laursen, E. D.; Meyn, G.; Rasmussen, E., *J. Pharm. Sci.* **1997**, 86, 517.
44. Abedini, A.; Meng, F.; Raleigh, D. P., *J. Am. Chem. Soc.* **2007**, 129, 11300.
45. Collinge, J., *Annu. Rev. Neurosci.* **2001**, 24, 519.
46. Deng, W.; Cao, A.; Lai, L., *Biochem. Biophys. Res. Commun.* **2007**, 362, 689.
47. Sorgjerd, K.; Klingstedt, T.; Lindgren, M.; Kagedal, K.; Hammarstrom, P., *Biochem. Biophys. Res. Commun.* **2008**, 377, 1072.
48. Nerelius, C.; Fitzen, M.; Johansson, J., *Biochem. Biophys. Res. Commun.* **2010**, 396, 2.
49. Popova, L. A.; Kodali, R.; Wetzel, R.; Lednev, I. K., *J. Am. Chem. Soc.* **2010**, 132, 6324.
50. Colombo, G.; Meli, M.; Simone, A. D., *Proteins* **2008**, 70, 863.
51. Tycko, R., *Q. Rev. Biophys.* **2006**, 39, 1.
52. Inouye, H.; Fraser, P.; Kirschner, D., *Biophys. J.* **1993**, 64, 502.
53. Malinchik, S. B.; Inouye, H.; Szumowski, K.; Kirschner, D., *Biophys. J.* **1998**, 74, 537.
54. Morante, S., *Curr. Alzheimer Res.* **2008**, 5, 508.
55. Hurshman, A. R.; White, J. T.; Powers, E. T.; Kelly, J. W., *Biochemistry* **2004**, 43, 7365.
56. Jain, S.; Udgaonkar, J. B., *J. Mol. Biol.* **2008**, 382, 1228.
57. Modler, A. J.; Gast, K.; Lutsch, G.; Damaschun, G., *J. Mol. Biol.* **2003**, 325, 135.
58. Xue, W. F.; Homans, S. W.; Radford, S. E., *Proc. Natl. Acad. Sci. USA* **2008**, 105, 8926.
59. Lomakin, A.; Chung, D. S.; Benedek, G. B.; Kirschner, D. A.; Teplow, D. B., *Proc. Natl. Acad. Sci. U. S. A.* **1996**, 93, 1125.
60. Wang, J.; Xia, H.; Zhang, Y.; Lu, H.; Kamat, R.; Dobrynin, A. V.; Cheng, J.; Lin, Y., *J. Am. Chem. Soc.* **2013**, 135, 11417–11420.
61. Gillam, J. E.; MacPhee, C. E., *J. Phys.: Condens. Matter* **2013**, 25, 373101.

62. Booth, D. R.; Sunde, M.; Bellotti, V.; Robinson, C. V.; Hutchinson, W. L.; Fraser, P. E.; Hawkins, P. N.; Dobson, C. M.; Radford, S. E.; Blake, C. C.; Pepys, M. B., *Nature* **1997**, 385, 787.
63. Gupta, R.; Yadav, S.; Ahmad, F., *Biochemistry* **1996** 35, 11925
64. Dzwolak, W.; Grudzielanek, S.; Smirnovas, V.; Ravindra, R.; Nicolini, C.; Jansen, R.; Lokszejn, A.; Porowski, S.; Winter, R., *Biochemistry* **2005**, 44, 8948.
65. Bryant, C.; Spencer, D. B.; Miller, A.; Bakaysa, D. L.; McCune, K. S.; Maple, S. R.; Pekar, A. H.; Brems, D. N., *Biochemistry* **1993**, 32, 8075.
66. Basu, A.; Man, C. D.; Basu, R.; Toffolo, G.; Cobelli, C.; Rizza, R. A., *Amer Diabetes Assoc* **2009**, 32, 866.
67. Roberts, R.; Hodson, L.; Dennis, A. L.; Neville, M. J.; Humphreys, S. M.; Harnden, K. E.; K.J.Mickle; Frayn, K. N., *Diabetologia* **2009**, 52, 882.
68. Biolo, G.; Williams, B. D.; Fleming, R. Y. D.; Wolfe, R. R., *Diabetes* **1999**, 48, 949.
69. Westermark, P.; Wernstedt, C.; Wilander, E.; Hayden, D. W.; O'Brien, T. D.; Johnson, K. H., *Proc. Natl. Acad. Sci. U. S. A.* **1987**, 84, 3881.
70. Westermark, P.; Wilander, E., *Diabetologia* **1983**, 24, 342.
71. Ehrlich, J.; Ratner, I. M., *Am. J. Pathol.* **1961**, 38, 49.
72. Sharp, J. S.; Forrest, J. A.; Jones, R. A. L., *Biochemistry* **2002**, 41, 15810.
73. Grudzielanek, S.; Velkova, A.; Shukla, A.; Smirnovas, V.; Tatarek-Nossol, M.; Rehage, H.; Kapurniotu, A.; Winter, R., *J. Mol. Biol.* **2007**, 370, 372.
74. Zako, T.; Sakono, M.; Hashimoto, N.; Ihara, M.; Maeda, M., *Biophys. J.* **2009**, 96, (3331-3340).
75. Heldt, C. L.; Kurouski, D.; Sorci, M.; Grafeld, E.; Lednev, I. K.; Belfort, G., *Biophys. J.* **2011**, 100, 2792.
76. Manno, M.; Craparo, E. F.; Martorana, V.; Bulone, D.; Biagio, P. L. S., *Biophys. J.* **2006**, 90, 4585.
77. Ahmad, A.; Millett, I. S.; Doniach, S.; Uversky, V. N.; Fink, A. L., *Biochemistry* **2003**, 42, 11404.
78. Sluzky, V.; Tamada, J. A.; Klibanov, A. M.; Langer, R., *Proc. Natl. Acad. Sci. U. S. A.* **1991**, 88, 9377.
79. Brange, J., *Galenics of Insulin: The Physico-Chemical and Pharmaceutical Aspects of Insulin and Insulin Preparations*. Springer-Verlag: Berlin/Heidelberg, 1987.
80. Brange, J.; L, L., *Insulin structure and stability. In Stability and Characterization of Protein and Peptide Drugs: Case Histories*. Springer: New York, 1993; p 315.
81. Hong, Y.; Meng, L.; Chen, S.; Wai, C.; Leung, T.; Da, L.-T.; Faisal, M.; Silva, D.-A.; Liu, J.; Lam, J. W. Y.; Huang, X.; Tang, B. Z., *J. Am. Chem.Soc.* **2012**, 134, 1680–1689.
82. Kline, A. D.; R. M. Justice, J., *Biochemistry* **1990**, 29, 2906.
83. Baker, E. N.; Blundell, T. L.; Cutfield, J. F.; Cutfield, S. M.; E. J. Dodson, *Philos. Trans. R. Soc. Lond. B Biol. Sci.* **1988**, 319, 369.
84. Blundell, T. L.; Cutfield, J. F.; Dodson, E. J.; Dodson, G. G.; Hodgkin, D. C.; Mercola, D. A., *Cold Spring Harbor Symp. Quant. Biol.* **1972**, 36, 233.
85. Whittingham, J. L.; Scott, D. J.; Chance, K.; Wilson, A.; Finch, J., *J. Mol. Biol.* **2002**, 318, 479.
86. Sipe, J. D.; Cohen, A. S., *J. Struc. Biol.* **2000**, 130, 88.

87. Campioni, S.; Mannini, B.; Zampagni, M.; Pensalfini, A.; C. Parrini; Evangelisti, E.; A. Relini; Stefani, M.; Dobson, C. M.; C. Cecchi; Chiti, F., *Nat. Chem. Biol.* **2010**, 6, 140.
88. Avidan-Shpalter, C.; Gazit, E., *Amyloid* **2006**, 13, 216.
89. Oliveira, C. L.; Behrens, M. A.; Pedersen, J. S.; Erlacher, K.; Otzen, D., *J. Mol. Biol.* **2009**, 387, 147.
90. Mok, Y. F.; Howlett, G. J., *Meth. Enzymol* **2006**, 413, 199.
91. Zhao, R.; So, M.; Maat, H.; Ray, N. J.; Arisaka, F.; Goto, Y.; Carver, J. A.; Hall, D., *Biophys. Rev* **2016**, 8, 445.
92. Gladytz, A.; Lugovoy, E.; Charvat, A.; Haupl, T.; Siefertmann, K. R.; Abel, B., *Phys. Chem. Chem. Phys.* **2015**, 17, 918.
93. Horvath, I.; Weise, C. F.; Andersson, E. K.; Chorell, E.; Sellstedt, M.; Bengtsson, C.; Olofsson, A.; Hultgren, S. J.; Chapman, M.; Watz, M. W.-.; Almqvist, F.; Wittung-Stafshede, P., *J. Am. Chem. Soc* **2012**, 134, 3439.
94. Khurana, R.; Ionescu-Zanetti, C.; Pope, M.; Li, J.; Nielson, L.; Ramí' rez-Alvarado, M.; Regan, L.; Fink, A. L.; Carter, S. A., *Biophys. J.* **2003**, 85, 1135.
95. Harper, J. D.; Lieber, C. M.; Jr., P. T. L., *Chem. Biol.* **1997**, 4, 951.
96. Measey, T. J.; Schweitzer-Stenner, R., *J. Am. Chem. Soc.* **2011**, 133, 1066.
97. Calero, M.; Gasset, M., *Methods Mol. Biol* **2005**, 299, 129.
98. Margittai, M.; Langen, R., *Q Rev. Biophys.* **2008**, 41, 265.
99. Heise, H., *Chem. Biochem* **2008**, 9, 179.
100. Kim, H. Y.; Cho, M. K.; Kumar, A.; Maier, E.; Siebenhaar, C.; Becker, S.; Fernandez, C. O.; Lashuel, H. A.; Benz, R.; Lange, A.; Zweckstetter, M., *J. Am. Chem. Soc* **2009**, 131, 17482.
101. Bertoncini, C. W.; Celej, M. S., *Curr. Protein Pept. Sci.* **2011**, 12, 206.
102. Cui, M., *Curr. Med. Chem.* **2014**, 21, 82.
103. Yanagisawa, D.; Taguchi, H.; Ibrahim, N. F.; Morikawa, S.; Shiino, A.; Inubushi, T.; Hirao, K.; Shirai, N.; Sogabe, T.; Tooyama, I., *J. Alzheimers Dis.* **2014**, 39, 617.
104. Higuchi, M.; Iwata, N.; Matsuba, Y.; Sato, K.; Sasamoto, K.; Saido, T. C., *Nat. Neurosci.* **2005**, 8, 527.
105. Nordberg, A., *Lancet Neurol.* **2004**, 3, 519.
106. Wang, Y.; Klunk, W. E.; Debnath, M. L.; Huang, G.-F.; Holt, D. P.; Shao, L.; Mathis, C. A., *J. Mol. Neurosci.* **2004**, 24, 55.
107. Cai, L.; Innis, R. B.; Pike, V. W., *Curr. Med. Chem.* **2007**, 14, 19.
108. Amatsubo, T.; Yanagisawa, D.; Morikawa, S.; Taguchi, H.; Tooyama, I., *Magn. Reson. Med. Sci.* **2010**, 9, 95.
109. Querbes, O.; Aubry, F.; Pariente, J.; Lotterie, J. A.; Demonet, J. F.; Duret, V.; Puel, M.; Berry, I.; Fort, J. C.; Celsis, P., *Brain* **2009**, 132, 2036.
110. Tirotta, I.; Dichiarante, V.; Pigliacelli, C.; Cavallo, G.; Terraneo, G.; Bombelli, F. B.; Metrangolo, P.; Resnati, G., *Chem. Rev.* **2015**, 115, 1106.
111. Wadghiri, Y.; Hoang, D.; Wisniewski, T.; Sigurdsson, E., *Methods Mol Biol.* **2012**, 849, 435.
112. XU, M.-m.; REN, W.-m.; TANG, X.-c.; HU, Y.-h.; ZHANG, H.-y., *Acta Pharmacologica Sinica* **2016**, 37, 719.
113. Nelissen, N.; Van Laere, K.; Thurfjell, L.; Owenius, R.; Vandenbulcke, M.; Koole, M., *J. Nucl. Med.* **2009**, 50, 1251.
114. Richards, D.; Sabbagh, M., *Neurol. Ther.* **2014**, 3, 79.

115. Wong, D.; Moghekar, A.; Rigamonti, D.; Brašić, J.; Rousset, O.; Willis, W., *Mol. Imaging. Biol.* **2013**, 15, 230.
116. Ono, M.; Ishikawa, M.; Kimura, H.; Hayashi, S.; Matsumura, K.; Watanabe, H., *Bioorg. Med. Chem.* **2010**, 20, 3885.
117. Ono, M.; Saji, H., *Med. Chem. Commun.* **2015**, 6, 391.
118. Raymond, S.; Skoch, J.; Hills, I.; Nesterov, E.; Swager, T.; Bacskai, B., *Eur J. Nucl. Med. Mol. Imaging* **2008**, 35, S93.
119. Klunk, W. E.; Debnath, M. L.; Pettegrew, J. W., *Neurobiol. Aging* **1994**, 15, 691.
120. Jung, S.-J.; Park, S.-H.; Lee, E. J.; Park, J. H.; Kong, Y. B.; Rho, J. K.; Hur, M. G.; Yang, S. D.; Park, Y. D., *Arch. Pharm. Res.* **2015**, 38, 1992.
121. Zhou, M.; Wang, X.; Liu, Z.; Yu, L.; Hu, S.; Chen, L., *Curr. Alzheimer Res.* **2014**, 11, 221.
122. Cui, M.; Ono, M.; Watanabe, H.; Kimura, H.; Liu, B.; Saji, H., *J. Am. Chem. Soc.* **2014**, 136, 3388.
123. Chang, W. M.; Dakanali, M.; Capule, C. C.; Sigurdson, C. J.; Yang, J.; Theodorakis, E. A., *ACS Chem. Neurosci.* **2011**, 2, 249.
124. Ono, M.; Hayashi, S.; Kimura, H.; Kawashima, H.; Nakayama, M.; Saji, H., *Bioorg. Med. Chem.* **2009**, 17, 7002.
125. Lakowicz, J. R., *Principles of Fluorescence Spectroscopy*. 3rd ed.; Springer: 2003.
126. Gustavsson, T.; Sarkar, N.; Banyasz, A.; Markovitsi, D.; Improta, R., *Chem. Phys.* **2008**, 350, 186.
127. Saha, S. K.; Purkayastha, P.; Das, A. B.; Dhara, S., *J. Photochem. Photobio. A: Chem.* **2008**, 199, 179.
128. Singh, P. K.; Kumbhakar, M.; Pal, H.; Nath, S., *J. Phys. Chem. B* **2010**, 114, 2541.
129. Khurana, R.; Coleman, C.; Ionescu-Zanetti, C.; Carter, S. A.; Krishna, V.; Grover, R. K.; Roy, R.; Singh, S., *J. Struct. Biol.* **2005**, 151, 229.
130. Singh, P. K.; Kumbhakar, M.; Pal, H.; Nath, S., *J. Phys. Chem. B* **2010**, 114, 5920.
131. Freire, S.; Rodriguez-Prieto, F.; Rodriguez, M. C. R.; Penedo, J. C.; Al-Soufi, W.; Novo, M., *Chem. Eu. J.* **2015**, 21, 1.
132. Grynkiewicz, G.; Poenie, M.; Tsein, R. Y., *J. Biol. Chem.* **1985**, 260, 3440.
133. Krystkowiak, E.; Dobek, K.; Burdziński, G.; Maciejewski, A., *Photochem. Photobiol. Sci.* **2012**, 11, 1322.
134. Horng, M.-L.; Gardecki, J. A.; Maroncelli, M., *J. Phys. Chem. A* **1997**, 101, 1030.
135. Lippert, V. Z., *Z. Naturforsch.* **1957**, 10a, 541.
136. Maroncelli, M., *J. Mol. Liq.* **1993**, 57, 1.
137. Maroncelli, M.; Fee, R. S.; Chapman, C. F.; Fleming, G. R., *J. Phys. Chem.* **1991**, 95, 1012.
138. Maroncelli, M.; Fleming, G. R., *J. Chem. Phys.* **1987**, 86, 6221.
139. Nilsson, K. P., *FEBS. Lett* **2009**, 583, 2593.
140. Nesterov, E. E.; Skoch, J.; Hyman, B. T.; Klunk, W. E.; Bacskai, B. J.; Swager, T. M., *Angew Chem. Int. Ed. Engl.* **2005**, 44, 5452.
141. Sen, P.; Roy, D.; Mondal, S. K.; Sahu, K.; Ghosh, S.; Bhattacharyya, K., *J. Phys. Chem. A* **2005**, 43, 9716.

142. Zhang, L.; Kao, Y.-T.; Qiu, W.; Wang, L.; Zhong, D., *J. Phys. Chem. B Letts.* **2006**, 110, 18097.
143. Qiu, W.; Zhang, L.; Okobiah, O.; Yang, Y.; Wang, L.; Zhong, D.; Zewail, A. H., *J. Phys. Chem. B* **2006**, 110, 10540.
144. Taboada, P.; Barbosa, S.; Castro, E.; Gutierrez-Pichel, M.; Mosquera, V., *Chem. Phys.* **2007**, 340, 59.
145. Makarov, V.; Pettitt, B. M.; Feig, M., *Acc. Chem. Res.* **2002**, 35 376.
146. Pant, D.; Levinger, N. E., *Langmuir* **2000**, 16, 10123.
147. Willard, D. M.; Riter, R. E.; Levinger, N. E., *J. Am. Chem. Soc.* **1998**, 120, 4151.
148. Arya, S.; Singh, A. K.; Khan, T.; Bhattacharya, M.; Datta, A.; Mukhopadhyay, S., *J. Phys Chem. Lett.* **2016**, 7, 4105.
149. Kim, Y. S.; Liu, L.; Axelsen, P. H.; Hochstrasser, R. M., *Proc. Natl. Acad. Sci. USA* **2009** 106, 17751.
150. Chong, S.-H.; Ham, S., *Angew. Chem. Int. Ed.* **2014**, 126, 4042.
151. Bhattacharyya, K.; Bagchi, B., *J. Phys. Chem. A* **2000**, 104, 10603.
152. Castner, E. W.; Fleming, G. R.; Bagchi, B.; Maroncelli, M., *J. Chem. Phys.* **1988**, 89, 3519.
153. Fee, R. S.; Maroncelli, M., *Chem. Phys.* **1994**, 183, 235.
154. Fee, R. S.; Milsom, J. A.; Maroncelli, M., *J. Phys. Chem.* **1991**, 95, 5170.
155. Prabhat, K. S. STUDIES ON THE DYNAMICS OF ULTRAFAST PHOTOINDUCED PROCESSES IN CONDENSED PHASE USING THIOFLAVIN-T AND COUMARIN AS THE PROBES. HBNI, Mumbai, 2010.
156. Maroncelli, M., *J. Mol. Liq.* **1993**, 57, 1.
157. Maroncelli, M.; Macinnis, J.; Fleming, G. R., *Science* **1989**, 243, 1674.
158. Förster, T., *Ann. Phys.* **1948**, 2, 55.
159. Stryer, L., *Annu. Rev. Biochem.* **1978**, 47, 819.
160. Mishra, R.; Sjölander, D.; Hammarström, P., *Mol. Biosyst.* **2011**, 7, 1232.
161. Deng, W.; Cao, A.; Lai, L., *Protein sci.* **2008**, 17, 1102.
162. Schierle, G. S. K.; Bertocini, C. W.; Chan, F. T. S.; Goot, A. T. v. d.; Schwedler, S.; Skepper, J.; Schlachter, S.; Ham, T. v.; Esposito, A.; Kumita, J. R.; Nollen, E. A. A.; Dobson, C. M.; Kaminski, C. F., *Chem. Phys. Chem.* **2011**, 12, 1.
163. Ran, C.; Zhao, W.; Moir, R. D.; Moore, A., *PLOS One* **2011**, 6, e19362.
164. Birks, J. B., *Photophysics of Aromatic Molecules*. Wiley: New York, 1970.
165. Xiang, H. F.; Cheng, J. H.; Ma, X. F.; Zhou, X. G.; Chruma, J. J., *Chem. Soc. Rev.* **2013**, 42, 6128.
166. Peccati, F.; Hernando, J.; Blancafort, L. s.; Solans-Monforta, X.; Sodupe, M., *Phys.Chem.Chem.Phys.* **2015**, 17, 19718.
167. Ma, X.; Sun, R.; Cheng, J.; Liu, J.; Gou, F.; Xiang, H.; Zhou, X., *J. Chem. Educ.* **2016**, 93, 345.
168. Pradhan, N.; Jana, D.; Ghorai, B. K.; Jana, N. R., *ACS Appl. Mater. Interfaces* **2015**, 7, 25813–25820.
169. Kawamura, K.; Nakayama, R.; Matsumoto, A.; Fujii, S.; Murashima, T., *J. Pharma. Med. Res.* **2015**, 1, 27.
170. Haidekera, M. A.; Theodorakis, E. A., *Org. Biomol. Chem.* **2007**, 5, 1669.
171. Paul, A.; Samanta, A., *J. Phys. Chem. B* **2008**, 112, 16626.
172. Murudkar, S.; Mora, A. K.; Singh, P. K.; Nath, S., *Chem. Commun.* **2012**, 48, 5301.

173. Haidekker, M. A.; Nipper, M.; Mustafic, A.; Lichlyter, D.; Dakanali, M.; Theodorakis, E. A., Dyes with segmental mobility: molecular rotors. In *Advanced Fluorescence Reporters in Chemistry and Biology I. Fundamentals and Molecular Design*, Demchenko, A. P., Ed. Springer-Verlag: Berlin, 2010; Vol. 8, pp 267.
174. Haidekker, M. A.; Theodorakis, E. A., *J. Biol. Engin.* **2010**, *4*, 11.
175. Gavvala, K.; Satpathi, S.; Hazra, P., *RSC Adv.* **2015**, *5*, 72793.
176. López-Duarte, I.; Vu, T. T.; Izquierdo, M. A.; Bull, J. A.; Kuimova, M. K., *Chem. Commu.* **2014**, *50*, 5282.
177. Raeburn, J.; Chen, L.; Awhida, S.; Deller, R. C.; Vatish, M.; Gibson, M. I.; Adams, D. J., *Soft Matt.* **2015**, *11*, 3706.
178. Singh, P. K.; Kumbhakar, M.; Pal, H.; Nath, S., *Phys. Chem. Chem. Phys.* **2011**, *13*, 8008.
179. Singh, P. K.; Kumbhakar, M.; Pal, H.; Nath, S., *J. Phys. Chem. B* **2009**, *113*, 8532.
180. Akers, W.; Haidekker, M. A., *J. Biomech. Eng.* **2004**, *126*, 340.
181. Stsiapura, V. I.; Maskevich, A. A.; Kuzmitsky, V. A.; Uversky, V. N.; Kuznetsova, I. M.; Turoverov, K. K., *J. Phys. Chem. B* **2008**, *112*, 15893.
182. Haidekker, M. A.; Brady, T. P.; Lichlyter, D.; Theodorakis, E. A., *Bioorg. Chem.* **2005**, *33*, 415.
183. Howell, S.; Dakanali, M.; Theodorakis, E.; Haidekker, M., *J. Fluores.* **2012**, *22*, 457.
184. Groenning, M., *J. Chem. Biol.* **2010**, *3*, 1.
185. Dzwolak, W.; Pecul, M., *FEBS Letts.* **2005**, *579*, 6601.
186. Groenning, M.; Norrman, M.; Flink, J. M.; M. van de Weert; Bukrinsky, J. T.; Schluckebier, G.; Frokjaer, S., *J. Struct. Biol.* **2007**, *159*, 483.
187. Singh, P. K.; Sujana, J.; Mora, A. K.; Nath, S., *J. Photochem. Photobio. A: Chem.* **2012**, *246*, 16.
188. Changenet, P.; Zhang, H.; van der Meer, M. J.; Glasbeek, M.; Plaza, P.; Martin, M. M., *J. Phys. Chem. A* **1998**, *102*, 6716.
189. van der Meer, M. J.; Zhang, H.; Glasbeek, M., *J. Chem. Phys.* **2000**, *112*, 2878.
190. Amdursky, N.; Huppert, D., *J. Phys. Chem. B* **2012**, *116*, 13389.
191. Mudliar, N. H.; Pettiwala, A. M.; Awasthi, A. A.; Singh, P. K., *J. Phys. Chem. B* **2016**, *120*, 12474.
192. Mudliar, N. H.; Sadhu, B.; Pettiwala, A. M.; Singh, P. K., *J. Phys. Chem. B* **2016**, *120*, 10496.
193. Allen, B. D.; Benniston, A. C.; Harriman, A.; Rostron, S. A.; Yu, C., *Phys. Chem. Chem. Phys.* **2005**, *7*, 3035.
194. Lindgren, M.; Sörgjerd, K.; Hammarström, P., *Biophys. J.* **2005**, *88*, 4200.
195. Thompson, A. J.; Herling, T. W.; Kubánková, M. t.; Vyšniauskas, A.; Knowles, T. P. J.; Kuimova, M. K., *J. Phys. Chem. B* **2015**, 10170–10179.
196. Kubankova, M.; Lopez-Duarte, I.; Bull, J. A.; Vadukul, D. M.; Serpell, L. C.; Victor, M. d. S.; Stride, E.; Kuimova, M. K., *Biomaterials* **2017**, *139*, 195.
197. LeVine, H., III, *Amyloid* **2005**, *12*, 5.
198. Biancalana, M.; Koide, S., *Biochim. Biophys. Acta Proteins Proteomics* **2010**, *1804*, 1405.
199. Bayliss, N., *J. Chem. Phys* **1950**, *18*, 292.

200. Kowski, A., *Solvent-shift effect of electronic spectra and excited state dipole moments*. In: *Progress in photochemistry and photophysics*. CRC Press: New York, 1992; p 1.
201. Benhold, H., *Muenchen. Med. Wochenschr.* **1922**, 69, 1537.
202. Divry, P., *J. Neurol. Psychiatr.* **1927**, 27, 643.
203. Westermark, G. T.; Johnson, K. H.; Westermark, P., *Methods Enzymol.* **1999**, 309, 3.
204. Khurana, R.; Uversky, V. N.; Nielsen, L.; Fink, A. L., *J. Biol. Chem* **2001**, 276, 22715.
205. Klunk, W. E.; Debnath, M. L.; Pettegrew, J. W., *Neurobiol. Aging* **1995**, 16, 541.
206. Skovronsky, D. M.; Zhang, B.; Kung, M. P.; Kung, H. F.; Trojanowski, J. Q.; Lee, V. M., *Proc. Natl. Acad. Sci. USA* **2000**, 97, 7609.
207. Schmidt, M. L.; Schuck, T.; Sheridan, S.; Kung, M. P.; Kung, H.; Zhuang, Z. P.; Bergeron, C.; Lamarche, J. S.; Skovronsky, D.; B. I. Giasson; Lee, V. M.; Trojanowski, J. Q., *Am. J. Pathol.* **2001**, 159, 937.
208. Crystal, A. S.; Giasson, B. I.; Crowe, A.; Kung, M. P.; Zhuang, Z. P.; Trojanowski, J. Q.; Lee, V. M., *J. Neurochem.* **2003**, 86, 1359.
209. Zhuang, Z. P.; Kung, M. P.; Hou, C.; Skovronsky, D. M.; Gur, T. L.; Plossl, K.; Trojanowski, J. Q.; Lee, V. M.; Kung, H. F., *J. Med. Chem.* **2001**, 44, 1905.
210. Klunk, W. E.; Bacskai, B. J.; Mathis, C. A.; Kajdasz, S. T.; McLellan, M. E.; Frosch, M. P.; Debnath, M. L.; Holt, D. P.; Wang, Y.; Hyman, B. T., *J. Neuropathol. Exp. Neurol.* **2002**, 61, 797.
211. Robbins, K. J.; Liu, G.; Lin, G.; Lazo, N. D., *J. Phys. Chem. Lett.* **2011**, 2 735.
212. Srivastava, A.; Singh, P. K.; Kumbhakar, M.; Mukherjee, T.; Chattopadhyay, S.; Pal, H.; Nath, S., *Chem. Eur. J.* **2010**, 16, 9257.
213. D'Amico, M.; Di Carlo, M. G.; Groenning, M.; Militello, V.; Vetri, V.; Leone, M., *J. Phys. Chem. Lett.* **2012**, 3, 1596.
214. Singh, P. K.; Mora, A. K.; Nath, S., *Chem. Commun.* **2015**, 51, 14042.
215. Klunk, W. E.; Wang, Y.; Huang, G. F.; Debnath, M. L.; Holt, D. P.; Mathis, C. A., *Life Sci.* **2001**, 69, 1471.
216. Mathis, C. A.; Bacskai, B. J.; Kajdasz, S. T.; McLellan, M. E.; Frosch, M. P.; Hyman, B. T.; Holt, D. P.; Wang, Y.; Huang, G.-F.; Debnath, M. L.; Klunk, W. E., *Bioorg. Med. Chem. Lett.* **2002**, 12, 295.
217. Klunk, W. E.; Engler, H.; Nordberg, A.; Wang, Y.; Blomqvist, G.; Holt, D. P.; Bergström, M.; Savitcheva, I.; Huang, G.-F.; Estrada, S.; Ausén, B.; Debnath, M. L.; Barletta, J.; Price, J. C.; Sandell, J.; Lopresti, B. J.; Wall, A.; Koivisto, P.; Antoni, G.; Mathis, C. A.; Långström, B., *Ann. Neurol.* **2004**, 55, 306.
218. Klunk, W. E.; Mathis, C. A., *Alzheimer Dis. Assoc. Disord.* **2008**, 22, 198.
219. Jung, S.; Park, Y.; Park, J.; Yang, S.; Hur, M.; Yu, K., *Med. Chem. Res.* **2013**, 22 4263.
220. Yang, F.; Lim, G.; Begum, A.; Ubeda, O.; Simmons, M.; Ambegaokar, S., *J. Biol. Chem* **2005**, 280, 5892.
221. Hamaguchi, T.; Ono, K.; Yamada, M., *CNS Neurosci. Ther.* **2010**, 16, 285.
222. Hafner-Bratkovi, D. I.; Gaperi, D. J.; Lojze, M. m.; Mara, B.; Roman, J., *J. Neurochem.* **2008**, 104, 1553.
223. Rabiee, A.; Ebrahim-Habibi, A.; Ghasemi, A.; Nemat-Gorgani, M., *Food Funct.* **2013**, 4, 1474.

224. Ran, C.; Xu, X.; Raymond, S. B.; Ferrara, B. J.; Neal, K.; Bacskai, B. J.; Medarova, Z.; Moore, A., *J. Am. Chem. Soc.* **2009**, 131, 15257.
225. Zhang, X.; Tian, Y.; Li, Z.; Tian, X.; Sun, H.; Liu, H., *J. Am. Chem. Soc.* **2013**, 135, 16397.
226. Thomas, S. W.; Joly, G. D.; Swager, T. M., *Chem. Rev.* **2007**, 107, 1339.
227. Nilsson, K. P. R.; Herland, A.; Hammarstrom, P.; Inganas, O., *Biochemistry* **2005**, 44, 3718.
228. Herland, A.; Nilsson, K. P. R.; Olsson, J. D. M.; Hammarstrom, P.; Konradsson, P.; Inganas, O., *J. Am. Chem. Soc.* **2005**, 127, 2317.
229. Volkova, K. D.; Kovalska, V. B.; Balanda, A. O.; Vermeij, R. J.; Subramaniam, V.; Slominskii, Y. L.; Yarmoluk, S. M., *J. Biochem. Biophys. Methods* **2007**, 70, 727.
230. Kuperman, M. V.; Chernii, S. V.; Losytskyy, M. Y.; Kryvorotenko, D. V.; Derevyanko, N. O.; Slominskii, Y. L.; Kovalska, V. B.; Yarmoluk, S. M., *Anal. Biochem.* **2015**, 484, 9.
231. Volkova, K. D.; Kovalska, V. B.; Balanda, A. O.; Losytskyy, M. Y.; Golub, A. G.; Vermeij, R. J.; Subramaniam, V.; Tolmachevc, O. I.; Yarmoluk, S. M., *Bioorg. Med. Chem.* **2008**, 16, 1452.
232. Schmidt, A.; Pahnke, J., *J. Alzheimers Dis.* **2012**, 30, 651.
233. Ulrich, G.; Ziessel, R.; Harriman, A., *Angew Chem. Int. Ed. Engl.* **2008**, 47, 1184.
234. Ono, M.; Watanabe, H.; Kimura, H.; Saji, H., *ACS Chem. Neurosci.* **2012**, 3, 319.
235. Watanabe, H.; Ono, M.; Matsumura, K.; Yoshimura, M.; Kimura, H.; Saji, H., *Mol. Imaging* **2013**, 12, 338.
236. Hintersteiner, M.; Enz, A.; Frey, P.; ALJaton; Kinzy, W.; Kneuer, R., *Nat. Biotech.* **2005**, 23, 577.
237. Fu, H.; Cui, M.; Zhao, L.; Tu, P.; Zhou, K.; Dai, J.; Liu, B., *J. Med. Chem.* **2015**, 58, 6972.
238. Krebs, M. R. H.; Bromley, E. H. C.; Donald, A. M., *J. Struct. Biol.* **2005**, 149 30.
239. Wu, C.; Wang, Z.; Lei, H.; Duan, Y.; Bowers, M. T.; Shea, J.-E., *J. Mol. Biol.* **2008**, 384, 718.
240. Morris, G. M.; Huey, R.; Lindstrom, W.; Sanner, M. F.; Belew, R. K.; Goodsell, D. S.; Olson, A. J., *J. Comput. Chem.* **2009**, 16, 2785.
241. Birks, J. B., *Photophysics of Aromatic Molecules*. Wiley: New York, 1970.
242. Gilbert, A.; Baggott, J.; Wagner, P. J., *Essential of Molecular Photochemistry*. Blackwell science Inc.: Cambridge, USA, 1991.
243. Rohatgi-Mukherjee, K. K., *Fundamentals of Photochemistry*. Wiley Eastern Ltd: India, 1986.
244. Becker, W., *Advanced time correlated single photon counting technique*. Springer: New York, 2005.
245. Demas, J. N., *Excited state lifetime measurement*. Academic press: New York, 1983.
246. O'Connor, D. V.; Phillips, D., *Time correlated single photon counting*. Academic: New York, 1984.
247. Ware, W. R., Creation and detection of the Excited State. In Lamola, A. A., Ed. Marcel Dekker: New York, 1971; Vol. 1, Part A. .

248. Bevington, P. R., *Data Reduction and Error Analysis for the Physical Sciences*. McGraw-Hill: New York, 1969.
249. Gedcke, D. A.; McDonald, W. J., *Nucl. Instrum. Meth.* **1967**, 55, 377.
250. Gedcke, D. A.; McDonald, W. J., *Nucl. Instrum. Meth.* **1968**, 58, 253.
251. Haugen, G. R.; Wallin, B. W.; Lytle, J. E., *Rev. Sci. Instrum.* **1972**, 50, 64.
252. Yguerabide, J., *Meth. Enzymol* **1972**, 26, 498.
253. McKinnon, A. E.; Szabo, A. G.; Miller, D. R., *J. Phys Chem.* **1977**, 81, 1564.
254. O'Connor, D. V.; Ware, W. R.; Andre, J. C., *J. Phys. Chem.* **1979**, 83, 1333.
255. Ware, W. R.; Doemeny, L. J.; Nemzek, T. L., *J. Phys Chem.* **1973**, 77, 2083.
256. Ito, M.; Kume, H.; Oba, K., *IEEE Trans. Nucl. Sci.* **1984**, NS-31, 408.
257. Bebelaar, D., *Rev. Sci. Instrum.* **1986**, 57, 1116.
258. Mahr, H.; Hirsch, M. D., *Opt. Commun.* **1975**, 13, 96.
259. Duguay, M. A., *Progress in Optics*. Amsterdam, Netherlands, 1976; Vol. XIV.
260. Duguay, M. A.; Hansen, J. M., *Opt. Commun* **1969**, 1, 254.
261. Kahlow, M. A.; Jarzeba, W.; DuBruil, T. P.; Barbara, P. F., *Rev. Sci. Instrum.* **1988**, 59, 1098.
262. Shah, J., *IEEE J. Quant. Elect.* **1988**, 24, 276.
263. Lichtman, J. W.; Conchello, J. A., *Nat. Methods* **2005**, 2, 910.
264. Sekar; Periasamy, *J. Cell Biol.* **2008**, 160, 629.
265. Pandey, N. K.; Ghosh, S.; Dasgupta, S., *J. Phys. Chem. B* **2010**, 114, 10228.
266. Vetri, V.; Canale, C.; Relini, A.; Librizzi, F.; Militello, V.; Gliozzi, A.; Leone, M., *Biophys. Chem.* **2007**, 125, 184.
267. Becke, A. D., *J. Chem. Phys.* **1993**, 98, 5648.
268. Lee, C.; Yang, W.; Parr, R. G., *Phys. Rev. B* **1998**, 37, 785.
269. Frisch, M. J.; Trucks, G. W.; Schlegel, H. B.; Scuseria, G. E.; Robb, M. A.; Cheeseman, J. R.; Montgomery Jr., J. A.; Vreven, T.; Kudin, K. N.; Burant, J. C.; Millam, J. M.; Iyengar, S. S.; Tomasi, J.; Barone, V.; Mennucci, B.; Cossi, M.; Scalmani, G.; Rega, N.; Petersson, G. A.; Nakatsuji, H.; Hada, M.; Ehara, M.; Toyota, K.; Fukuda, R.; Hasegawa, J.; Ishida, M.; Nakajima, T.; Honda, Y.; Kitao, O.; Nakai, H.; Klene, M.; Li, X.; Knox, J. E.; Hratchian, H. P.; Cross, J. B.; Adamo, C.; Jaramillo, J.; Gomperts, R.; Stratmann, R. E.; Yazyev, O.; Austin, A. J.; Cammi, R.; Pomelli, C.; Ochterski, J. W.; Ayala, P. Y.; Morokuma, K.; Voth, G. A.; Salvador, P.; Dannenberg, J. J.; Zakrzewski, V. G.; Dapprich, S.; Daniels, A. D.; Strain, M. C.; Farkas, O.; Malick, D. K.; Rabuck, A. D.; Raghavachari, K.; Foresman, J. B.; Ortiz, J. V.; Cui, Q.; Baboul, A. G.; Clifford, S.; Cioslowski, J.; Stefanov, B. B.; Liu, G.; Liashenko, A.; Piskorz, P.; Komaromi, I.; Martin, R. L.; Fox, D. J.; Keith, T.; Al-Laham, M. A.; Peng, C. Y.; Nanayakkara, A.; Challacombe, M.; Gill, P. M. W.; Johnson, B.; Chen, W.; Wong, M. W.; Gonzalez, C.; Pople, J. A., *GAUSSIAN 03, Revision C. 01*. Gaussian, Inc.: Wallingford, CT, 2004.
270. Morris, G. M.; Goodsell, D. S.; Halliday, R. S.; Huey, R.; Hart, W. E.; Belew, R. K.; Olson, A. J., *J. Comput. Chem.* **1998**, 19, 1639.
271. Xiao, Y.; Ma, B.; McElheny, D.; Parthasarathy, S.; Long, F.; Hoshi, M.; Nussinov, R.; Ishii, Y., *Nat. Struct. Mol. Biol.* **2015**, 22, 499.
272. Dragan, A. I.; Casas-Finet, J. R.; Bishop, E. S.; Strouse, R. J.; Schenerman, M. A.; Geddes, C. D., *Biophys. J.* **2010**, 99, 3010.
273. Okoshi, M.; Saparpakorn, P.; Takada, Y.; Hannongbua, S.; Nakai, H., *Bull. Chem. Soc. Jpn.* **2014**, 87, 267.
274. Dragan, A.; Graham, A. E.; Geddes, C. D., *J. Fluores.* **2013**, 24, 397.

275. Zipper, H.; Brunner, H.; Bernhagen, J.; Vitzthum, F., *Nucleic Acids Res.* **2004**, 32, e103.
276. Manno, M.; Giacomazza, D.; Newman, J.; Martorana, V.; Biagio, P. L. S., *Langmuir* **2010**, 26, 1424.
277. Pagano, R. S.; Medus, M. x. L. p.; Go´mez, G. E.; Couto, P. M.; Labanda, M. a. S.; Landolfo, L.; D’Alessio, C.; Caramelo, J. J., *Biophys. J.* **2014**, 107, 711.
278. Benesi, M. L.; Hildebrand, J. H., *J. Am. Chem. Soc.* **1949**, 71, 2703.
279. Singh, C.; Modak, B.; Mondal, J. A.; Palit, D. K., *J. Phys. Chem. A* **2011**, 115, 8183.
280. Sabate, R.; Saupe, S. J., *Biochem. Biophys. Res. Comm.* **2007**, 360, 135.
281. Allsop, D.; Swanson, L.; Moore, S.; Davies, Y.; York, A.; El-Agnaf, O. M. A.; Soutar, I., *Biochem. Biophys. Res. Comm.* **2001**, 285, 58.
282. Crespi, F.; Croce, A. C.; Fiorani, S.; Masala, B.; Heidbreder, C.; Bottioli, G., *Lasers Surg. Med.* **2004**, 34, 39.
283. Kitts, C. C.; Bout, D. A. V., *J. Phys. Chem. B* **2009**, 113, 12090.
284. Lackowicz, J. R., *Principles of fluorescence spectroscopy*. 3rd ed.; Springer: New York, 2006.
285. Weast, R. C., *CRC Handbook of Chemistry and Physics*. The Chemical Rubber Co.: 1970.
286. Sackett, D. L.; Wolff, J., *Anal. Biochem.* **1987**, 167, 228.
287. Neunert, G.; Polewski, P.; P.Walejko; Markiewicz, M.; S.Witkowski; Polewski, K., *Spectrochim. Acta Part A* **2009**, 73, 301.
288. Förster, T.; Hoffmann, G., *Z. Phys. Chem.* **1971**, 75, 63.
289. Park, M.; Im, D.; Rhee, Y. H.; Joo, T., *J. Phys. Chem. A* **2014**, 118, 5125–5134.
290. Coto, P. B.; Serrano-Andres, L.; Gustavsson, T.; Fujiwara, T.; Lim, E. C., *Phys. Chem. Chem. Phys.* **2011**, 13, 15182.
291. Aloise, S.; Pawlowska, Z.; Ruckebusch, C.; Sliwa, M.; Dubois, J.; Poizat, O.; Buntinx, G.; Perrier, A.; Maurel, F.; Jacques, P., *Phys. Chem. Chem. Phys.* **2012**, 14, 1945.
292. Mandal, U.; Adhikari, A.; Dey, S.; Ghosh, S.; Mondal, S. K.; Bhattacharyya, K., *J. Phys. Chem. B* **2007**, 111, 5896.
293. Parkinson, P.; Müller, C.; Stingelin, N.; Johnston, M. B.; Herz, L. M., *J. Phys. Chem. Lett.* **2010**, 1, 2788.
294. Horng, M. L.; Gardecki, J. A.; Papazyan, A.; Maroncelli, M., *J. Phys. Chem.* **1995**, 99, 17311.
295. Singh, P. K.; Nath, S., *J. Photochem. Photobio. A: Chem.* **2012**, 248, 42.
296. Changenet, P.; Zhang, H.; van der Meer, M. J.; Hellingwerf, K. J.; Glasbeek, M., *Chem. Phys. Lett.* **1998**, 282, 276.
297. Koti, A. S. R.; Krishna, M. M. G.; Periasamy, N., *J. Phys. Chem. A* **2001**, 105, 1767.
298. Koti, A. S. R.; Periasamy, N., *Proc. Indian Acad. Sci. (Chem. Sci.)* **2001**, 113, 157.
299. Koti, A. S. R.; Periasamy, N., *J. Chem. Phys.* **2001**, 115, 7094.
300. Park, M.; Kim, C. H.; Joo, T., *J. Phys. Chem. A* **2013**, 117, 370.
301. Stsiapura, V. I.; Maskevich, A. A.; Kuzmitsky, V. A.; Turoverov, K. K.; Kuznetsova, I. M., *J. Phys. Chem. A* **2007**, 111, 4829.

302. Rodríguez-Rodríguez, C.; Rimola, A.; Rodríguez-Santiago, L.; Ugliengo, P.; Álvarez-Larena, A.; Gutiérrez-De-Terán, H.; Sodupe, M.; González-Duarte, P., *Chem. Commun.* **2010**, 46, 1156.
303. Maskevich, A. A.; Stsiapura, V. I.; Kuzmitsky, V. A.; Kuznetsova, I. M.; Povarova, O. I.; Uversky, V. N.; Turoverov, K. K., *J. Proteome Res.* **2007**, 6, 1392.
304. Lockhart, A.; Ye, L.; Judd, D. B.; Merrittu, A. T.; Lowe, P. N.; Morgenstern, J. L.; Hong, G.; Gee, A. D.; Brown, J., *J. Biol. Chem.* **2005**, 280, 7677.
305. Yona, R. L.; Mazeris, S.; Faller, P.; Gras, E., *ChemMedChem* **2008**, 3, 63.
306. Nelissen, N.; Van Laere, K.; Thurfjell, L.; Owenius, R.; Vandembulcke, Koole, M., *J. Nucl. Med.* **2009**, 50, 1251.
307. Masuhara, H.; Hino, T.; Mataga, N., *J. Phys. Chem.* **1975**, 79, 994.
308. Nad, S.; Kumbhakar, M.; Pal, H., *J. Phys. Chem. A* **2003**, 107, 4808.
309. Satpati, A. K.; Kumbhakar, M.; Nath, S.; Pal, H., *Photochem. Photobiol.* **2009**, 85, 119.
310. Senthilkumar, S.; Nath, S.; Pal, H., *Photochem. Photobiol.* **2004**, 80, 104.
311. Nath, S.; Pal, H.; Sapre, A. V., *Chem. Phys. Letts.* **2002**, 360, 422.
312. Lippert, V. E., *Z. Electrochem.* **1957**, 61, 962.
313. Hard, T.; Fan, P.; Kearns, D. R., *Photochem. Photobiol.* **1990**, 51, 77.
314. Robbins, K. J.; Liu, G.; Selmani, V.; Lazo, N. D., *Langmuir* **2012**, 28, 16490–16495.
315. Barik, A.; Nath, S.; Pal, H., *J. Chem. Phys.* **2003**, 119, 10202.
316. Arbeloa, T. L.; Arbeloa, F. L.; Estevez, M. J. T.; Arbeloa, I. L., *J. Lumin.* **1994**, 59, 369.
317. Arbeloa, T. L.; Arbeloa, F. L.; Estevez, M. J. T.; Arbeloa, I. L., *J. Phys. Chem.* **1993**, 97, 4704.
318. Kamlet, M. J.; Abboud, J. L. M.; Taft, R. W., *An examination of linear solvation energy relationships. In Progress in Physical Organic Chemistry*. John Wiley & Sons: New York., 1981; Vol. 13.
319. Marcus, Y., *J. Soln. Chem.* **1991**, 20, 929.
320. Barik, A.; Kumbhakar, M.; Nath, S.; Pal, H., *Chem. Phys.* **2005**, 315, 277.
321. Shirota, H.; Pal, H.; Tominaga, K.; Yoshihara, K., *J. Phys. Chem.* **1996**, 100, 14575.
322. Sasmal, D. K.; Dey, S.; Das, D. K.; Bhattacharyya, K., *J. Chem. Phys.* **2009**, 131, 44509.
323. Barik, A.; Goel, N. K.; Priyadarsini, K. I.; Mohan, H., *J. Photosci.* **2004**, 11, 95.
324. Kahlow, M. A.; Kang, T. J.; Barbara, P. F., *J. Chem. Phys.* **1988**, 88, 2372.
325. LeVine, H., III, *Protein Sci.* **1993**, 2, 404.
326. Murudkar, S.; Mora, A. K.; Jakka, S.; Singh, P. K.; Nath, S., *J. Photochem. Photobiol. A: Chem.* **2014**, 295, 17.
327. Sabate, R.; Lascu, I.; Saupe, S. J., *J. Struct. Biol.* **2008**, 162, 387.
328. Davis, J.; Van Nostrand, W. E., *Proc. Natl. Acad. Sci. U. S. A.* **1996**, 93, 2996.
329. Luheshi, L. M.; Tartaglia, G. G.; Brorsson, A.-C.; Pawar, A. P.; Watson, I. E.; Chiti, F.; Vendruscolo, M.; Lomas, D. A.; Dobson, C. M.; Crowther, D. C., *PLoS Biol.* **2007** 5, e290.
330. Wu, C.; Bowers, M. T.; Shea, J.-E., *Biophys. J.* **2011**, 100, 1316.
331. Deane, R.; Bell, R. D.; Sagare, A.; Zlokovic, B. V., *CNS & Neurological Disorders - Drug Targets* **2009**, 8, 16.

332. Tran, N., *Blood Brain Barrier*. Springer New York, 2011; p 426.
333. Ballabh, P.; Braun, A.; Nedergaard, M., *Neurobiol. Dis.* **2004**, 16, 1.
334. Gosselet, F.; Saint-Pol, J.; Candela, P.; Fenart, L., *Curr. Alzheimer Res.* **2013**, 10, 1015.
335. Banks, W. A.; Kastin, A. J., *Brain Research Bulletin* **1985**, 15, 287.
336. Waterhouse, R. N., *Molecular Imaging & Biology* **2003**, 5, 376.
337. Pardridge, W. M., *NeuroRX* **2005**, 2, 3.
338. Tsuji, A., *J. Am. Soc. Exp. NeuroTherap.* **2005**, 2, 54.
339. Helvoort, A. V.; Smith, A. J.; Sprong, H.; Fritzsche, I.; A.H.Schinkel; Borst, P.; Meer, G. v., *Cell* **1996**, 87, 507.
340. Graaf, D. D.; Sharma, R. C.; Mechetner, E. B.; Schimke, R. T.; Ronninson, I. B., *Proc. Natl. Acad. Sci. USA* **1996**, 93, 1238.
341. Mazák, K. r.; Noszál, B. l., *J. Med. Chem.* **2012**, 55, 6942.
342. Wang, N.; Jin, X.; Zhu, X., *RSC Adv.* **2017**, 7, 20766.
343. Volkova, K. D.; Kovalska, V. B.; Yarmoluk, S. M., *Biotechnic & Histochemistry* **2007**, 82, 201.
344. Kroeger, T.; Frieg, B.; Zhang, T.; Hansen, F. K.; Marmann, A.; Proksch, P.; Nagel-Steger, L.; Groth, G.; Smits, S. H. J.; Gohlke, H., *PLOS One* **2017**, 12, e0177024.
345. Niesen, F. H.; Berglund, H.; Vedadi, M., *Nat. Protoc.* **2007**, 2, 2212.
346. Layton, C. J.; Hellinga, H. W., *Prot. sci* **2011**, 20, 1439.
347. TH, S.; LJ, J.; RP, H.; VL, S., *Anal. Biochem.* **1996**, 239, 223.
348. Lo, M.-C.; Aulabaugh, A.; Jin, G.; Cowling, R.; Bard, J.; Malamas, M.; Ellestad, G., *Anal. Biochem.* **2004**, 332, 153.
349. Wong, A. G.; Raleigh, D. P., *Protein Sci.* **2016**, 25, 1834.
350. Kuznetsova, I. M.; Sulatskaya, A. I.; Uversky, V. N.; Turoverov, K. K., *PLoS One* **2012**, 7, e30724.
351. Guo, S.; Akhremitchev, B. B., *Biomacromolecules* **2006**, 7, 1630.
352. Neumann, M.; Gabel, D., *J. Histochem. Cytochem.* **2002**, 50, 437.
353. IUPAC, *Compendium of Analytical Nomenclature: Definitive Rules*. Pergamon Press: Oxford, 1981.
354. M.Pettiwala, A.; K.Sing, P., *Spectrochim. Acta A* **2018**, 188, 120.
355. Bajorek, A.; Trzebiatowska, K.; Beata Je, d.; Pietrzak, M.; Gawinecki, R.; Jerzy Pa, c., *J. Fluores.* **2004**, 14, 295.
356. Moyano, F.; Silber, J. J.; Correa, N. M., *J. Colloid Interface Sci.* **2008**, 317, 332.
357. Abdel-Halim, S. T.; Awad, M. K., *J. Mol. Struct.* **2009**, 920, 332.
358. Bojt'ar, M. a.; Szak'acs, Z. a.; Hessz, D. o.; Kubinyi, M. o.; Bitter, I. a., *RSC Adv.*, 2015, 5, 26504–26508 **2015**, 5, 26504.
359. Hirose, Y.; Yui, H.; Sawada, T., *J. Phys. Chem. B* **2004**, 108, 9070.
360. Kuimova, M. K., *Phys. Chem. Chem. Phys.* **2012**, 14, 12671.
361. Liley, P. E.; Makita, T.; Tanaka, Y., Properties of Inorganic and Organic Fluids. In Ho, C. Y., Ed. Hemisphere: New York, 1988.
362. Saltiel, J.; Megarity, E. D., *J. Am. Chem. Soc* **1972**, 94, 2742.
363. Wróblewski, S.; Trzebiatowska, K.; Jędrzejewska, B.; Pietrzak, M.; Gawinecki, R.; Pączkowski, J., *J. Chem. Soc. : Perkin Trans. 2* **1999**, 0, 1909.
364. Choudhury, S. D.; Bhasikuttan, A. C.; Pal, H.; Mohanty, J., *Langmuir* **2011**, 27, 12312.

365. Mudliar, N.; Singh, P. K., *Chem. Eur. J.* **2016**, 10.1002/chem.201600925.
366. Zerovnik, E., *Eur. J. Biochem.* **2002**, 269, 3362.
367. Dovidchenko, N. V.; Leonova, E. I.; Galzitskaya, O. V., *Biochemistry* **2014**, 79, 1515.
368. Aroraa, A.; Hab, C.; Park, C. B., *FEBS Lett.* **2004**, 564, 121.
369. Sood, A.; Abid, M.; Sauer, C.; Hailemichael, S.; Foster, M.; Török, B.; Török, M., *Bioorg. Med. Chem. Lett.* **2011**, 21, 2044.
370. Zhang, H.; Xu, L.-Q.; Perrett, S., *Methods* **2011**, 53, 285.
371. Janus, C.; Chishti, M. A.; Westaway, D., *Biochim. Biophys. Acta* **2000**, 1502, 63.
372. Pepys, M. B.; Herbert, J.; Hutchinson, W. L.; Tennent, G. A.; Lachmann, H. J.; Gallimore, J. R.; Lovat, L. B.; Bartfai, T.; Alanine, A.; Hertel, C.; Hoffmann, T.; Jakob-Roetne, R.; Norcross, R. D.; Kemp, J. A.; Yamamura, K.; Suzuki, M.; Taylor, G. W.; Murray, S.; Thompson, D.; Purvis, A.; Kolstoe, S.; Wood, S. P.; Hawkins, P. N., *Nature* **2002**, 417, 254.
373. Bhowmik, D.; MacLaughlin, C. M.; Chandrakesan, M.; Ramesh, P.; Venkatramani, R.; Walker, G. C.; Maiti, S., *Phys. Chem. Chem. Phys.* **2014**, 16, 885.
374. Jahn, T. R.; Radford, S. E., *FEBS J.* **2005**, 272, 5962.
375. Ball, P., *Chem. Rev.* **2008**, 108, 74.
376. Chong, S.-H.; Ham, S., *Proc. Natl. Acad. Sci. USA* **2012**, 109, 7636.
377. Simone, A. D.; Dodson, G. G.; Verma, C. S.; Zagari, A.; Fraternali, F., *Proc. Natl. Acad. Sci. USA* **2005**, 102, 7535.
378. Movaghati, S.; Moosavi-Movahedi, A. A.; Khodaghali, F.; Digaleh, H.; Kachooei, E.; Sheibani, N., *Colloids Surf B Biointerfaces* **2014**, 122, 341.
379. Pandey, N. K.; Ghosh, S.; Nag, N. V.; Dasgupta, S., *J. Biomol. Struct. Dyn.* **2014**, 32, 1366.
380. Taboada, P.; Barbosa, S.; Castro, E.; Mosquera, V., *J. Phys. Chem. B* **2006**, 110, 20733.
381. Kelkar, D. A.; Chattopadhyay, A., *Biophys. J.* **2005**, 88, 1070.
382. Kumaran, R.; Ramamurthy, P., *J. Fluoresc.* **2011**, 21, 1499.
383. Sahoo, B.; Balaji, J.; Nag, S.; Kaushalya, S. K.; Maiti, S., *J. Chem. Phys.* **2008**, 19, 75103.
384. Siemiarczuk, A.; Petersen, C. E.; Ha, C.-E.; Yang, J.; Bhagavan, N. V., *Cell Biochem. Biophys.* **2004**, 40, 115.
385. Juarez, J.; Taboada, P.; Mosquera, V., *Biophys. J.* **2009**, 96, 2353.
386. Josue, J.; Manuel, A.; Adriana, C.; Antonio, T.; Silvia, B.; Pablo, T.; Victor, M., *Soft Matter* **2012**, 8, 3608.
387. Juarez, J.; Lopez, S. G.; Cambon, A.; Taboada, P.; Mosquera, V., *J. Phys. Chem. B* **2009**, 113, 10521.
388. Juarez, J.; Alatorre-Meda, M.; Cambon, A.; Topete, A.; Barbosa, S.; Taboada, P.; Mosquera, V., *Soft Matter* **2012**, 8, 3608.
389. Pablo, T.; Silvia, B.; Emilio, C.; Victor, M., *J. Phys. Chem.* **2006**, 110, 20733.
390. Bhattacharya, S.; Pandey, N. K.; Roy, A.; Dasgupta, S., *Int. J. Biol. Macromol.* **2014**, 70, 312.
391. Gelamo, E. L.; Tabak, M., *Spectrochim. Acta, Part A* **2000**, 56A, 2255.
392. Chen, Y.; Barkley, M. D., *Biochemistry* **1998**, 37, 9976.
393. Vivian, J. T.; Callis, P. R., *Biophys. J.* **2001**, 80, 2093.

394. Sugio, S.; Kashima, A.; Mochizuki, S.; Noda, M.; Kobayashi, K., *Protein Eng.* **1999**, 12, 439.
395. Aklu, M.; Cessna, S. G.; Wurku, Y., *FASEB J.* **2007**, 21, (6), A1025.
396. Buzady, A.; Erostyak, J.; Somogyi, B., *Biophys. Chem.* **2000**, 88, 153.
397. Schiro, G.; Vetri, V.; F, N.; M, K. M.; Leone, M.; Cupane, A., *J. Phys. Chem. B* **2014**, 118, 2913.
398. Schiro, G.; Vetri, V.; Frick, B.; Militello, V.; Leone, M.; Cupane, A., *J. Phys. Chem. Lett.* **2012**, 3, 992.
399. Zheng, J.; Jang, H.; Ma, B.; Tsai, C.-J.; Nussinov, R., *Biophys. J.* **2007**, 93, 3046.
400. Mely, Y.; Duportail, G., *Fluorescent Methods to Study Biological Membranes*. Springer: 2012.
401. Jurkiewicz, P.; S'ykora, J.; .zy'nska, A. O.; Humpol'ı'ckov', J.; Hof, M., *J. Fluoresc* **2005**, 15, 883.
402. Richert, R., *J. Chem. Phys* **2001**, 115, 1429.
403. Rieber, K.; S'ykora, J.; Olzy'nska, A.; Jelinek, R.; Cevc, G.; Hof, M., *Biochim. Biophys. Acta* **2007**, 1768, 1050.
404. Richert, R., *J. Chem. Phys.* **2001**, 114, 7471.
405. Goldsbury, C.; Frey, P.; Olivieri, V.; Aebi, U.; Muller, S. A., *J. Mol. Biol.* **2005**, 352, 282.
406. Paravastua, A. K.; Leapmanb, R. D.; Yaua, W.-M.; Tyckoa, R., *Proc. Natl. Acad. Sci. USA* **2008**, 105, 18349.
407. Bauer, H. H.; Aebi, U.; Häner, M.; Hermann, R.; Müller, M.; Arvinte, T.; Merkle, H. P., *J. Struc. Biol.* **1995**, 115, 1.
408. Sarkar, B.; Mithu, V. S.; Chandra, B.; Mandal, A.; Chandrakesan, M.; Bhowmik, D.; Madhu, P. K.; Maiti, S., *Angew. Chem. Int. Ed.* **2014**, 53 6888.
409. Kamal, J. K. A.; Behere, D. V., *J. Biol. Inorg. Chem.* **2002**, 7, 273.
410. Fu, H.; Cui, M.; Zhao, L.; Tu, P.; Zhou, K.; Dai, J.; Liu, B., *J. Med. Chem.* **2015**, 58, 6972.
411. Zhang, X.; Tian, Y.; Zhang, C.; Tian, X.; Ross, A. W.; Moir, R. D.; Sun, H.; Tanzi, R. E.; Moore, A.; Ran, C., *Proc. Natl. Acad. Sci. U. S. A.* **2015**, 31, 9734.